Constrained Control for Load Alleviation in Very Flexible Aircraft

by

Mateus de Freitas Virgilio Pereira

A dissertation submitted in partial fulfillment
of the requirements for the degree of
Doctor of Philosophy
(Aerospace Engineering)
in the University of Michigan
2022

Doctoral Committee:

Professor Carlos E. S. Cesnik, Co-Chair
Professor Ilya V. Kolmanovsky, Co-Chair
Professor Peter Seiler
Dr. Fabio Vetrano

Mateus de Freitas Virgilio Pereira
mfvp@umich.edu
ORCID iD: 0000-0002-7654-021X

ACKNOWLEDGMENTS

I would like to thank my co-advisors Prof. Carlos E. S. Cesnik and Prof. Ilya Kolmanovsky for their support and guidance.

I would also like to thank Bernardo Monteiro, Bilal Sharqi, Braden Frigoletto, Dominic Liao-McPherson, Christopher Lupp, Cristina Riso, Divya Sanghi, Fabio Vetrano (Airbus), Guilherme Barbosa, Leandro Lustosa, Mauricio Pajon, Molong Duan, Rafael Bertolin, Thiago Guimaraes, Thiago Versiani, and Xiao Li for their help in the development of this work.

This material is based upon work supported by Airbus in the frame of the Airbus-Michigan Center for Aero-Servo-Elasticity of Very Flexible Aircraft (CASE-VFA).

TABLE OF CONTENTS

LIST OF FIGURES

FIGURE

LIST OF TABLES

TABLE

LIST OF APPENDICES

LIST OF ACRONYMS

A^{2}SRL Active Aeroelasticity and Structures Research Laboratory

B2T Bottom-to-Top

BFGS Broyden–Fletcher–Goldfarb–Shanno

CASE-VFA Center for Aero-Servo-Elasticity of Very Flexible Aircraft

CL Closed Loop

CS Control Surface

DAQ Data Acquisition

DOF Degree of Freedom

EASE Enhanced Aeroservoelastic

ECG Extended Command Governor

FA Flexible Aircraft

FCS Flight Control System

FSI Fluid-Structure Interaction

GE Generalized Equation

GLA Gust Load Alleviation

GTA Generic Transport Aircraft

HALE High-Altitude Long-Endurance

HTP Horizontal Tail Plane

ILC Inner-Loop Controller

IMU Inertial Measurement Unit

INS Inertial Navigation System

KS Kreisselmeier-Steinhauser

LA Load Alleviation

LICQ Linear Independence Constraint Qualification

LIDAR Light Detection and Ranging

LMI Linear Matrix Inequality

LOS Line of Sight

LPV Linear Parameter Varying

LQG Linear Quadratic Gaussian

LQ-I Linear Quadratic Integral

LQR Linear Quadratic Regulator

LTI Linear Time Invariant

MLE Maximum Likelihood Estimator

MINLP Mixed Integer Nonlinear Programming

MLA Maneuver Load Alleviation

MOR Model Order Reduction

MPC Model Predictive Control

MPCS Model Predictive Control via Scenario Optimization

MVS Maneuver Stretched Vertical

NLP Nonlinear Programming

NMPC Nonlinear Model Predictive Control

NMPC-AC Nonlinear Model Predictive Control with Aggregated Constraints

OCP Optimal Control Problem

OL Open Loop

OOP Out-of-Plane

PaPA Pitch and Plunge Apparatus

PID Proportional-Integral-Derivative

PWM Pulse-Width Modulation

QCQP Quadratically Constrained Quadratic Program

QP Quadratic Programming

RG Reference Governor

ROM Reduced-Order Model

RT Real Time

SOSC Second-Order Sufficient Optimality Condition

SQP Sequential Quadratic Programming

SSOSC Strong Second-Order Sufficient Optimality Condition

T2B Top-to-Bottom

UM/NAST University of Michigan's Nonlinear Aeroelastic Simulation Toolbox

VFA Very Flexible Aircraft

ABSTRACT

Air travel has had an increasing contribution to global CO_2 and non-CO_2 emissions, and climate change. Compelled by the need for a greener aviation industry, aircraft designs are evolving toward higher aspect ratio wings to improve aerodynamic performance and reduce fuel consumption. Consequently, these vehicles are becoming increasingly flexible, thus more vulnerable to structural failure, especially when performing maneuvers or during encounters with gusts.

In this work, constrained control methods are investigated to design maneuver and gust load alleviation systems to keep the loads on these very flexible aircraft within safety limits. Two control architectures based on Model Predictive Control are proposed: one that integrates the automatic pilot and the load alleviation objectives into a single system; and the other that augments an existing flight control system with a reference governor to enable load alleviation. Load alleviation is achieved by performing shape control of the flexible structure by imposing curvature constraints on critical stations on the wing and tail. Linear and nonlinear Model Predictive Control designs are considered for aircraft with different levels of flexibility, as well as a formulation based on scenario optimization for handling multiple mass configurations. For gust load alleviation, feedforward control is applied based on disturbance preview provided by LIDAR measurements.

Because these vehicles are infinite dimensional systems, the main obstacle to the deployment of these load alleviation systems is their computational cost. The control design for these large-scale systems is tackled by using model order reduction techniques and strategies to reduce the constrained control implementation cost. The use of linear and nonlinear reduced-order aeroservoelastic models for prediction in Model Predictive Control is studied. Furthermore, methods to reduce the number of constraints are proposed. In particular, constraint aggregation methods in optimal control are investigated by applying sensitivity analysis tools. It is shown that these methods can yield significant reductions in the computational footprint of Model Predictive Control.

The proposed load alleviation system is tested in a wind tunnel experiment. A half-aircraft model with a very flexible wing and free pitch is used to assess the performance of the controller in enforcing constraints on the vehicle while performing a longitudinal maneuver.

Experimental results are presented to showcase the potential of the proposed system in addressing multiple objectives in load alleviation and its successful implementation in real time.

CHAPTER 1

Introduction

1.1 Motivation

Commercial aircraft designs are evolving towards being increasingly lightweight, having high-aspect ratio and becoming flexible in order to improve aerodynamic performance and meet increasingly demanding flight mission specifications, such as reduced fuel consumption, heavier payload and greater range and endurance [9]. Modern designs of High-Altitude Long-Endurance (HALE) aircraft have gained great attention in academia recently, and the need to develop them has boosted the development of new multidisciplinary analysis methodologies for these vehicles. The Airbus Zephyr (Fig. 1.1a) is an example of platform that exploit the capabilities of very flexible aircraft. The next generation of commercial aircraft, such as the Airbus ZEROe Turbofan (Fig. 1.1b), may benefit from these design concepts in order to optimize vehicle performance.

(a) Airbus Zephyr [10]
(Airbus S.A.S. 2017 - All rights reserved).

(b) Airbus ZEROe Turbofan [11]
(Airbus S.A.S. 2022 – All rights reserved).

Figure 1.1: Examples of very flexible aircraft.

The design of very flexible vehicles has brought significant challenges to aeronautical engineering since it requires geometrically nonlinear structural models for the primary structures

in order to fully capture the large deformations that are likely to appear when the vehicle is subjected to operational loads [12]. Since natural structural vibration characteristics of these vehicles are of low frequency, a strong coupling between structural and rigid body modes is expected, resulting in a significant impact on the aerodynamic properties and the vehicle stability. From a control design standpoint, the large static and dynamic deformations in very flexible aircraft introduce state-dependent variations in the aircraft dynamics, and thus linear time invariant models may no longer be suitable to describe the motion of the aircraft. A unified aeroelastic model that simultaneously incorporates rigid-body, elastic and aerodynamic contributions is needed [13].

The high-aspect ratio configuration goes against the intent of designing robust and strong structures with respect to forces induced by flight maneuvers, wind gusts and turbulence. The long spans and flexible structures usually result in an increase of the torsion and bending moment loads on the wing, which can ultimately lead to failure. Such issue is even worse when the aircraft performs a maneuver or encounters gusts. One way to cope with this problem is the development of maneuver and gust load alleviation systems (MLA and GLA, respectively), which reduce the load impact on the structure by deflecting the control surfaces [14]. MLA systems typically use trailing edge deflection to concentrate lift inboard and reduce wing bending moment, while GLA techniques also use control surfaces to attenuate the rigid body and elastic responses to measurable disturbances. Studies have shown that the combination of MLA and GLA may yield significant aero-structural benefits. For instance, a MLA system can typically achieve cost and fuel savings of 3.1% and 4.3% for rigid-body aircraft, respectively, and the addition of a GLA system may double such benefits [1]. Figure 1.2 shows the comparison of weight and cost gains for a rigid-body aircraft with MLA and GLA systems. Similar results are expected for flexible aircraft.

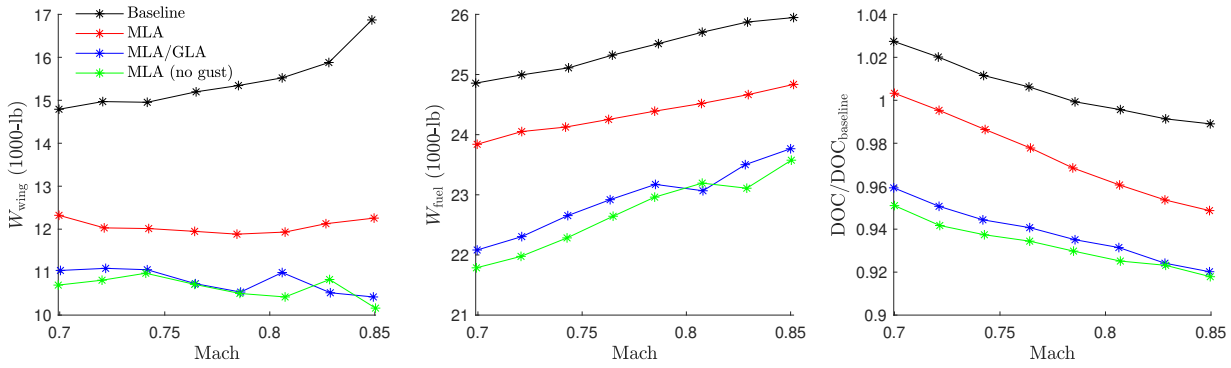

Figure 1.2: Optimized aircraft direct operating cost (DOC) and weight parameters as functions of cruise Mach number [1].

Control and estimation algorithms are necessary to exploit conventional and non-conventional control effectors for MLA and GLA in flexible aircraft. Existing work addressed some specific cases with specific solutions (e.g., coordinated control of ailerons/spoilers to reduce wing curvature) and several MLA/GLA systems have been implemented in production, tested in experiments and researched in simulations. A systematic control design framework that allows the optimal coordination of multiple conventional and non-conventional control effectors is desirable for effective MLA/GLA in increasingly flexible aircraft and very flexible aircraft that exhibits larger maneuver and gust load sensitivity.

1.2 Literature Review

In this section, the GLA and MLA control design objectives are presented, as well as control strategies that have been proposed in the literature or implemented in commercial aircraft. Control techniques found in the literature span from classical control theory to modern optimal control methods. A special emphasis is given to constrained control approaches due to their unique features that will be highlighted in the next sections.

1.2.1 Maneuver Load Alleviation

Airworthiness qualifications mandated by regulatory agencies require the proof that critical loads in the aircraft do not exceed certain limits in order to ensure safety and structural integrity. These requirements also apply to loads generated during different maneuver conditions. The objective of limiting wing loads imposes restrictions to the V-n envelope and thus invariably conflicts with maximizing maneuver performance. However, with the knowledge of how each control surface affects maneuvers and loads, the control system design can exploit the relative strengths of the various control effectors to minimize conflicts [15].

The fundamental operation of MLA systems calls for automatically deflecting the wing flight control surfaces, usually in a symmetrical way, proportional to the normal incremental acceleration of the airplane and directed with proper sensors, such as wing deflection sensors, load factor sensor, or wing angle of attack sensors [16]. The objective is to concentrate lift inboard and reduce critical loads such as the wing out-of-plane bending moment, as depicted in Fig. 1.3, while maintaining the same normal load factor.

Maneuver load alleviation systems can actively control wing loads and therefore allow lighter structures and high-aspect ratio designs. According to Xu and Kroo [1], aircraft with MLA systems can typically achieve increases of 10 - 15% in span length and drag reduction of $8 - 13\%$.

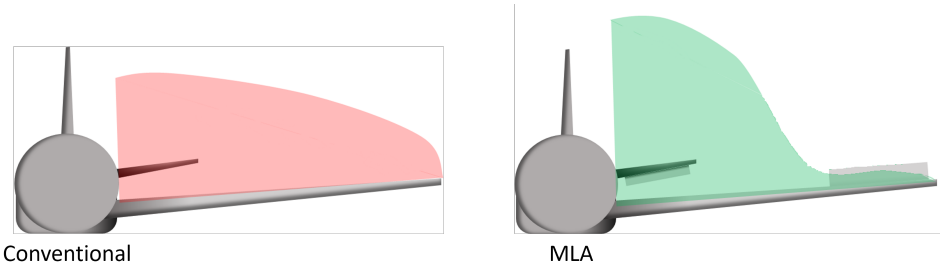

Figure 1.3: The maneuver lift distribution on a conventional (left) and MLA aircraft (right) [1].

Yang et al. [17] performed a maneuver load alleviation efficiency analysis of control surfaces in flexible airplanes. Using a state-space model of a flexible aircraft based on the modal method and the rational function approximation, and the mode displacement method to compute dynamic loads, the assessment was carried out by dividing the control surface into multiple chordwise strips. It was found that the efficient deflections for inner and outer control surfaces are downward and upward, respectively. Furthermore, using the most efficient control combination, the analysis also considered a multi control surface and its effect on final trim variables and wing root bending moment. The conclusion was that multi control surfaces in MLA schemes can reduce the dynamic loads while reducing the oscillation of trim variables. As pointed out by the authors, multiple control surfaces increase the potential of MLA, especially in new flexible aircraft configuration with active control systems.

1.2.1.1 Classical approaches for MLA

Classical approaches for MLA systems use accelerometers to measure the load factor and then deflect the control surfaces accordingly. In the system described in [2], vertical accelerometers implanted at the front of the vehicle are used to detect and measure the vertical acceleration of the aircraft, as shown in Fig. 1.4. If the vertical acceleration exceeds a predetermined threshold, the ailerons are activated and deflected by an angle proportional to the acceleration beyond the threshold. The definition of a threshold avoids repeated and superfluous operation of the control surfaces, which should be deflected only when the loads on the wing root are likely to reach a critical value. To counteract the pitch moment created by the deflection of ailerons, the elevator is simultaneously deflected for pitch control.

1.2.1.2 Constrained Control for MLA

Model predictive control (MPC) techniques derive from Optimal Control Theory and aim at overcoming the issues that limit the application of the classical theory. MPC is a structured

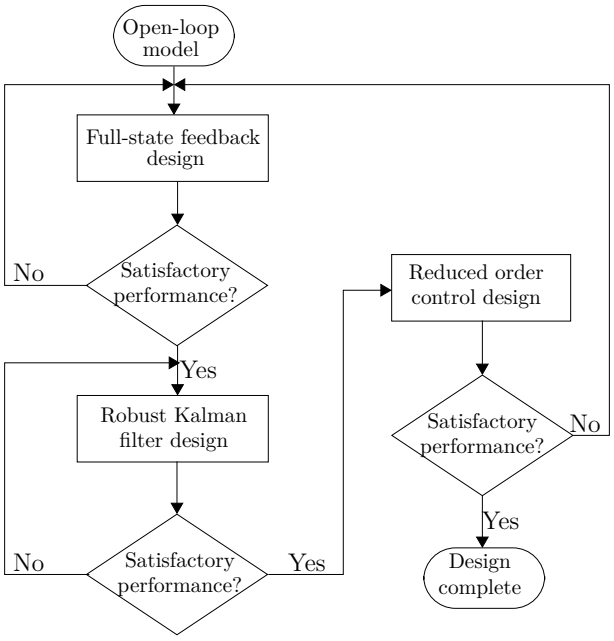

Figure 1.4: MLA system using vertical accelerometer [2]. Ailerons are used for load alleviation and elevators are used for pitch control.

controller design process that allows the explicit incorporation of constraints on both states and control inputs, and it offers the possibility of on-line optimization of the cost index [14, 18]. In addition, MPC formulations can account for unmodeled plant dynamics and nonlinearities, and deal with uncertainties in the outputs in a robust way [13]. MPC has found interesting applications in MLA control systems, since the MLA design problem aims at keeping the structural loads within prescribed design limits.

Galoucher et al. [19] exploited the redundancy of control surfaces in airplanes to propose an MLA system that does not modify the baseline controller responsible for ensuring good handling qualities. Model predictive control was used to design the MLA system under actuator amplitude and slew rate constraints to limit the magnitude of structural load outputs to an admissible interval while keeping the flight behavior close to the nominal one. The authors also proposed an identification procedure in the frequency domain to synthesize a mixing unit that can reproduce the optimal strategy obtained through the controller. The application of such a controller was tested in a linear model of a flexible transport aircraft with 77 states, with ailerons, elevators, rudder and spoilers as the control effectors. The structural load considered was the wing bending moment during a roll maneuver. Numerical simulations showed that all load alleviation and tracking objectives were fulfilled with the mixing unit and model predictive controller. The structural load remained within the prescribed bounds of ± 500.00Nm. Furthermore, the tests showed that even more tightened

constraints on the loads can be enforced if the spoilers are used in the control design. The complexity of the mixing strategy was deemed to remain moderate by the authors.

Duan et al. [20] combined MPC and control allocation for MLA in a very flexible aircraft with redundant control inputs. The control system exploited the properties of input redundancy in a way that the rigid body responses were kept unchanged while the flexible states were modified to satisfy given structural bounds. The proposed method exploited the nonlinear decoupling control theory applied to nonlinear aircraft models to generate time-varying feedforward control signals during the maneuver. A nonlinear 6-degree-of-freedom rigid body dynamic model augmented with linear aerodynamics and structural dynamics, represented by mode shapes, were used for control design. Numerical simulations showed that the controller is able to keep the amplitude of the dominant mode shape inside the desired bounds while preserving the rigid body outputs, however, at the cost of increased transients and magnitudes in the control effectors.

1.2.1.3 Other Control Techniques for MLA

Classical Control: Woods-Vedeler et al. [21] and Andrews [22] presented a classical control theory approaches for designing digitally implemented active control laws to alleviate wing loads. In the former, the considered loads were generated during fast rolling maneuvers. The objective was to design control laws that minimize the peak deviation of the wing loads from their steady state values prior to the maneuver. The control laws were designed considering a linear rigid-body model augmented with a pendulum term. Two control laws were designed that utilized outboard control surface pairs (leading and trailing edges) to counteract the loads and used trailing-edge control surface pairs to maintain roll performance. The control architecture comprised low pass filters and a gain-feedback that were iterated to determine the combination that effectively reduces the targeted dynamic loads. Simulations showed that there was a substantial decrease in peak incremental outboard and inboard torsion moments. There was, however, an increase in the peak incremental bending moment, even though such increase was sometimes smaller than that observed for the baseline controller.

Open-loop optimal control: Optimal control methods seek the calculation of control inputs that minimize a performance index. In MLA systems, such performance indices usually reflect the structural loads in the flexible aircraft. Even though feedback control laws can be obtained for linear systems through the classical optimal control theory, closed form solutions are not known when state or input constraints are incorporated into the design. Numerical techniques can be used to obtain open loop solutions in constrained optimal control problems, i.e., following a trajectory optimization approach. Such methods have been used to compute the control inputs that fly the vehicle along an optimal path

during maneuvers that keep the maximum structural load within the desired limits.

In the paper by Maraniello et al. [23], the single shooting method was used to compute optimal maneuvers in the lateral dynamics of wings with very low stiffness. The idea was to be able to deal with the nonlinear behavior of the flexible wing during the maneuver as an opportunity for extra performance, rather than a constraint. The task of designing aircraft maneuvers was recast as an open-loop optimal control problem and solved numerically via nonlinear programming techniques. The nonlinear aeroelastic solution was obtained by loosely coupling a geometrically exact beam model with an unsteady vortex lattice method for rigid and flexible vehicle aerodynamics. As for control design, the aileron deflection was the only control input considered, and constraints were imposed on its amplitude and rate of change. When the wing flexibility was increased, more aggressive actuation caused larger amplitude oscillations around the final reference side force. Regardless of the level of flexibility of the wing, the single shooting approach managed to capture the system features and lead to satisfactory results.

Adaptive control: Adaptive control techniques are intended for control of systems with uncertainties. Indirect adaptive control fuses a real-time control law with an on-line identification algorithm. Such solutions can incorporate control architectures based on classical linear control, optimal control, stochastic control, neural networks, etc, which gives the control engineer flexibility to choose the best strategy that fits the control problem objectives. The application of adaptive control to flexible aircraft has been studied, for example, in [24, 25, 26, 27, 28, 29, 30] motivated by extending the operating range of an aircraft which includes preventing the potential excitation of aeroelastic modes during maneuvers. Therefore, the design of MLA systems has taken advantage of adaptive structures to develop control systems that operate properly under variable flight conditions, such as changing Mach number and dynamic pressure.

Nguyen and Hashemi [31] developed a multi-objective performance-based adaptive optimal control solution for MLA control in flexible transport aircraft. The proposed technique incorporates a performance optimization objective of the uncertain plant that seeks to minimize both the tracking and predictor error. The method modifies the initial reference model into a time-varying reference model which satisfies the requirements defined in the optimal control problem and allows asymptotic tracking. The authors used a linearized reduced-order longitudinal model with 65 states of a flexible aircraft with matched uncertainty in the rigid aircraft states, and the control surfaces utilized were the position of the variable camber continuous trailing edge flap and the elevator. For the maneuver load alleviation, the performance metric was the wing root bending moment, which was inferred from strain gauge sensors. Numerical simulations showed that the closed loop system was able to track

the reference, and the amplitude of the wing root bending moment was reduced by 38.8%.

Li et al. [32] presented an adaptive controller based on recurrent neural networks for MLA systems based on the identification of the aeroelastic model of a fighter. The linear mathematical model of the flexible aircraft used in the control design considered the first seven symmetric elastic modes and a minimum-state approximation for the aerodynamic force coefficients. To realize system identification and load alleviation, the control system involved two recurrent neural networks: one identification network, used to identify the open-loop transient response, and one control network, used to alleviate the wing root bending moment and trace the open-loop responses of the load factor and angle of attack to match the desired values. The recurrent control network was then able to perform the load alleviation, reaching up to 26% of reduction in the maximum wing root bending moment.

Lavretsky and Henderson [33], and McLean [34] also investigated the use of neural networks for MLA and structural mode suppression. The authors attested to the efficiency of neural networks which, according to them, is comparable to linear control designs, but with the inherent ability of adaptability.

Fuzzy control: Chiu et al. [15] proposed a fuzzy logic-based, multi-input/ multi-output roll rate and load alleviation controller for a flexible aircraft. According to the authors, the use of fuzzy controllers was motivated by their ability to capture qualitative control strategies and implement flexible control architectures, and by its robustness characteristics, especially when applied to imprecise systems whose behavior is only known in the large. The controller was tested in a scaled aircraft model. The task of the controller was to determine the appropriate control surface deflections that would achieve a command roll rate while satisfying torsion moment constraints. The linearized equations of motion were used to design the fuzzy controller. The controller was divided into two modules containing set of rules in the form of a proportional-derivative control for determining the deflection command during roll maneuvers, and for alleviating the sensed and anticipated excessive torsion moments. The simulations carried out to evaluate the controller showed that it was able to follow the roll rate command while enforcing the torsion moment bounds without any significant degradation in roll rate performance.

1.2.2 Gust Load Alleviation

Atmospheric disturbances are a problem in aircraft operations due to the undesirable dynamic loads generated, which may result in reduction of the airframe structural life or catastrophic failure. Such issues are even more pronounced in the operation of very flexible aircraft due to the great deformations that the structure can experience during flight. The mishap

of NASA's Helios prototype in 2003 shows the unfavorable effects caused by gusts in very flexible aircraft. The Helios aircraft broke apart during flight after penetrating turbulence, which caused a high dihedral deformation that ultimately resulted in instability [35].

To overcome the undesirable effects of turbulence without the need of structural reinforcement, GLA systems can be incorporated into the automatic flight control architecture. The main objective of GLA systems is to attenuate loads caused by encounters with gusts or turbulence by using active controls. Such active controls can be developed using modern control theory. As described by McLean [36], GLA systems can reduce loads due to airframe flexibility, decrease levels of acceleration at particular aircraft stations and improve flying qualities. Consequently, fatigue life is increased, lightweight high-aspect ratio designs are allowed, fuel expenditure is reduced and flight comfort is enhanced. Furthermore, GLA systems can improve the airworthiness in the aircraft design in order to comply with the standards specified by regulatory agencies.

In a typical GLA system, when the aircraft penetrates the gust, sensors provide feedback signals to the control system, which generates inputs to the control surface actuators according to some logic, so as to create aerodynamic forces and moments to cancel undesirable effects of the external perturbations [36]. From a control perspective, GLA is a disturbance rejection problem [14], in which gusts can be modeled either as discrete-deterministic or continuous-stochastic perturbations. Recent work in GLA control applies various modern control techniques to reduce aircraft loads by minimizing the vertical acceleration, the wingtip deflection or the span-wise shape of the wing [37].

The first reference to GLA system is from 1914 [38], but this topic only drew attention of the aeronautical community after the development of mathematical models to represent turbulence in 1937 [36]. Early designs were concerned with alleviating the effects of gusts on rigid body dynamics only by symmetrical aileron deflection. The results were unsatisfactory, since the handling qualities were compromised by the reduction of the stability margins due to the adverse pitching moment caused by the aileron deflection required by the GLA system. Furthermore, early designs depended on gust vanes to detect entry to the turbulence field, which did not account for the gust field normal components with respect to the plane of symmetry of the aircraft, and secondary aerodynamic effects such as downwash or time delays. The design approaches have evolved since then. Modern GLA systems use gust angle measurements at the aircraft nose or feedback local load factor measurements, and some suggest the use of auxiliary control surfaces to create the appropriate forces and moments to diminish the loads caused by gusts [14]. Control effectors typically include designated control surfaces, such as canards or a centerline control surface, or conventional, multipurpose effectors, such as flaps and ailerons [39]. More recent works propose the use of the airborne

Light Detection and Ranging (LIDAR) turbulence sensor to provide preview information about the vertical gust velocity at a considerable distance ahead of the aircraft. Moreover, modern designs also take into consideration the elastic effects inherent to the vehicle structure and, due to the advancement of very flexible aircraft configurations, the recent trend is to incorporate the nonlinear aeroelastic analysis into the GLA system design.

To show how aeroelastic effects are an important factor, Dillsaver et al. [40] have performed a comprehensive study of the gust response sensitivity of a representative baseline of a very flexible aircraft model. The open loop response of the baseline aircraft to disturbances of differing amplitudes was found to be nonlinear and the duration of the turbulence can play an important role, since the response grows larger the longer the aircraft remains in the gust field, which consequently causes a drop in altitude. In addition, it was found that the maximum pitch angle decreases with the increase of both the bending and in-plane frequencies, while the trends for maximum curvature were the opposite. The maximum pitch angle excursion was found to be dependent on the first torsion-to-first in-plane bending frequency, while the maximum root curvature depends on the first bending frequency. Therefore, the analysis of the structural elastic effects is crucial in the design of an automatic flight system with gust load alleviation capabilities.

1.2.2.1 Classical approaches for GLA

Typical approaches found in the aeronautical industry for GLA systems usually rely on passively deflecting the control surfaces when a disturbance due to wind is encountered during flight. For instance, in [41] probes are mounted at the nose of the aircraft to provide information about incidence, which can be linked to a disturbance if it exceeds a predetermined value. When such a disturbance is detected, the ailerons are deflected symmetrically so as to alleviate the structural loads. The deflection remains constant for a predetermined time after the end of a the disturbance is detected. The implementation of such systems uses high-pass filtering to retain only the high-frequency part of the wind which represents the disturbance, thus limiting the activation range of the alleviation function, in order to not reduce the maneuverability and to not activate it in flight conditions that do not pose any structural problems.

In [3], a method for GLA is based on the deflection of control surfaces, comprised by internal and external flaps, when the airplane flies inside the load exceeding envelope (Fig. 1.5), which is defined by couples of values of altitude and speed gathered during flight, so that the loads applied to the airplane are equal or greater that the theoretical predefined load threshold (e.g. 92% of the dimensioning loads of the airplane) [3]. The load exceeding envelope is a function of parameters that vary during the flight, such as the mass, the filling level

of the tanks, or the centering. Whenever the aircraft flies within such envelope, the ailerons are deflected symmetrically based on values in a matching table, which associates a given reference load to a particular aileron deflection angle. The control surfaces are maintained deflected during a predefined time. This approach claims to preventively deflect the control surfaces before aerodynamic disturbances possibly occur.

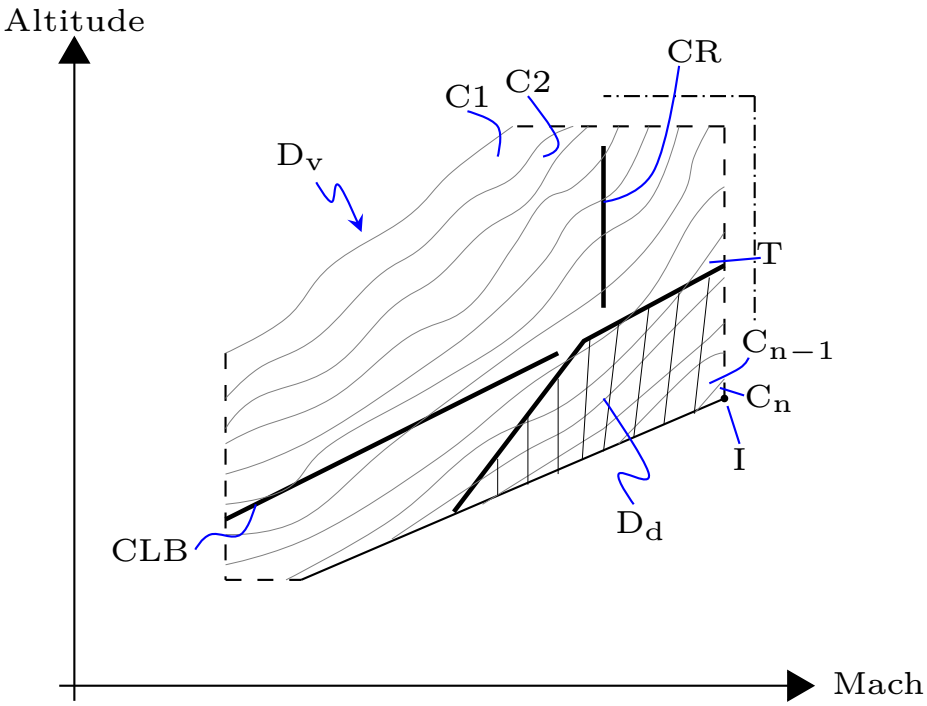

Figure 1.5: Baseline GLA system: Load exceeding envelope as a function of Mach and altitude [3].

1.2.2.2 Constrained Control for GLA

As discussed in Section 1.2.1.2, Model Predictive Control allows the handling of state and inputs constraints in the control design procedure. Similarly to MLA systems, the GLA design problem aims at keeping the structural loads within prescribed design limits. MPC is a powerful control method that has found application in GLA systems. In this method, a dynamic discrete-time representation of the plant is used to propagate the states into the future and then determine the control actions that minimize a performance index subject to constraints.

Giesseler et al. [14] presented a GLA strategy using MPC design that accounts for look ahead measurements of incoming gust disturbances via LIDAR. The benefit of LIDAR sensors is that the information available about the upcoming turbulence can be integrated

into the GLA system to compensate for the gust effects and thus proactively reduce the induced loads. A fully flexible aircraft model was considered. The model captured the gust effects at five aeropanels along the vehicle body. Based on the available measurement information, the goal was to minimize the relevant loads via control surface (inner ailerons, spoilers and elevators) deflections with control constraints. To apply a tailored MPC scheme, the large scale system was linearized around a trim point and a model order reduction method was employed, yielding a system with 24 states, 30 outputs and 24 inputs. To achieve GLA, in the MPC design the authors considered the use of the L_2 norm to minimize the integral of fatigue load. In the simulations, four types of gust were considered: discrete up-down gusts, discrete down-up gusts, continuous turbulence, and sweep gusts. The simulations also considered two different gust sensor layouts: sensors at the nose, and LIDAR sensors. Even though for the first sensor layout the MPC reacted earlier and therefore the spoilers were used more effectively, the second sensor layout had the largest bending moment reduction at root and mid wing, except for continuous turbulence. Even though the use of LIDAR gust measurements could generally improve the load reduction at the wing stations, the horizontal tail plane root faced increased loads. This work did not focus on nominal and robust stability of the control scheme proposed. However, the same research group came up later with a similar MPC strategy with nominal stability guarantees based on terminal penalties and that requires no terminal constraint [42, 43].

Artola et al. [44] presented the application of nonlinear Model Predictive Control (NMPC) for a very flexible, high aspect ratio clamped wing in a GLA control problem. Differently from the linear MPC approach, NMPC utilizes the nonlinear equations of motion for prediction to potentially achieve increased accuracy and performance. A low-order nonlinear aerolastic model was built combining geometrically nonlinear intrinsic beam equations in a reduced modal bases with a linearized Unsteady Vortice Lattice Method projected onto a reduced-order subspace using the Krylov moment matching technique. The linearized aerodynamics relied on the assumption of frozen wake geometry and small deformations in the lifting surfaces geometry. The NMPC controller was coupled with Moving Horizon Estimation for both state and disturbance estimation. Nonlinear simulations showed that the NMPC-based GLA system was able to reduce the peak wing root bending moment by 16.6% in addition to reducing the time the wing was overloaded. In a subsequent work [45], the authors showcased the feasibility of the combined NMPC and Moving Horizon Estimation control system in a hardware-in-the-loop simulation, however no load alleviation objectives were considered.

Other investigations of the application of MPC (or variations thereof, such as control allocation with receding horizon control) to design GLA systems include the works of Haghighat et al. [46], Simpson et al. [13], Wang et al. [47], and Hansen et al. [48]. The general conclu-

sion was that MPC techniques outperform equivalent linear control schemes in the task of controlling flexible aircraft in the presence of discrete gusts. Experimentally, the application of MPC in GLA was demonstrated by Barzgaran et al. [49] in a preliminary wind tunnel experiment with a flexible half-aircraft model and gust vanes to generate the disturbance. Using a simplified control formulation with a single input constraint, the real-time feasibility of the system was achieved.

Another constrained control technique considered for GLA is reference governors, which are add-on schemes for handling constraints on states and controls by modifying set-point commands to a closed loop system. Dillsaver et al. [50] proposed a dynamic inversion inner-loop controller and a PID outer-loop controller with a reference governor to enforce curvature limits of very flexible aircraft. For the very flexible aircraft, the objective was to reduce the wing bending moment. The full vehicle model consisted of 531 coupled nonlinear equations of motion. Since the linearization of the open-loop system was difficult, the authors performed a system identification on the closed-loop dynamics. As for the control architecture, the stable inner loop consisted of the longitudinal translational and rotational velocities and errors. It contained a dynamic inversion controller for the elevator deflection serving as the only control input; the pseudo-control input was obtained applying LQR techniques. The outer loop contained a PID controller and a nonlinear transformation. It converted the desired flight path angle to state commanded values for the inner loop. To ensure that bending moment limits were not violated, limits were enforced on the curvature values by a reference governor (RG) and an Extended Command Governor (ECG). To handle disturbances, the authors considered that the perturbation remained constant over the prediction horizon. They also proposed the use of soft constraints to guarantee constraint admissibility and recursive feasibility. Simulations were carried out with both RG and ECG, using a linearized model to determine if a constraint violation occurred. In still air simulations, the RG successfully enforced the curvature limits, but at the cost of modifications to the flight path. The ECG modified the flight path much less, but did have a slight constraint violation. In simulations with gust disturbances, it was found that ECG provided no improvement over the original closed loop system, and that the use of ailerons to counteract curvature would be a more effective strategy.

1.2.2.3 Other Control Techniques for GLA

Robust Control: In Control Theory, robust control is a typical approach to design controllers for systems subjected to bounded uncertainties or external disturbances. The objective of such techniques is to design robust control laws, that is, capable of working properly, within the designed specifications, even when subject to model uncertainties. The robust

control design usually relies on the worst-case scenario analysis to guarantee the stability and performance exploiting a linear system model. Such techniques have been successfully applied in the control of very flexible aircraft, such as in [51, 52, 53, 54].

Robust control has been applied in GLA systems for flexible aircraft. For instance, Aouf et al.[55] designed H_2 and H_∞ robust controllers to attenuate loads induced by wind gusts for the longitudinal dynamics of the B-52 bomber based on a rigid body model augmented with five flexible modes. The gust signal considered was generated by a deterministic bounded-energy Dryden model in order to create a more faithful representation of the fact that the aircraft usually experiences the effect of turbulence for a brief period of time. The consideration of a bounded set of disturbances allowed the worst-case H_∞ design. The goal of the control design was to reduce the transient peak loads on the airplane by using the elevator and canard deflection to regulate the vertical acceleration of the vehicle. Three designs were simulated: regular H_2, weighted H_2, and H_∞ control. The latter outperformed the H_2 designs by dramatically reducing the effect of wind gusts on the vertical acceleration with small control surface deflection angles. A similar control design approach was used by Cook and Palacios [56] to reduce loads in a very flexible aircraft.

The integration between robust control techniques and LIDAR measurements for GLA was demonstrated by Fezans and Joos [57], Khalil and Fezans [58, 59], Cavaliere et al. [60], and Fournier et al. [61]. For example, in [59] a multi-channel H_∞ controller was designed for reducing loads in a flexible sailplane. The selected performance channels for minimization were the vertical load factor at the pilot's location and a vector of load variations on three wing stations corresponding to the torsional moment, bending moment, and vertical shear force. The gust preview information provided by the LIDAR sensor was introduced into the control design by using an explicit buffering of the previewed disturbance, such that the whole previewed disturbance, as well as some of the previous values, are explicitly passed to the controller. The resultant system combined both feedback and feedforward control actions. Simulations results using a full-order and fixed-order controllers obtained from the H_∞ synthesis showed that the LIDAR sensor led to much better load alleviation performance, compared to either the open-loop system or the feedback-only control.

Unconstrained optimal control: Optimal Control Theory has also been extensively applied in GLA systems for decades. Even though nonlinear or constrained optimal control problems usually do not have a closed form solution, the solution to linear problems with quadratic cost index is well known and is referred to as a linear quadratic regulator (LQR). The LQR and the Kalman filter can be used together to design a dynamic regulator for partially observed linear systems disturbed by additive white Gaussian noise, in an approach referred to as a linear Gaussian quadratic (LQG) regulator. The Kalman filter is based on

a probabilistic treatment of process and measurement noises, and it is fundamentally a low-pass filter, thus having good noise rejection capabilities [62].

McLean [36] devised a suitable GLA system based on optimal control by proposing a performance index that reflected the effectiveness of the control action on the ride quality of the aircraft. The objective of the LQR control design was to minimize the ride-discomfort index and the ride-comfort rating, which could be achieved by minimizing the normal and lateral accelerations. As pointed out by McLean, the implementation of an LQR would require complete state-feedback, which usually is not possible since not every state variable of the mathematical model is available for measurement. Therefore, an output feedback approach is more suitable for GLA in flexible aircraft.

More recent publications exploited the LQG design for GLA system. For example, this approach is pursued by Dillsaver et al. [37, 40]. In their work, different gust time histories were generated using the Dryden and Von Kármán models to simulate the encounter of a very flexible aircraft with the gust. The methodology utilized for the LQG control design was to alleviate the gust loads by controlling the shape of the wing by minimizing the curvature along the span. An integrator was added to the control system to track pitch angle commands and a reference governor was used for modifying the pitch angle reference. The controller was able to reduce the linear model peak wing curvatures by an average of 47% and RMS curvatures by 83.7%. The control system was also able to track the pitch angle command and the reference governor was successful in limiting the curvatures. The same control strategy was used to track lateral commands in presence of wind gusts [63].

Liu and Sun [64] introduced an improved LQG method for GLA, which is robust to variations of flight and structural parameters, and modeling errors, and which is suitable for application in structure/ control design optimization. The longitudinal dynamical model of the flexible aircraft during continuous gust encounters was approximated by a linear time-invariant model with additive white noise. The controlled outputs included the wing root bending and torsional moments, and the pitch rate. As for the LQG control design, the authors proposed a method in which the Kalman filter is redesigned after introducing fictitious high-frequency colored noise to controller inputs in the design phase, in order to reduce the high-frequency response of the control actuators, and simulate modeling errors. In numerical simulations, the improved LQG method was shown to outperform an H_∞ controller, and to have performance comparable to a μ synthesis design in the task of reducing the wing root bending moment and the aircraft pitch rate, with a less troublesome design procedure.

Adaptive Control: Zeng et al. [65] proposed an adaptive feedforward control framework to suppress structural vibrations induced by gust perturbations in very flexible aircraft.

Adaptive control was deemed to be suitable for such an application due to the time-varying characteristics of the aircraft. The control structure presented had a LIDAR turbulence sensor for measurements of the vertical gust velocity at a distance ahead of the aircraft, which were fed into the feedforward controller to calculate the control surface demand for vibration compensation. The feedforward filter was parameterized using orthonormal basis expansions along with a recursive least-square algorithm with variable forgetting factor. The orthonormal basis expansion allowed the incorporation of the prior flexible modes information into the feedforward controller, resulting in a reduced order filter. The controller was tested via simulation using a six degree of freedom linear model of a very flexible aircraft. The gust perturbation considered was a low-pass filter followed by a Dryden vertical velocity shaping filter. The results showed that the structural vibration could be largely suppressed with the adaptive feedforward controller.

1.3 Challenges of Load Alleviation

The main challenges of designing a control system with maneuver and gust load alleviation capabilities for flexible aircraft are:

1. High-order nonlinear models: The discussion presented in the previous sections made it evident that flexible aircraft are nonlinear systems due to the combination of rigid body dynamics, structural deformation and unsteady aerodynamics. In addition, mathematical models of such vehicles usually have hundreds of state variables in order to describe all degrees of motion of the structure. Even though nonlinear control techniques have already been used to control flexible aircraft, e.g., dynamic inversion [66, 67, 68, 69, 70], the vast majority of control methods discussed in Sections 1.2.2 and 1.2.1, and implemented in actual vehicles, are based on linear control theory. Hence, linearization of the dynamics is necessary, which results in high-order linear time-varying models, since, in contrast to rigid aircraft, flexible vehicles have geometries that are dependent on time. Due to the computational cost of synthesizing control laws for these models, model order reduction methods (e.g., balanced truncation) are usually required to approximate the complicated model by a simpler one with fewer dynamic states [71]. The reduced order linear model should capture nonlinearities within a neighborhood of the design point. Linear parameter varying techniques, such as in [72, 73, 74], can also be applied to represent the time-variation of the linear models due to deformations and different flight conditions, such as speed and Mach number.

2. Partial observation and model uncertainty: Even though the dynamical models of

flexible aircraft may contain hundreds of state variables, typically only a few of them are measured due to lack of sensors in the vehicle. Partial observation is also due to output noise. Additionally, other sources of uncertainty come from unmodeled vehicle dynamics, unknown parameters, or external disturbances not accounted for in the mathematical model. Therefore, the control design strategy has to ensure good robustness characteristics and usually has to be used in conjunction with a state estimation algorithm.

3. Anticipation of wind gust disturbances: The majority of the control techniques reviewed in Section 1.2.2 only activate the control surfaces to alleviate loads after the gust disturbance hits the vehicle and is measured by sensors. Consequently, there is usually a lag between the perturbation and the GLA system response that may degrade the overall performance of the system in an actual operation, especially after the first hit by gust, and reduce the life of the aircraft structure. To avoid such issues, feedforward control solutions along with the selection of the appropriate set of sensors are of interest that look ahead, anticipate and compensate for disturbances. For instance, LIDAR beam airborne wind sensors, such as described in [14, 42, 65], can be used to accurately measure incoming disturbances and feed the signal into the feedforward controller.

4. Constraint enforcement: The imposition of constraints to the control design problem comes inevitably from the main objective of the MLA/GLA systems of maintaining the aircraft structural loads within specified safety limits. State constraints can be, for example, the limitation of the wing tip deflection or twist angle due to the bending and torsion moments generated by gust encounters or maneuvers. Control constraints arise when the control inputs magnitude and rates are restricted by the specifications of the actuators. Among the various control design strategies presented in Section 1.2, only Model Predictive Control and Reference Governors incorporate systematically the constraints into the control design procedure. Even though classical Optimal, Robust and Adaptive Control techniques can be based on the minimization of a certain performance index that takes into account the deviation of states and control variables from the reference values, these control strategies are not able to enforce the constraint compliance. Therefore, MPC and RG, possibly in combination with other techniques, are of interest for MLA/GLA systems design.

5. Loss of control authority, actuator saturation and faults: Due to the flexible characteristics of the aircraft, e.g., insufficient torsional stiffness of the wing structure, the deflection of control surfaces during flight can twist the wing, resulting in a reduction

of the control effectiveness as dynamic pressure increases. This aeroelastic behavior can ultimately lead to control reversal, i.e., the reversal of the expected response due to structural deformation of the wing. In addition to that, the control surfaces operation can be impaired by actuator saturation, which physically constrains the control input magnitude and can lead to nonlinear oscillations that degrade the closed-loop performance, and actuator faults, which result in undesired transients, large steady-state errors and increase of the saturation of actuators. Therefore, a fault-tolerant control strategy, such as the one presented in [65], would have interesting applications in the design of control systems for flexible aircraft.

From the discussion above, among the different control strategies presented, it is apparent that there is no true standout in the task of designing a control system with MLA/GLA capabilities for very flexible aircraft. Nonetheless, Adaptive Control, MPC and Reference Governors probably have the most interesting features for this application. The last two take the lead, due to their capability of enforcing output and input constraints, which aligns well with the main objective of MLA/GLA systems. One of the drawbacks of these methods is the high computational cost of running a real-time optimization during the aircraft operation, especially due to the high-order models [43].

1.4 Scope of this Work

This dissertation attempts to address the challenges described in Section 1.3, with special focus on constraint enforcement. The formulation of the load alleviation system design as a constrained control problem is presented, including the translation of certification requirements into control design parameters. Furthermore, strategies are investigated to reduce the computational footprint of these controllers aiming at real-time implementations. Finally, the verification of the proposed controllers is conducted through numerical simulations and experimental work.

The remainder of this dissertation is organized as follows:

Chapter 2 presents the mathematical and numerical models used for control design and simulation of flexible and very flexible aircraft. A review of the aeroelastic equations of motion that govern the dynamics of these vehicles is presented. Next, different model order reduction techniques utilized in this work for creating more computationally tractable system representations for control design are shown. Following that, the University of Michigan's Nonlinear Aeroelastic Simulation Toolbox (UM/NAST) is described, which provided the main tools used for simulating and analyzing the aircraft models considered in this dissertation. Special emphasis is given to the features developed in UM/NAST to support

the control design process shown in this dissertation. Finally, the several models used to showcase the proposed control systems are introduced.

Chapter 3 presents the theoretical development of the load alleviation systems developed in this work. The foundations of Model Predictive Control are briefly reviewed, and two MPC-based architectures for load alleviation are introduced. The state estimation algorithm used alongside the MPC controller is also presented. Next, methods to reduce the computational footprint of the MPC solutions and increase its robustness against parametric uncertainty are presented. In particular, it is shown through numerical simulations how constraint aggregation can be used to reduce the computational cost of MPC solutions for large-scale aeroelastic systems.

Chapter 4 describes the application of the MPC architectures in MLA. The requirements of the MLA system design are presented, as well as how these requirements drive the formulation of the MPC problem. In particular, it is shown how to select the optimal control objective function and constraints. Numerical simulations are then presented to verify the proposed MPC-based MLA systems for flexible and very flexible aircraft. Furthermore, a comparison between the different reduced-order models considered in the design is presented.

Chapter 5 describes the application of MPC in GLA. The proposed system builds upon the MLA system presented in Chapter 4 to create an integrated MLA and GLA system. The requirements of the GLA systems are presented, as well as the modification in the MPC formulation to accommodate them. A feedforward system based on the gust preview is also proposed, and the details of the design is described.

Chapter 6 describes the wind tunnel experiment that was designed and conducted to validate the proposed MPC-based load alleviation systems. The half-aircraft model design and analysis is presented, along with the control system, instrumentation, and methodology. Next, the results of the experimental work is presented and the performance of the load alleviation system is assessed.

Finally, Chapter 7 provides a summary of the dissertation, of the main conclusions and of the key benefits of the proposed load alleviation system. Recommendations are given for future work.

CHAPTER 2

Very Flexible Aircraft Dynamics and Simulation

This section presents high and low-order representations of the dynamics of flexible and very flexible aircraft (FA and VFA, respectively). Additionally, several tools utilized to design, analyze and simulate these vehicles are also described.

2.1 Equations of Motion

The dynamics of FA and VFA can be represented by coupled aeroleastic and rigid body equations of motion. A brief review of these equations is presented next based on the work of Cesnik and coworkers [4, 75, 76, 77], which use a strain-based approach for representing the structural dynamics of a flexible beam, which is then used to model each member of the vehicle

In this formulation, the beam is represented by n_ε elastic elements, for each of which three nodes positioned along a reference line and a strain vector are associated. The strain vector for the ith node contains four local strain degrees of freedom, and it is represented by

$$\varepsilon_i = \begin{bmatrix} \epsilon_i & \kappa_{x_i} & \kappa_{y_i} & \kappa_{z_i} \end{bmatrix}^T \in \mathbb{R}^4, \tag{2.1}$$

where ϵ_i is the extension, κ_{x_i} the twist, κ_{y_i} the out-of-plane curvature, and κ_{z_i} the in-plane curvature. The vector that concatenates the strain vector for all structural elements is denoted by ε:

$$\varepsilon = \begin{bmatrix} \varepsilon_1^T & \varepsilon_2^T & \cdots & \varepsilon_{n_\varepsilon}^T \end{bmatrix}^T \in \mathbb{R}^{4n_\varepsilon}. \tag{2.2}$$

Several coordinate frames are defined to facilitate the derivation of the dynamic equations. These frames[1], shown in Fig. 2.1, are the ground frame G, which is fixed on the ground; the

[1]The frames used in here are consistent with Refs. [4, 75, 76, 77], which differ from the typical coordinate

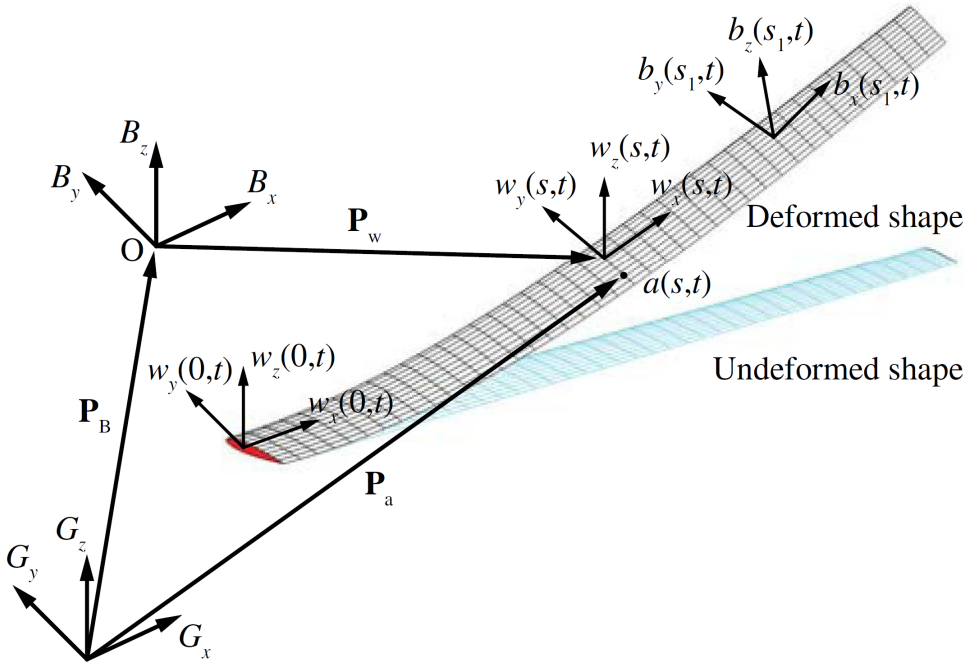

Figure 2.1: Coordinate frames [4].

body frame B, which describes position and orientation for the vehicle; and the local frame w_i, which is used to describe the orientation and position of the ith node, as well as its strain vector ε_i. The local frame is conveniently represented into unit bases w_{x_i}, w_{y_i}, and w_{z_i}, each of which in $\mathbb{R}^3$ and resolved in the body frame.

For node i located at position s along the beam reference line, its position with respect to the ground frame is given by

$$h_i = \begin{bmatrix} (p_B + p_{w_i}(s))^T & w_{x_i}^T & w_{y_i}^T & w_{z_i}^T \end{bmatrix}^T \in \mathbb{R}^{12}, \tag{2.3}$$

where

$$p_B = \begin{bmatrix} x_B & y_B & z_B \end{bmatrix}^T \in \mathbb{R}^3 \tag{2.4}$$

is the position of the vehicle in the ground frame, and $p_{w_i}(s) \in \mathbb{R}^3$ is the position of the ith node resolved in the body frame.

The position p_B and the orientation $\theta_B \in \mathbb{R}^3$ of the body frame with respect to the ground frame can be defined as

$$b = \begin{bmatrix} p_B^T & \theta_B^T \end{bmatrix}^T \in \mathbb{R}^6. \tag{2.5}$$

frames usually found in the literature of flight dynamics and structural dynamics, in which the x and y directions are aligned with the longitudinal and lateral axis of the aircraft, respectively.

The time derivative of vector b is then

$$\dot{b} = \beta = \begin{bmatrix} v_B^T & \omega_B^T \end{bmatrix}^T, \tag{2.6}$$

where

$$v_B = \begin{bmatrix} v_B & u_B & w_B \end{bmatrix}^T \in \mathbb{R}^3, \tag{2.7}$$

$$\omega_B = \begin{bmatrix} q_B & p_B & r_B \end{bmatrix}^T \in \mathbb{R}^3, \tag{2.8}$$

are, respectively, the linear velocity and the angular velocity[2] of the vehicle's rigid body motion resolved in the body frame. Together, vectors ε and b form a complete independent set $\boldsymbol{q}$ of variables of the strain-based formulation.

$$\boldsymbol{q} = \begin{bmatrix} \varepsilon^T & b^T \end{bmatrix}^T \in \mathbb{R}^{4n_\varepsilon+6}. \tag{2.9}$$

The generalized coordinates $\boldsymbol{q}$ is used to describe the coupled elastic and rigid body equations of motion, which are derived by following the principle of virtual work. The virtual work of the aeroelastic beam consists of the contributions of inertia forces, internal strains and strain rates, and external loads. In Ref. [77], the contribution of each virtual work is derived separately and then summed at the end to represent the total virtual work of the complete vehicle.

External loads are comprised by aerodynamic forces and moments on lifting surfaces, control effectors such as flaps or propulsive forces (usually represented by point forces), gust disturbances, among others. The aerodynamic loads can be represented by several different models, including Peters' 2-D finite state inflow theory [78]. In this model, the unsteady aerodynamic loads, which include lift, drag and moment, are computed for a thin-airfoil section undergoing large motions in an incompressible inviscid subsonic flow. The unsteady wake effects in each lifting surface element are modeled using 6th-order finite inflow states:

$$\lambda_i = \begin{bmatrix} \lambda_{1_i} & \lambda_{2_i} & \lambda_{3_i} & \lambda_{4_i} & \lambda_{5_i} & \lambda_{6_i} \end{bmatrix}^T \in \mathbb{R}^6. \tag{2.10}$$

Vector λ_i is defined for each one of the n_λ lifting surface elements in the model. These vectors can be concatenated in one single vector denoted by λ, where:

$$\lambda = \begin{bmatrix} \lambda_1^T & \lambda_2^T & \cdots & \lambda_{n_\lambda}^T \end{bmatrix}^T \in \mathbb{R}^{6n_\lambda}, \tag{2.11}$$

[2]The nomenclature of the components of the linear and angular velocity vectors is consistent with the flight dynamics convention in which, for example, u_B is the longitudinal velocity and q_B is the pitch rate.

for which an ordinary differential equation describes its evolution in time:

$$\dot{\lambda} = F_1(\boldsymbol{q}, \dot{\boldsymbol{q}})\ddot{\boldsymbol{q}} + F_2(\boldsymbol{q}, \dot{\boldsymbol{q}})\dot{\boldsymbol{q}} + F_3(\boldsymbol{q}, \dot{\boldsymbol{q}})\lambda, \tag{2.12}$$

where $F_1(\cdot)$, $F_2(\cdot)$, and $F_3(\cdot)$ are functions of the generalized coordinates and its derivatives.

The kinematic relations for the structure and rigid body are also defined. For the former, the position and orientation of a point on the beam reference line can be recovered from the root node of the mean at position s_1 and displacement h_1 as follows:

$$h_i(s) = e^{\mathbb{K}(s-s_1)}h_1, \tag{2.13}$$

where $\mathbb{K}(s)$ is a matrix function of the strains, i.e.,

$$\mathbb{K}(s) = \begin{bmatrix} 0 & \epsilon_{x_i}(s) & 0 & 0 \\ 0 & 0 & \kappa_{z_i}(s) & -\kappa_{y_i}(s) \\ 0 & -\kappa_{z_i}(s) & 0 & \kappa_{x_i}(s) \\ 0 & \kappa_{y_i}(s) & -\kappa_{x_i}(s) & 0 \end{bmatrix}. \tag{2.14}$$

The orientation of the body frame is given by quaternions ζ:

$$\zeta = \begin{bmatrix} q_0 & q_1 & q_2 & q_3 \end{bmatrix}^T, \tag{2.15}$$

for which an ordinary differential equation describes its evolution in time:

$$\dot{\zeta} = \frac{1}{2}\Omega_\zeta(\beta)\zeta, \tag{2.16}$$

where $\Omega_\zeta(\beta)$ is the propagation matrix:

$$\Omega_\zeta(\beta) = \begin{bmatrix} 0 & q_B & p_B & r_B \\ -q_B & 0 & -r_B & p_B \\ -p_B & r_B & 0 & -q_B \\ -r_B & -p_B & q_B & 0 \end{bmatrix}. \tag{2.17}$$

Furthermore, the rotation matrix from ground frame G to body frame B can be computed from ζ as follows:

$$C^{BG}(\zeta) = \begin{bmatrix} q_0^2 + q_1^2 - q_2^2 - q_3^2 & 2(q_1q_2 + q_0q_3) & 2(q_1q_3 - q_0q_2) \\ 2(q_1q_2 - q_0q_3) & q_0^2 - q_1^2 + q_2^2 - q_3^2 & 2(q_2q_3 + q_0q_1) \\ 2(q_1q_3 + q_0q_2) & 2(q_2q_3 - q_0q_1) & q_0^2 - q_1^2 - q_2^2 + q_3^2 \end{bmatrix} \tag{2.18}$$

For control design applications, the orientation can be conveniently expressed in Euler angles[3] ϕ_B (roll), θ_B (pitch), and ψ_B (yaw) as follows:

$$\phi_B = -\sin^{-1}\left(2(q_1q_3 - q_0q_2)\right), \tag{2.19}$$

$$\theta_B = \tan^{-1}\left(\frac{2(q_2q_3 + q_0q_1)}{q_0^2 - q_1^2 - q_2^2 + q_3^2}\right), \tag{2.20}$$

$$\psi_B = \tan^{-1}\left(\frac{2(q_1q_2 + q_0q_3)}{q_0^2 + q_1^2 - q_2^2 - q_3^2}\right). \tag{2.21}$$

Finally, the coupled aeroelastic and rigid body equations of motion can be expressed as:

$$\mathscr{M}(\boldsymbol{q})\ddot{\boldsymbol{q}} + \mathscr{C}(\boldsymbol{q},\dot{\boldsymbol{q}})\dot{\boldsymbol{q}} + \mathscr{K}\boldsymbol{q} = \mathscr{R}(\boldsymbol{q},\dot{\boldsymbol{q}},\ddot{\boldsymbol{q}},\lambda,\zeta,u,w_g), \tag{2.22}$$

$$\dot{\zeta} = -\frac{1}{2}\Omega_\zeta(\beta)\zeta, \tag{2.23}$$

$$\dot{p}_B = \begin{bmatrix} C^{BG}(\zeta)^T & 0 \end{bmatrix}\beta, \tag{2.24}$$

$$\dot{\lambda} = F_1(\boldsymbol{q},\dot{\boldsymbol{q}})\ddot{\boldsymbol{q}} + F_2(\boldsymbol{q},\dot{\boldsymbol{q}})\dot{\boldsymbol{q}} + F_3(\boldsymbol{q},\dot{\boldsymbol{q}})\lambda, \tag{2.25}$$

where $\mathscr{M}(\cdot)$, $\mathscr{C}(\cdot)$, $\mathscr{K}(\cdot)$, and $\mathscr{R}(\cdot)$ are the generalized mass, damping, stiffness, and force matrices, respectively. Vectors $u \in \mathbb{R}^{n_u}$ and $w_g \in \mathbb{R}^{n_w}$ represent, respectively, the control effectors in the aircraft and the gust disturbances. The latter is usually composed of the local gust speed $w_g^i \in \mathbb{R}^3$ at different stations on the aircraft, which in the B frame is represented by

$$w_g^i = \begin{bmatrix} w_{g_x}^i & w_{g_y}^i & w_{g_z}^i \end{bmatrix}^T. \tag{2.26}$$

This system of nonlinear continuous-time differential equations can be represented in a compact form as:

$$\dot{x} = f(x,u,w_g), \tag{2.27}$$

where x is the state vector

$$x = \begin{bmatrix} \varepsilon^T & \dot{\varepsilon}^T & \beta^T & \zeta^T & p_B^T & \lambda^T \end{bmatrix}^T \in \mathbb{R}^{n_x}, \tag{2.28}$$

with $n_x = 8n_\varepsilon + 6n_\lambda + 13$, and $f : \mathbb{R}^{n_x} \times \mathbb{R}^{n_u} \to \mathbb{R}^{n_x}$ is a time-invariant, continuously differentiable function.

[3]The nomenclature of the Euler angles is consistent with the flight dynamics convention in which, for example, θ_B is the pitch angle.

The outputs $y \in \mathbb{R}^{n_y}$ of model, which are represented by

$$y = g(x, u), \tag{2.29}$$

where $g : \mathbb{R}^{n_x} \times \mathbb{R}^{n_u} \to \mathbb{R}^{n_y}$ is a continuously differentiable function, typically include rigid body related outputs, such as the true airspeed (V_T) and the angles of attack (α), sideslip (β), and flight path (γ) given by

$$\begin{aligned} V_T &= \sqrt{(u_B - w^i_{g_y})^2 + (v_B - w^i_{g_x})^2 + (w_B - w^i_{g_z})^2}, && (2.30)\\ \alpha &= -\tan^{-1}\left(\frac{w_B - w^i_{g_z}}{u_B - w^i_{g_y}}\right), && (2.31)\\ \beta &= \sin^{-1}\left(\frac{v_B - w^i_{g_x}}{V_T}\right), && (2.32)\\ \gamma &= \sin^{-1}\left(\frac{\dot{z}_B}{V_T}\right) \approx \theta_B - \alpha, && (2.33) \end{aligned}$$

as well as sensor measurements that depend explicitly on the strain states ε, such as accelerometers, gyroscopes, and strain gauges. Pang [79] has presented the derivation of several sensor outputs attached to a flexible structure in a strain-based model. Additionally, y can include the local loads on the structure, which in the local frame are given by:

$$\begin{bmatrix} F^i_x \\ M^i_{\text{torsion}} \\ M^i_{\text{oop}} \\ M^i_{\text{ip}} \end{bmatrix} = K_i \varepsilon_i \tag{2.34}$$

$$\begin{aligned} F^i_y &= \frac{\partial M^i_{\text{ip}}}{\partial s} && (2.35)\\ F^i_z &= \frac{\partial M^i_{\text{oop}}}{\partial s} && (2.36) \end{aligned}$$

where F^i_x, F^i_y, and F^i_z are shear forces; M^i_{torsion}, M^i_{oop}, and M^i_{ip}, are the torsion, out-of-plane and in-plane bending moments; and $K_i \in \mathbb{R}^{4\times4}$ is the local stiffness matrix at the ith beam element.

For a given a triple $(x_*, u_*, w_{g*}) \in \mathbb{R}^{n_x} \times \mathbb{R}^{n_u} \times \mathbb{R}^{n_w}$, Eqs. 2.27 and 2.29 can be locally

approximated by

$$\dot{x} = f(x_*, u_*, w_{g*}) + A(x - x_*) + B(u - u_*) + B_w(w_g - w_{g*}), \tag{2.37}$$

$$y = g(x_*, u_*) + C(x - x_*) + D(u - u_*), \tag{2.38}$$

where

$$A = \left.\frac{\partial f(x,u,w_g)}{\partial x}\right|_{(x_*,u_*,w_{g*})},\ B = \left.\frac{\partial f(x,u,w_g)}{\partial u}\right|_{(x_*,u_*,w_{g*})},\ B_w = \left.\frac{\partial f(x,u,w_g)}{\partial w_g}\right|_{(x_*,u_*,w_{g*})} \tag{2.39}$$

$$C = \left.\frac{\partial g(x,u)}{\partial x}\right|_{(x_*,u_*)},\ D = \left.\frac{\partial g(x,u)}{\partial u}\right|_{(x_*,u_*)}. \tag{2.40}$$

2.2 University of Michigan's Nonlinear Aeroelastic Simulation Toolbox (UM/NAST)

The University of Michigan's Nonlinear Aeroelastic Simulation Toolbox (UM/NAST) [80] is a software developed by the Active Aeroelasticity and Structures Research Laboratory (A^2SRL) for design, analysis and simulation of very flexible aircraft. It employs the geometrically nonlinear strain-based finite elements described in Section 2.1, different options for steady and unsteady aerodynamics, and nonlinear 6-degree of freedom (DOF) rigid body equations of motion to numerically simulate the dynamics of the aircraft. UM/NAST was the primary simulation framework utilized in this dissertation.

UM/NAST v4 is organized in a kernel containing several solvers, in which the Structural Solver and the Coupled Solver are the primary ones. From these two solver classes, other solvers are derived such as the Static Solver, Trim Solver, Linearization Solver, Dynamic Solver, among others. These solvers provide several tools to aid the control design for VFA, such as the matrices (A, B, B_w, C, D) of the linearized system in Eqs. 2.37-2.38 for a given trim condition, or the time response of the states of the nonlinear system in Eqs. 2.22-2.25 for a given load condition. A detailed description of the UM/NAST v4 organization is presented in Ref. [81].

The Coupled Solver also contains interfaces for establishing the connection between the UM/NAST kernel to its several external modules. These modules extend the functionalities of the kernel and provide flexibility to the user to implement their own routines while preserving the base solvers. Currently, these modules include user-defined aerodynamic models, gust models, sensor models, and controllers. The last three of these were extensively used in the work presented here, and several features were developed or enhanced throughout the process. The main contributions are highlighted next.

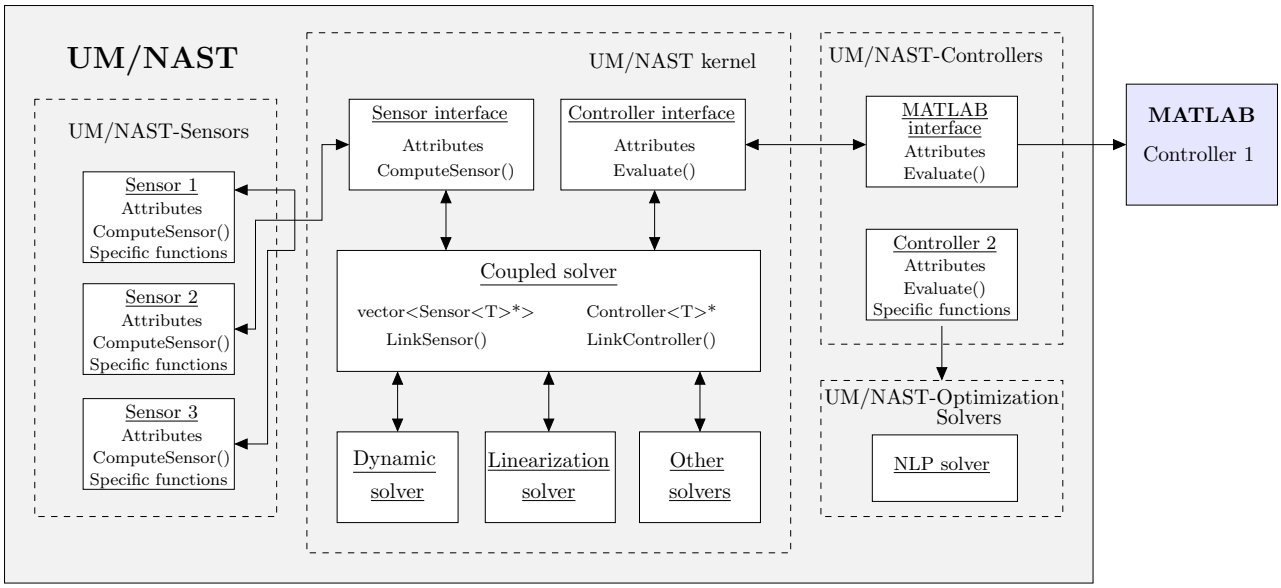

Figure 2.2: UM/NAST Sensors and Controller modules.

2.2.1 Sensor Module

The UM/NAST-Sensors module connects to the UM/NAST kernel through a generic sensor interface class (see Fig 2.2), which allows the access to relevant internal variables such as the state vector and its derivatives, jacobians, model properties, among others. This base sensor class has attributes common to all the types of sensors along with a prototype for a sensor output evaluation function. Inside the Sensors module, there is a collection of derived sensor classes with the specific implementations of different sensor units including, *inter alia*, accelerometers, strain gauges, inertial measurement units (IMUs), and inertial navigation systems (INSs). This architecture allows for independence between the UM/NAST kernel and the sensor implementations, so that new sensors can be added and used with UM/NAST without requiring modifications to the UM/NAST kernel.

When setting up a dynamic problem, sensors are defined independently on the UM/NAST model and solver and they are linked to the solver by means of the LinkSensor function. This establishes a two-way pointer between the sensor and the solver. Thus, the solver is able to call the sensor evaluation function for computing sensor outputs, and sensors have access to the dynamic solver data to obtain information for evaluating such outputs. Currently, the UM/NAST Dynamic Solver and Linearization Solver are able to call the sensor functions for time simulations or obtaining the linearized output response. These solvers can use multiple sensors with different types.

2.2.2 Controller Module

The UM/NAST-Controller module connects to the UM/NAST kernel through a base controller interface class (see Fig 2.2), which allows the access to internal variables in the dynamic solver such as the state, output, and input vectors. The Controller module is composed of several derived classes containing different types of controller implementation, such as PID, LQR and MPC. In a dynamic simulation, the user can connect one of these types to the UM/NAST Dynamic Solver using the LinkController function, and then call the controller function to update the control effectors based on a given control law. The control update is done at a rate defined by the user, which should be equal or greater than then simulation integration time step.

To run closed-loop simulations, the user has several options. Firstly, they can leverage the existing controller implementations shipped with the controller module, which only require entering the controller data, such as gains or prediction models. The MPC controller already contains the routines to solve the optimization problems, which is provided by the UM/NAST-Optimization Solvers package, which is a front-end interface to several unconstrained and constrained solvers for linear and nonlinear programming specifically designed for MPC applications. The second option is to implement their own C++ code with their controller implementation. Due to the modularity of UM/NAST, such an implementation can be done by just adding a new derived class to the Controller module with no modifications to the UM/NAST kernel.

The third option is to implement the controller using the MATLAB interface, also shipped with the Controller module. The MATLAB interface provides a connection between UM/NAST and MATLAB (see Fig 2.2) through which information can be mutually exchanged. This information can include the current simulation time, states, outputs, and the computed controller action. It facilitates the design and verification of controllers for VFA since it makes several control-related built-in MATLAB functions available to the user, therefore integrating the environments used for design and simulation. Additionally, because MATLAB is an interpreted programming language, any changes in the controller code do not require the re-compilation of the module, as it would in a C++ implementation. The connection between the two software is established through the MATLAB Engine API for C++, which allows calling MATLAB from a C++ program. Compared to an equivalent C++ implementation, the controller implemented in MATLAB interface has a small increase in computational time, usually less or equal than 25%.

2.3 Model Order Reduction

UM/NAST provides finite-element models for representing the coupled aeroelastic and rigid body dynamics of VFA that are suitable for vehicle design, analysis and simulation. However, even though being considered low-order among models provided by other fluid-structure interaction (FSI) solvers, these UM/NAST models are regarded as high-order for control design. As discussed in Section 2.1, the number of states depend on the number of flexible structural elements and lifting surfaces in the model. A typical aircraft model will have above 600 states. A lower order model could be created with a coarser discretization at the expense of reduced modeling accuracy which is undesirable. Therefore, model order reduction (MOR) techniques are necessary to create a low-order representation that preserves, within some tolerance, the relevant characteristics of the full-order model, such as outputs or modal frequencies.

Being a model-based controller that calls for solving an optimization problem online (see discussion in 3.1), MPC demands a low-order model for prediction and update to achieve real-time implementation. This is especially critical for fast dynamical systems, such as flight control systems (FCS), that have short control cycle times. While a more powerful computer could tackle the problem, they usually entail additional component mass in the vehicle, which can potentially clash with the stringent weight restrictions in aeronautical design. A reduced-order model (ROM) with less than fifty states is desirable.

The next sections present the MOR techniques considered in this work. They are divided into classical linear methods, which are applicable to systems whose dynamics can be approximated by linearized systems such as FA; and nonlinear MOR methods that create a nonlinear representation that are suitable for systems with more pronounced nonlinearities such as VFA.

2.3.1 Classical Model Order Reduction Methods

The linearized system in Eqs. 2.37-2.38 with zero disturbance is considered here with $(x_*, u_*, 0)$ being an equilibrium point. The inflow states λ are removed from the model by assuming that they are constant and equal to zero. This is based on the fact that these states describe the shed trailing vorticity, which are not controllable states. Henceforth, vector x will represent the state vector without the inflow states, unless stated otherwise. Define $\Delta x = x - x_*$, $\Delta u = u - u_*$, and $\Delta y = y - g(x_*, u_*)$ such that the non-disturbed linear

system can be represented as

$$\Delta\dot{x} = A\Delta x + B\Delta u, \tag{2.41}$$

$$\Delta y = C\Delta x + D\Delta u, \tag{2.42}$$

The objective of MOR for linear systems is to find $P_r \in \mathbb{R}^{n_{xr} \times n_x}$ associated with subspace $D_r \subseteq \mathbb{R}^{n_{xr}}$ such that $\Delta x_r \in \mathbb{R}^{n_{xr}}$ is the projection of Δx onto D_r, i.e.,

$$\Delta x_r = P_r \Delta x, \tag{2.43}$$

for $n_{xr} < n_x$. The definition of the reduced-order subspace D_r depends on the MOR technique and its ancillary objectives, as it will be exemplified later in this section.

Most linear MOR techniques follow these steps:

1. Change of basis: In this step, the reduced-order states are explicitly represented in the linear dynamical system. Transformation matrix $Q \in \mathbb{R}^{n_x \times n_x}$ can be selected to express Δx in a new basis, resulting in a transformed state vector $\Delta\bar{x}$ containing the states of interest, x_r, and the ones to discard, $x_d \in \mathbb{R}^{n_x - n_{xr}}$, i.e.,

$$\Delta\bar{x} \triangleq \begin{bmatrix} \Delta x_r \\ \Delta x_d \end{bmatrix} = Q\Delta x, \tag{2.44}$$

   for which the dynamical system can be written as:

$$\Delta\dot{\bar{x}} = Q^{-1}AQ\Delta\bar{x} + Q^{-1}B\Delta u, \tag{2.45}$$

$$\Delta y = CQ\Delta\bar{x} + D\Delta u. \tag{2.46}$$

   For Δx_r and Δx_d, the new state, input, and output matrices can be partitioned as follows:

$$Q^{-1}AQ = \begin{bmatrix} \bar{A}_{11} & \bar{A}_{12} \\ \bar{A}_{21} & \bar{A}_{22} \end{bmatrix}, \quad Q^{-1}B = \begin{bmatrix} \bar{B}_1 \\ \bar{B}_2 \end{bmatrix}, \quad CQ = \begin{bmatrix} \bar{C}_1 & \bar{C}_2 \end{bmatrix}. \tag{2.47}$$

2. Truncation or residualization: In this step, states x_d are removed from the model. Using the truncation method, x_d and its derivative are set equal to zero, thus resulting in the elimination of rows and columns associated with these variables. The truncated

model is then:

$$\Delta\dot{x}_r = \bar{A}_{11}\Delta x_r + \bar{B}_1\Delta u, \tag{2.48}$$

$$\Delta y = \bar{C}_1 x_r + Du. \tag{2.49}$$

The truncation method preserves the infinite frequency response of the original system. Alternatively, the residualization method can be applied to discard Δx_d. In this method, $\Delta\dot{x}_d$ is set equal to zero, and then Δx_d can be expressed as function of Δx_r and Δu as follows:

$$\Delta\dot{x}_d = \bar{A}_{21}\Delta x_r + \bar{A}_{22}\Delta x_d + \bar{B}_2\Delta u = 0. \tag{2.50}$$

Assuming that $\bar{A}_{22}$ is non-singular, then:

$$\Delta x_d = -\bar{A}_{22}^{-1}(\bar{A}_{21}\Delta x_r + \bar{B}_2\Delta u). \tag{2.51}$$

Using back substitution, the residualized model is then:

$$\Delta\dot{x}_r = (\bar{A}_{11} - \bar{A}_{12}\bar{A}_{22}^{-1}\bar{A}_{21})\Delta x_r + (\bar{B}_1 - \bar{A}_{12}\bar{A}_{22}^{-1}\bar{B}_2)\Delta u \tag{2.52}$$

$$\Delta y = (\bar{C}_1 - \bar{C}_2\bar{A}_{22}^{-1}\bar{A}_{21})\Delta x_r + (D - \bar{C}_2\bar{A}_{22}^{-1}\bar{B}_2)\Delta u \tag{2.53}$$

In contrast with truncation, residualization preserves the steady-state (DC gain) of the original system. Hence, for better accuracy at low frequencies, residualization is preferred. This is the case for VFA control, in which the low frequency (usually below 100 Hz) rigid body and aeroelastic modes are the ones of interest. Next, two MOR methods based on residualization are presented.

Modal-based residualization: In this method, the system is firstly put in modal form by choosing transformation matrix $Q = V$, where V is the eigenvector matrix from the eigen decomposition:

$$A = V^{-1}\Lambda V, \tag{2.54}$$

where Λ is a diagonal (or block-diagonal) matrix whose main diagonal contains the n_x eigen-

values of A in increasing order of frequencies.

$$\Lambda = \begin{bmatrix} \bar{\lambda}_1 & 0 & 0 & \cdots & 0 \\ 0 & \bar{\lambda}_2 & 0 & \cdots & 0 \\ 0 & 0 & \bar{\lambda}_3 & \cdots & 0 \\ \vdots & \vdots & \vdots & \ddots & \vdots \\ 0 & 0 & 0 & \cdots & \bar{\lambda}_{n_x} \end{bmatrix} \tag{2.55}$$

Subspace D_r is then formed by selecting the eigenvectors associated with the first n_{xr} eigenvalues of interest. Hence, the matrix P_r in Eq. 2.43 is equal to

$$P_r = \begin{bmatrix} I_{n_{xr}} & 0_{n_{xr}\times(n_x-n_{xr})} \end{bmatrix} V. \tag{2.56}$$

Advantages of the modal-based residualization include the preservation of the physical meaning of the reduced-order states, which correspond to the amplitudes of the retained modes.

Balanced residualization: In this method, it is assumed that the full-order system is both controllable and observable, with associated positive-definite controlability ($W_c \in \mathbb{R}^{n_x\times n_x}$) and observability ($W_o \in \mathbb{R}^{n_x\times n_x}$) Grammian matrices. The former can be decomposed into its Cholesky form $W_c = L_c^T L_c$ to form the joint controlability-observability measure:

$$W_{co} = L_c^T W_o L_c. \tag{2.57}$$

Matrix W_{co} can be expressed in its eigen form as follows

$$W_{co} = V_{co}^{-1} \Lambda_{co} V_{co}, \tag{2.58}$$

where Λ_{co} is a diagonal matrix whose main diagonal contains the eigenvalues $\lambda_i^{co}, i \in \mathbb{Z}_{[1,n_x]}$ of W_{co} in increasing order of magnitude, and V_{co} is a matrix whose columns are the corresponding eigenvectors. Define $\sigma_i = \sqrt{\lambda_i^{co}}, i \in \mathbb{Z}_{[1,n_x]}$, as the Hankel singular values, which provide a measure of the energy of each state in the system. The balanced residualization method relies on projecting the system onto the subspace D_r formed by the n_{xr} states with highest energy. These states are determined by applying transformation matrix $Q = L_c V_{co} \Sigma^{1/2}$, where $\Sigma \in \mathbb{R}^{n_x\times n_x}$ is a diagonal matrix with σ_i, to to put the system in balanced form. Residualization is then applied to remove the states below a certain threshold. Hence, the matrix P_r in Eq. 2.43 is equal to

$$P_r = \begin{bmatrix} I_{n_{xr}} & 0_{n_{xr}\times(n_x-n_{xr})} \end{bmatrix} L_c V_{co} \Sigma^{1/2}. \tag{2.59}$$

Advantages of the balanced residualization include the preservation of the stability, controllability, and observability characteristics of the original system. On the downside, the reduced order states lose their physical meaning.

2.3.2 Top-to-Bottom Model

Lanchares et al. [5] introduced a Top-to-bottom (T2B) reduced-order model for creating a nonlinear ROM. The ROM is obtained by constructing a piecewise-linear surrogate model in continuous time and then reducing it using local bases computed by balanced truncation. The resulting ROM is a hybrid system with continuous dynamics corresponding to the evolution within each individual set of reduced-order bases. The T2B ROM has shown to provide a good approximation for the dynamics of both FA and VFA.

Consider the model for a VFA in Eqs. 2.27-2.27 with zero disturbance. Given a pair $(x^i, u^i) \in \mathbb{R}^{n_x} \times \mathbb{R}^{n_u}$, a first-order local approximation of the nonlinear system in the neighborhood $(x, u) \in B_{(x^i,u^i)}(\varepsilon),\ \varepsilon \geq 0$, is given by:

$$\dot{x} \approx K_i + A_i x + B_i u \tag{2.60}$$

$$y \approx L_i + C_i x + D_i u, \tag{2.61}$$

where

$$A_i = \left.\frac{\partial f(x,u)}{\partial x}\right|_{(x^i,u^i)},\ B_i = \left.\frac{\partial f(x,u)}{\partial u}\right|_{(x^i,u^i)},\ K_i = f(x^i,u^i) - A_i x^i - B_i u^i \tag{2.62}$$

$$C_i = \left.\frac{\partial g(x,u)}{\partial x}\right|_{(x^i,u^i)},\ D_i = \left.\frac{\partial g(x,u)}{\partial u}\right|_{(x^i,u^i)},\ L_i = g(x^i,u^i) - C_i x^i - D_i u^i \tag{2.63}$$

The linearized system in Eqs. 2.60-2.61 is denoted by $\mathcal{S}_i$. Now consider a collection of M pairs $\mathscr{M} = \{(x^i, u^i) \in \mathbb{R}^{n_x} \times \mathbb{R}^{n_u}, i = 1, \ldots, M\}$ and their associated linearized systems. Then, the nonlinear system is approximated in the region defined by the convex hull of $\mathscr{M}$, $\text{conv}(\mathscr{M})$, by the convex combination of the linearized models (i.e., $\mathcal{S}_i,\ i = 1, \ldots, M$) as follows:

$$\dot{x} = f(x,u) \approx \sum_{i=1}^{M} w_i(x,u)\left(K_i + A_i x + B_i u\right), \tag{2.64}$$

$$y = g(x,u) \approx \sum_{i=1}^{M} w_i(x,u)\left(L_i + C_i x + D_i u\right), \tag{2.65}$$

where w_i are interpolation weights satisfying

$$\sum_{i=1}^{N} w_i(x,u) = 1, \tag{2.66}$$

$$w_i(x,u) \geq 0, \ i = 1, \ldots, M. \tag{2.67}$$

These weights are defined based on the distance defined over a subset of outputs representing the flight conditions. Define the subsets of the output to be y^p. Examples of selected outputs include altitude, Mach number, or wing deformation. Vector y_i^p represents the selected outputs values at the linearization point of linearized system $\mathcal{S}_i$. The weights are defined using distance function $d_i(x,u)$ as

$$w_i(x,u) = \frac{e^{-\beta_d d_i(x,u)/m(x,u)}}{\sum_{j=1}^{N} e^{-\beta_d d_j(x,u)/m(x,u)}}, \tag{2.68}$$

where

$$d_i(x,u) = ||y^p - y_i^p||_2, \qquad m(x,u) = \min_i d_i(x,u). \tag{2.69}$$

Note that the conditions specified in Eq. 2.67 are satisfied by the definitions of Eq. 2.68.

For each one of y_i^P, the corresponding pair (x_i, u_i) is a trimmed state-input pair, for which a linearized system can be determined. These linearized systems capture the change in dynamics within the specified flight envelope. The UM/NAST Trim and Linearization Solvers can be used to create these linearized systems.

Each linearized model $\mathcal{S}_i$ generated by UM/NAST will have a large number of states. This can preclude control applications due to the high computational cost. Therefore, MOR is performed through balanced truncation. As discussed in 2.3.1, this projection-based technique relies on the assumption that the state of the $\mathcal{S}_i$ system in Eqs. 2.60-2.61 evolves within a reduced-order subspace $D_r^i \subset \mathbb{R}^{n_x}$ of the original system. Let n_{xr} be the dimension of D_r^i.

The subset D_r^i passing through an arbitrary $x^0 \in \mathbb{R}^{n_x}$ is defined by the triple (x^0, V_i, W_i), where $V_i, W_i \in \mathbb{R}_{n_x \times n_{xr}}$ are projection matrices. Define the reduced-order linearized dynamics to be $\mathcal{S}_{r,i,j}$, where the subscript in $\mathcal{S}_{r,i,j}$ means that the reduced-order model was created by projecting the dynamics of system $\mathcal{S}_i$ onto the subspace D_r^j generated by the balance

truncation of system $\mathcal{S}_j$. Accordingly, $\mathcal{S}_{r,i,j}$ is given by:

$$\begin{aligned}
\dot{x}_r &= P_j K_i + P_j A_i (I - V_j P_j) x^0 + P_j A_i V_j x_r + P_j B_i u && (2.70)\\
&= K_{r,i,j} + A_{r,i,j} x_r + B_{r,i,j} u, && (2.71)\\
y &= L_i + C_i (I - V_j P_j) x^0 + C_i V_j x_r + D_i u && (2.72)\\
&= L_{r,i,j} + C_{r,i,j} x_r + D_{r,i,j} u, && (2.73)\\
& && (2.74)
\end{aligned}$$

where x^0 is the initial condition of the full-order $\mathcal{S}_i$ model and

$$\begin{aligned}
&P_j = (W_j^T V)^{-1} W_j^T, && (2.75)\\
&K_{r,i,j} = P_j K_i + P_j A_i (I - V_j P_j) x^0,\ A_{r,i,j} = P_j A_i V_j,\ B_{r,i,j} = P_j B_i, && (2.76)\\
&L_{r,i,j} = L_i + C_i (I - V_j P_j) x^0,\ C_{r,i,j} = C_i V_j,\ D_{r,i,j} = D_i. && (2.77)
\end{aligned}$$

Therefore, for M linearization points, M^2 reduced-order models are created. For models in the jth subspace, that is, $\mathcal{S}_{r,i,j}$ for $i = 1, \ldots, M$, an interpolation similar to the one in Eqs. 2.64 and 2.65 is performed to provide a reduced-order approximation of the original nonlinear system on such subspace:

$$\begin{aligned}
\dot{x}_r &= P_j f(V_j x_r + (I - V_j P_j) x^0, u) && (2.78)\\
&\approx \sum_{i=1}^{M} w_i (V_j x_r + (I - V_j P_j) x^0, u) \left(K_{r,i,j} + A_{r,i,j} x_r + B_{r,i,j} u\right) && (2.79)\\
y &= g(V_j x_r + (I - V_j P_j) x^0, u) && (2.80)\\
&\approx \sum_{i=1}^{M} w_i (V_j x_r + (I - V_j P_j) x^0, u) \left(L_{r,i,j} + C_{r,i,j} x_r + D_{r,i,j} u\right), && (2.81)
\end{aligned}$$

As the system evolves in time, the distance between the full-order state x and the different subspaces D_r^j for $j = 1, \ldots, M$ varies, as shown in Fig. 2.3. The closest the subspace is from the current state, the better reduced-order approximation it can provide. Therefore, it is reasonable to switch to the closest subspace, that is, update matrices V_j and W_j in Eqs. 2.79-2.81 based on the following rule:

$$j \in \mathbb{Z}_{[1,M]} \text{ such that } m(x_r, u) = d_j (V_j x_r + (I - V_j P_j) x^0, u), \tag{2.82}$$

where $m(\cdot)$ and $d(\cdot)$ are given in Eq. 2.69. The piecewise-linear reduced-order system in Eqs. 2.79-2.81 along with the switching rule in Eq. 2.82 are referred to as the T2B ROM. Figure 2.4 depicts the schematic operation of such a model. Note that the reduced-order

models and their respective bases are computed off-line, thus making the evaluation of the T2B ROM cheaper than the original nonlinear system.

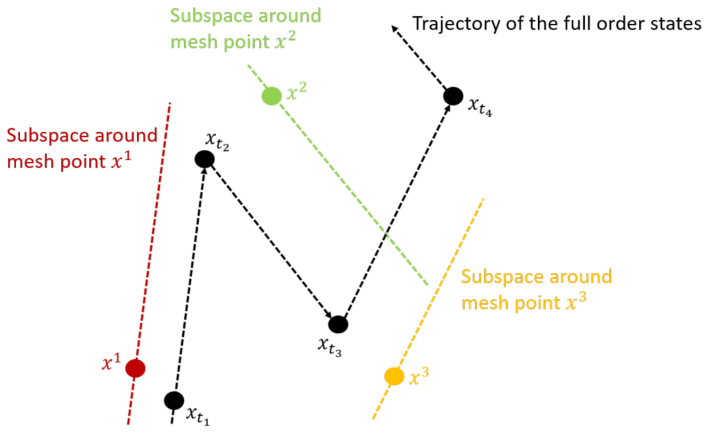

Figure 2.3: Graphical illustration of the piecewise-linear ROM [5].

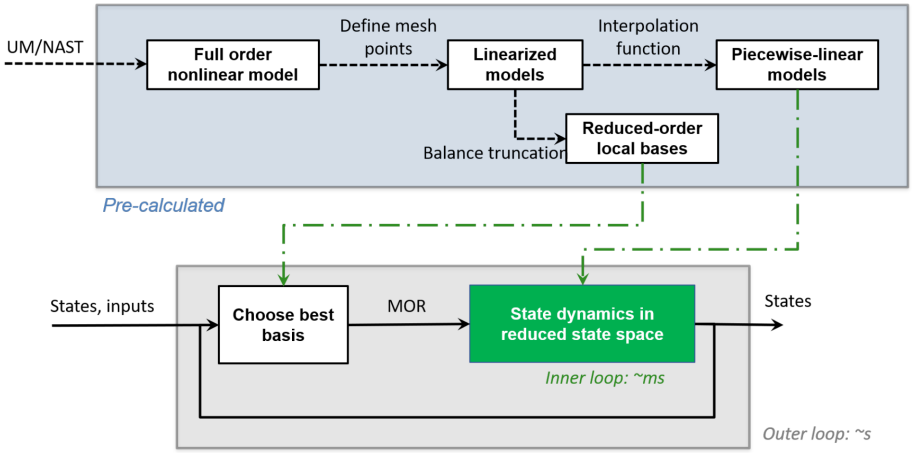

Figure 2.4: Schematic operation of piecewise-linear ROM algorithm [5].

For control design purposes, it is useful to define the T2B ROM as a function of the variation of x_r from the projected initial condition. By applying the following change of coordinates to each system $\mathcal{S}_i$

$$\Delta x = x - x^i, \tag{2.83}$$

$$\Delta u = u - u^i, \tag{2.84}$$

$$\Delta y = y - g(x^i, u^i), \tag{2.85}$$

and then building the reduced-order model following the aforementioned procedure, the following T2B ROM is obtained:

$$\Delta \dot{x}_r \approx \sum_{i=1}^{M} w_i(V_j \Delta x_r + (I + P_j - V_j P_j)x^0, u)\left(A_{r,i,j}\delta x_r + B_{r,i,j}\Delta u\right), \tag{2.86}$$

$$\Delta y \approx \sum_{i=1}^{M} w_i(V_j \Delta x_r + (I + P_j - V_j P_j)x^0, u)\left(C_{r,i,j}\Delta x_r + D_{r,i,j}\Delta u\right), \tag{2.87}$$

$$j \in \mathbb{Z}_{[1,M]} \text{ such that } m(x_r, u) = d_j(V_j \Delta x_r + (I + P_j - V_j P_j)x^0, u), \tag{2.88}$$

where

$$\Delta x_r = x_r - P_j x^0. \tag{2.89}$$

2.3.3 Bottom-to-Top Model

Duan et al. [6] presented the Bottom-to-top (B2T) modeling framework, a method to incrementally build a low-order aeroservoelastic model combining the conventional 6 DOF rigid body aircraft model, nonlinear structural dynamics, and data-driven low-order aerodynamics. The B2T model has shown be provide a good approximation of the nonlinear dynamics of both FA and VFA.

In the B2T model, the elastic displacement field r_P can be represented by either a linear modal discretization truncated up to the first n_η nodes:

$$r_P = \sum_{k=1}^{n_\eta} \Psi_k \eta_k = \Psi \eta, \tag{2.90}$$

where Ψ_k is the vector describing the mode shape connected with mode amplitude η_k, which can be arranged, respectively, in matrix $\Psi \in \mathbb{R}^{n_\eta \times n_\eta}$ and vector $\eta \in \mathbb{R}^{n_\eta}$; or by a nonlinear function representing the nonlinear displacement due to deformation:

$$r_P = r_{P_0} + \varphi(\eta), \tag{2.91}$$

where r_{P_0} is the initial displacement and $\varphi(\eta)$ is a function of the reduced-order nonlinear states η. The linear representation is appropriate for FA whose structural dynamics can still be represented by linear mode shapes. On the other hand, VFA is better represented by the nonlinear formulation, especially to capture the geometric nonlinearities. Similarly, for the aerodynamic loads the B2T accepts either a linear representation along the linear modal decomposition in Eq. 2.90, or a nonlinear representation depending on the nonlinear displacement field in Eq. 2.91.

The B2T low-order coupled nonlinear aeroelastic-flight mechanics equation of motion is given by:

$$E\begin{bmatrix}\dot{v}_B\\ \dot{\omega}_B\\ \ddot{\eta}\\ \dot{\eta}\end{bmatrix} = -\begin{bmatrix} m\tilde{\omega}v_B + m\dot{\eta}^T\frac{\partial^2 r_C(\eta)}{\partial\eta^2}\dot{\eta} + 2m\tilde{\omega}_B\frac{\partial r_C(\eta)}{\eta}\dot{\eta} + m\tilde{\omega}_B^2 r_C(\eta)\\ m\tilde{r}_C(\eta)(\tilde{\omega}_B v_B) + \dot{\eta}^T H_{\text{hess}}(\eta)\dot{\eta} + 2(J_0(\eta)\dot{\eta})\omega_B + \tilde{\omega}_B I_B(\eta)\omega_B\\ m\left(\frac{\partial r_C(\eta)}{\partial\eta}\right)^T(\tilde{\omega}_B V) + \frac{1}{2}\dot{\eta}^T\frac{\partial M}{\partial\eta}\dot{\eta} + 2(\nu(\eta)\dot{\eta}\omega_B) - \omega^T J_0(\eta)\omega_B + K_\eta\eta\end{bmatrix} + F(\eta), \tag{2.92}$$

where

$$E = \begin{bmatrix} m & -m\tilde{r}_C(\eta) & m\frac{\partial r_C(\eta)}{\partial\eta} & 0\\ m\tilde{r}_C(\eta) & I_B(\eta) & H_{\text{jac}}(\eta) & 0\\ m\left(\frac{\partial r_C(\eta)}{\partial\eta}\right)^T & H_{\text{jac}}^T(\eta) & M(\eta) & 0\\ 0 & 0 & 0 & I_n\end{bmatrix},\ F(\eta) = \begin{bmatrix} F_{\text{g}}(\eta) + F_{\text{aero}}(\eta) + F_{\text{thrust}}(\eta)\\ M_{\text{g}}(\eta) + M_{\text{aero}}(\eta) + M_{\text{thrust}}(\eta)\\ Q_{\text{g}}(\eta) + Q_{\text{aero}}(\eta) + Q_{\text{thrust}}(\eta)\\ 0\end{bmatrix}, \tag{2.93}$$

The detailed derivation is presented in Ref. [6]. In Eq. 2.92, m represents the mass of the vehicle, $I_B(\eta)$ its inertia matrix, $r_C(\eta)$ the position of the center of mass, $M(\eta)$ the modal mass matrix, K_η a stiffness matrix, and v_B and ω_B are the linear and angular velocities as defined in Eqs. 2.7-2.8. Variables $H_{\text{hess}}(\eta)$, $H_{\text{jac}}(\eta)$, $J_0(\eta)$, and $\nu(\eta)$ are composite function of $\varphi(\eta)$, and their definitions are presented in [6]. Vector $F(\eta)$ contains forces and moments due to gravity, aerodynamics, and the propulsion system.

Several properties of the vehicle that are necessary to build the B2T model can be extracted from higher-order models, such as the ones provided by NASTRAN or UM/NAST. These properties include, among others, the mass and inertia properties, modal decomposition, and data regarding the several variables in Eq. 2.92 that depend on the aeroelastic deformation. These variables can be approximated by a constant or linear relation when the representation in Eq. 2.90 is used, but they will require a nonlinear characterization when the nonlinear displacement field in Eq. 2.91 is used. Due to the size and complexity of these models, a nonlinear analytical representation is usually not available, but data-driven approximations can provide good results as shown in Ref. [6]. In this work, Duan et al. used UM/NAST as a tool to generate the values of the nonlinear terms for a large number of random inputs within prescribed bounds, that was then used to train a shallow neural network. Figure 2.5 shows the schematic of the process of approximating each one of the terms in Eq. 2.92 by neural networks.

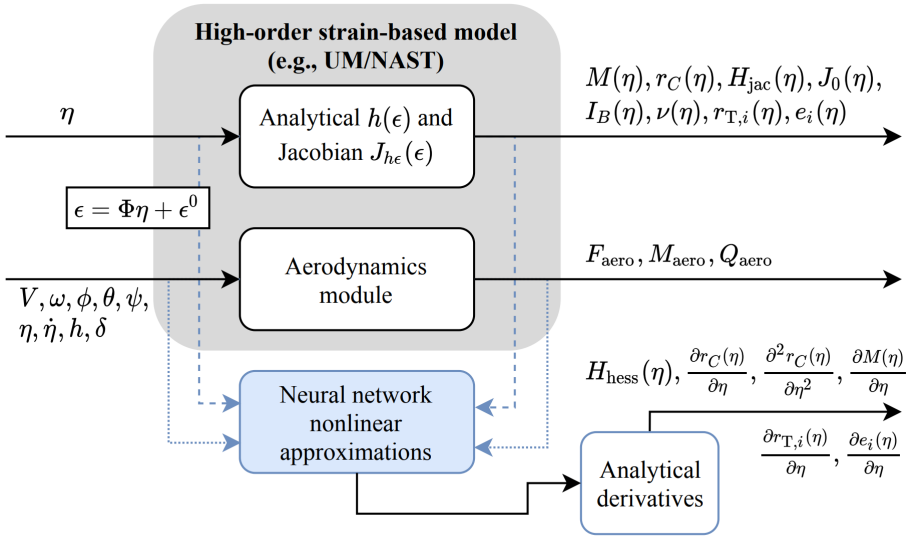

Figure 2.5: Nonlinear function training in the Bottom-to-top model using UM/NAST data [6].

2.4 Aircraft Models

Aircraft models with different levels of structural flexibility were studied in this dissertation. Models for these aircraft were available in the UM/NAST framework. Next, each aircraft model is introduced in increasing order of flexibility.

- **Generic Transport Aircraft (GTA):** The GTA aircraft represents a flexible aircraft (Fig. 2.6). The model has throttle control and three control surfaces, namely, elevators, rudder, and ailerons. The 22-m long fuselage is rigid, as well as the tail. The 19-m span wing has varying structural flexibility, and the dominant mode is the out-of-plane bending at 1.45 Hz.

- **XRF1 aircraft:** The XRF1 is an Airbus provided industrial standard multi-disciplinary research testcase representing a typical configuration for a long range wide body aircraft. The XRF1 research testcase is used by Airbus to engage with external partners on development and demonstration of relevant capabilities/technologies. A front view of the aircraft is shown in Fig. 2.7. The fuselage, wing and tail structures of XRF1 are flexible, but the level of flexibility falls within a range where the flexible and rigid body dynamics can still be decoupled for control design. Hence this baseline XRF1 model is representative of a flexible aircraft. The aircraft model has 7 different mass configurations that vary with respect to the total mass, mass distribution, and consequently, inertia properties and aeroelastic response.

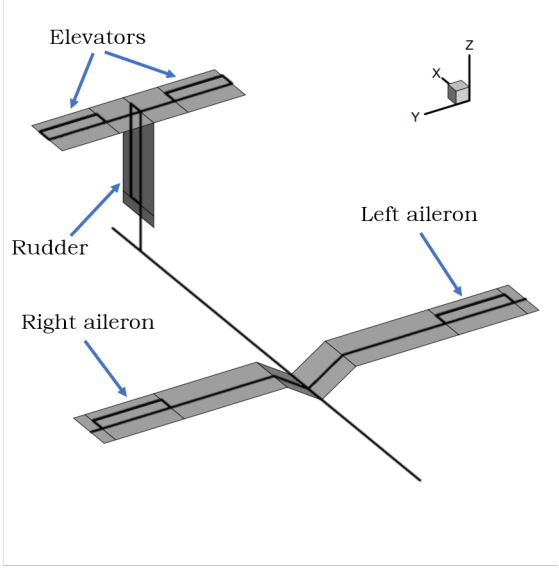

Figure 2.6: GTA aircraft.

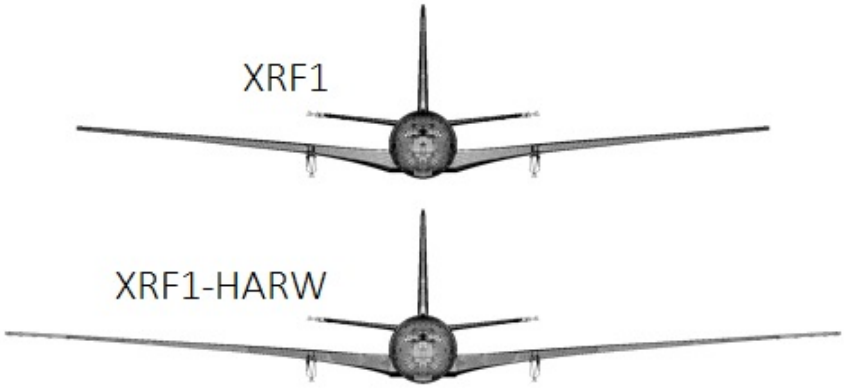

Figure 2.7: XRF1 and XRF1-HARW aircraft.

XRF1 has eleven control effectors available for control design (Fig. 2.8), namely, flaps, outer and inner ailerons at each semi-wing, elevators at the left and right horizontal tail planes, a rudder at the vertical tail plane, and left and right point forces acting as thrust. For control design purposes, the degrees of freedom of the control effectors are reduced to eight by imposing the elevators to deflect symmetrically, the inner ailerons to deflect anti-symmetrically, and symmetric thrust. The flaps and outer ailerons work independently as flaperons/elevons.

- **XRF1-HARW aircraft:** To create a model that represents a flexible aircraft with increased flexibility, the Airbus-Michigan Center for Aero-Servo-Elasticity of Very Flexible Aircraft (CASE-VFA) modified the baseline XRF1 to create XRF1-HARW [82], a

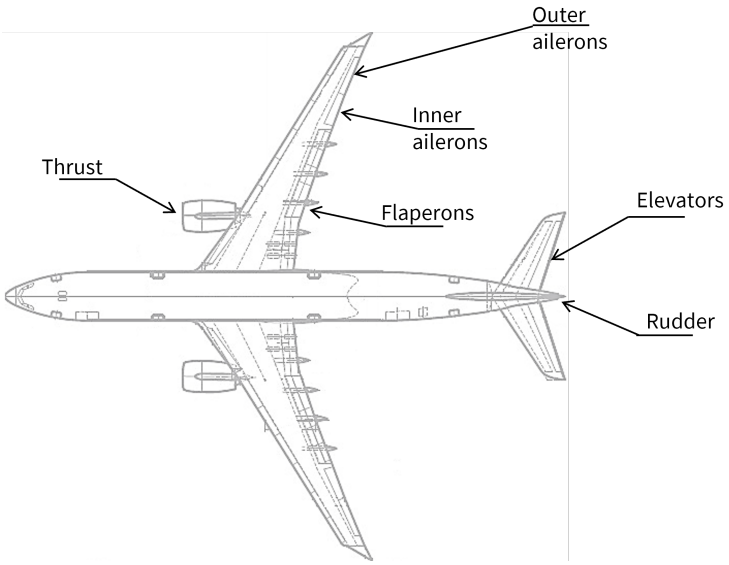

Figure 2.8: XRF1 aircraft control effectors.

model for a future high-aspect-ratio-wing commercial transport vehicle. XRF1-HARW has the same geometry and properties as XRF1, but with a wing 20% longer, as shown in Fig. 2.7. Therefore, the nonlinear effects become more pronounced, and the flexible and rigid body responses can have frequencies of similar magnitude. In fact, the first out-of-plane bending moment of XRF1-HARW is 40.26% smaller than the same frequency of the baseline XRF1. The XRF1-HARW model has the same control effectors as the baseline XRF1 model.

- **X-HALE aircraft:** The X-HALE is a very flexible, remote-piloted aircraft developed at the University of Michigan with the primary objective to collect experimental aeroelastic data and to serve as a platform to evaluate control strategies [83]. The X-HALE aircraft is shown in Fig. 2.9. It is a wing-boom-tail type aircraft with a 6-meter span, divided into six sections of 1-meter long each, with the tip sections set at a dihedral angle of 10 deg. The wing has an EMX-07 airfoil profile with 0.2 m chord, while the tails employ the NACA 0012 airfoil profile with chord length of 0.12 m.

  As shown in Fig. 2.10, there are eleven control effectors available: two roll spoilers located at the dihedral sections, four elevators situated at each outboard tail (represented by T1-T4), and five motors (represented by P0-P4). The center tail is not used as a control surface. For control design, six control inputs are considered, namely, the inner elevator deflection (symmetrical for both surfaces), the outer elevator deflection on the right wing, the outer elevator deflection on the left wing, the roll spoiler deflection (given by the difference between the deflection of the right and left spoilers), the

Figure 2.9: University of Michigan's X-HALE aircraft.

differential thrust (difference between the revolutions per second of the left motors and right motors), and the overall thrust (average of revolutions per second of all motors). Note that the spoiler can only have positive deflection.

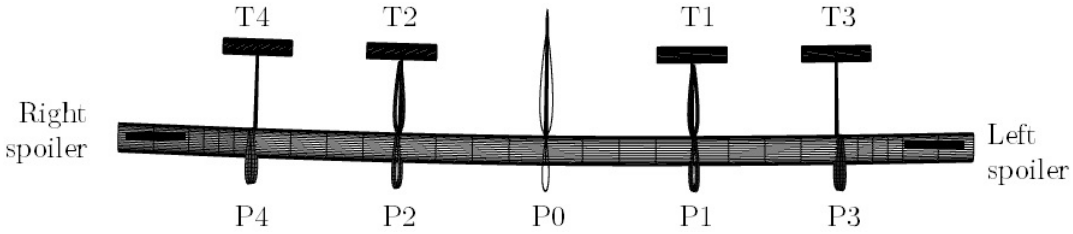

Figure 2.10: X-HALE aircraft control effectors.

CHAPTER 3

Constrained Control of Very Flexible Aircraft

Most practical control systems are subject to operational constraints such as actuator or safety limits. FA and VFA are examples of such systems. Load alleviation in these vehicles can be approached as a constrained control problem in which loads at critical stations must be kept within safety limits by deflecting the control surfaces. Model predictive control (MPC) and reference governors (RG) are of significant interest for MLA due to their ability to enforce pointwise-in-time constraints on the loads and actuation of control effectors. Solving the MPC optimization problem in real-time for these systems still remains a challenge for being large-scale systems which usually have a high number of states and constraints. This section presents MPC-based load alleviation systems and investigates methods for efficient implementation.

3.1 Model predictive control

Model Predictive Control (MPC) is the most widespread approach for systematically incorporating constraints into the design process. It has been adopted on a broad scale in chemical process industry and is becoming popular also for systems with faster dynamics, especially in the aerospace and automotive fields.

Traditional MPC schemes use the current state information to predict the response over a specified future horizon. Based on a performance index and the system constraints, a sequence of control inputs is determined by solving a discrete optimization problem within a prescribed update time interval.

The prediction step in MPC typically uses a mathematical or numerical model that represents the dynamics of the system. The MPC formulation can be divided into two categories depending on the choice of such a prediction model: Nonlinear MPC (NMPC), in which a nonlinear model is used to represent the system; and linear MPC, in which a linear (or linearized) model is used for prediction.

3.1.1 Nonlinear MPC

Consider a system represented by the nonlinear time-invariant discrete-time dynamical equation

$$x^+ = f_s(x, u), \tag{3.1}$$

where $x \in \mathbb{R}^{n_x}$ is the state vector, $u \in \mathbb{R}^{n_u}$ is the input vector, and $f_s : \mathbb{R}^{n_x} \times \mathbb{R}^{n_u} \to \mathbb{R}^{n_x}$ is a specified function. For a FA or VFA, this function can be, for example, a discrete-time version of the B2T model presented in Section 2.3.3. The discretization of the B2T model can be performed by applying methods such as forward Euler or 4^{th}-order Runge Kutta.

Assumption 1 *$f_s(x, u)$ is a twice continuously differentiable function with respect to x and u.*

The state and input at sampling time $k \in \mathbb{Z}_{++}$ are denoted by x_k and u_k, respectively. The following constraints are imposed:

$$x_k \in X \quad \forall\ k, \tag{3.2}$$

$$u_k \in U \quad \forall\ k, \tag{3.3}$$

where X and U are compact sets such that $0 \in \text{int}X$ and $0 \in \text{int}U$. It is assumed that these sets can be represented by finitely many constraint functions as follows:

$$X = \{x \in \mathbb{R}^{n_x} | g_i(x) \leq 0, \text{ for } i = 1, \ldots, n_{cx}\}, \tag{3.4}$$

$$U = \{u \in \mathbb{R}^{n_u} | h_i(u) \leq 0, \text{ for } i = 1, \ldots, n_{cu}\}, \tag{3.5}$$

where $g_i(x) : \mathbb{R}^{n_x} \to \mathbb{R}$ for $i = 1, \ldots, n_{cx}$ and $h_i(u) : \mathbb{R}^{n_u} \to \mathbb{R}$ for $i = 1, \ldots, n_{cu}$ are twice continuously differentiable functions. The total number of constraints is denoted by $n_c = n_{cx} + n_{cu}$.

A model predictive control law $\kappa_N(x)$ is then designed to stabilize the origin of (3.1). The control law is obtained online as the solution of an open-loop discrete-time optimal control problem over a fixed prediction horizon $N \in \mathbb{Z}_{++}$ with cost function,

$$V_N(x, \mathbf{x}, \mathbf{u}) = V_f(x_N) + \sum_{k=0}^{N-1} l(x_k, u_k), \tag{3.6}$$

where $x_0 = x$, i.e., the current state. Define $\mathbf{u} \triangleq [u_0(x)^T, \ldots, u_{N-1}^T(x)]^T$ and $\mathbf{x} \triangleq [x_1(x)^T, \ldots, x_N^T(x)]^T$, respectively, as the sequence of control actions and resulting state trajectory of (3.1) up to N steps ahead of the current time. The constrained optimization

problem that is solved at each sampling time is formulated as follows:

$$\mathrm{P}_N(x, X_f): \quad V_N^*(x) = \min_{\mathbf{u}} \{V_N(x, \mathbf{x}, \mathbf{u}) | (\mathbf{x}, \mathbf{u}) \in \mathscr{F}_N,\ x_N \in X_f\}, \tag{3.7}$$

where $\mathscr{F}_N$ is the set of constraints

$$\mathscr{F}_N \triangleq \{(\mathbf{x}, \mathbf{u}) | x_{k+1} \in X, u_k \in U,\ k \in \mathbb{Z}_{[0,N-1]}\}, \tag{3.8}$$

$V_f(x)$ is the terminal cost, and $X_f \subset X$ is the terminal set such that $0 \in X_f$. The stage cost $l(x, u)$ is assumed to be a positive definite function in x. The cost function $V_N(x, \mathbf{u})$ is assumed to be twice continuously differentiable. The MPC law is defined as the first move in the optimal sequence $\mathbf{u}^*$:

$$\kappa_N(x) = u_0^*(x). \tag{3.9}$$

The next assumption establishes the sufficient ingredients for stability of closed-loop system.

Assumption 2 *Let $V_f(x)$ be a Control Lyapunov Function and X_f be a set such that $X_f = \{x \in \mathbb{R}^{n_x} | V_f(x) \leq \alpha\}$, with $\alpha > 0$ such that $X_f \subset X$ and for all $x \in X_f$ the following holds:*

$$\alpha_1(||x||) \leq V_f(x) \leq \alpha_2(||x||) \tag{3.10}$$

$$\inf_{u \in U} \{F(f(x, u)) - F(x) + l(x, u)\} \leq 0, \tag{3.11}$$

where $\alpha_1(\cdot)$ and $\alpha_2(\cdot)$ are class $\mathscr{K}$-functions.

If the terminal cost and terminal set satisfy Assumption 3, then the optimal cost $V_N^*(x)$ of $P_N(x, X_f)$ is a Lyapunov function and the MPC control law asymptotically stabilizes the equilibrium at origin of (3.1) for all initial states for which $P_N(x, X_f)$ is feasible [84].

The calculation of terminal set X_f that satisfies Assumption 2 may be cumbersome for large-scale systems. Under some additional assumptions, set X_f can be replaced by X. The next proposition establishes the domain of attraction of the MPC without the terminal constraint.

Proposition 1 ([85], Theorem 1) *Consider $V_f(x)$ and X_f such that Assumption 2 holds. Let $\beta \in \mathbb{R}_{++}$ such that $l(x, u) > \beta\ \forall x \notin X_f$ and $\forall u \in U$. Then the MPC controller with $N \geq 1$ derived from $P_N(x, X)$ asymptotically stabilizes the system (3.1) subject to (3.2) and (3.3) for any initial state in*

$$\Gamma_N = \{x \in \mathbb{R}^{n_x} | V_N^*(x) \leq l(x, \kappa_N(x)) + \beta \cdot (N - 1) + \alpha\}. \tag{3.12}$$

As discussed in [85], the domain of attraction Γ_N can be approximated by $\Upsilon_N \subset \Gamma_N$, which is also a domain of attraction and is defined as:

$$\Upsilon_N \triangleq \{x \in \mathbb{R}^{n_x} | V_N^*(x) \leq N \cdot \beta + \alpha\}. \tag{3.13}$$

While recursive feasibility is guaranteed by the ingredients presented in Assumption 2 [84], in practice, model mismatch, external disturbances, and noise can lead the NMPC to an infeasible condition. To prevent such a situation, the hard constraints in the states and outputs of the system in Eq. 3.4 can be transformed into soft constraints by the introduction of slack variables $\varepsilon_{s,k} \geq 0, k \in \mathbb{Z}_{[1,N]}$, as follows:

$$X(\varepsilon_{s,k}) = \{x \in \mathbb{R}^{n_x} | g_i(x) \leq \varepsilon_{s,k}, \text{ for } i = 1, \ldots, n_{cx}\}. \tag{3.14}$$

To mitigate constraint violations due to the soft constraints, a large weight $\mu \in \mathbb{R}_{++}$ is then added to the objective function to penalize the slack variables. The relaxed NMPC problem

$$\mathrm{P}_N^{\varepsilon}(x, X): \; V_N^*(x) = \min_{\mathbf{u}, \boldsymbol{\varepsilon}_s} \left\{ V_N(x, \mathbf{x}, \mathbf{u}) + \mu \boldsymbol{\varepsilon}_s^T \boldsymbol{\varepsilon}_s | (\mathbf{x}, \mathbf{u}) \in \mathscr{F}_N^{\varepsilon}, \; \boldsymbol{\varepsilon}_s \succeq 0 \right\}, \tag{3.15}$$

where $\boldsymbol{\varepsilon}_s \triangleq \begin{bmatrix} \varepsilon_{s,1} & \cdots & \varepsilon_{s,N} \end{bmatrix}^T \in \mathbb{R}^N$ is a vector that concatenates the slack variables, and $\mathscr{F}_N^{\varepsilon}$ is the set of relaxed constraints

$$\mathscr{F}_N^{\varepsilon} \triangleq \{(\mathbf{x}, \mathbf{u}) | x_{k+1} \in X(\varepsilon_{s,k+1}), u_k \in U, \; k \in \mathbb{Z}_{[0,N-1]}\}. \tag{3.16}$$

Note that the input constraints are usually not relaxed because they are trivially satisfied.

The optimal control problem (OCP) $P_N^{\varepsilon}(x, X)$ is a nonconvex nonlinear program (NLP). The solution of this NLP is obtained through numerical optimization. The selection of the solver is important for achieving real-time implementation, especially when dealing with large-scale problems as the control of VFA. Depending on the selected solver, specific strategies can be implemented to reduce the computational footprint. Interior point methods, for example, can take advantage of the sparse structure of system of equations to speed-up computations. Sequential quadratic programming (Sequential Quadratic Programming (SQP)), which is an iterative algorithm that consecutively solves quadratic programs (QPs) to approximate the NLP solution, can benefit from warmstarting whenever coupled with QP solvers such as active-set methods or Newton-type solvers. Other implementation strategies for fast solutions include: i) the use of ROMs, such as the B2T model, to reduce the number of states; ii) the condensed NMPC formulation, especially when using SQP, in which the equality constraints and the states as decision variables are eliminated (see Appendix B.2

for details); iii) suboptimal solutions by limiting the number of iterations in the solver (see Ref [86]); iv) constraint aggregation in which a set of constraints is represented by fewer functions (see discussion in Section 3.3.1).

3.1.2 Linear MPC

Linear MPC is a subclass of NMPC problems in which the prediction model is linear, i.e.,

$$f_s(x,u) = A^d \Delta x + B^d \Delta u, \tag{3.17}$$

where the superscript d denotes the discrete-time version of matrices A and B in Eq. 2.37. Therefore the results for stability and recursive stability presented in Section 3.1.1 still apply.

If the constraints in Eqs. 3.4-3.3 are affine functions, then they can be represented as:

$$E_0 + E_1 x_{k+1} + E_2 u_k \preceq 0, \quad \text{for } k \in \mathbb{Z}_{[0,N-1]}, \tag{3.18}$$

or in the relaxed form:

$$E_0 + E_1 x_{k+1} + E_2 u_k \preceq E_3 \varepsilon_{s,k+1}, \quad \text{for } k \in \mathbb{Z}_{[0,N-1]}, \tag{3.19}$$

where $E_0 \in \mathbb{R}^{n_c}$, $E_1 \in \mathbb{R}^{n_c \times n_x}$, $E_2 \in \mathbb{R}^{n_c \times n_u}$, and $E_3 \in \mathbb{R}^{n_c}$ are constraint matrices. These affine constraint functions appear, for example, when upper and lower limits are imposed on state, input and output variables.

A typical choice for the cost function in Eq. 3.6 is a quadratic function, which is related to the energy of states and inputs in the system. For vectors $\Delta \mathbf{u} \triangleq [\Delta u_0^T, \ldots, \Delta u_{N-1}^T]^T$ and $\Delta \mathbf{x} \triangleq [\Delta x_1^T, \ldots, \Delta x_N^T]^T$, such cost function usually has the following form:

$$V_N(\Delta x, \Delta \mathbf{x}, \Delta \mathbf{u}) = ||\Delta x_N||_{P_f}^2 + \sum_{k=0}^{N-1} ||\Delta x_k||_Q^2 + ||\Delta u_k||_R^2, \tag{3.20}$$

with weighting matrices $Q \in \mathbb{R}^{n_x \times n_x}, Q \succeq 0$, $R \in \mathbb{R}^{n_u \times n_u}, R \succ 0$. The terminal weight $P_f \in \mathbb{R}^{n_x \times n_x}, P_f \succ 0$, is the solution of the discrete-time algebraic Riccati equation:

$$P_f = A^{dT} P_f A^d - \left(A^{dT} P_f B^d\right)\left(R + B^{dT} P_f B^d\right)^{-1}\left(B^{dT} P_f A^d\right) + Q. \tag{3.21}$$

The OCP $P_N(x, X)$ with prediction model in Eq. 3.17, inequality constraints in Eq. 3.18, and cost function in 3.20 forms a convex QP. Several commercial solvers are available for QP problems, including interior-point methods (e.g., CPLEX), active-set methods (e.g.,

qpOASES [87], qpkwik [88]), and Newton-type methods (e.g., FBstab [89]). In the VFA control application, active-set methods have shown to provide the best performance.

The implementation strategies for reduced computational cost that were mentioned in Section 3.1.1 are still applicable to linear MPC. For instance, this QP can be put in the condensed form as follows (see details in Appendix B.1):

$$V_N^*(\Delta x) = \min_{\Delta \mathbf{u}} \Delta \mathbf{u}^T H_c \Delta \mathbf{u} + 2 q_c^T \Delta \mathbf{u} \tag{3.22}$$

$$\text{s.t.} \quad \Delta x_0 = \Delta x, \tag{3.23}$$

$$G_c \Delta \mathbf{u} + W_c \preceq 0. \tag{3.24}$$

To reduce the number of decision variables in the optimization problem even further, a common practice in linear MPC design is to use move blocking. With move blocking, groups of adjacent-in-time predicted inputs are constrained to the same value, so that the number of degrees of freedom of the predicted input actions is reduced. Move blocking results in a modified QP problem of the form,

$$V_{N,M}^*(\Delta x) = \min_{\Delta \bar{\mathbf{u}}} \Delta \bar{\mathbf{u}}^T \bar{H}_c \Delta \bar{\mathbf{u}} + 2 \bar{q}_c^T \Delta \bar{\mathbf{u}} \tag{3.25}$$

$$\text{s.t.} \quad \Delta x_0 = \Delta x, \tag{3.26}$$

$$\bar{G}_c \Delta \bar{\mathbf{u}} + W_c \preceq 0, \tag{3.27}$$

where

$$\bar{H}_c \triangleq V_{M_u}^T H_c V_{M_u}, \quad \bar{q} \triangleq V_{M_u}^T q_c, \quad \bar{G}_c \triangleq G_c V_{M_u}, \tag{3.28}$$

$$V_{M_u} = \begin{bmatrix} T_k \otimes I_{n_u} & 0 \\ 0 & I_N \end{bmatrix} \in \mathbb{R}^{N n_u \times M_u n_u}, \tag{3.29}$$

$\Delta \mathbf{u} = V_{M_u} \Delta \bar{\mathbf{u}}$ and the matrix $T_k \in \mathbb{R}^{N \times M_u}$ is the blocking matrix, with $M_u \in \mathbb{Z}_{(1,N)}$ designating the number of degrees of freedom given to the predicted inputs (also known as the control horizon).

The blocking matrix can be designed in a number of different ways [90]. Here the input blocking method is used, in which inputs are fixed to be constant over $t \geq k + M_u$ time-steps within the prediction horizon. Hence, the blocking matrix is given by:

$$T_k = \begin{bmatrix} I_{M_u} \\ [0_{(N-M_u)\times(M_u-1)} \quad 1_{N-M_u}] \end{bmatrix}. \tag{3.30}$$

3.1.3 MPC using LPV models

In Section 2.3.2, the T2B model was presented, which is a reduced-order LPV representation for FA and VFA. This model can be used for prediction in MPC. To this end, the T2B ROM in Eqs. 2.86-2.88 can be converted to discrete-time assuming a zero-order hold with a given sample time so that the control inputs are constant over each sampling period. The discretization is performed for each model $\mathcal{S}_{r,i,j}$. The resulting discrete-time T2B ROM has the following form:

$$\Delta x_{r,k+1} = \sum_{i=1}^{M} w_i(V_j \Delta x_{r,k} + (I + P_j - V_j P_j)x^0, u_k) \left(A^d_{r,i,j}\Delta x_{r,k} + B^d_{r,i,j}\Delta u_k\right), \quad (3.31)$$

$$\Delta y_k = \sum_{i=1}^{M} w_i(V_j \Delta x_{r,k} + (I + P_j - V_j P_j)x^0, u_k) \left(C^d_{r,i,j}\Delta x_{r,k} + D^d_{r,i,j}\Delta u_k\right), \quad (3.32)$$

$$j \in \mathbb{Z}_{[1,M]} \text{ s.t. } m(x_{r,k}, u_k) = d_j(V_j \Delta x_{r,k} + (I + P_j - V_j P_j)x^0, u_k), \quad (3.33)$$

where the superscript d denotes the corresponding discrete-time matrices.

An MPC formulation with quadratic cost similar to Eq. 3.20 is considered here. However, the selection of terminal cost P_f as shown in Section 3.1.2 may not be possible. Ideally, a single matrix P_f should be computed such that the feedback gain stabilizes all systems $\mathcal{S}_{r,i,j}$. This is equivalent to finding P_f and stabilizing gain K_f that solves the discrete-time Lyapunov inequality for all systems $\mathcal{S}_{r,i,j}$. This leads to a linear matrix inequality (LMI) problem, which may be difficult to solve depending on the number of ROMs, and the existence of a solution is not guaranteed. Therefore, the terminal penalty is not considered here. To preserve stability of the MPC controller, the prediction horizon can be chosen long enough to approximate the solution of an LQR [91]. The optimization problem solved at each MPC step reads as follows:

$$V^*_N(x) = \min_{\Delta\mathbf{u}, \Delta\mathbf{x}_r, \boldsymbol{\varepsilon}_s} \sum_{k=0}^{N-1} ||\Delta x_{r,k}||^2_{Q_r} + ||\Delta u_k||^2_R + \mu\varepsilon^2_{s,k} \quad (3.34)$$

$$\text{s.t.} \quad E_0 + E_1\Delta x_{r,k+1} + E_2\Delta u_k \leq E_3\varepsilon_{s,k} \text{ for } k \in \mathbb{Z}_{[0,N-1]}, \quad (3.35)$$

$$\varepsilon_{s,k} \geq 0 \text{ for } k \in \mathbb{Z}_{[1,N]}, \quad (3.36)$$

$$x^0 = x, \quad (3.37)$$

$$x_{r,0} = P_j x^0, \quad (3.38)$$

$$\Delta x_{r,0} = P_j(x^0 - \bar{x}), \quad (3.39)$$

$$\text{Eqs. } 2.68, 2.69, 3.31, 3.32, 3.33, \quad (3.40)$$

where E_0, E_1, E_2 and E_3 are matrices of appropriate sizes to represent the linear constraints,

and Q_r and R are positive definite weighting matrices. The pair $(\bar{x}, \bar{u})$ represents the initial full-order state and control input. Note that a relaxed constraints are considered here in order to avoid feasibility issues due to the use of ROMs for prediction.

Since the weights w_i in Eqs. 3.31-3.32 depend on $x_{r,k}$, they can vary within the prediction horizon. They are updated according to the nonlinear equations in Eqs. 2.68-2.69, therefore, this optimization problem is nonconvex. Furthermore, the switching rule in Eq. 3.33 can be incorporated into the optimization problem as mixed-integer linear inequalities, thus making this optimization problem a mixed-integer nonlinear programming (MINLP) problem. This class of problems is NP-complete, making it hard to be solved in real-time in an application that demands small sampling times such as the control of a VFA.

To circumvent this issue, the MPC problem is reformulated by simplifying the prediction model. The weights w_i are evaluated at the current full-order state and input, and kept fixed over the prediction horizon. In doing so, the equations used for prediction become linear time-invariant (LTI) models in solving each optimization problem. In addition, the switching rule can be dropped from the optimization problem. The resulting optimization has the following form:

$$V_N^*(x,u) = \min_{\Delta\mathbf{u},\Delta\mathbf{x}_r,\boldsymbol{\varepsilon}_s} \sum_{k=0}^{N-1} ||\Delta x_{k,r}||_{Q_r}^2 + ||\Delta u_k||_R^2 + \mu\varepsilon_{s,k}^2 \tag{3.41}$$

$$\text{s.t.} \quad \Delta x_{k+1} = \sum_{i=1}^{M} w_i(x^0,u^0)\left(A_{r,i,j}^d \delta x_{r,k} + B_{r,i,j}^d \delta u_k\right), \tag{3.42}$$

$$\Delta y_k = \sum_{i=1}^{M} w_i(x^0,u^0)\left(C_{r,i,j}^d \Delta x_{r,k} + D_{r,i,j}^d \Delta u_k\right), \tag{3.43}$$

$$j \in \mathbb{Z}_{[1,M]} \text{ s.t. } m(x^0,u^0) = d_j(x^0,u^0), \tag{3.44}$$

$$E_0 + E_1\Delta x_{r,k+1} + E_2\Delta u_k \leq E_3\varepsilon_{s,k} \quad \text{for } k \in \mathbb{Z}_{[0,N-1]}, \tag{3.45}$$

$$\varepsilon_{s,k+1} \geq 0 \quad \text{for } k \in \mathbb{Z}_{[1,N]}, \tag{3.46}$$

$$x^0 = x, \tag{3.47}$$

$$u^0 = u, \tag{3.48}$$

$$x_{r,0} = P_j x^0, \tag{3.49}$$

$$\Delta x_{r,0} = P_j(x^0 - \bar{x}). \tag{3.50}$$

The optimization problem now becomes a QP problem, which can be efficiently solved using commercial solvers. The potential prediction errors due to freezing the model over the prediction horizon are mitigated by employing the shortest prediction horizon possible, and because MPC is based on a receding-horizon principle, in which only the first move of the

optimal sequence is applied to the plant. In the next MPC step, the prediction model is updated based on the new values of (x^0, u^0), and the same process is repeated recursively.

Silimlar to the linear MPC formulation presented in Section 3.1.2, the number of decision variables can be reduced by using the condensed MPC formulation (Appendix B.1). Because the prediction model is updated at each MPC step, this process has to be repeated whenever the model changes.

3.2 Control Architectures for Load Alleviation

Two control architectures based on MPC for load alleviation are presented next.

3.2.1 MPC Architecture

The MPC architecture in Fig. 3.1 is conceived as an integrated flight control system, that is, it is responsible for both command tracking and load alleviation. In this sense, the controller not only prevents the aircraft from exceeding structural safety limits, but also makes use of the aircraft flexibility to potentially improve the aircraft performance by computing the optimal control action based on predictions of both rigid and flexible dynamics.

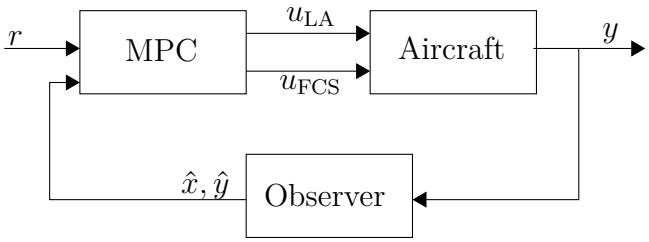

Figure 3.1: MPC architecture.

The available control effectors u in the aircraft are divided into two groups:

$$u = \begin{bmatrix} u_{\text{FCS}}^T & u_{\text{LA}}^T \end{bmatrix}^T, \tag{3.51}$$

where:

- u_{FCS} : These are the control effectors typically used by a FCS for speed and attitude control during cruise. This can include the propulsion system throttle (u_T), and the primary control surfaces (u_a): elevator, rudder and ailerons.
- u_{LA} : These are the primary control effectors to perform load alleviation. For instance, flaperons or elevons on the wing.

In the MPC architecture, the MPC controller coordinates both u_{FCS} and u_{LA}. The control objective is to track the reference r while enforcing the load constraints. The vector $r \in \mathbb{R}^{n_r}$ of references usually include the desired airspeed r_V, sideslip angle r_β, heading angle r_ψ, and flight path angle r_γ (refer to Section 2.1 for the definition of these outputs):

$$r \triangleq \begin{bmatrix} r_V & r_\beta & r_\psi & r_\gamma \end{bmatrix}^T. \tag{3.52}$$

The reference is assumed to be constant in time. Let $y_k^{\text{track}} \in \mathbb{R}^{n_r}$ be a subset of the output vector corresponding to the tacked variables. Let $S^{\text{track}} \in \mathbb{R}^{n_r, n_y}$ be a selection matrix such that $y_k^{\text{track}} = S^{\text{track}} y_k$ The tracking error is then defined as:

$$e_k = r - y_k^{\text{track}} = S^{\text{track}} g(x_k, u_k). \tag{3.53}$$

To design a tracking MPC controller, the incremental rate-based MPC formulation is considered, which results in a robust augmentation of the controller with an integral action. This ensures, under reasonable assumptions, zero steady-state tracking error even when a mismatch between the model used for the design and the actual plant is present. The OCP is formulated as follows:

$$V_N^*(\hat{x}) = \min_{\delta\mathbf{x}, \delta\mathbf{u}, \boldsymbol{\varepsilon}_s} ||e_N||_{P_f}^2 + \sum_{k=0}^{N-1} ||e_k||_{Q_e}^2 + ||\delta u_k||_R^2 + ||u_{\text{LA},k}||_{R_{\text{LA}}}^2 + \mu \varepsilon_{s,k}^2, \tag{3.54}$$

$$\text{s.t.} \quad \delta x_{k+1} = f_s(x_{k+1}, u_{k+1}) - f_s(x_k, u_k) \quad \text{for} \quad k \in \mathbb{Z}_{[0,N-1]} \tag{3.55}$$

$$e_k = r - S^{\text{track}} g(x_k, u_k) \quad \text{for} \quad k \in \mathbb{Z}_{[0,N]} \tag{3.56}$$

$$u_{k+1} = u_k + \delta u_k \quad \text{for} \quad k \in \mathbb{Z}_{[0,N-1]} \tag{3.57}$$

$$x_{k+1} = x_k + \delta x_k \quad \text{for} \quad k \in \mathbb{Z}_{[0,N-1]} \tag{3.58}$$

$$x_0 = \hat{x}, \tag{3.59}$$

$$(\mathbf{x}, \mathbf{u}) \in \mathcal{F}_N^\varepsilon \tag{3.60}$$

$$\boldsymbol{\varepsilon}_s \succeq 0, \tag{3.61}$$

where

$$\delta u_k \triangleq u_{k+1} - u_k, \tag{3.62}$$

$$\delta x_k \triangleq x_{k+1} - x_k, \tag{3.63}$$

and $\delta\mathbf{u}$ and $\delta\mathbf{x}$, respectively, are the vectors that concatenate these variables over the prediction horizon. Q_e, R, R_{LA} and P are symmetric positive definite weighting matrices, and $\mu > 0$ is a scalar weight. The definition of constraint set $\mathcal{F}_N^\varepsilon$ for load alleviation problems

will be presented in Chapter 4. The terminal penalty is computed on δx_N and e_N, defined based on the solution of the algebraic Riccati equation (Eq. 3.21) for the subsystem which represents the linearized dynamics of δx_k and e_k. The current state x is replaced by its estimate $\hat{x}$ provided by a state observer as it will be discussed in Section 3.5.

The prediction model in Eqs. 3.55-3.56 can be either the nonlinear B2T ROM model, the T2B LPV ROM model, or a linearized ROM model about a given condition, as discussed in Section 3.1. Differently than the MPC formulations presented in Section 3.1, the MPC control law of the incremental rate-based formulation returns the relative increment $\delta u_0^*(\hat{x})$ in the control action, rather than its absolute value $u_0^*(\hat{x})$. Nevertheless, the properties and implementation strategies presented in Section 3.1 still apply.

The cost function in Eq. 3.54 includes a penalty on u_{LA} in addition to the usual penalization of its rate of change δu_{LA}. The penalty on u_{LA} ensures that the control effectors used for load alleviation return back to the trim condition after reducing loads. This is desired to minimize drag and deviation from the nominal trajectory when the MLA system is deactivated. Note that the control efectors assigned to perform load alleviation are not dedicated, meaning that, in addition to performing alleviating loads, they can also assist the effectors u_{FCS} for attitude and speed control. This supplementary behavior can be minimized by tuning the controller, usually by choosing the weights on u_{LA} greater than the weights on the remaining control effectors.

3.2.2 Load Alleviation Governor Architecture

In the load alleviation (LA) governor architecture shown in Fig. 3.2, the MPC controller plays the role of a reference governor for the inner loop, in addition to manipulating the extra degrees of freedom provided by u_{LA} to alleviate loads. The signal tracking task is assigned to the inner loop. Appealing features of this architecture include the preservation of the nominal controller in the inner loop, which can be advantageous from a design perspective, since the conventional flight control system is augmented rather than replaced. Moreover, the performance and stability of the vehicle is protected even if the outer loop has to be deactivated.

A nominal discrete-time controller is designed for output tracking in the inner-loop. This controller is divided into two linear-quadratic-integral (LQ-I) controllers that independently manipulate control effectors u_a and u_T for attitude and speed tracking, respectively. The control signals, u_{LA}, are assumed to be zero at this design step, i.e., the corresponding control effectos are assumed to be at the trim values. Figure 3.3 shows a schematic of the implementation.

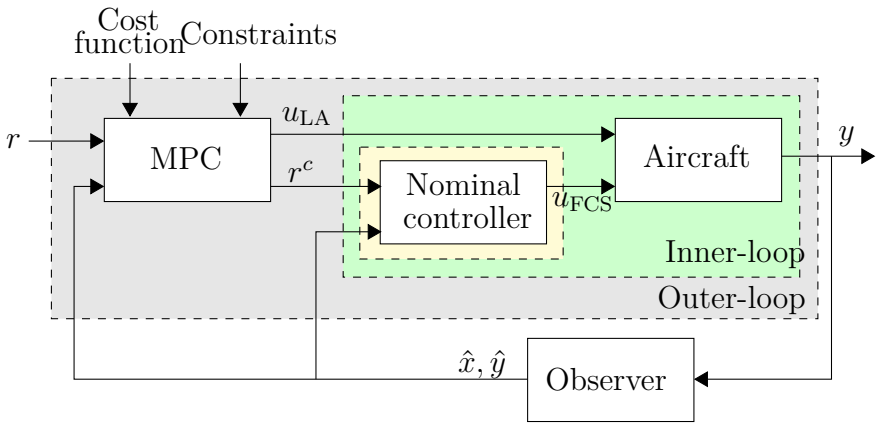

Figure 3.2: Load alleviation governor architecture.

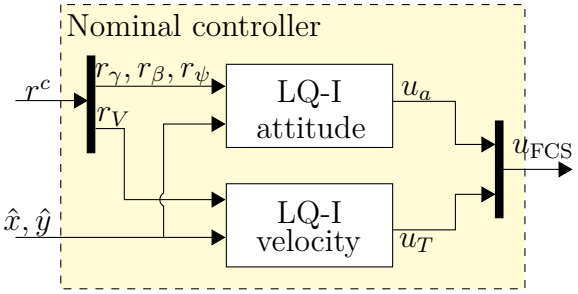

Figure 3.3: Inner loop for speed and attitude tracking.

The LQ-I controllers are designed based on the linearized dynamics of the aircraft in Eqs. 2.37-2.38 with respect to a trim condition. The continuous-time linearized model is shown next, in which subscripts F and R stand for flexible and rigid, respectively:

$$\begin{bmatrix} \Delta\dot{x}_F \\ \Delta\dot{x}_R \end{bmatrix} = \begin{bmatrix} A_{FF} & A_{FR} \\ A_{RF} & A_{RR} \end{bmatrix} \begin{bmatrix} \Delta x_F \\ \Delta x_R \end{bmatrix} + \begin{bmatrix} B_F \\ B_R \end{bmatrix} \Delta u \tag{3.64}$$

$$\Delta y = \begin{bmatrix} C_F & C_R \end{bmatrix} \begin{bmatrix} \Delta x_F \\ \Delta x_R \end{bmatrix} + D\Delta u, \tag{3.65}$$

The rigid body part of the linear model in Eq. 3.64 is used to design the nominal controller. To obtain the residualized linear model for the rigid-body dynamics with states $x_R \in \mathbb{R}^{12}$, the flexible states are assumed to be in steady-state, and then the residualization procedure in Section 2.3.1 is applied, yielding a ROM described by matrices $\left(\bar{A}_R, \bar{B}_R, \bar{C}_R, \bar{D}_R\right)$. The model in is then discretized using zero-order hold with the sampling period T_{inner} to obtain the discrete-time model with matrices $\left(\bar{A}_R^d, \bar{B}_R^d, \bar{C}_R^d, \bar{D}_R^d\right)$. The control law design for tracking r_γ, r_β and r_ψ is shown next. Similar derivations are performed to obtain the gains for the

LQ-I controller responsible for tracking velocity set-point, r_V, by adjusting u_T (the details are skipped). Let $(\Delta u_a)_k$ be the control effectors manipulated by the controller at instant k. The LQ-I control design for $(\Delta u_a)_k$ minimizes the following cost function,

$$V_\infty = \sum_{k=0}^{\infty}(e_{a_k}^T Q_e e_{a_k} + (\delta u_a)_k^T R_z (\delta u_a)_k) = \sum_{k=0}^{\infty}(z_k^T Q_z z_k + (\delta u_a)_k^T R_z (\delta u_a)_k), \tag{3.66}$$

where $(\delta u_a)_k = (\Delta u_a)_{k+1} - (\Delta u_a)_k$, Q_e and R_z are symmetric positive definite weighting matrices, e_{a_k} is the attitude tracking error, and

$$Q_z \triangleq \begin{bmatrix} 0 & 0 \\ 0 & Q_e \end{bmatrix}. \tag{3.67}$$

The vector z_k is the augmented state vector defined as

$$z_k \triangleq \begin{bmatrix} \delta x_{R_k}^T & e_{a_k}^T \end{bmatrix}^T, \tag{3.68}$$

where $\delta x_{R_k} = \Delta x_{R_{k+1}} - \Delta x_{R_k}$. Hence, the augmented model is given by

$$z_{k+1} = \begin{bmatrix} \bar{A}_R^d & 0 \\ [\bar{C}_R^d]_a & I \end{bmatrix} z_k + \begin{bmatrix} [\bar{B}_R^d]_a \\ [\bar{D}_R^d]_a \end{bmatrix} (\delta u_a)_k = A_z z_k + B_z (\delta u_a)_k. \tag{3.69}$$

The notation $[\cdot]_a$ in Eq. 3.69 means the selection of the matrix columns and/or rows that are connected to the tracked attitude variables and/or the control effectors Δu_a. The solution of this optimal control problem has the form:

$$(\delta u_a)_k = -\left(R_z + B_z^T P_z B_z\right)^{-1} B_z^T P_z A_z z_k = K_1 \delta x_k + K_2 e_k, \tag{3.70}$$

where $P_z = P_z^T$ is the solution of the algebraic Riccati equation,

$$P_z = A_z^T P_z A_z - (A_z^T P_z B_z)(R_z + B_z^T P_z B_z)^{-1}(B_z^T P_z A_z) + Q_z, \tag{3.71}$$

and K_1, K_2 are the resulting control gains.

From Eq. 3.70, the controller update equation has the form,

$$(\Delta u_a)_{k+1} = (\Delta u_a)_k + K_1(\Delta x_{k+1} - \Delta x_k) + K_2(\left[S^{\text{track}} \Delta y_k\right]_a - r^c). \tag{3.72}$$

Eq. 3.72 shows that the control law includes an integral action, which allows the tracking of commands with zero steady-state offset.

Let $\kappa_{\text{LQI}}(x, y, r)$ represent the combined control law for attitude and control tracking in the inner-loop, such that u in Eq. 3.51 is modified to u_{LQI} as follows:

$$u_{\text{LQI}}(x, y, r, u_{\text{LA}}) = \begin{bmatrix} \kappa_{\text{LQI}}(x, y, r)^T & u_{\text{LA}}^T \end{bmatrix}^T. \tag{3.73}$$

The closed-loop inner-loop system is then denoted by

$$x^+ = f_s(x, u_{\text{LQI}}(x, y, r, u_{\text{LA}})). \tag{3.74}$$

The MPC in the outer-loop of the LA governor uses Eq. 3.74 as the prediction model. It modifies the references $r^c \in \mathbb{R}^{n_r}$ to be fed into the inner-loop and u_{LA} to avoid constraint violations. The modifications are kept to a minimum, so that $r^c = r$ and $u_{\text{LA}} = 0$ whenever there is no danger of constraint violation. Denote by u^r the vector that concatenates these variables:

$$u^r = \begin{bmatrix} r^{cT} & u_{\text{LA}}^T \end{bmatrix}^T. \tag{3.75}$$

Define $\delta u_k^r \triangleq u_{k+1}^r - u_k^r$, and $\delta \mathbf{u}^r$ the vector that concatenates these variables over the prediction horizon. The OCP is then written in the rate-based formulation as follows:

$$V_N^*(\hat{x}, \hat{y}) = \min_{\mathbf{x}, \delta\mathbf{u}^r, \boldsymbol{\varepsilon}_s} \sum_{k=0}^{N-1} ||r_k^c - r||_{Q_c}^2 + ||\delta u_k^r||_R^2 + ||u_{\text{LA},k}||_{R_{\text{LA}}}^2 + \mu\varepsilon_{s,k}^2, \tag{3.76}$$

$$\text{s.t.} \quad x_{k+1} = f_s(x, u_{\text{LQI}}(\hat{x}, \hat{y}, r, u_{\text{LA},k})) \quad \text{for} \quad k \in \mathbb{Z}_{[0,N-1]} \tag{3.77}$$

$$u_{k+1}^r = u_k^r + \delta u_k^r \quad \text{for} \quad k \in \mathbb{Z}_{[0,N-1]} \tag{3.78}$$

$$x_0 = \hat{x}, \tag{3.79}$$

$$(\mathbf{x}, \mathbf{u}) \in \mathscr{F}_N^{\varepsilon} \tag{3.80}$$

$$\boldsymbol{\varepsilon}_s \succeq 0, \tag{3.81}$$

where $Q_c \succeq 0$ is a weighting matrix. Vectors $\hat{x}$ and $\hat{y}$ denote the estimated states and outputs, respectively. State estimation will be covered in Section 3.5. Differently from the designs presented previously, the MPC in the LA architecture does not stabilize the system, since such task is taken over by the inner-loop controller. Therefore, the cost function in Eq. 3.76 does not need to have a terminal cost.

The prediction model in Eq. 3.77 can be either the B2T ROM model, or a linearized ROM model for the FA or VFA. However, the T2B model cannot be used by this architecture, since it is required that the aircraft along with an inner-loop controller to be stable, since the LA governor alone may not be able enforce stability. The projection of model $\mathcal{S}_i$ onto subspace D_p^j only preserves stability if $i = j$. In the T2B ROM, this projection is done for

$i = 1, \ldots, M$ and, therefore, stability may be lost, making this ROM not suitable for the LA governor design.

3.3 MPC with Aggregated Constraints

Solving the MPC optimization problem in real-time can be challenging, especially for large-scale systems such as VFA that have a high number of states and constraints. Long prediction horizons, which are desired in some cases to avoid instability or infeasibility issues, can also engender a large number of constraints. For these problems, the computational cost of numerical optimization can be high, possibly hindering applications due to time or hardware limitations.

Several strategies have been proposed to decrease the computational cost of implementing MPC solutions, *inter alia*, by reducing the number of decision variables [90], by exploiting the structure of the optimization problem [92], or by relying on off-line computed control laws [93]. Likewise, the reduction in the number of constraints has also been investigated by either approximating convex polytopic feasible sets by ellipsoids [94], or by employing constraint aggregation methods. In the latter approach, the constraints are lumped into a few composite functions that approximately represent the feasible set. A classical choice for these composite functions is the maximum-value function. However, this type of function is not differentiable and cannot be used with the conventional gradient-based solvers [95]. Motivated by the need to handle large-scale optimization problems especially in the Multidisciplinary Design Optimization field, various methods have been proposed for approximating the maximum-value function in a differentiable manner. Examples include the Kreisselmeier-Steinhauser (KS) function, p-norm, and induced aggregation functionals [96].

Named after the researchers that firstly proposed it, the KS function was introduced in robust control to handle non-smooth optimization problems. Subsequent works on open-loop optimal control confirmed its potential to reduce the computational footprint of numerical solutions [97, 98, 99]. In MPC design, Richards [100] was able to speed up the computational performance of the online optimization by reducing the number of decision variables when adopting the KS function for inclusion of soft constraints.

In the next sections, the use of constraint aggregation for reducing the number of constraints in NMPC will be investigated using tools from sensitivity analysis. Appendix C presents some useful notation and results from sensitivity analysis.

3.3.1 Constraint Aggregation

Consider a nonlinear program with inequality constraints of the form:

$$(\mathrm{P}_0): \quad p_0 = \min_{z\in\mathbb{R}^{n_z}} \{f(z)|z \in \mathscr{F}_0\} \tag{3.82}$$

with the feasible set,

$$\mathscr{F}_0 \triangleq \left\{z \in \mathbb{R}^n | g_i(z) \leq 0, \text{ for } i \in \mathbb{Z}_{[1,n_c]}\right\}. \tag{3.83}$$

Define $g_{\max}(z) \triangleq \max_{i=1,\ldots,n_c}\{g_i(z)\}$. The number of constraints in (P_0) can be reduced by replacing the n_c constraints with a function that aggregates all g_i by creating a smooth approximation of $g_{\max}(z)$:

$$c(g_i(z), \rho) = g_{\max}(z) + r(g_i(z), \rho), \tag{3.84}$$

where $\rho \in \mathbb{R}$ is an aggregation parameter that controls the approximation and $r(g_i(z), \rho)$ is a residual term [96]. An example of aggregation of the form (3.84) such that $c(g_i(z), \rho)$ is smooth will be given later in Section 3.3.2.

The optimization problem in (3.82) is reformulated with constraint aggregation as follows:

$$(\mathrm{P}_\rho): \quad p_\rho = \min_{z\in\mathbb{R}^{n_z}} \{f(z)|z \in \mathscr{F}_\rho\} \tag{3.85}$$

with the feasible set,

$$\mathscr{F}_\rho \triangleq \{z \in \mathbb{R}^n | c(g_i(z), \rho) \leq 0\}. \tag{3.86}$$

Definition 1 *The aggregation in Eq. (3.84) is said to be conservative if there exists $\bar{\rho} > 0$ such that $r(g_i(z), \rho) > 0$ for all $\rho > \bar{\rho}$ and all $z \in \mathbb{R}^n$, i.e.,*

$$\mathscr{F}_\rho \subseteq \mathscr{F}_0. \tag{3.87}$$

Definition 2 *The constraint aggregation function is said to be tight at ρ_t if $r(g_i(z), \rho) \to 0$ as $\rho \to \rho_t$ for all $z \in \mathbb{R}^n$.*

Note that even if $\mathcal{S}_{P_0} \neq \emptyset$ and ρ is chosen such that $\mathscr{F}_\rho \neq \emptyset$, the set of solutions $\mathcal{S}_{P_\rho}$ may still be empty. For instance, consider the following non-convex minimization problem:

$$\min_{x\in\mathbb{R}, y\in\mathbb{R}} \{-(4/3)x^3 - 4x^2 | \max(x^5, 0) - y \geq 0, x \geq -3, y \geq 0\}. \tag{3.88}$$

The unique local minimizer is $(x, y) = (-2, 0)$. However, for any smooth conservative ag-

gregation function, the set of local minimizers of the aggregated problem is empty. This anomaly is due to the minimizer located at a cusp formed by constraint intersections, which cannot be approximated by a smooth function.

The next theorem establishes the connection between nonlinear programs with aggregated constraints and the perturbed nonlinear programs in Section C.2 to provide sufficient conditions for the existence of a local minimizer of (P_ρ), and a relationship between the optimal value and solution of (P_0).

Theorem 1 *Let (z_0, λ_0) be a strongly regular solution of the GE associated with (P_0). Assume that there exists $\rho_t \in \mathbb{R}$ such that the constraint aggregation function in Eq. (3.84) is tight. Let $\rho \in \mathbb{R}$ be such that $\mathcal{F}_\rho \neq \emptyset$. Then for ρ sufficiently close to ρ_t:*
a) There exists z_ρ that is a unique local minimizer of (P_ρ) with an associated unique Lagrange multiplier λ_ρ;
b) $||z_\rho - z_0|| = O(t)$;
c) $p_\rho = p_0 + t p_{PL_d} + \frac{1}{2} t^2 p_{PQ} + o(t^2)$,
with $t = |\rho - \rho_t|$, $d = sign(\rho - \rho_t)$, and p_{PL_d} and p_{PQ} as defined in Eq. (C.7) and (C.15), respectively.

Proof: Let $c(g_i(z), \rho)$ be tight at ρ_t. Consider the sequence $\mathcal{P} = \rho_1, \rho_2, \ldots$ of real numbers such that $\lim_{n\to\infty} \rho_n = \rho_t$. Define the indicator functions $\mathbf{1}_{\mathcal{F}_0} : \mathbb{R}^{n_z} \to \{0, 1\}$ and $\mathbf{1}_{\mathcal{F}_\rho} : \mathbb{R}^{n_z} \times \mathbb{R} \to \{0, 1\}$ as follows:

$$\mathbf{1}_{\mathcal{F}_0}(z) = \begin{cases} 1 & \text{if } z \in \mathcal{F}_0 \\ 0 & \text{otherwise} \end{cases} \tag{3.89}$$

$$\mathbf{1}_{\mathcal{F}_\rho}(z, \rho) = \begin{cases} 1 & \text{if } z \in \mathcal{F}_\rho \\ 0 & \text{otherwise} \end{cases} \tag{3.90}$$

with $\mathcal{F}_0$ and $\mathcal{F}_\rho$ as defined in Eqs. (3.83) and (3.86), respectively. Because the aggregation is tight at ρ_t then

$$\lim_{n\to\infty} \mathbf{1}_{\mathcal{F}_\rho}(z, \rho_n) = \mathbf{1}_{\mathcal{F}_0}(z). \tag{3.91}$$

Let $\mathcal{F}_{\rho_1}, \mathcal{F}_{\rho_2}, \ldots$ be a sequence of sets associated with each $\rho \in \mathcal{P}$ and defined as in (3.86). Then:

$$\begin{aligned} \liminf_{n\to\infty} \mathcal{F}_{\rho_n} &= \{z \in \mathbb{R}^{n_z} | \liminf_{n\to\infty} \mathbf{1}_{\mathcal{F}_\rho}(z, \rho_n) = 1\} && (3.92) \\ &= \{z \in \mathbb{R}^{n_z} | \mathbf{1}_{\mathcal{F}_0}(z) = 1\} && (3.93) \\ &= \mathcal{F}_0 && (3.94) \end{aligned}$$

and

$$\begin{aligned}
\limsup_{n\to\infty} \mathscr{F}_{\rho_n} &= \{z \in \mathbb{R}^{n_z} | \limsup_{n\to\infty} \mathbf{1}_{\mathscr{F}_\rho}(z, \rho_n) = 1\} && (3.95)\\
&= \{z \in \mathbb{R}^{n_z} | \mathbf{1}_{\mathscr{F}_0}(z) = 1\} && (3.96)\\
&= \mathscr{F}_0 && (3.97)
\end{aligned}$$

Therefore,

$$\lim_{n\to\infty} \mathscr{F}_{\rho_n} = \mathscr{F}_0. \tag{3.98}$$

Hence (P_{ρ_t}) is equivalent to (P_0). Define $d = \mathrm{sign}(\rho - \rho_t)$ and $t = |\rho - \rho_t|$, such that $\rho = \rho_t + td$. Then (P_ρ) is a perturbed (P_0) problem in the feasible direction d. Because (z_0, λ_0) is a strongly regular solution of (P_0), z_ρ exists in a neighborhood of z_0, it is the unique local minimizer of (P_ρ) with an associated unique Lagrange multiplier λ_ρ, and $z_\rho \to z_0$ as $t \downarrow 0$. Furthermore, strong regularity implies that z_0 is the unique local minimizer of (P_0). Since LICQ along with SSOSC holds, then $\Lambda(z_0) = \{\lambda_0\}$ (i.e., a singleton), and SOSC and Gollan's condition are satisfied in any direction d. Then results of Theorem 3 in Appendix C apply.

Remark 1 *As will be discussed in Section 3.3.4, due to numerical reasons it may be advantageous to split the constraints into separate groups and then perform the aggregation. In such a case, for each aggregation group there is an associated value of ρ. Theorem 1 still applies with vectors t and d whose elements are defined as $t_i = |\rho_i - \rho_t|$, $d_i = sign(\rho_i - \rho_t)$ for each group i.*

3.3.2 The Kreisselmeier-Steinhauser Aggregation Function

The Kreisselmeier-Steinhauser (KS) function [101] is a smooth constraint aggregation function that has the following form[1]:

$$KS(g_i(z), \rho) = \rho \ln \left[\sum_{i=1}^{n_c} e^{\frac{1}{\rho}(g_i(z))} \right]. \tag{3.99}$$

The KS function provides a conservative approximation of convex or non-convex feasible sets, and the residual is $\mathcal{O}(\rho)$.

[1]The definition of the KS function in here differs from the usual definition in the literature $KS(g_i(z), \rho) = \frac{1}{\rho} \ln \left[\sum_{i=1}^{n_c} e^{\rho(g_i(z))} \right]$ (cf. [102]).

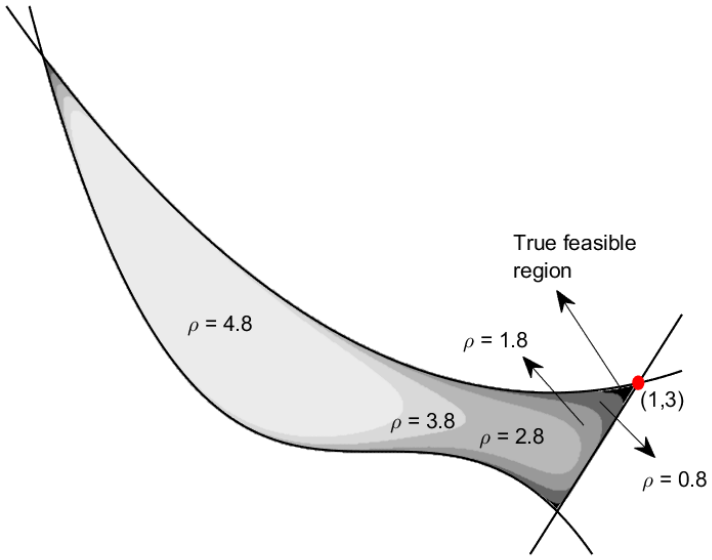

Figure 3.4: Approximation of the non-convex feasible region $\{x \in \mathbb{R}^2 | 2x_1 + 1 - x_2 \leq 0, -(x_1 + 2)^3 + 20 - 10x_2 \leq 0,\ -x_1^2 - 20 + 7x_2 \leq 0\}$ for different values of ρ.

An alternative and equivalent formulation of the KS function is given by [102]:

$$KS(g_i(z), \rho) = g_{\max}(z) + \rho \ln \left[\sum_{i=1}^{n_c} e^{\frac{1}{\rho}(g_i(z) - g_{\max}(z))} \right]. \tag{3.100}$$

Such a formulation is better numerically behaved, e.g., it avoids the overflow in the computation of exponentials.

Equation (3.100) can be written in a more compact form as:

$$KS(g_i(z), \rho) = g_{\max}(z) + \rho \ln \left[E(z)^T 1_{n_c} \right], \tag{3.101}$$

where

$$E(z) = \left[\ e^{\frac{1}{\rho}(g_1(z) - g_{\max}(z))}, \ \cdots, \ e^{\frac{1}{\rho}(g_{n_c}(z) - g_{\max}(z))} \ \right]^T, \tag{3.102}$$

and $1_{n_c} \in \mathbb{R}^{n_c}$ is a vector whose entries are ones.

The KS function is continuously differentiable, and its gradient vector and Hessian matrix with respect to z are given by, respectively:

$$\nabla_z KS(g_i(z), \rho) = \frac{J(z)E(z)}{E(z)^T 1_{n_c}}, \tag{3.103}$$

$$\nabla_z^2 KS(g_i(z),\rho) = \frac{1}{\left(E(z)^T 1_{n_c}\right)^2}\left\{\frac{1}{\rho}J(z)\left[\left(E(z)^T 1_{n_c}\right)\mathrm{diag}(E(z)) - E(z)E(z)^T\right]J^T(z) + \left(E(z)^T 1_{n_c}\right)\sum_{i=1}^{n_c} H_i(z)E_i(z)\right\}, \tag{3.104}$$

where

$$J(z) = \begin{bmatrix} \nabla_z g_1(z) & \cdots & \nabla_z g_{n_c}(z) \end{bmatrix} \in \mathbb{R}^{n_z \times n_c}, \tag{3.105}$$

$$H_i(z) = \nabla_z^2 g_i(z) \in \mathbb{R}^{n_z \times n_z}, \tag{3.106}$$

$E_i(z)$ is the ith entry of vector $E(z)$, and $\mathrm{diag}(E(z))$ is a diagonal matrix whose ith entry in the diagonal is equal to $E_i(z)$.

The following properties of the KS function hold for all z (see [103] for proofs):

1. $KS(g_i(z),\rho) \geq g_{\max}(z)$ for $\rho > 0$
2. $\lim_{\rho\to 0} KS(g_i(z),\rho) = g_{\max}(z)$
3. $KS(g_i(z),\rho_2) \geq KS(g_i(z),\rho_1)$ if $\rho_1 > \rho_2 > 0$
4. $g_{\max}(z) < KS(g_i(z),\rho) < g_{\max}(z) + \rho \ln n_c$
5. If all constraints $g_i(z)$ are convex, then $KS(g_i(z),\rho)$ is convex in z.

Note, in particular, Property 1 shows that the KS aggregation is conservative; Property 2 shows that it is tight at $\rho \to 0$; and Property 4 shows that the upper bound on the approximation depends of the number of constraints being aggregated and on the aggregation parameter. Figure 3.4 shows an example of the KS aggregation over a non-convex set of constraints for different values of ρ.

The aggregation works similarly to a barrier function. The approximation accuracy degrades close to non-smooth constraint intersections, which can be mitigated by making ρ closer to 0. However, numerical difficulties can arise for very small values of ρ. For instance, at a constraint intersection, it is easy to see from Eq. (3.104) that $||\nabla_z^2 KS(g_i(z),\rho)||_F \to \infty$ when $\rho \to 0$, where F is the Frobenius norm. Figure 3.5 shows the condition number of the Hessian of the KS function that aggregates the constraints shown in Fig. 3.4 when evaluated at a constraint intersection. High condition numbers can degrade the numerical stability of optimization solvers. To attenuate such problem, Poon and Martins [104] have developed an adaptive approach by defining a nominal aggregation parameter at the beginning of the optimization, and increasing it as needed according to the sensitivity of KS function with respect to the aggregation parameter at the current evaluation point.

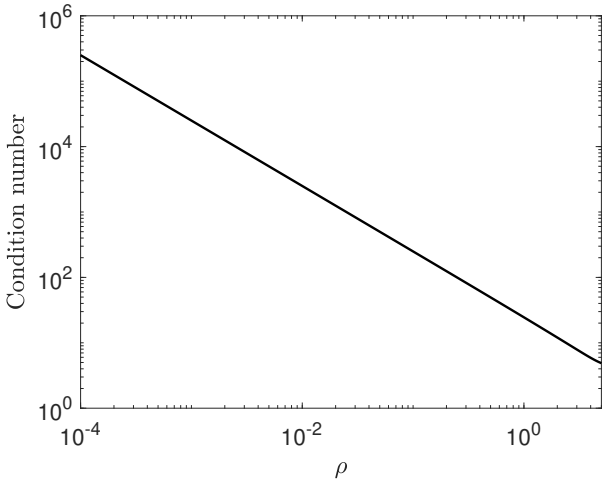

Figure 3.5: Condition number of $\nabla^2_z KS$ at constraint intersection $x = [1\ 3]^T$ as a function of ρ.

3.3.3 Nonlinear MPC with Aggregated Constraints

Consider the NMPC problem presented in Section 3.1.1 and the assumptions therein.

The next assumption guarantees that $\mathbf{u}^*$ is the unique local minimizer of $\mathrm{P}_N(x, X_f)$ and the solution map is stable.

Assumption 3 *The optimal solution $\boldsymbol{u}^*$, along with the associated Lagrange multiplier $\boldsymbol{\lambda}^*$, are a strongly regular solution of the GE associated with $P_N(x, X_f)$.*

In NMPC problems with only convex control constraints [105], or with polyhedral state and control constraints [106, 86], the optimal solution is strongly regular if SOSC holds.

The next assumption replaces Assumption 2 in Section 3.1.1.

Assumption 4 *Let $V_f(x)$ be a Control Lyapunov Function and X_f be a set such that $X_f = \{x \in \mathbb{R}^{n_x} | V_f(x) \leq \alpha\}$, with $\alpha > 0$ such that $X_f \subset X$ and for all $x \in X_f$ the following holds:*

$$\alpha_1(||x||) \leq V_f(x) \leq \alpha_2(||x||) \tag{3.107}$$

$$\inf_{u \in \mathrm{int}U} \{V_f(f_s(x,u)) - V_f(x) + l(x,u)\} \leq 0, \tag{3.108}$$

where $\alpha_1(\cdot)$ and $\alpha_2(\cdot)$ are class $\mathcal{K}$-functions.

Remark 2 *Note the restriction $u \in \mathrm{int}U$ in Eq. (3.108) makes this assumption more stringent than, for instance, the one in Assumption 2. This restriction is included in order to*

ensure that there exists an inner approximation of the set U in which the stability ingredients are satisfied.

Now consider the MPC problem with aggregated constraints. The aggregation is performed using an aggregation function for the constraints in $\mathscr{F}_N$. The specifics of how to aggregate these constraints will be discussed in Section 3.3.4. Let $\mathscr{F}_{N_\rho}$ be the feasible set obtained from the aggregated constraints and ρ the aggregation parameter. Let X_ρ and U_ρ be the corresponding conservative approximations of X and U, respectively, after performing the constraint aggregation.

Assumption 5 *The aggregation function is tight at ρ_t. Furthermore, the aggregation parameter ρ is chosen such that the aggregation is conservative, $0 \in X_\rho$, $0 \in U_\rho$, $X_f \subseteq X_\rho$, and Eq. (3.108) is satisfied when U is replaced by U_ρ.*

The associated MPC problem is formulated as follows:

$$\begin{aligned} \mathrm{P}_{N_\rho}(x, X_f): \quad V^*_{N_\rho}(x) = \min_{\mathbf{u}} \{V_N(x,\mathbf{u}) | \\ (\mathbf{x},\mathbf{u}) \in \mathscr{F}_{N_\rho},\ x_N \in X_f \Big\}. \end{aligned} \tag{3.109}$$

Note that the cost function and terminal set in $\mathrm{P}_{N_\rho}(x, X_f)$ are the same as in $\mathrm{P}_N(x, X_f)$. The next theorem uses the results of Theorem 1 to give a quantitative factor of shrinkage of the domain of attraction of the MPC controller with aggregated constraints without terminal set, and bounds on the deviation between the system states generated by $\mathrm{P}_N(x, X)$ and $\mathrm{P}_{N_\rho}(x, X_\rho)$.

Theorem 2 *Consider the MPC problem $P_N(x, X)$, for $N \geq 1$, with the domain of attraction Υ_N, and the associated control law $\kappa_N(x)$. Consider also the MPC problem $P_{N_\rho}(x, X_\rho)$ created by aggregating the constraints of $P_N(x, X)$. Let κ_{N_ρ} be the associated control law and suppose Assumptions 1,3-5 hold. Then:*
a) There exists $M > 0$ and $\varepsilon > 0$ such that, for all states $x \in X_\rho$,

$$||f_s(x, \kappa_{N_\rho}(x)) - f_s(x, \kappa_N(x))|| \leq Mt, \tag{3.110}$$

when $0 \leq t < \varepsilon$;
b) There is a closed-loop domain of attraction with κ_{N_ρ} which can be expressed as

$$\Upsilon_{N_\rho} = \left\{ x \in \mathbb{R}^{n_x} | V^*_N(x) \leq N \cdot \beta + \alpha - t p_{PL_d} - \frac{1}{2} t^2 p_{PQ} - o(t^2) \right\} \subseteq \Upsilon_N, \tag{3.111}$$

where $t = |\rho - \rho_t|$, $d = sign(\rho - \rho_t)$, and p_{PL_d} and p_{PQ} as defined in Eq. (C.7) and (C.15), respectively.

Proof: Assumptions 1, 3 and 4 are sufficient to satisfy the conditions of Theorem 1, thus the results therein apply. a) The continuous differentiability property of $f_s(x,u)$ implies Lipchitz continuity, therefore there exists $C>0$ such that, for all states $x \in X_\rho$,

$$\begin{aligned} ||f_s(x,\kappa_{N_\rho}(x)) - f_s(x,\kappa_N(x))|| &\leq C||\kappa_{N_\rho}(x) - \kappa_N(x)|| \\ &= \mathcal{O}(t), \end{aligned}$$

where the last equality is due to Lipschitz stability of the solution of the optimization problem. Using the usual definition of $\mathcal{O}(\cdot)$, and the fact that the aggregation is tight for $t=0$, (a) follows.

b) Assumptions 3 and 4 are sufficient for the assumptions in Proposition 1 to hold, thus the MPC controller derived from $P_{N_\rho}(x, X_\rho)$ stabilizes asymptotically the system (3.1) subject to X_ρ and U_ρ for any initial state x that satisfies

$$V^*_{N_\rho}(x) \leq N \cdot \beta + \alpha \tag{3.112}$$

Based on Theorem 1, (3.112) can be restated as

$$V^*_N(x) + tp_{\mathrm{PL}_d} + \frac{1}{2}t^2 p_{\mathrm{PQ}} + o(t^2) \leq N \cdot \beta + \alpha \tag{3.113}$$

and as

$$V^*_N(x) \leq N \cdot \beta + \alpha - tp_{\mathrm{PL}_d} - \frac{1}{2}t^2 p_{\mathrm{PQ}} - o(t^2), \tag{3.114}$$

where $t = |\rho - \rho_t|$. Since the aggregation is conservative, $\mathscr{F}_{N_\rho} \subseteq \mathscr{F}_N$, therefore $V^*_{N_\rho}(x) \geq V^*_N(x)$, and hence

$$tp_{\mathrm{PL}_d} + \frac{1}{2}t^2 p_{\mathrm{PQ}} + o(t^2) \geq 0 \tag{3.115}$$

for all $t \geq 0$. Hence, the set

$$\Upsilon_{N_\rho} = \left\{ x \in \mathbb{R}^{n_x} | V^*_N(x) \leq N \cdot \beta + \alpha - tp_{\mathrm{PL}_d} - \frac{1}{2}t^2 p_{\mathrm{PQ}} - o(t^2) \right\} \tag{3.116}$$

is contained in Υ_N.

Remark 3 *Since $tp_{PL_d} + \frac{1}{2}t^2 p_{PQ} + o(t^2)$ is finite (Theorem 3), the prediction horizon N can be increased to a value $\bar{N}$ such that $\Upsilon_{\bar{N}_\rho} = \Upsilon_N$ in order to recover the original domain of attraction before constraint aggregation. As will be discussed in the next sections, the constraint aggregation method reduces significantly the computational cost of increasing N, in comparison to the original problem. Alternatively, one can also enlarge the domain of attraction without terminal set by weighting the terminal cost, as suggested in [85].*

Corollary 1 *There exists a finite* $\bar{N} \in \mathbb{Z}_{++}$ *such that*

$$\Upsilon_{N_\rho} \subseteq \Upsilon_N \subseteq \Upsilon_{\bar{N}_\rho}. \tag{3.117}$$

The smallest $\bar{N}$ *for which this is true is approximately given by:*

$$\bar{N} \approx N + \left\lceil \frac{t p_{PL_d} + \frac{1}{2} t^2 p_{PQ}}{\beta} \right\rceil + 1. \tag{3.118}$$

3.3.4 Procedure to Aggregate Constraints

The NMPC problem in Eq. (3.7) with constraints (3.2) and (3.3) has a total of Nn_c constraints. Different strategies for aggregation exist depending on the problem. When exploiting the KS function for aggregation, the following guidelines can be used:

1. Avoid very small values for the parameter ρ. Due to the numerical issues discussed in Section 3.3.2, the aggregation parameter should not be too small, especially when using solvers that use information about the Hessian of the KS function. Studies in the literature (e.g., [104]) recommend starting with $\rho = 1/50$ and then adjust the parameter if necessary.

2. Divide the constraints into several groups. KS function's Property 4 in Section 3.3.2 shows that the upper bound of the aggregation residual depends on the number of constraints. Therefore, for a problem with a large number of constraints, it is recommended to divide the constraints into groups that are aggregated separately in order to decrease the aggregation error.

3. Take into consideration the magnitude of constraints (see [107, 108]). In particular, from Property 4 in Section 3.3.2, a measure of the aggregation conservativeness is given by comparing the magnitudes of $g_{\max}(z)$ and $\rho \ln(n_c)$. If the order of magnitude of the latter is similar or greater than of the former, then the resulting feasible set is too conservative or even empty. Knowing the magnitude of the constraints is helpful when defining the aggregation groups and selecting the parameter ρ. It is recommended to aggregate constraints that have similar magnitude, which can be done by grouping together constraints on variables that have the same nature, or by scaling the variables so that they have similar magnitude.

As suggested in [108], the aggregation can be performed in time. For example, consider the set of state constraints in Eq. (3.4) to be enforced over the prediction horizon. The

aggregation can be performed as follows:

$$\begin{aligned} g_1(x_k) \text{ for } k \in \mathbb{Z}_{[1,N]} &\longrightarrow KS_1(g_1(x_k), \rho_1) \\ g_2(x_k) \text{ for } k \in \mathbb{Z}_{[1,N]} &\longrightarrow KS_2(g_2(x_k), \rho_2) \\ \vdots &\quad\vdots \\ g_{n_{c_x}}(x_k) \text{ for } k \in \mathbb{Z}_{[1,N]} &\longrightarrow KS_{n_{c_x}}(g_{n_{c_x}}(x_k), \rho_{n_{c_x}}). \end{aligned} \tag{3.119}$$

This way, the number of constraints in the NMPC problem is reduced by a factor of N. Further reduction, at the cost of increased conservativeness, can be achieved by aggregating some of the KS functions in (3.119). The nested aggregation has the following form:

$$\begin{aligned} KS_j(g_j(x_k), \rho_j) \text{ for } j \in \mathcal{J} \subseteq \mathbb{Z}_{[1,n_{c_x}]} \longrightarrow \\ KS(KS_j(g_j(x_k), \rho_j), \rho). \end{aligned} \tag{3.120}$$

The final number of constraints in the NMPC with aggregated constraints (NMPC-AC) problem is denoted by n_{KS}, such that $n_{KS} << n_c$.

3.3.5 Implementation

Similarly to the NMPC in Eq. (3.15), the real-time implementation of the NMPC-AC requires solving a nonlinear optimization problem. Second-order methods, which rely on Newton's method in some form, are the usual numerical optimization approaches in MPC due to the fast convergence rate. In these methods, the bottleneck is solving a system of linear equations of size n, which depends on the number of decision variables and constraints and that can have arithmetic complexity of up to $\mathcal{O}(n^3)$ per iteration. Therefore, the computational footprint of the NMPC-AC implementation is expected to be smaller than of the original NMPC problem.

In this work, SQP is considered. In this iterative method, a sequence of QP subproblems is solved, in which the solution to the previous QP problem informs the next QP problem. Let $z \triangleq [\mathbf{u}^T \ \mathbf{x}^T]^T \in \mathbb{R}^{N(n_x+n_u)}$ be the vector of decision variables, $f(z) = V_{N_\rho}(x, \mathbf{x}, \mathbf{u})$ be the objective function, $h(z) : \mathbb{R}^{N(n_x+n_u)} \to \mathbb{R}^{Nn_x}$ be the equality constraint function, and $q(z) : \mathbb{R}^{N(n_x+n_u)} \to \mathbb{R}^{n_{KS}}$ be the inequality constraint function after aggregation. Assuming an iterate z_k has been computed, the following QP problem is solved to find Δz_k that

minimizes the quadratic cost subject to linear constraints:

$$\begin{aligned} \min_{\Delta z_k} \quad & \frac{1}{2}\Delta z_k^T H_k \Delta z_k + \nabla f(z_{k-1})^T \Delta z_k \\ \text{s.t.} \quad & \nabla h(z_{k-1})^T \Delta z_k + h(z_{k-1}) = 0 \\ & \nabla q(z_{k-1})^T \Delta z_k + q(z_{k-1}) \preceq 0 \end{aligned} \tag{3.121}$$

where H_k approximates the Hessian of the Lagrangian function of the optimization problem. SQP requires multiple iterations for convergence, however, these QP subproblems are computationally cheap due to the reduced number of constraints if aggregation is used. For instance, the complexity of a QP solver to reach a defined accuracy depends linearly on the number of constraints when a primal interior point method is used [109]. For active-set methods, the complexity is also reduced since fewer working set re-computations are required [110].

In practice, the SQP algorithm converges quickly, especially with warm-starting in MPC, and sub-optimal solutions that provide good performance can be obtained by limiting the number of iterations [86, 111]. Other strategies can be implemented to speed up the computations, especially when updating the Hessian and Jacobians in Eq. (3.121). Firstly, one can take advantage of the analytical expressions for the gradient vector (Eq. 3.103) and Hessian matrix (Eq. 3.104) of the KS function. This avoids the need for online numerical differentiation. The modified Newton-Kantorovich [112, 113] method can be considered to avoid the evaluation of the Hessian at each iteration. In this method, the Hessian at the first iteration is kept for the following steps. Alternatively, approximations for the Hessian matrix can be used such as the Gauss-Newton approximation [114]. For quadratic cost functions, this is equivalent to choosing $H_k = \nabla^2 f(z_{k-1})$. Another option is the Broyden–Fletcher–Goldfarb–Shanno (BFGS) iterative update. In these two approximations, the second order derivatives of the constraint functions do not have to be computed. This is interesting especially when the KS function is used for aggregation, since numerical problems due to the ill-conditioned Hessian matrices, as discussed in Section 3.3.2, would be avoided. Note, however, that these Hessian approximations reduce the update phase computations at the cost of reduced convergence rate.

3.3.6 Examples

Linear MPC: The design of a FCS for X-HALE is shown next [108]. The objective is to perform a pitch-up maneuver by tracking a flight path angle γ while maintaining the out-of-plane curvature κ_x at the wing root within safety limits. UM/NAST was used to create a

linearized model with respect to a straight level flight trim condition. The linear model has 60 states. Box constraints were imposed on 16 outputs and inputs, namely, the curvature at each semi-wing root, angle of attack, ailerons and elevators deflection and rate of deflection, and propellers rotation and rate of change.

A rate-based MPC controller was designed with sampling rate of 50 Hz and prediction horizon of 100 steps. The full OCP had 700 decision variables and 3300 constraints. Simple aggregation in time was performed for each constrained variable, and the nested aggregation was performed for the constraints on aileron and elevator input channels. The total number of constraints was reduced to 13. QPKWIK (with warm-starting) and IBM ILOG CPLEX v12.9 were used to solve the QPs in order to compare the performance of, respectively, an active-set method versus an interior-point method. The maximum number of iterations of the SQP algorithm was limited to 3.

Figure 3.6 shows the simulation results. In both MPC formulations, the target was reached with similar response, and the wing curvature constraint was satisfied. However, when the KS aggregation was used, the constraints were enforced more conservatively. Table 3.1 presents the maximum and average computation time observed during the simulation. For the simulation with QPKWIK, reductions of 92% and 21% in the maximum and average computation time, respectively, were obtained when the KS aggregation was used. For CPLEX, the reduction was 83% for the maximum time, and 87% for the average time. While the computation time even with KS aggregation exceeds the time step, it should be noted that the implementation of the optimization is in MATLAB and (except for aggregation) has not been optimized for computational performance. Nevertheless, these results show the potential of KS aggregation in linear MPC. While the approach appears to be somewhat counter-intuitive at a first glance as the QP problem is replaced by a nonlinear optimization problem, significant reductions in the computational cost can be achieved.

Table 3.1: Maximum and average computation time per time step [s]

	Linear constraints		KS aggregation	
	Max.	Avg.	Max.	Avg.
QPKWIK	1.7542	0.1313	0.1399	0.1041
CPLEX	4.5069	1.7265	0.8285	0.2289

Nonlinear MPC: A numerical example of NMPC-AC applied to the control of the GTA aircraft is presented next, for which a low-order nonlinear model was created using the B2T modeling framework.

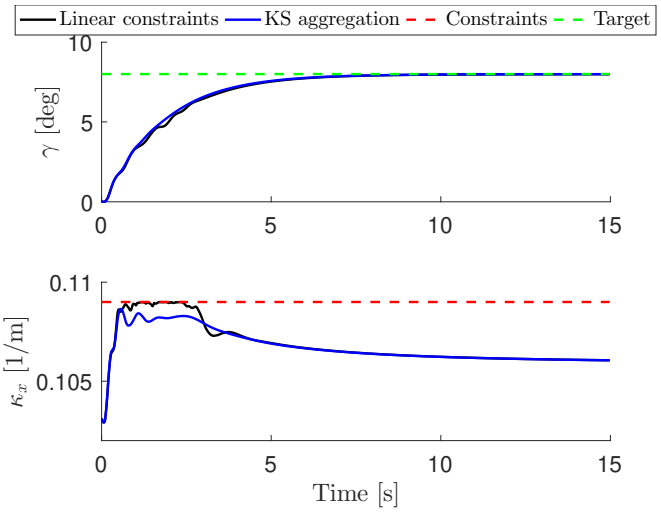

Figure 3.6: The time histories of the flight path angle and wing root curvature in the closed-loop simulations of the very flexible aircraft.

The discretization of the aircraft dynamics in time was performed using a fourth-order Runge-Kutta method. The model contains 20 states corresponding to rigid-body and 4 structural modes. The control inputs are the 4 control effectors for speed, longitudinal and lateral control. The control objective is to perform a descent while enforcing constraints on the upper and lower bounds of the angular rates, orientation angles, altitude, and amplitude of the dominant flexible mode. Box constraints were also imposed on the control inputs magnitude and rate of change.

The NMPC problem was formulated for various prediction horizons, ranging from 30 to 80 steps. The full optimization problem has $5N$ decision variables and $31N$ linear inequality constraints, where N is the prediction horizon. Constraint aggregation using the KS function was performed at each constrained channel, lumping together the upper and lower bounds in time. The resulting NMPC-AC has $5N$ decision variables which translates into 16 constraints in the optimization problem. The equality constraints due to the aircraft equations of motion were eliminated through online condensing.

The control problem was set up in MATLAB using the CasADi toolbox [115]. The optimization problem was solved using the SQP algorithm, with Hessian approximations computed via the BFGS method. The maximum number of iterations of the SQP method was limited to six. The QP subproblems were solved using three different solvers: a dual active set (AS) method [116], a primal-dual interior point (IP) method [117], and the proximally stabilized Fischer–Burmeister (FBstab) method [89]. The AS and FBstab solvers were warmstarted using information from previous iterations of the SQP algorithm. All computations were performed on an Intel i7-8650U, 1.9 GHz, 16 GB RAM laptop.

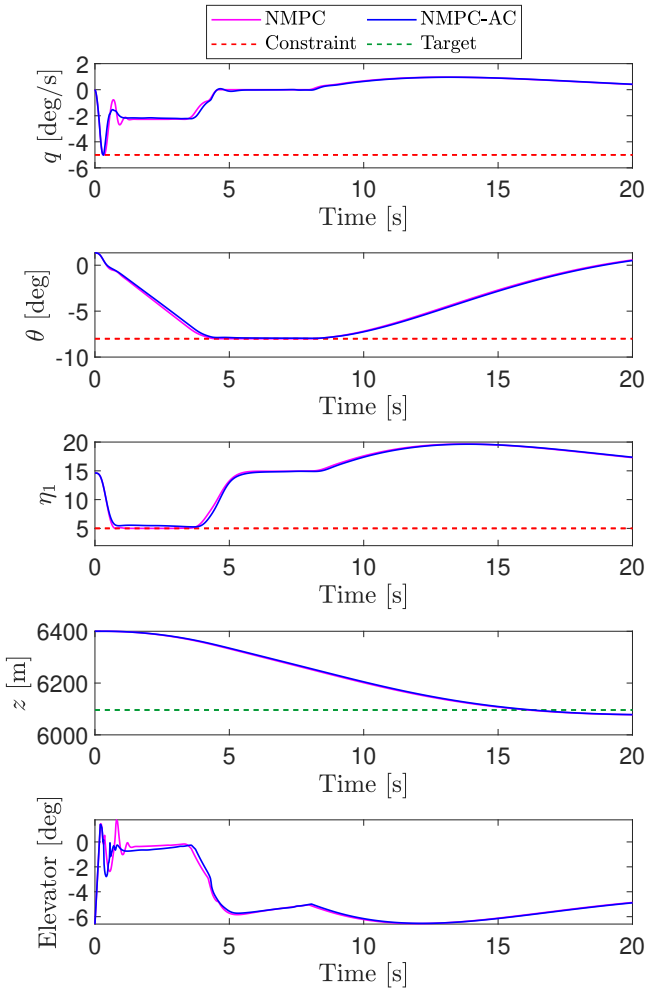

Figure 3.7: Closed-loop results of aircraft descent with NMPC and NMPC-AC controllers.

Figure 3.7 shows closed-loop results of the first 20 s of the aircraft descent with the NMPC and NMPC-AC controllers. In both scenarios, the aircraft is able to reach the target altitude (z) with very similar trajectories. During the descent, the pitch rate (q), pitch angle (θ) and first out-of-plane bending mode (η_1) were constrained, among other variables. In both cases, the constraints were satisfied. The conservative constraint enforcement imposed by the constraint aggregation resulted in a different elevator control input computed by each controller when the constraints were active. Figure 3.8 shows a magnification on the time interval that the bending mode constraint becomes active, and how the NMPC-AC response varies for different values of the aggregation parameter ρ. As ρ is decreased, the η_1 response gets closer to the baseline obtained when applying the conventional NMPC. However, for very small values of ρ, numerical issues lead to an undesirable controller response, such as the oscillations seen for $\rho = 0.25$. Even smaller values of ρ would ultimately cause the

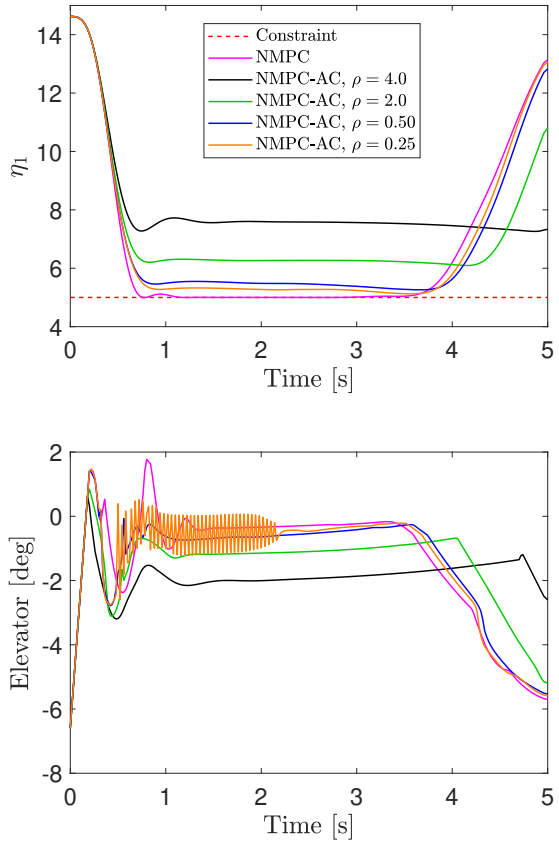

Figure 3.8: Constraint enforcement in NMPC-AC for different values of aggregation parameter ρ.

optimization solver to fail.

Nonetheless, when choosing the appropriate value of ρ, good results are achieved with a significant smaller computational cost. Figure 3.9 shows the reduction in the maximum and mean computation time of an MPC step in the NMPC-AC formulation when compared against NMPC. The reduction is observed for the three different QP solvers tested, and for different control horizons. By increasing N, the number of constraints in the conventional NMPC formulation also increases, while for the NMPC-AC formulation it stays the same. For large-scale problems, e.g., $N = 80$ with 2480 constraints, the reduction in the maximum time can reach as high as 70%. In practice, the worst-case execution time drives the selection of the processor hardware. These results indicate that the proposed method can potentially facilitate the real-time implementation of NMPC controllers for large-scale systems using microcontrollers with limited computing capabilities.

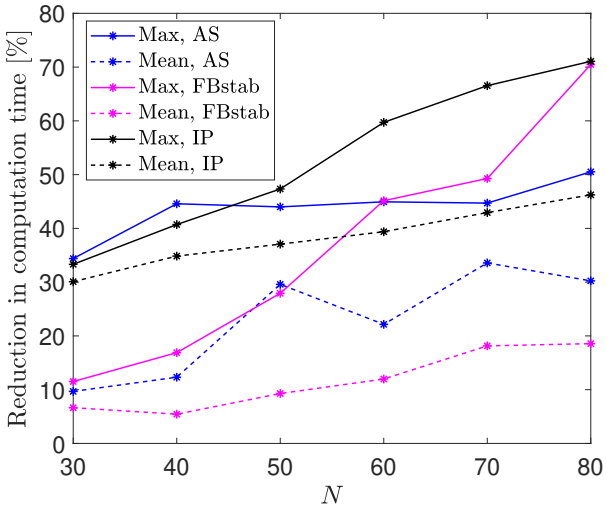

Figure 3.9: Reduction on the mean and maximum computation time of an MPC step when aggregating constraints.

3.4 Scenario-based MPC

The MPC design presented in Section 3.1 considered that the models used for prediction are accurate. However, in practical applications, the vehicle is subject to unforeseen exogenous disturbances, unmodeled nonlinear behavior, and unknown parameters, among other factors that introduce uncertainty into the system. As a result, the controller performance may degrade and the load constraints constraints may not be enforced. To cope with these shortcomings, the load alleviation system has to be robust to noise factors and uncertainties.

Model predictive controllers are inherently robust. As discussed in [118], under some conditions, the predictive controller obtained from the solution of a nominal MPC problem confers robustness to the closed-loop system to sufficiently small bounds of uncertainties. However, to guarantee stability and constraint satisfaction in a wider range of unmeasured disturbances, the knowledge about uncertainty can be systematically taken into consideration in the design of MPC controllers. Designs following such an approach are referred to as robust MPC designs.

Typical approaches for robust MPC include tube-based and scenario-based MPC. The former consists of a form of feedback MPC in which a policy, i.e., a sequence of control laws, is obtained online as a solution to the optimal control problem. The controller uses a tube whose central-path is obtained from the nominal uncertainty-free MPC solution. The tube, which is used to attenuate the effect of uncertainties, is obtained by adding to its center a pre-computed invariant set [119, 120, 121]. Tube-based MPC designs often assume that the

disturbance or uncertainty lies inside a compact convex set that contains the origin.

MPC via scenario optimization (MPCS), on the other hand, assumes only boundedness of the uncertainty set [122]. In this approach, the information on the statistics of the uncertain parameters and disturbances is exploited to create a randomized algorithm that ensures constraint enforcement with a probability higher than a user-defined value [123]. The algorithm relies on solving the optimal control problem for a finite number of randomly chosen instances (i.e., scenarios) of the uncertainty, rather than for all possible outcomes. Appendix D presents a review on MPCS.

In the context of load alleviation system design for FA and VFA, a single MPC controller that is capable of robustly enforcing constraints on different configurations of an airliner is desirable. As mentioned in Section 2.4, the XRF1 model can have different mass configurations which affects its aeroservoelastic response. Chapter 4 will discuss the controller design in this situation.

The approach presented in the next section builds upon the general idea of scenario-based optimization to handle the unknown mass-related parameters. Since only a few scenarios for the mass cases are known, and the convexity of the model with respect to the uncertain parameters are not guaranteed due to its nonlinearity, the flexibility of MPCS regarding the uncertainty set seems advantageous.

3.4.1 Time-distributed scenario-based MPC for MLA

Let $\delta \in \Delta$ represent the uncertain parameters in the aircraft dynamics, such as the unknown mass properties, and Δ the bounded set of all possible scenarios. The discrete-time linearized uncertain aircraft dynamics around a trim condition is represented by

$$\Delta x_{k+1} = A^d(\delta)\Delta x_k + B^d(\delta)\Delta u_k, \tag{3.122}$$

$$\Delta y_k = C^d(\delta)\Delta x_k + D^d(\delta)\Delta u_k. \tag{3.123}$$

The objective is to design a linear MPC controller, similar to the one discussed in Section 3.1.2, that stabilizes the system and enforces constraints for all $\delta \in \Delta$. The constraint sets are still the ones defined in Eqs. 3.5 and 3.14, but now they depend of δ, i.e., $X(\varepsilon_{k,s}, \delta)$ and $U(\delta)$. It is assumed that Assumption 1-4 in Appendix D hold. In particular, that there exists terminal gain K_f that renders the origin of the system in Eq. 3.122 stable for all $\delta \in \Delta$. The

OCP with quadratic cost is formulated as follows:

$$\min_{\boldsymbol{\nu},\Delta\mathbf{x},\boldsymbol{\varepsilon}_s} \max_{\delta\in\Delta} \quad \left\{ V_N(x_k,\nu_k,\delta) = \sum_{k=0}^{N-1} ||\Delta x_k||_Q^2 + ||\Delta u_k||_R^2 + \mu\varepsilon_{s,k} \right\} \tag{3.124}$$

$$\text{s.t.} \quad \Delta x_{k+1} = A^d(\delta)\Delta x_k + B^d(\delta)\Delta u_k k \ \text{ for } k \in \mathbb{Z}_{[0,N-1]}.\forall\delta\in\Delta \tag{3.125}$$

$$x_0 = x \tag{3.126}$$

$$u_k = K_f x_k + \nu_k \ \text{ for } k \in \mathbb{Z}_{[0,N-1]} \tag{3.127}$$

$$g_c(x_{k+1},u_k,\delta) - 1_{n_c}\varepsilon_{s,k+1} \preceq 0 \ \text{ for } k \in \mathbb{Z}_{[0,N-1]}, \forall\delta\in\Delta \tag{3.128}$$

$$\varepsilon_{s,k} \geq 0 \ \text{ for } k \in \mathbb{Z}_{[1,N]}, \tag{3.129}$$

where $g_c : \mathbb{R}^{n_x} \times \mathbb{R}^{n_u} \times \Delta \to \mathbb{R}^{n_u}$ is a C^2 convex function representing the state, input and output constraints, $\nu_k \in \mathbb{R}^{n_u}$ is an incremental control action calculated by the MPC controller, and $\boldsymbol{\nu} \in \mathbb{R}^{Nn_u}$ is the vector that concatenates the values of ν_k in the prediction horizon.

Theorem 1 in Appendix D defines the minimum number of samples to reach a desired reliability level in the design of an MPCS controller for the OCP defined in Eqs. 3.124-3.129. An explicit bound on the value of M in Eq. D.11 is given by [122]:

$$M \geq \frac{2}{(1-p)}\left(\log(\beta^{-1}) + d - 1\right). \tag{3.130}$$

For large-scale problems, such as the control of flexible aircraft, the required amount of samples may be substantial. For instance, the MPC controller designed in [107] had 400 decision variables. For $p = 0.99$ and $\beta = 10^{-9}$, Eq. 3.130 returns $M \geq 8.4 \times 10^4$. The resulting OCP would be impractical for real-time implementation due to the large number of constraints.

Furthermore, for the load alleviation application considered here, generating samples, i.e., aircraft models, on the fly for different mass cases can be an arduous task in face of the size and complexity of the finite element models. Therefore, for this application, usually only a finite number of pre-computed samples are available.

In view of these challenges, the traditional MPCS is modified to handle the different mass cases in the load alleviation system design. In the present problem reformulation, the assumptions 1-4 in Appendix D still hold. Let $\Delta_{\bar{M}} \subset \Delta$ be a subset of the original uncertainty set such that $|\Delta_{\bar{M}}| = \bar{M} << M$, where $\bar{M} \in \mathbb{N}_{++}$, and M is obtained from Eq. 3.130 for some high reliability level p and some low probability level β. The $\bar{M}$ samples in $\Delta_{\bar{M}}$ may be, for example, the most likely conditions to happen among all possible elements in Δ. For the load alleviation system considered here, these $\bar{M}$ samples will be the different

mass cases.

Define $\Theta_{\bar{M}}$ as the set of linear systems associated with each sample in $\Delta_{\bar{M}}$, i.e.,

$$\Theta_{\bar{M}} = \{(A(\delta), B(\delta), C(\delta), D(\delta)) : \delta \in \Delta_{\bar{M}}\}. \tag{3.131}$$

An element in $\Theta_{\bar{M}}$ associated with sample $\delta^{(i)}$ is denoted by $\Theta_{\bar{M}}^{(i)}$ and forms the linear system in 3.122-3.123. For the application considered here, $\Theta_{\bar{M}}^{(i)}$ is the linearized aircraft dynamics with respect to the same trim condition for all $i \in \mathbb{N}_{[1;\bar{M}]}$.

The OCP in 3.124-3.129 is then reformulated with the $\bar{M}$ samples in $\Delta_{\bar{M}}$. Note that resulting OCP does not satisfy Theorem 1, and therefore its solution is not necessarily feasible for OCP 3.124-3.129. On the other hand, the solution will be feasible for all relevant realizations of δ selected based on engineering judgment.

Even though the proposed approach reduces significantly the number of constraints in the OCP in comparison to the traditional approach forMPCS, the simultaneous enforcement of constraints for all models in $\Delta_{\bar{M}}$ can still be a hard task, especially for flexible aircraft for which the control computation time is restricted to only a few milliseconds (e.g., 10-30 ms [43]). The constraint aggregation methods discussed in Section 3.3.3 can be employed to reduce the computational burden, but if $\bar{M}$ is large, the solution may be too conservative or numerical issues may arise due to the number of nonlinear constraints. To circumvent such a problem, the set of constraints can be broken into smaller groups that are enforced separately at each MPC computation time. This is equivalent to distributing constraints over time. In this way, the size of the working set of constraints can be capped based on the computational restrictions. Constraint aggregation can then be applied to each group separately to reduce even more the computation time.

Let N_m be the number of models extracted from $\Theta_{\bar{M}}$ to form a group of constraints, and let R_d be the number of groups. Define the following sets:

$$\mathcal{J}_j = \left\{ i \in \mathbb{N}_{++} : \Theta_{\bar{M}}^{(i)} \text{ is in group } j \right\} \quad \text{where} \quad |\mathcal{J}_j| = N_m, \tag{3.132}$$

$$\begin{aligned} \mathfrak{X}_{\text{all}} \triangleq \{ s : g_c(x_{k+1}, u_k, \delta) - 1_{n_c}\varepsilon_{s,k+1} \preceq 0, V_N(x_k, \nu_k, \delta) - \alpha \leq 0, -\varepsilon_{s,k+1} \leq 0, \\ \forall k \in \mathbb{N}_{[0;N-1]}, \forall \delta \in \Delta_{\bar{M}} \Big\}, \end{aligned} \tag{3.133}$$

$$\begin{aligned} \mathfrak{X}_j \triangleq \Big\{ s : g_c(x_{k+1}, u_k, \delta^{(i)}) - 1_{n_c}\varepsilon_{s,k+1} \preceq 0, V_N(x_k, \nu_k, \delta^{(i)}) - \alpha \leq 0, -\varepsilon_{s,k+1} \leq 0, \\ \forall k \in \mathbb{N}_{[0;N-1]}, \forall i \in \mathcal{J}_j \Big\}, \end{aligned} \tag{3.134}$$

$$\bar{\mathfrak{X}}_j \triangleq \left\{ s : \max \left\{ \max_{k\in\mathbb{N}_{[0;N-1]}, i\in\mathcal{J}_j} \left\{ g_c(x_{k+1}, u_k, \delta^{(i)}) - 1_{n_c}, V_N(x_k, \nu_k, \delta^{(i)}) - \alpha, \right. \right. \right. \\ \left. \left. \left. -\varepsilon_{s,k+1} \right\} \right\} \preceq 0 \right\}. \tag{3.135}$$

where $\alpha \in \mathbb{R}$. Note that $\mathfrak{X}_j = \bar{\mathfrak{X}}_j$, however, the latter can be described with fewer constraints. In fact, $\bar{\mathfrak{X}}_j$ is described by either the constraint that has the maximum value for some feasible point, or by the set of active constraints. One could think of $\bar{\mathfrak{X}}_j$ the set obtained after applying constraint aggregation to set $\mathfrak{X}_j$ using the maximum-value function. In the next developments, the set $\bar{\mathfrak{X}}_j$ will be constructed using information of the future trajectory and control sequence computed by previous MPC solutions. In this way, constraints associated with a model $\Theta_{\bar{M}}^{(i)}$ that was used in a previous iteration, but is not contained in the group of models considered at the current iteration, can be taken into account by replacing them with the predicted maximum constraint or set of active constraints. In doing so, constraint violations for model $\Theta_{\bar{M}}^{(i)}$ should be avoided. Since the set of maximum or active constraints changes as new outputs are received and new predicted trajectories are generated, the set $\bar{\mathfrak{X}}_j$ will be kept for only R_d iterations, referred to as the constraint window, and then replaced by newer sets. The resulting OCP is written in epigraph form as follows:

$$\begin{aligned} \min_{s} \quad & \alpha + \mu 1_N^T \boldsymbol{\varepsilon}_s \\ \text{s.t.} \quad & s \in \mathcal{F} \end{aligned} \tag{3.136}$$

$$\text{where} \quad \begin{cases} \mathcal{F} = \mathfrak{X}_{\text{all}}, & \text{if } 0 \le t < R_d - 1 \\ \mathcal{F} = \mathfrak{X}_t \cap \left(\cap_{j=t-R_d+1}^{t-1} \bar{\mathfrak{X}}_j \right), & \text{if } t \ge R_d - 1 \end{cases} \tag{3.137}$$

where $t \in \mathbb{N}$ is the current discrete time. Figure 3.10 shows a schematic of the proposed method. Denote the predicted state value at time k based on information at time t by $x(k|t)$, and the true state by $x(t)$.Let $s^* = \left[\begin{array}{c} v_0^{T*}, \ldots, v_{N-1}^{T*}, \alpha^*, \boldsymbol{\varepsilon}_s^{T*} \end{array} \right]^T$ be the optimal solution to OCP 3.136 at time t^*. The first element of the control sequence, v_0^* is then applied to the system, which evolves to state $x(t^*+1)$. Since the following is true

$$\begin{aligned} x(t^*+1) &= x^*(t^*+1|t^*) && (3.138) \\ &= (A(\delta^{(i)}) + K_f)x(t^*|t^*) + B(\delta^{(i)})v_0^* && (3.139) \end{aligned}$$

then

$$\begin{aligned} & v_0^* \in \mathfrak{X}_{t^*} \cap \left(\cap_{j=t^*-R_d+1}^{t^*-1} \bar{\mathfrak{X}}_j \right) = \cap_{j=t^*-R_d+1}^{t^*} \mathfrak{X}_j && (3.140) \\ \implies & x^*(t^*+1|t^*) \in \cap_{j=t^*-R_d+1}^{t^*} \left(\cap_{i\in\mathcal{J}_j} X(\varepsilon_{k,s}, \delta^{(i)}) \right) && (3.141) \\ \implies & x(t^*+1) \in \cap_{j=t^*-R_d+1}^{t^*} \left(\cap_{i\in\mathcal{J}_j} X(\varepsilon_{k,s}, \delta^{(i)}) \right). && (3.142) \end{aligned}$$

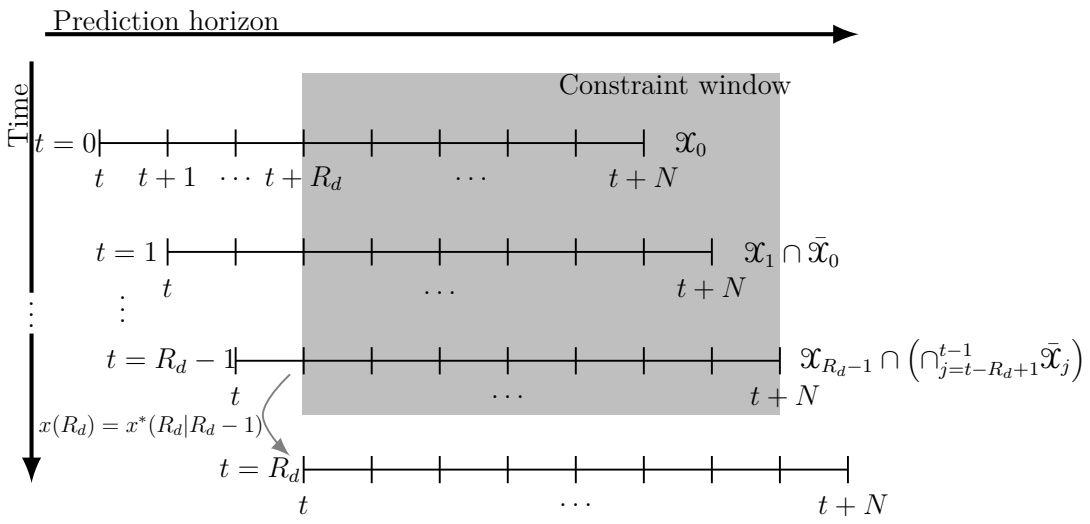

Figure 3.10: Time-distributed constraints.

Therefore, $x(t^*+1)$ satisfies constraints for all $\delta \in \Delta_{\bar{M}}$ as long as the constraints associated with model $\Theta_{\bar{M}}^{(i)}$ were in one of the groups within the constraint window, for all $i \in \mathbb{N}_{[1,\bar{M}]}$. This is easily enforced by the appropriate construction of the groups. The groups can be formed such that all models in $\Theta_{\bar{M}}$ appear in the constraint window in the same frequency. However, one can exploit the underlying probability distribution of the elements in set $\Delta_{\bar{M}}$ to pick the N_m models $\Theta_{\bar{M}}^{(i)}$ whose constraints will form a certain group. In this way, constraints associated with the cases that are more likely to happen will be enforced more often than constraints for the other cases.

3.4.2 Implementation

A procedure to implement the modified MPCS with time-distributed constraints is given in Algorithm 1. If the constraints $g_c(x, \nu, \delta)$ are linear, then the OCP in 3.136 is a quadratically constrained quadratic program (QCQP). Note that if the stage cost does not depend on δ, i.e., $V_N(x_k, \nu_k, \delta) = V_N(x_k, \nu_k)$, then the OCP is a QP. This will be the case, for example, for the LA governor architecture presented in Section 3.2.2. An example of the application of this approach with the LA governor will be presented in Chapter 4 for designing a MLA system for XRF1 with different mass configurations.

Algorithm 1 MPCS with time-distributed constraints

Inputs: x_0,T_f,N,R_d,N_m,Q,R,$\Theta_{\bar{M}}$, K_f constraints
Outputs: u_k,x_k

procedure MPCS-TDC
  while $t < T_f$ **do**
    if $t < R_d - 1$ **then**
      $\mathfrak{F} \longleftarrow \mathfrak{X}_{\text{all}}$
    else
      Pick N_m models from $\Theta_{\bar{M}}$
      Form set of constraints $\mathfrak{X}_t$
      $\mathfrak{F} \longleftarrow \mathfrak{X}_t$
      for $j = t - R_d + 1, t - R - d, \ldots, t - 1$ **do**
        $\mathfrak{F} \longleftarrow \mathfrak{F} \cap \bar{\mathfrak{X}}_j$
      end for
    end if
    Solve OCP 3.136 with constraints $\mathfrak{F}$ to obtain s^*
    Identify maximum or active constraints at s^*
    Form set $\bar{\mathfrak{X}}_t$
    $u_k = K_f x_k + v_0^*$
    Apply u_k to plant to obtain x_{k+1}
    $t \longleftarrow t + 1$
  end while
end procedure

3.5 State Estimation

The feedback control laws that presented in Section 3.2 depend on the state vector x at a certain discrete-time k. Such an information, however, is not available in practice because not all states are measured by the sensors, besides the fact that the dynamics and sensor measurements are corrupted by noise. A Kalman filter is then designed for real-time state estimation.

In this work, an observer is designed to estimate the states of a reduced low-order linear approximation of a high-order nonlinear system. The full order nonlinear system is described by Eqs. 2.27-2.29. The model used for observer design is obtained through the discretization of system and subsequent model order reduction. The resultant discrete-time reduced-order linear model given by:

$$\Delta x_{r,k+1} = A_r^d \Delta x_{r,k} + B_r^d \Delta u_k + w_k, \tag{3.143}$$

$$\Delta y_k = C_r^d \Delta x_{r,k} + D_r^d \Delta u_k + v_k, \tag{3.144}$$

where the terms $w_k \in \mathbb{R}^{n_{xr}}$ and $v_k \in \mathbb{R}^{n_y}$ are, respectively, the associated process and measurement noise representing uncertainties in the model 3.143-3.144. Let the sequences $\{w_k\}$ and $\{v_k\}$ be realizations of uncorrelated zero mean white Gaussian processes $\{W_k\}$ and $\{N_k\}$, respectively, such that $W_k \sim (0, Q_w)$ and $N_k \sim (0, R_v)$, where $Q_w \in \mathbb{R}^{n_{xr} \times n_{xr}}$ and $R_v \in \mathbb{R}^{n_y \times n_y}$ are known covariance matrices. These matrices can be obtained from experimental data, sensor specifications provided by manufactures, or simulations. A procedure to tune these matrices based on UM/NAST data is proposed in Appendix E.

The objective is to design a state observer that minimizes the mean squared error (MSE)

$$\text{MSE} = E[||\Delta x_{r,k} - \Delta \hat{x}_{r,k|k}||^2], \tag{3.145}$$

where $E[\ ]$ is the expected value and $\Delta \hat{x}_{r,k|k} \in \mathbb{R}^{n_{xr}}$ represents the estimated state vector based on outputs. The Kalman filter gives the optimal solution to this problem. In the recursive formulation, the Kalman filter observer performs a 1-step prediction:

$$\Delta \hat{x}_{r,k|k-1} = A_r^d \Delta \hat{x}_{r,k-1|k-1} + B_r^d \Delta u_k, \tag{3.146}$$

which is then corrected based on the current sensor measurement y_k:

$$\Delta \hat{x}_{r,k|k} = \Delta \hat{x}_{r,k|k-1} + K_k \left(\Delta y_k - C_r^d \Delta \hat{x}_{r,k|k-1} - D_r^d \Delta u_k \right). \tag{3.147}$$

The matrix K_k is the Kalman filter gain at time k, which is calculated as follows:

$$K_k = P_{k|k-1} C^T \left(C_r^d P_{k|k-1} C_r^{dT} + R_\nu \right)^{-1} \tag{3.148}$$

$$P_{k|k-1} = A_r^d P_{k-1|k-1} A_r^{dT} + Q_\omega \tag{3.149}$$

$$P_{k|k} = \left(I_{n_{xr}} - K_k C_r^d \right) P_{k|k-1}. \tag{3.150}$$

In the equations above, $P_{k|k}$ represents the a posteriori estimate of the covariance matrix of the state estimation.

When $k \to \infty$, $K_k \to K_\infty$ where $K_\infty \in \mathbb{R}^{n_{xr} \times n_y}$ is given by

$$K_\infty = \left(A_r^d P_\infty C^T \right) \left(C_r^d P_\infty C_r^{dT} + R_v \right)^{-1}, \tag{3.151}$$

where P is solution to the discrete-time algebraic Riccati equation:

$$A_r^d P_\infty A_r^{dT} - P_\infty - A_r^d P_\infty C_r^{dT} \left(C_r^d P_\infty C_r^{dT} + R_v \right)^{-1} C_r^d P_\infty A_r^{dT} + Q_w = 0. \tag{3.152}$$

The error $\hat{e}_k = \Delta x_{r,k} - \Delta \hat{x}_{r,k|k}$ dynamics for the case when $\Delta u_k = 0$ is then given by

$$\hat{e}_{k+1} = (A_r^d - K_\infty C_r^d)\hat{e}_k, \tag{3.153}$$

which is stable provided that the pair (A_r^d, C_r^d) is detectable and the pair $(A_r^d, Q_w^{1/2})$ is stabilizable.

Once the estimated states are available, the control action is computed based on the certainty equivalence property, i.e., it is obtained as the same as would be computed in the absence of additive noise.

Next, results of numerical simulations to illustrate the application of the proposed state observer are presented. The simulations are implemented using the XRF1 model built in UM/NAST.

To design the state observer, one INS and twenty-four IMUs were placed on the aircraft fuselage, wing, tail and pylons using the UM/NAST Sensors module. The sensors were evenly distributed on these structures and the number of IMU sensors was selected as the smallest one that made the reduced-order model fully observable.

The LA governor architecture was designed to track a flight-path angle command signal while keeping the curvature at critical stations on the wing within safety limits. The load alleviation is performed by deflecting the outer ailerons and elevators. The complete description of the MLA system can will be presented in Section 4.

The following sensor channel uncertainties were considered:

1. Load factor sensor uncertainty: ± 0.15 g
2. Gyros uncertainty (angular rates): ± 1 deg/s
3. Calibrated airspeed uncertainty due to exogenous disturbances: ± 8 kt and ± 25 kt
4. Mach number uncertainty due to exogenous disturbances: ± 0.025 and ± 0.05
5. Altitude uncertainty due to exogenous disturbances: ± 1500 ft
6. GNSS receiver uncertainty (in local North-East-Down position): ± 10 m

To incorporate such uncertainty, a zero-mean Gaussian distribution approximation was used. The standard deviation was chosen as one fifth of the maximum uncertainty range for each sensor. For instance, the standard deviation attributed to gyros was 1/5 deg/s. The corresponding distribution is shown in Fig. 3.11a. In this way, more than 99.99 % of realizations of the assigned Gaussian distribution is within the expected uncertainty range (e.g.: ± 1 deg/s for rate-gyros).

To account for nonlineariries, model order reduction and discretization errors, the procedure presented in Section E was applied. A series of eight closed-loop nonlinear trajectories were computed in UM/NAST for different flight-path angle references. The recorded state and output time histories were then used to estimate $\hat{Q}_w$ and $\hat{R}_v$ by approximating the estimation error by a Gaussian distribution. Figure 3.11b shows an example obtained for one of the reduced-order model states. Note that the resulting Gaussian distribution has a non-zero mean.

The resultant steady-state Kalman filter along with the LA governor were implemented in UM/NAST. The results of a closed-loop nonlinear simulation are shown in the next results. The objective was to track a 4-degree flight-path angle reference while keeping the out-of-plane curvature at the wing root below 3×10^{-4} 1/m. A Monte Carlo analysis was performed with 100 sample trajectories.

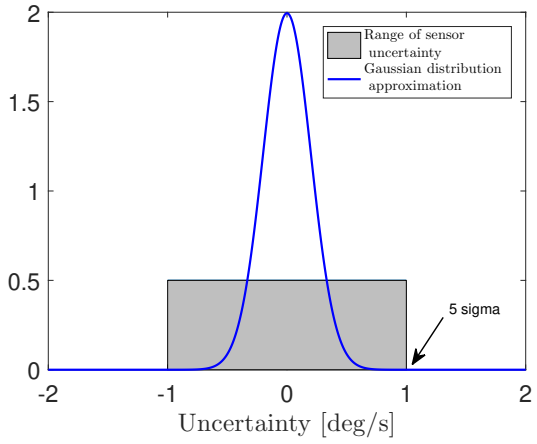

(a) Gyros uncertainty.

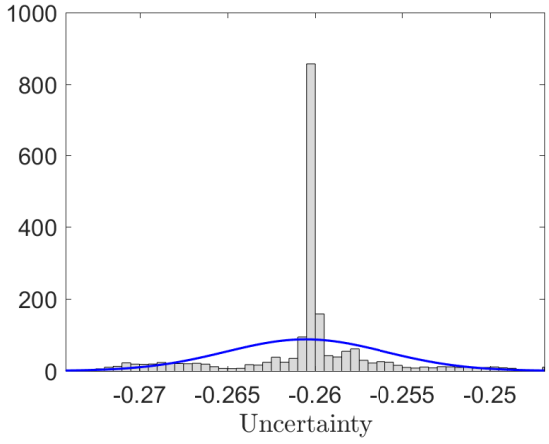

(b) Uncertainty in reduced order state #104.

Figure 3.11: Examples of approximation of sensor and process noise by Gaussian distributions.

Figure 3.12 shows the left wing root curvature and corresponding bending moment. The gray curves represent individual realizations of the outputs, while the black curves represent their statistics (solid line is the mean while the dashed line is the standard deviation). The blue curve is the trajectory obtained when no curvature constraints are enforced, i.e., the MLA system is deactivated. For all simulations in which the constraints were enforced, there was a significant load reduction. The mean result shows that there is a small constraint violation, possibly due to the model mismatch between the reduced order linear model used for prediction and the nonlinear plant not entirely capture by the proposed procedure. Nevertheless, the overall performance of the MLA system was satisfactory, and

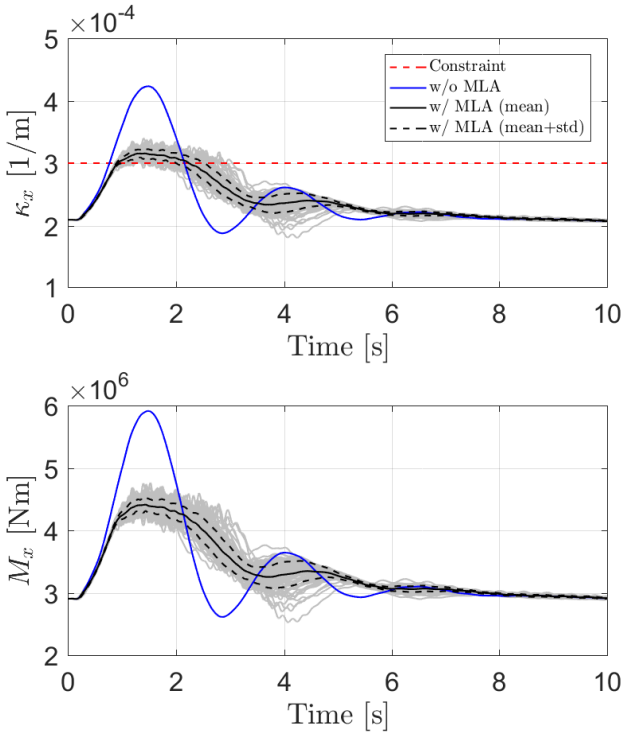

Figure 3.12: Out-of-plane curvature and bending moment on left wing root.

the constraint violation could be mitigated by constraint tightening. Figure 3.13 shows the reference command computed by the LA governor, which was fed into the inner loop, and the corresponding flight-path angle time history. Note that the variation of the computed reference when the MLA system is active was greatly affected by the measurement noise. However, such dispersion did not result in a significant deviation from the mean flight-path angle trajectory. The control inputs to perform such maneuver are shown in Fig. 3.14. The average outer aileron deflection to perform MLA was below 10 degrees. In all simulations, the outer aileron returned to the trim condition when there was no danger of violating constraints.

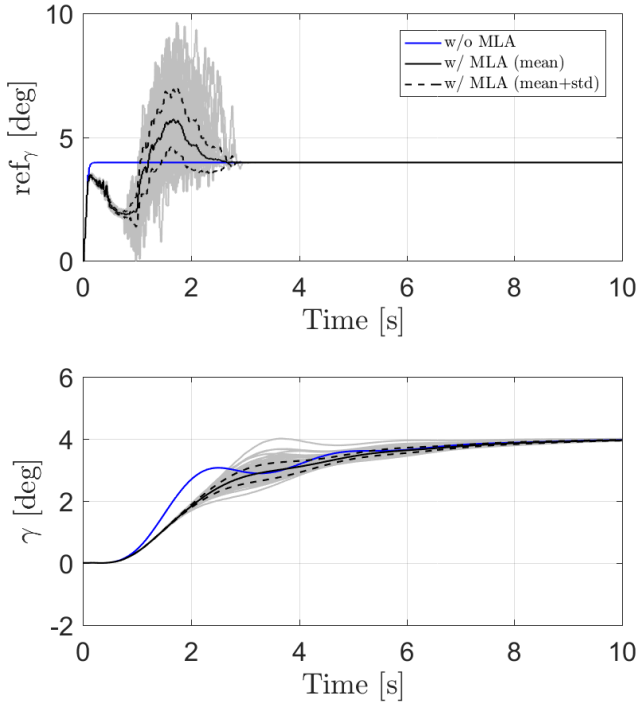

Figure 3.13: Flight-path angle reference and time history.

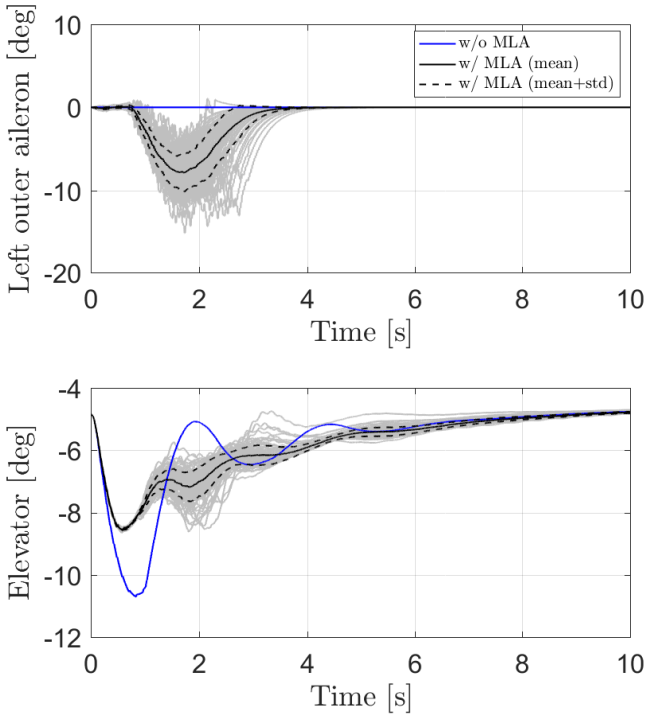

Figure 3.14: Control inputs time histories.

CHAPTER 4

Maneuver Load Alleviation

The demonstration that critical loads on commercial flexible aircraft do not exceed specified limits is part of the certification process to ensure structural integrity throughout the operation of the vehicle. For such purpose, maneuver load alleviation (MLA) can be integrated into the flight control system (FCS) to coordinate control effectors capable of shifting the load distribution on the aircraft structure in order to provide both performance and safety. Constrained control techniques align well with load alleviation objectives due to their ability to enforce pointwise-in-time constraints on the loads and actuation of control effectors.

4.1 MLA System Requirements

The main requirements of an FCS with MLA capabilities for a large transport flexible aircraft are:

1. Track defined command signals and meet response specifications while ensuring stability during operation.

2. Keep loads at critical stations within pre-defined limits.
   Load attenuation between 20% and 33%. Even if attenuation above 33% can be achieved, it cannot be accounted for in structural design, since the structure itself should be able to sustain a certain load profile without an MLA system [7].

3. Minimize the effect of the MLA system on the nominal trajectory of the aircraft.
   Altitude deviation should be less than 250 ft (76.8 m). FCS should generate a compensatory control input to counteract the pitching moment due to the MLA actuation.

Secondary requirements include:

4. Actuator rates should be limited to 45 deg/s.

5. Design should take into consideration different mass cases, center of gravity positions, fuel and payload re-partitions, and flight conditions.

6. Failure mode handling.
   MLA system should be robust against actuator and sensor failures.

These requirements apply to the aircraft category CS25 as defined in the European Union Aviation Safety Agency [7]. Modifications in limits and allowed deviations may change for other aircraft categories.

As part of the certification campaign, the aircraft is required to show that it is able to perform certain maneuvers while preserving structural integrity. The maneuver stretched vertical (MVS) is the one usually considered when evaluating the MLA system. This maneuver consists in, from a leveled flight at 1g condition, applying the following stick trajectory: (i) push the pilot stick with a sine shape until a load factor (n_z) of 2.5g is reached, then (ii) release to turn back to 1g with a sine-like function [124]. In this work, to simulate the stick input, an equivalent pitch rate command (Fig. 4.1a) is fed to the tracking controller described in Section 3.2, such that the resultant vertical load factor at the aircraft nose follows the desired profile, as shown in Fig. 4.1b.

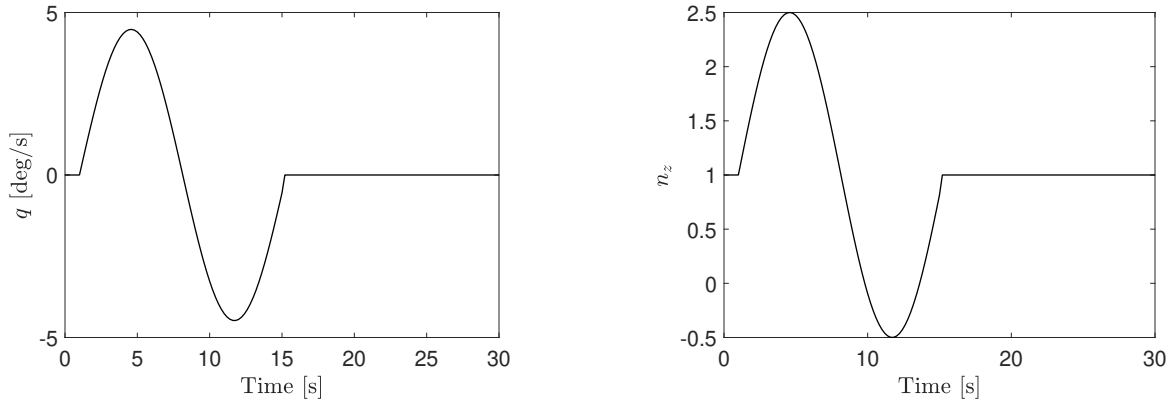

(a) Commanded pitch rate.

(b) Vertical load factor at aircraft nose.

Figure 4.1: MVS maneuver.

Another maneuver considered in this work for assessing the performance of the MLA system is a step change in the flight path angle from the trim condition (0 deg) to 4-8 deg. These are typical values commanded during flight by the pilot when changing altitude, and differently from the MVS maneuver, has a sharp change in the tracked reference value.

4.2 MLA System Design

The MLA system design to meet the requirements presented in Section 4.1 is based on the architectures described in Section 3.2. The requirements can be satisfied as follows:

1. Trajectory tracking:
   The tracker controller with integral action (the MPC itself in the MPC architecture, or the nominal (LQ-I) controller in the LA governor architecture) will be responsible for changing the aircraft attitude and speed to follow the trajectory commanded by the guidance system.

2. Keep loads within limits:
   Load constraints can be directly incorporated into the MPC design and be enforced pointwise-in-time in order to keep them within the desired bounds. The modeling of these constraints will be discussed in Section 4.2.1.

3. Minimize trajectory deviation:
   This can be achieved by the proper selection of gains in the controllers. The penalty on the tracking error in the MPC architecture, or in the deviation of the generated trajectory by the LA governor architecture with respect to the reference value, should be high to minimize trajectory deviations due the actuation of the MLA system.

4. Actuator rate limits:
   A constraint can be added to the MPC problem on the upper and lower bounds on the control deflection rate.

5. Design for different aircraft configurations:
   The scenario-based MPC presented in Section 3.4 can be used to design a single controller that can handle multiple aircraft configurations.

6. Failure mode handling:
   Redundancy of actuators and sensors is the standard approach to handle failures. This can be achieved by the proper selection of these components, as it will be discussed in Section 4.2.2 and 4.2.3. However, a systematic way to detect failure and design MPC controllers for failure handling is out of the scope of the work presented in here.

The MLA objective considered in this work is to keep the loads on the aircraft below the critical ones. To this end, the reduction of peak loads with respect to the trim condition when the vehicle performs the maneuver is sought. The minimization of the average loads during the maneuver to increase fatigue life, similar to what was done in Ref. [14], is not part

of the MLA objective. The out-of-plane bending moment is the main critical load considered here. This is because such load is usually connected with the lowest aeroelastic frequency, which is more likely to couple with the rigid body modes. Even though not shown in here, the reduction of in-plane and torsion moments would also be possible with the architectures in Section 3.2.

The reduction of critical loads on both wing and horizontal tail plane (HTP) are desirable when performing MLA in a transport aircraft. The inclusion of the latter into the controller design is justified by the increase in bending moment on the tail root due to the actuation of the MLA system on the wing. Such an increase is due to the higher elevator deflection to mitigate trajectory deviation due to the reduction of pitch moment caused the deployment of the flaps or ailerons on the wing while alleviating loads on that structure.

The next section will discuss how to model load constraints in MLA, the selection of control surfaces to enforce these limits, and the sensors for feedback control.

4.2.1 Modeling Constraints in MLA

In MLA systems, the aircraft loads are alleviated by deflecting the control surfaces proportionally to some monitored parameters (e.g., load factor or wing curvature), which are obtained from sensor measurements. While the load factor is a usual choice of a monitored parameter in traditional MLA systems, this parameter only captures the transient behavior of loads during maneuvers. For instance, pitch-up maneuvers performed at a slow rate may develop small to moderate accelerations that do not trigger the MLA system. However, the aerodynamic forces that build up as the angle of attack gradually increases can result in significant structural loads.

An alternative approach to perform MLA is by monitoring the curvature at critical stations, since this parameter is directly connected to the magnitude of loads at those stations. Indeed, considering the wing modeled as an Euler-Bernoulli beam, the axial strain at a spanwise station located at distance y and deflected by z from its neutral position is given by

$$\epsilon_{yy} = -\kappa_x z, \tag{4.1}$$

where κ_x is the curvature about the x axis. The resultant bending moment $M_x(y)$ at wing station y is given by:

$$M_x(y) = EI_{xx}(y)\kappa_x, \tag{4.2}$$

where $EI_{xx}(y)$ is the out-of-plane bending stiffness at wing station y.

Although it is possible to impose constraints on the function $M_x(y)$ to guarantee that the bending moment is within the specified limits at all stations on the continuous wing

model, the resultant problem would be of infinite dimensionality. As a result, conventional, finite-dimensional optimization methods could not be applied to solve the problem. Finite element methods are usually used to model the dynamics in this kind of structure. In these methods, the continuum is represented by a finite number of degrees of freedom by means of a collection of elements that are connected according to some rule or function. While this circumvents the infinite dimensionality problem by creating a finite set of elements upon which constraint can be imposed, the cardinality of the set is usually of high order to give an accurate representation of the continuous model. Therefore, imposing constraints at each element of the discrete model would not be practical from a numerical perspective.

The set of constrained stations can be reduced by identifying the critical stations, i.e., the stations that are subject to the highest loads during maneuvers in comparison to adjacent stations. For instance, Eq. 4.1 and 4.2 indicate that a uniform wing (i.e., all properties such as $EI_{xx}(y)$ are constant in the spanwise direction) will develop the highest bending moment at the root. Therefore, by imposing constraints on the curvature at that station only, one would guarantee that the moments at all other stations along the wing are within the specified limits. The same analysis is possible, even tough more involved, for non-uniform wings. For these, the properties are not constant along the span and therefore the critical stations may not be located at the root, and there may be multiple critical stations. To identify these stations, open-loop simulations of longitudinal and/or lateral maneuvers can be performed and the moments and loads at each station monitored. The following procedure is proposed:

1. Define typical maneuvers, inputs or disturbances that the vehicle is usually subject to during operation or extreme conditions. For example, step or doublets inputs on the control surfaces that will generate significant accelerations.

2. Run open-loop simulations for each condition specified in 1. Monitor the loads, such as bending moment or shear force, at each station of the model.

3. Identify the stations that develop the highest loads for each condition simulated in 2. These stations will form the set of critical stations.

4. For each critical station, define the maximum and minimum load limits according to some safety specification or structural analysis.

The procedure above will define a reduced set of stations to impose constraints on their out-of-plane curvature. Note that the enforcement of constraints on the curvature is equivalent to performing shape control for achieving load alleviation. Figure 4.2 shows the critical stations of XRF1 obtained using the procedure described above based on lateral and longitudinal maneuvers. The same stations are also critical for the XRF1-HARW configuration.

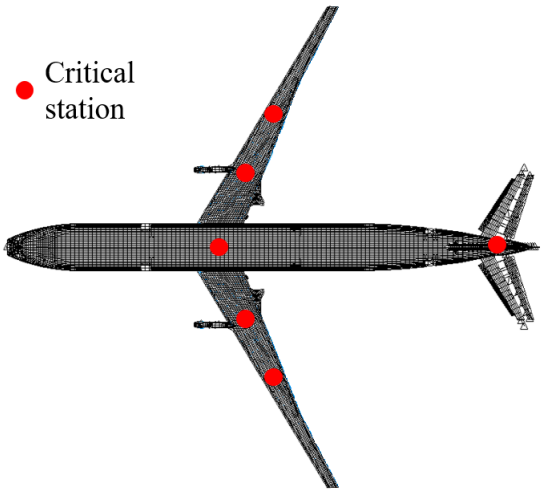

Figure 4.2: Critical stations in XRF1.

The out-of-plane curvature constraints are usually upper and lower bounds on this variable, which is connected to the maximum magnitude of the allowed loads (e.g., the yielding load of the member plus a safety factor). This information is usually obtained from an structural strength analysis that precede the control design stage. Such information was not available for the aircraft models considered in this work (Section 2.4). Therefore, in the cases considered in this Chapter, the curvature limits were illustrative numbers selected to demonstrate the performance of the control system.

4.2.2 Control Effectors for MLA

The selection of the set of control effectors to perform load alleviation will depend on the aircraft model for which the system is being designed. In general, extra degrees of freedom are desirable for increasing the authority in controlling the shape of the vehicle and mitigate the use of effectors u_{FCS} which could cause trajectory deviation. Furthermore, these extra degrees of freedom also provide redundancy, which helps with failure handling. Note that while extra degrees of freedom are optional in the MPC architecture in Section 3.2.1, they are required by the LA governor architecture in Section 3.2.2 because, by design, effectors u_{LA} and u_{FCS} should be independent.

For controlling the out-of-plane bending moment near the wing root, control surfaces placed in the mid and outboard section of the wing can provide higher authority due to the longer moment arm. However, control surfaces close to the wing tip should be avoided

because of the reduced lift generated at that wing portion due to three-dimensional aerodynamic effects, and because control surfaces at this location are more likely to suffer control reversal. While the same rationale applies to the selection of control surfaces for load alleviation on the HTP, conventional aircraft configurations usually do not have multiple control surfaces on the tail. Therefore, the elevator is usually the only control surface used for alleviating loads on the HTP.

In the XRF1 and XRF1-HARW aircraft models (see Section 2.4), the main control surfaces used for load alleviation on the wing are the left and right outer ailerons (δ_{oal} and δ_{oar}, respectively) working as elevons, and the flaps (δ_{fl}):

$$u_{\text{LA}} = \begin{bmatrix} \delta_{oal} & \delta_{oar} & \delta_{fl} \end{bmatrix}^T \tag{4.3}$$

In X-HALE, the control surfaces used for load alleviation are the left and right outer tail planes (δ_{T3} and δ_{T4}, respectively):

$$u_{\text{LA}} = \begin{bmatrix} \delta_{T3} & \delta_{T4} \end{bmatrix}^T. \tag{4.4}$$

The other control surfaces available in these vehicles are part of effectors u_{FCS} that are used for speed and attitude control.

4.2.3 Sensors for MLA

Sensors used in MLA applications include wing deflection sensors, accelerometers, strain gauges and wing angle of attack sensors [16]. The next sections describe these devices.

4.2.3.1 Strain Gauges

Foil strain gauges can be placed at the critical stations on the aircraft wing and HTP where the load constraints are enforced. The outputs of these sensor can be used to directly monitor the loads on these stations during flight. The use of strain gauges for feedback control, however, is usually avoided in commercial aircraft. These sensors are known for having reliability issues and difficult calibration [125].

An alternative to foil strain gauges are optical fiber monitoring systems, which provide greater reliability. However, these systems are considerably more expensive than foil strain gauges.

4.2.3.2 Inertial Sensors

Inertial sensors are sensors based on inertia and relevant measuring principles, such as accelerometers and gyroscopes. These sensors can be used to recover the local acceleration and angular rates during a maneuver at different stations of the flexible wing or HTP. From angular rates, the local attitude in Euler angles can also be obtained. These measurements can then be used to estimate the shape of the flexible structure.

Inertial sensors will be the main sensors used for feedback control in the MLA systems designed in this work. One INS and thirty IMUs were placed on the XRF1 and XRF1-HARW aircraft fuselage, wing, tail and pylons, as shown in Fig. 4.3. The sensors were evenly distributed on these structures and the number of IMU sensors was selected to make the ROM fully observable. This number is slightly bigger than the minimum to render the system observable, and the extra sensor provide redundancy in case of failure. The nonlinear kinematics of sensor attached to a flexible structure simulated using UM/NAST-Sensor module. In this software, each IMU sensor provides linear accelerations, angular velocities, and Euler angles. The INS sensor provides, in addition to these outputs, linear velocities and inertial position.

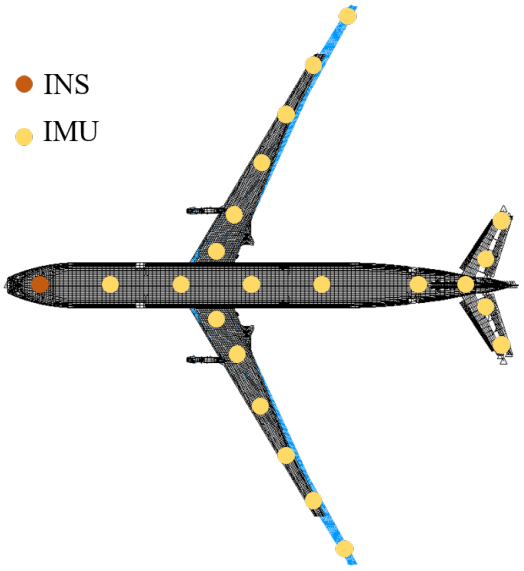

Figure 4.3: Sensor placement in XRF1 and XRF1-HARW.

4.2.3.3 Other Sensors

Shape estimation during flight can be done using cameras. An example of such an estimation system has been proposed by Lustosa et al. [126], in which gyroscopes and cameras are used

together to reconstruct the shape of very flexible wings undergoing large and nonlinear deflections. The use of cameras in flight, however, is still challenging due to the different lighting conditions and geometries that the aircraft wing is subject to during flight, which can preclude the accurate detection of markers. For this reason, camera-based systems are not considered in this work.

Other sensors used in FCS systems that can also be included in MLA systems are pitot tubes, alpha vanes, control surfaces encoders, magnetometers, among others.

4.3 Numerical Results

This section presents several numerical simulation results to illustrate and verify the proposed MLA systems. Furthermore, the MPC implementation strategies discussed in Chapter 3 are also showcased in the next results.

Five examples are shown in here. Firstly, a comparison between the MPC architecture and the LA governor architecture for MLA is presented based on results for the X-HALE aircraft. This aircraft model was chosen to demonstrate these control architectures for having the highest degree of flexibility among the models in Section 2.4. Next, simulation results were generated for the XRF1 and XRF1-HARW models, which better represent a flexible and very flexible airliner. MLA examples using constraint aggregation are shown, as well as using the scenario-based approach for handling different mass configurations. Results using the T2B and B2T ROMs for MPC design are also presented.

In all results shown next, UM/NAST was the primary tool used for design and simulation. This includes the UM/NAST Sensors and Controllers modules presented in Section 2.2.

4.3.1 Comparison between MLA System Architectures

In this section, the results of the numerical simulations of the two control architectures proposed in Sections 3.2 based on linear MPC are presented [127]. The linearized full-order model and ROM of X-HALE are used for control design. To obtain the ROM, the MPC prediction models were reduced from 128 states to 70 states using balanced residualization.

In the simulations, the aircraft flies in closed-loop configuration at the trim condition for 1.0 s and then a pitch up maneuver is commanded. The objective is to reach the flight path angle of $r_\gamma = 8$ deg while maintaining the same speed, and keeping the heading and side-slip angles close to zero.

The constraints imposed on the control problem are shown in Table 4.1. Note that the constraints on the out-of-plane curvature at the wing root are defined according to the

method discussed in Section 4.2.1, and their limits are chosen according to the variation allowed with respect to the trim condition. In addition to these constraints, limits on the control effector values and rates are imposed, and limits on the angle of attack to prevent stall.

Table 4.1: X-HALE's output and input constraints on.

Description	**Min**	**Max**	**Unit**
Out-of-plane curvature ($\kappa_{x_{right}}$, $\kappa_{x_{left}}$) at wing root on very flexible aircraft model	0.096	0.110	[1/m]
Angle of attack (α)	-10	10	[deg]
Elevator deflection ($\delta_{T1}, \delta_{T2}, \delta_{T3}, \delta_{T4}$)	-30	30	[deg]
Spoiler deflection (δ_{sp})	0	30	[deg]
Differential thrust (δ_{dT})	50	-50	[rps]
Average propeller rotation (δ_T)	20	120	[rps]
Rate of deflection of elevators and spoilers	-90	90	[deg/s]
Rate of variation of propeller rotation	-50	50	[rps/s]

For both controllers, the sampling rate is 50 Hz and the prediction horizon is 100 steps. This means that the MPC controllers looks 2 s ahead of the current time to predict constraint violations and then determine the optimal control action. Full state feedback was assumed. The solver qpOASES [87] was used, which is an open source C++ code based on an online active set optimization algorithm.

Figure 4.4 shows the out-of-plane curvature and the corresponding bending moments at the right and left wing root, and the wing tip deflection for the very flexible X-HALE aircraft model performing the pitch up maneuver with both control architectures. There was no constraint violation. However, the ROM in the LA governor architecture overestimated the wing curvature, resulting in a greater load alleviation than expected. While the load alleviation with the full-order model was around 42.7%, it reached 56.5% for the case with the ROM. When the MPC architecture was used, the load alleviation with either linear model was approximately 50.7% at each semi-wing. The wing tip deflection was above 10% in all cases tested, which indicates that the nonlinear effects may not be insignificant, and consequently the prediction obtained with the linear ROM model may be degraded.

Both control architectures were successful in tracking the commanded references as shown in Fig. 4.5. For all controllers, the tracking targets were reached within reasonable time, and with similar performance when either full-order model or ROM was used for prediction.

Figure 4.6 shows control inputs computed by both architectures to perform MLA and track the references. In both of them, the inner elevators are deflected downwards in order to shift the lift distribution to the inner portion of the wing, and therefore reduce the root bending

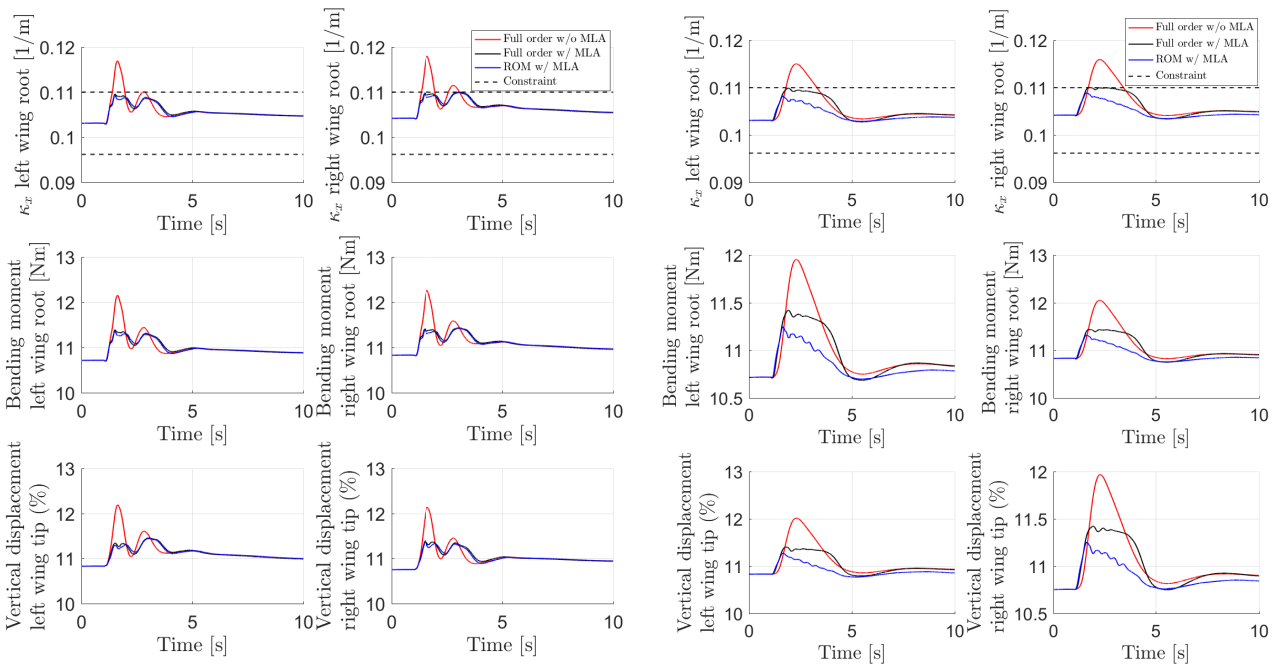

(a) MPC architecture.

(b) LA governor architecture.

Figure 4.4: X-HALE closed-loop simulations for load alleviation using two different control architectures.

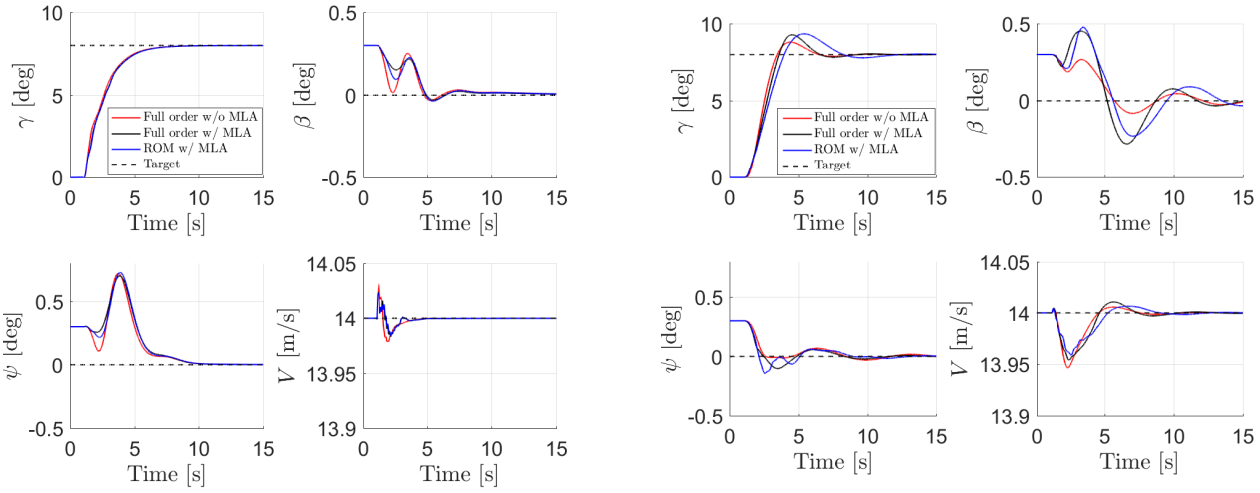

(a) MPC architecture.

(b) LA governor architecture.

Figure 4.5: Command tracking performance of the X-HALE.

moment. In the LA governor architecture designed with the ROM, the overestimation of the curvature resulted in a larger deflection of the inner elevators to perform MLA. The outer elevators returned to the trim condition after performing the load alleviation in order to reduce drag and the impact on the trajectory of the vehicle.

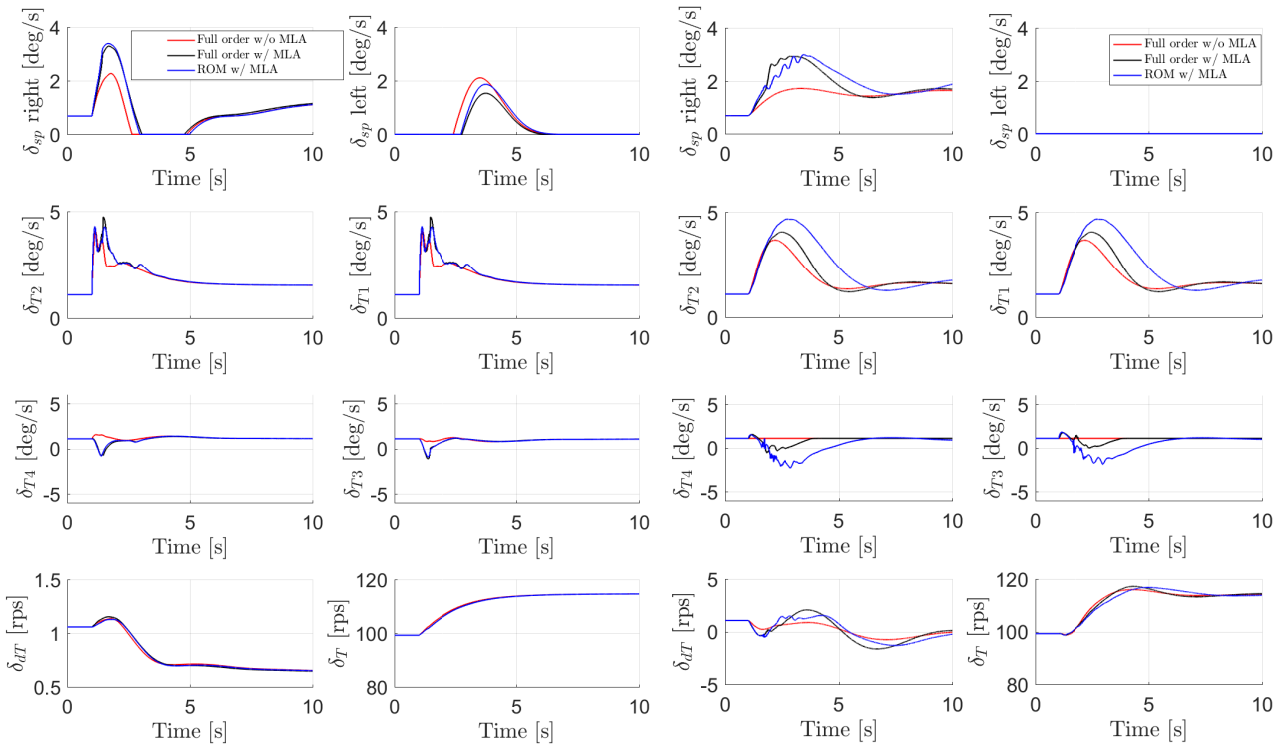

(a) MPC architecture.

(b) LA governor architecture.

Figure 4.6: Time histories of control inputs of X-HALE.

Incidentally, the impact of the MLA system on the nominal trajectory was small, below 0.4%, as shown in Fig. 4.7. The impact of the actuation performed by the LA governor architecture was, in general, greater than the impact in case where the MPC architecture was used, but still within the acceptable range.

Table 4.2 shows the maximum and average computation time of the optimizer for each simulation case normalized by the sampling time $T_s = 0.02$ s. All simulations were performed on a Dell XPS 15 laptop (Intel i7-7700HQ, 2.8GHZ, 16 GB RAM). The prediction based on the ROM provided a reduction of the average computation time. The level of reduction was 8.7% and 55.7%, respectively, when the MPC architecture or the LA governor architecture was used. In general, the MPC architecture had lower computational cost.

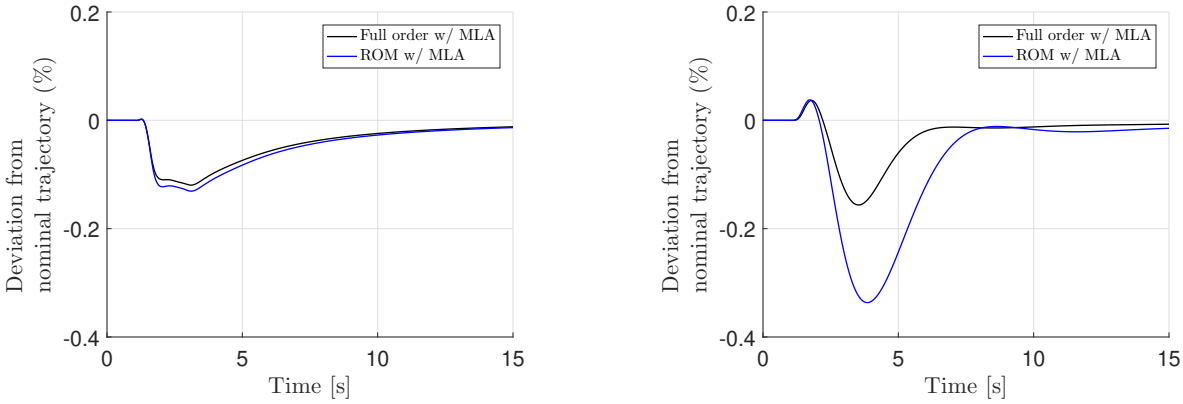

(a) MPC architecture.

(b) LA governor architecture.

Figure 4.7: Trajectory deviation of the X-HALE.

Table 4.2: Average normalized optimization wall time of MPC for X-HALE

Model	**MPC**	**LA governor**
Full order w/o MLA	0.390	0.380
Full order w/ MLA	1.04	3.34
ROM w/ MLA	0.95	1.48

These simulation results show that both control architectures were successful in achieving command tracking while enforcing the curvature constraints, resulting in load alleviations around 42-56% for the VFA. The use of ROMs decreased the average computation time involved in solving MPC optimization problems, with little impact on the controller's performance. The MLA systems, when activated, produced negligible changes in the trajectory of the aircraft, which was the design intent. The MPC architecture showed a slight better performance in enforcing constraints with the ROM with a smaller computation time. The LA governor, on the other hand, has the advantage of preserving the nominal FCS as discussed in Section 3.2.2. Such characteristic may be of interest to airframe manufacturers that already have a certified FCS for their aircraft.

4.3.2 MLA System for XRF1

Next, simulation results are shown for MLA in XRF1, a representative model of a flexible airliner. The LA governor architecture with linear MPC is considered here. The controller design was based on a ROM with 310 states that was obtained from applying balanced residualization to the 1020-state full-order model. In this simulations, only the outer ailerons are used for load alleviation on the wing. This simulations also illustrates the use of constraint

aggregation (Section 3.3)in a MLA system.

The sampling rate used by the LA governor was 50 Hz and the prediction horizon had 100 steps. This means that the MLA governor looks 2 seconds ahead of the current time to predict constraint violations and then determine the optimal control action. The LQ-I controllers in the inner-loop system were updated at sampling rate of 200 Hz.

The constraints imposed on the control problem for the MLA governor architecture are shown in Table 4.3. The constraints on the out-of-plane curvature on the wing and horizontal tail plane are defined according to the MLA objective discussed in Section 4.2.1. In addition to these constraints, limits on the angle of attack, and on control effector values and rates were imposed.

Table 4.3: XRF1 output and input constraints.

Description	**Min**	**Max**	**Unit**
Out-of-plane curvature (κ_x) at critical stations on wing	-3.0×10^{-4}	3.0×10^{-4}	[1/m]
Out-of-plane curvature (κ_x) at critical station on HTP	-5.0×10^{-4}	5.0×10^{-4}	[1/m]
Control surfaces deflection ($\delta_{oal}, \delta_{oar}, \delta_{ia}, \delta_e, \delta_r$)	-30	30	[deg]
Thrust (δ_T)	0	60000	[N]
Rate of deflection of control surfaces	-45	45	[deg/s]
Rate of variation of thrust	-1000	1000	[N/s]
Angle of attack (α)	-10	10	[deg]

The final QP had 3900 constraints. Following the constraint aggregation procedures (Section 3.3), the problem was reformulated with 39 constraints. The SQP was then implemented to solve the nonlinear program. The solver QPKWIK [88], which is an active set optimization algorithm, was used to solve each QP sub-problem. In all simulations, the solver was warmstarted.

In the simulations presented next, the aircraft starts at the trim condition and then a pitch up maneuver is commanded. The objective is to reach a flight path angle of $r_\gamma = 4$ deg while keeping the heading angle, side-slip angle and velocity at the trim values.

Figure 4.8 shows the out-of-plane curvature at the left wing and HTP roots for XRF1. The results shown correspond to simulations without the MLA system (i.e., with only the nominal controller to track signals), simulations with the linear MPC-based MLA system, and simulations with the MPC-based MLA system with constraint aggregation. Note that both MLA systems were able to enforce the constraints on the curvature of the wing and

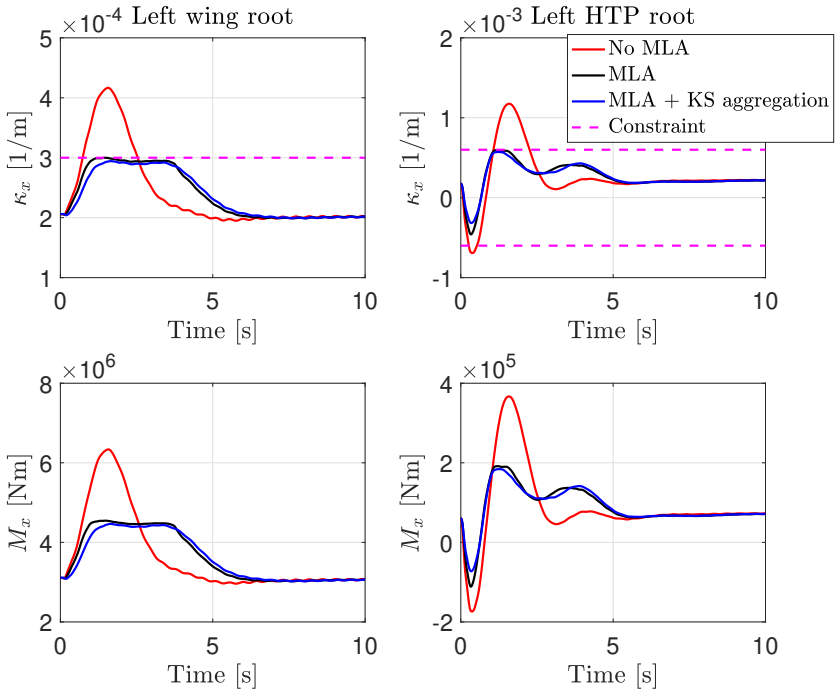

Figure 4.8: Out-of-plane curvature and bending moment at wing and horizontal tail root.

HTP, therefore reducing the bending moment at these stations. Constraints at other critical stations were not active. Figure 4.9 shows the percentage of maximum load alleviation as a function of spanwise position. Both MLA systems were able to reduce loads at all stations on the wing and HTP. Smilar results were obtained for the right wing and HTP. Note that the MLA system with constraint aggregation had higher percentages of alleviation, since the constraints were tighter than in the linear MPC case as a result of the conservative approximation of the feasible region provided by the KS function.

Figure 4.10 shows the control effectors time history. The linear MPC-based MLA system resulted in higher deflections of the inner ailerons used for lateral control. This explains the drop in the alleviation percentage on the left wing at stations near this control surface, as observed in Fig. 4.9. Figure 4.11 shows that both autopilot systems were able to track the desired flight path angle r_γ with similar performance. In the figure, the signal r_γ^c is the command computed by the MLA governor to avoid constraint violations.

Additional results for the maneuver simulation can be found in Appendix F, including the moments at the various stations along the wing and HTP.

Table 4.4 resents the maximum and average computation time observed during the simulation. Reductions of 92% and 57% in the maximum and average computation time, respectively, were obtained when the KS aggregation was used. While the computation time even

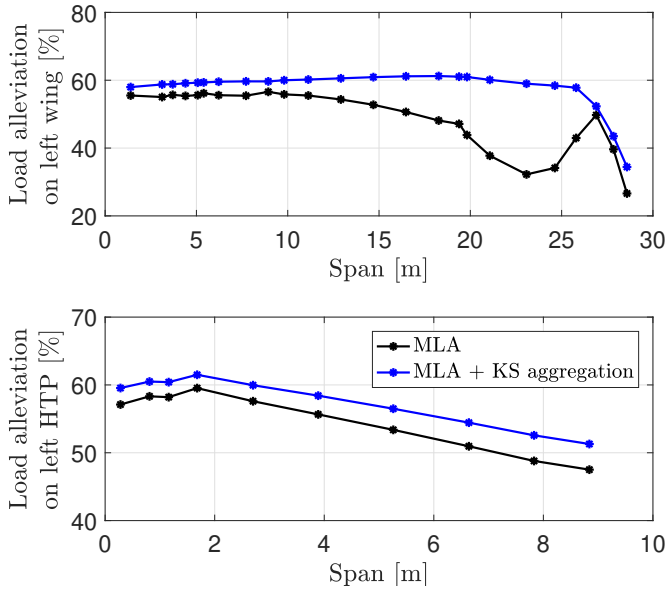

Figure 4.9: Maximum bending moment alleviation at wing and horizontal tail as a function of span position.

with KS aggregation exceeds the time step of 0.02 s, it should be noted that the implementation of the optimization was not optimized for computational performance.

Table 4.4: Maximum and average computation time of an MPC step.

	Max.	**Avg.**
Linear MPC	2.8890 s	0.4176 s
MPC with KS aggregation	0.2358 s	0.1792 s
Reduction	91.8%	57.1%

In practice, the worst-case execution time drives the selection of the processor hardware. The results presented here indicate that the proposed method can facilitate the real-time implementation of MPC controllers for large-scale systems, such as flexible aircraft, using microcontrollers with limited computing power.

4.3.3 MLA System for Different XRF1 Mass Configurations

In this section, results of numerical simulations to illustrate the application of the proposed scenario MPC-based MLA system in Section 3.4 are presented [128]. The objective is to perform MLA in the XRF1 aircraft models with different mass cases. The UM/NAST XRF1 model associated with each mass case was trimmed and linearized at 10 km, 240 m/s. The next simulations on a Dell XPS 15 laptop (Intel i7-7700HQ, 2.8GHZ, 16 GB RAM).

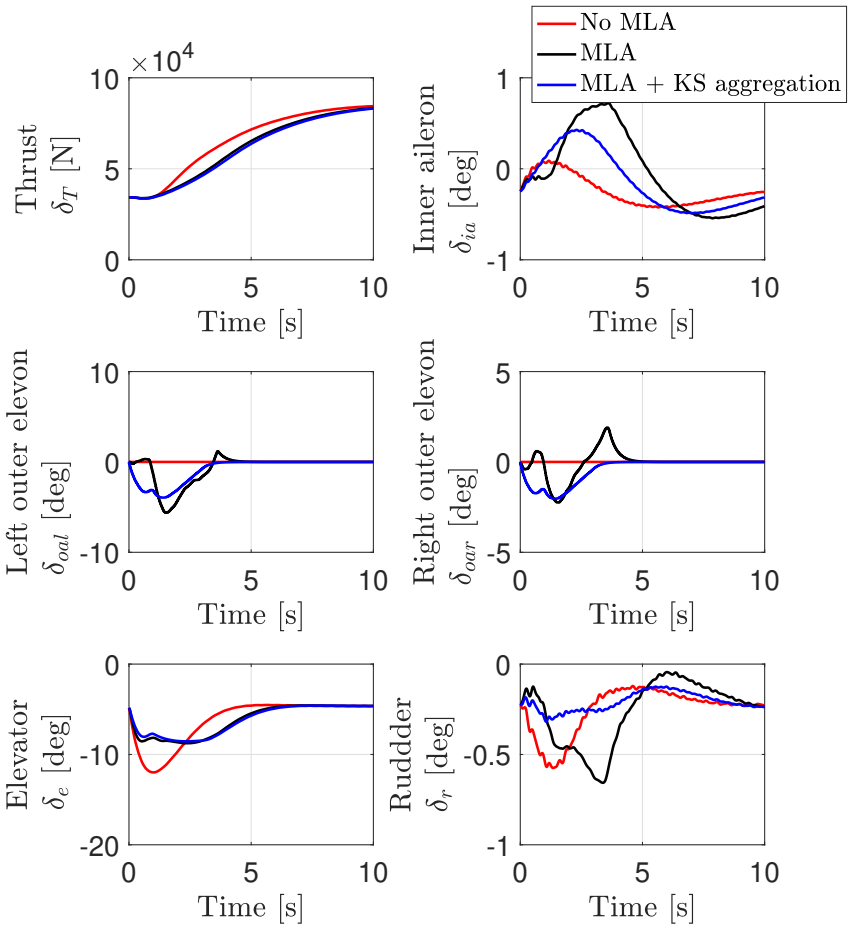

Figure 4.10: XRF1 control effectors time history.

The LA governor 4.3.2 was used to track a 4-degree flight path angle (a pitch-up maneuver) while keeping the out-of-plane curvature within the specified limits. The nominal controller, composed of a combination of linear quadratic regulators with integral action (LQ-I), was designed to handle all mass cases. To illustrate the need for a robust MPC design, Fig. 4.13 shows that a nominal MPC design based on just one mass case (e.g., OWE) is unable to avoid constraint violations when applied to an aircraft model with another mass configuration (e.g., FT8T), resulting in large control surface deflections that lead to an undesired dynamical behavior.

Therefore, the scenario-based MPC design described in Section 3.4 is used. Note that the nominal controller stabilizes the origin and provides the gain matrix K_f described in Section 3.4. The MPC controller was designed with a prediction horizon of $N = 100$ steps and sampling time of 0.02 s. Since the prediction horizon is long, there is no need to specify a terminal set X_f. The resulting QP optimization problem was solved with QPKWIK [88].

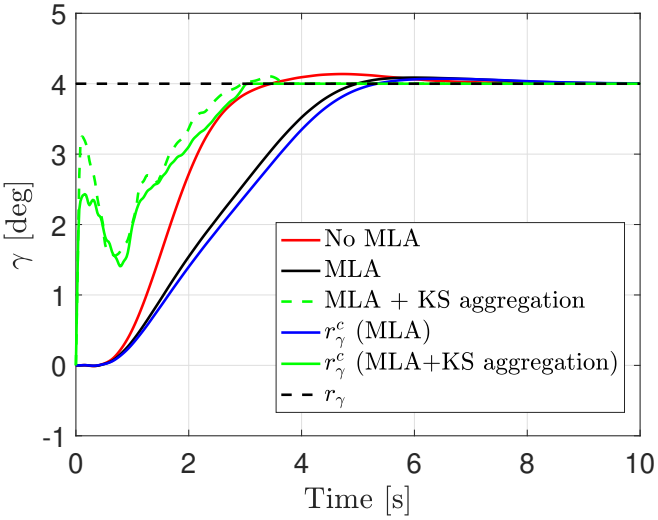

Figure 4.11: XRF1 flight path angle tracking.

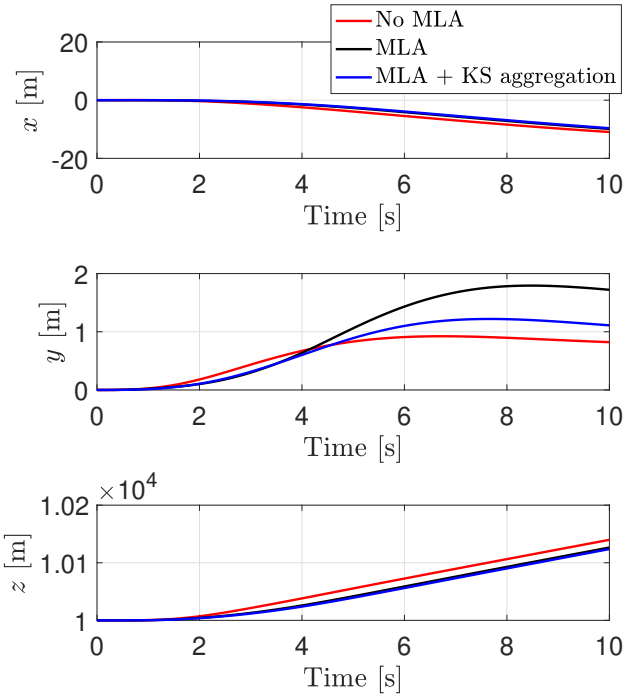

Figure 4.12: XRF1 inertial position.

The constraints applied to the problem are shown in Table 4.5. In Algorithm 1, the constraints were distributed in $R_d = 9$ groups of $N_m = 3$ models.

Figure 4.14 shows the out-of-plane curvature at the right wing root and corresponding

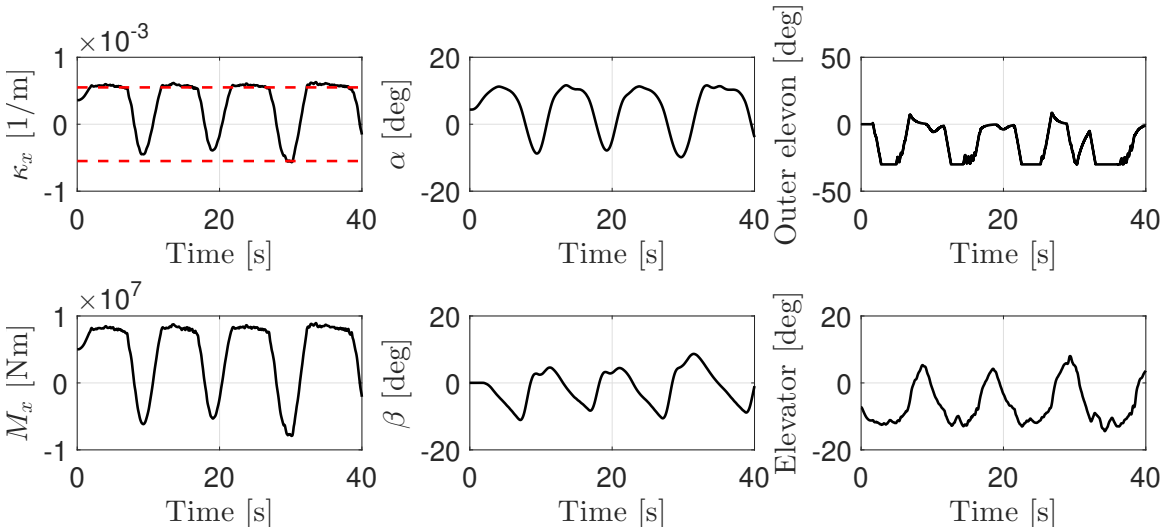

Figure 4.13: Nominal MPC design based on OWE mass case when applied to mass case FT8T.

Table 4.5: Output and input constraints for XRF1 models with different mass.

Description	**Min**	**Max**	**Unit**
Out-of-plane curvature (κ_x) at critical stations	-5.5×10^{-4}	5.5×10^{-4}	[1/m]
Control surfaces deflection	-30	30	[deg]
Thrust	0	60000	[N]
Rate of deflection of control surfaces	-45	45	[deg/s]
Rate of variation of thrust	-1000	1000	[N/s]

bending moment for all mass cases. Note that each model has a different trim condition. The constraints were enforced for all models, although conservatively in some cases (e.g.: model FT8T). Models OWE and F000 had the smallest initial curvature, which did not reach the limiting value during the maneuver. Therefore, the MLA system remained inactive for these models. On the other hand, the MLA governor was able to reduce in 30.5 - 57.6% the loads on the other models, as shown in Tab. 4.6. The percentages presented in Tab. 4.6 were computed having as reference the simulation results for the maneuver without the MLA system, which are not shown in here.

Table 4.6: Percentage of load alleviation at right wing root

Model	OWE	F000	FA2M	FA2T	FA9M	FC8T	FT8T
% of load alleviation	N/A	N/A	30.5	40.4	57.6	43.6	42.3

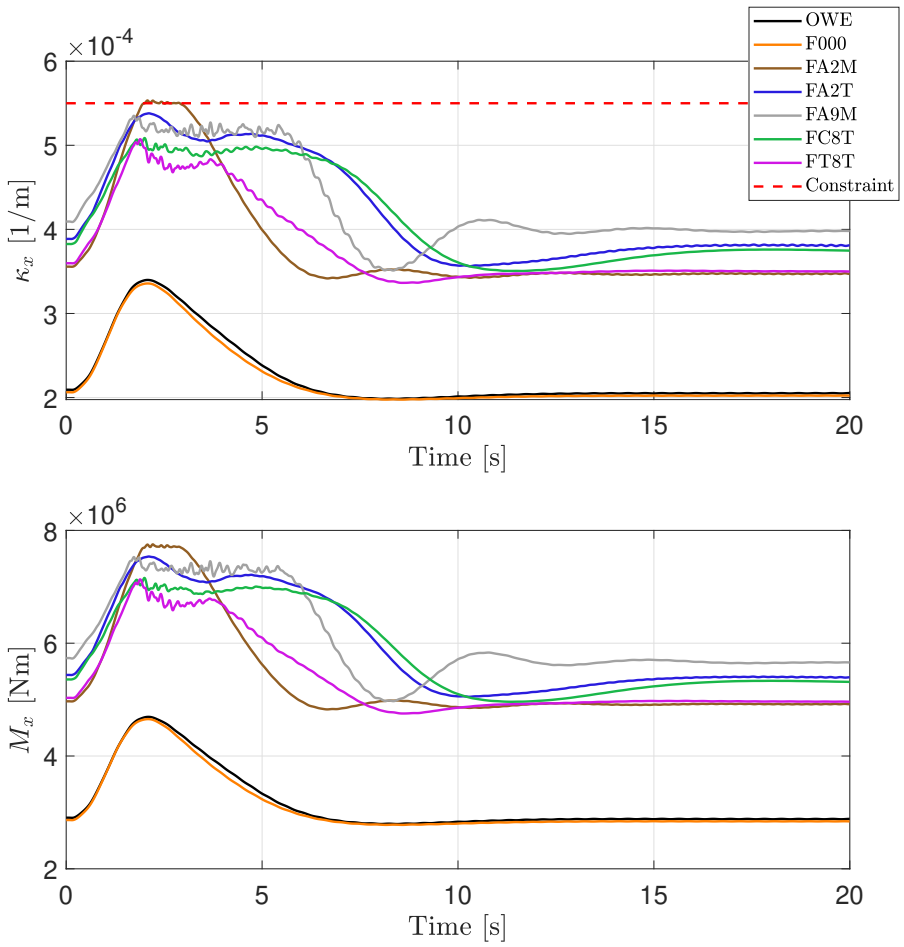

Figure 4.14: Right wing root out-of-plane curvature and bending moment of XRF1 mass cases.

Figure 4.15 shows the time histories of the angle of attack, side-slip angle, and flight path angle. Note that all models reached the desired 4-degree flight path angle. Figure 4.16 shows the orientation angles and angular rates during the maneuver. To develop these responses, the control effectors time histories shown in Fig. 4.17 were applied to the vehicles. Note that the outer ailerons, working as elevons, were used as the main effectors to perform MLA. The elevators were also used as a result of the change of the reference command (Fig. 4.18) computed by the MLA governor that was fed into the nominal controller. The elevons were deflected only when there was a danger of violating the curvature constraints. After performing the load alleviation, they returned to their trim condition. The maximum elevon deflection was 14.8 deg for the FT8T model. Since the MLA system was not activated for the simulations with models OWE and F000, the elevons for these models remained at the trim condition for the entire maneuver.

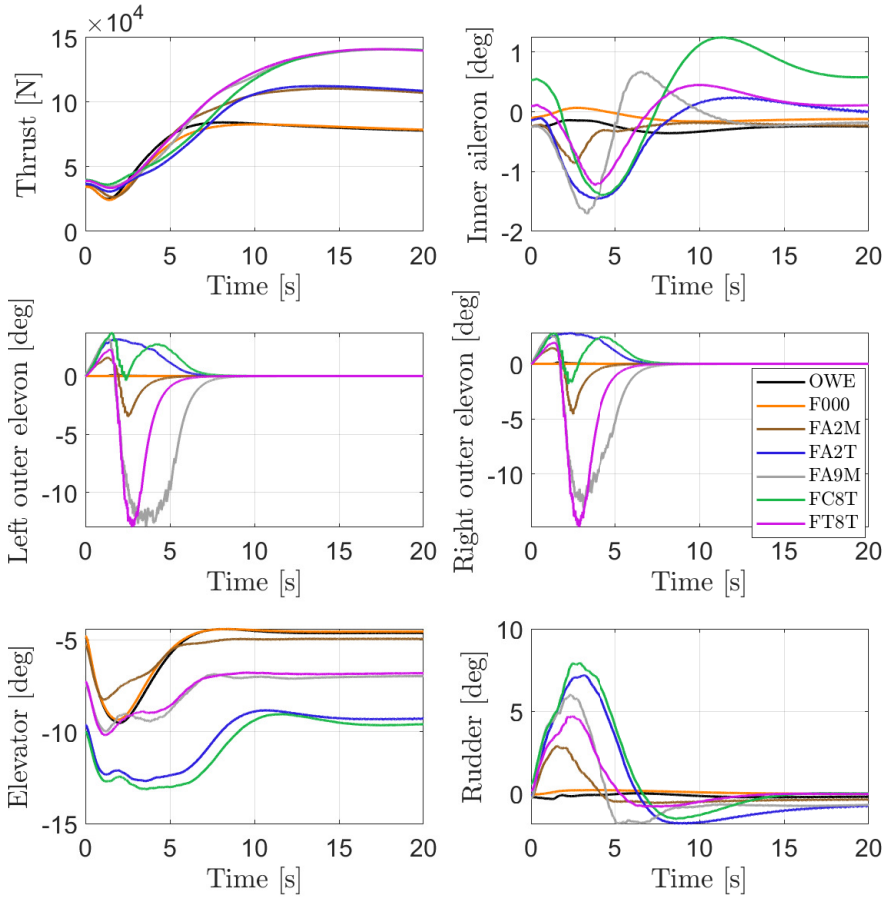

Figure 4.15: Angle of attack, side-slip angle and flight path angle of XRF1 mass cases.

Table 4.7 shows the maximum computation time observed for an MPC optimization step for the nominal MPC (designed based on only one mass case), the conventional scenario-based MPC in which the constraints for all models are enforced simultaneously, and the proposed scenario-based MPC with time-distributed constraints. Due to the larger number of constraints, there was an increase of 45% in the computation time between the nominal case and the time-distributed approach. Nevertheless, the latter provided a 67% reduction when compared to the conventional approach. Constraint aggregation methods, such as the one presented in Section 3.3, can be applied to potentially decrease even more the computational footprint of the scenario-based MPC controller.

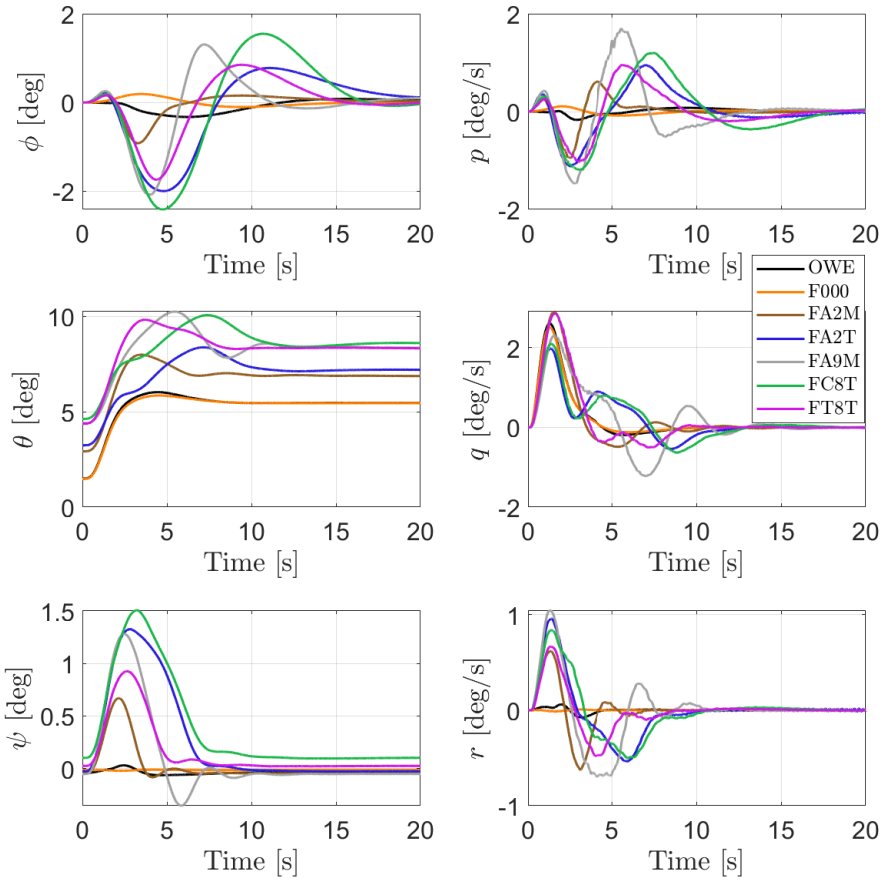

Figure 4.16: Euler angles and angular rates of XRF1 mass cases.

Table 4.7: Maximum computation time for nominal and scenario-based MPC approaches.

Formulation	**Max.** [s]
Nominal MPC	1.10
Scenario-based MPC: conventional approach	4.59
Scenario-based MPC: time-distributed constraints	1.51

4.3.4 MLA System for XRF1-HARW using the T2B Model

In this section, the results of numerical simulations to illustrate the application of the MPC-based MLA system using the T2B ROM for XRF1-HARW are presented. The objective is to perform the MVS maneuver while maintaining the out-of-plane bending (prescribed by the curvatures at the critical stations) within prescribed safety limits. The MPC architecture is used in these simulations.

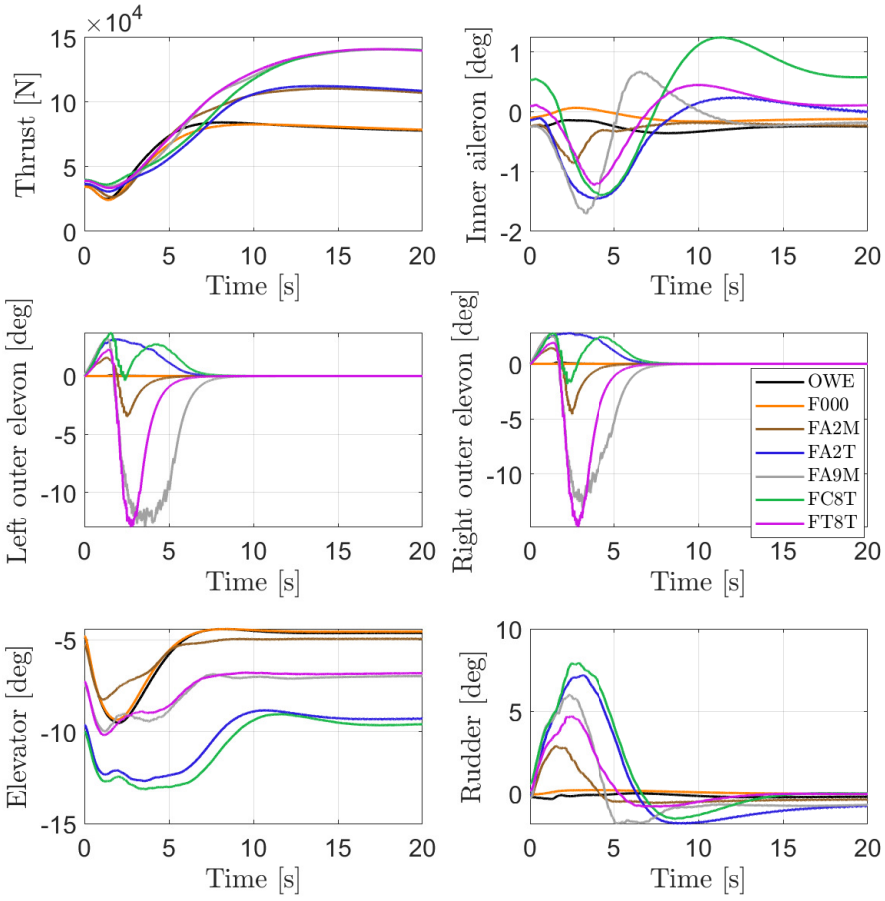

Figure 4.17: Control effectors time history of XRF1 mass cases.

For the XRF1-HARW test case, the linearization points correspond to different values of altitude (h) and Mach number (M), i.e., $\zeta = [h \quad M]^T$, as shown in Tab. 4.8. Each pair (h_i, M_i) is identified by a number from 1 to 96. For each one of them, the corresponding pair (x_i, u_i) is a trimmed state-input pair provided by UM/NAST trim solver. The linearized systems are then obtained using the complex-step differentiation method in UM/NAST. These linearized systems capture the change in dynamics within the specified flight envelope.

Each linearized model generated by UM/NAST has 1084 states. Such a high number of states can preclude MPC applications due to the high computational cost. Therefore, model order reduction is performed through balanced residualization. For XRF1-HARW, $n_{xr} = 100$ is selected in this report.

The input and output constraints considered in this example are shown in Tab. 4.9. The out-of-plane curvature constraints on critical stations on the wing and HTP are defined as

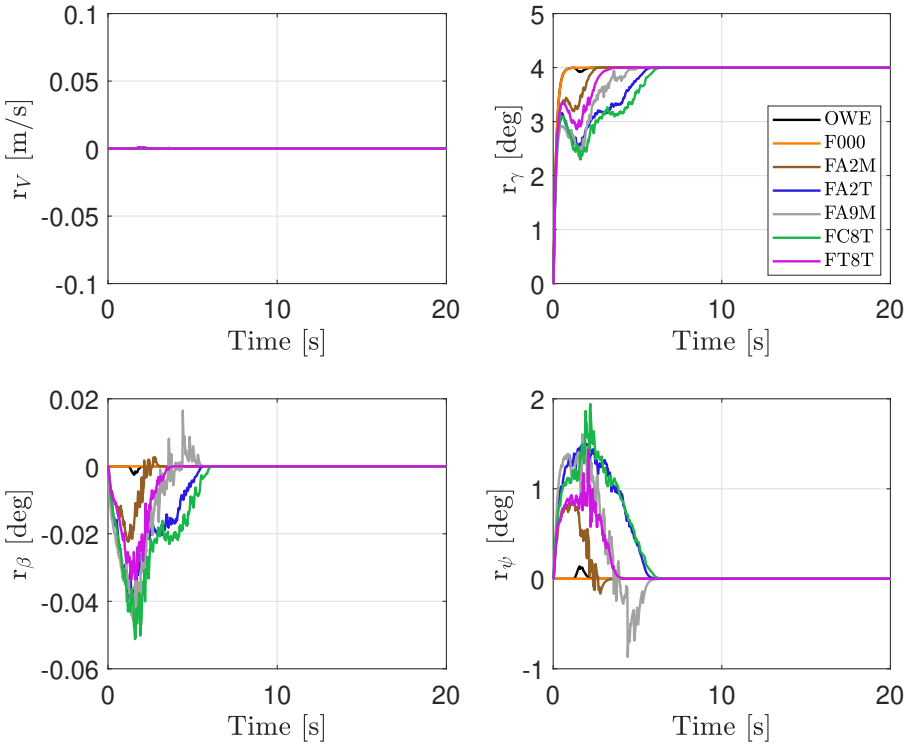

Figure 4.18: References computed by MLA governor (as variations from the trim values).

an equivalent reduction of approximately 30% from the maximum/minimum peak observed when the MVS maneuver is performed with the MLA system deactivated. The constraints on the control surfaces deflection and rate are in accordance with typical values found in actual large commercial aircraft. The rate of deflection of this control surface are chosen smaller than the other control surfaces to account for the reduced bandwidth of this type of actuator.

The next XFR1-HARW nonlinear simulations were performed with two different control surfaces configurations: Configuration 1 uses only the outer ailerons (working as elevons) for load alleviation; Configuration 2 uses, in additions to the elevons, the flaps, whcih work as flaperons. The starts at flight condition 54 ($h = 8800$ m and $M = 0.85$). In both cases, the MPC prediction horizon had 50 steps, corresponding to a 1.0 s look ahead into the future. In addition to the results using the T2B ROM for prediction, simulations were also performed using the linear MPC design presented, in which the linearized prediction model is fixed at the beginning of the simulation. The computations were performed on a Dell XPS 15 laptop (Intel i7-7700HQ, 2.8GHZ, 16 GB RAM). The QP problem was solved using QPKWIK with warmstarting.

Table 4.8: Linearization points of XRF1-HARW and their respective label.

		Mach					
		0.80	**0.81**	**0.82**	**0.83**	**0.84**	**0.85**
Altitude [m]	**8000**	1	2	3	4	5	6
	8100	7	8	9	10	11	12
	8200	13	14	15	16	17	18
	8300	19	20	21	22	23	24
	8400	25	26	27	28	29	30
	8500	31	32	33	34	35	36
	8600	37	38	39	40	41	42
	8700	43	44	45	46	47	48
	8800	49	50	51	52	53	54
	8900	55	56	57	58	59	60
	9000	61	62	63	64	65	66
	9100	67	68	69	70	71	72
	9200	73	74	75	76	77	78
	9300	79	80	81	82	83	84
	8400	85	86	87	88	89	90
	9500	91	92	93	94	95	96

Table 4.9: XRF1-HARW output and input constraints.

Description	**Min**	**Max**	**Unit**
Out-of-plane curvature (κ_x) at critical stations on the wing	-13.5×10^{-4}	4.47×10^{-4}	[1/m]
Out-of-plane curvature (κ_x) at critical stations on the HTP	-1.51×10^{-4}	2.57×10^{-4}	[1/m]
Control surfaces deflection	-25	25	[deg]
Flaperon deflection	-25	25	[deg]
Rate of deflection of control surfaces	-45	45	[deg/s]
Rate of deflection of flaperon	-30	30	[deg/s]

Configuration 1:

In configuration 1, the elevons are used to perform load alleviation while the flaperons are kept at the trim condition. Figure 4.19 shows the rigid body outputs of XRF1-HARW while performing the MVS maneuver with and without the MLA system. The latter corresponds to the case when the curvature constraints are not enforced and served as a baseline. The structural outputs at selected stations are shown in Fig. 4.20. The different color intervals shown in the background of each subplot identifies the reduced-order subspace onto which the dynamics was projected. The color code can be read in Table 4.8. In this example, the sub-

space was switched ten times in the following order: $\{54, 53, 60, 59, 58, 64, 63, 69, 68, 74, 73\}$.

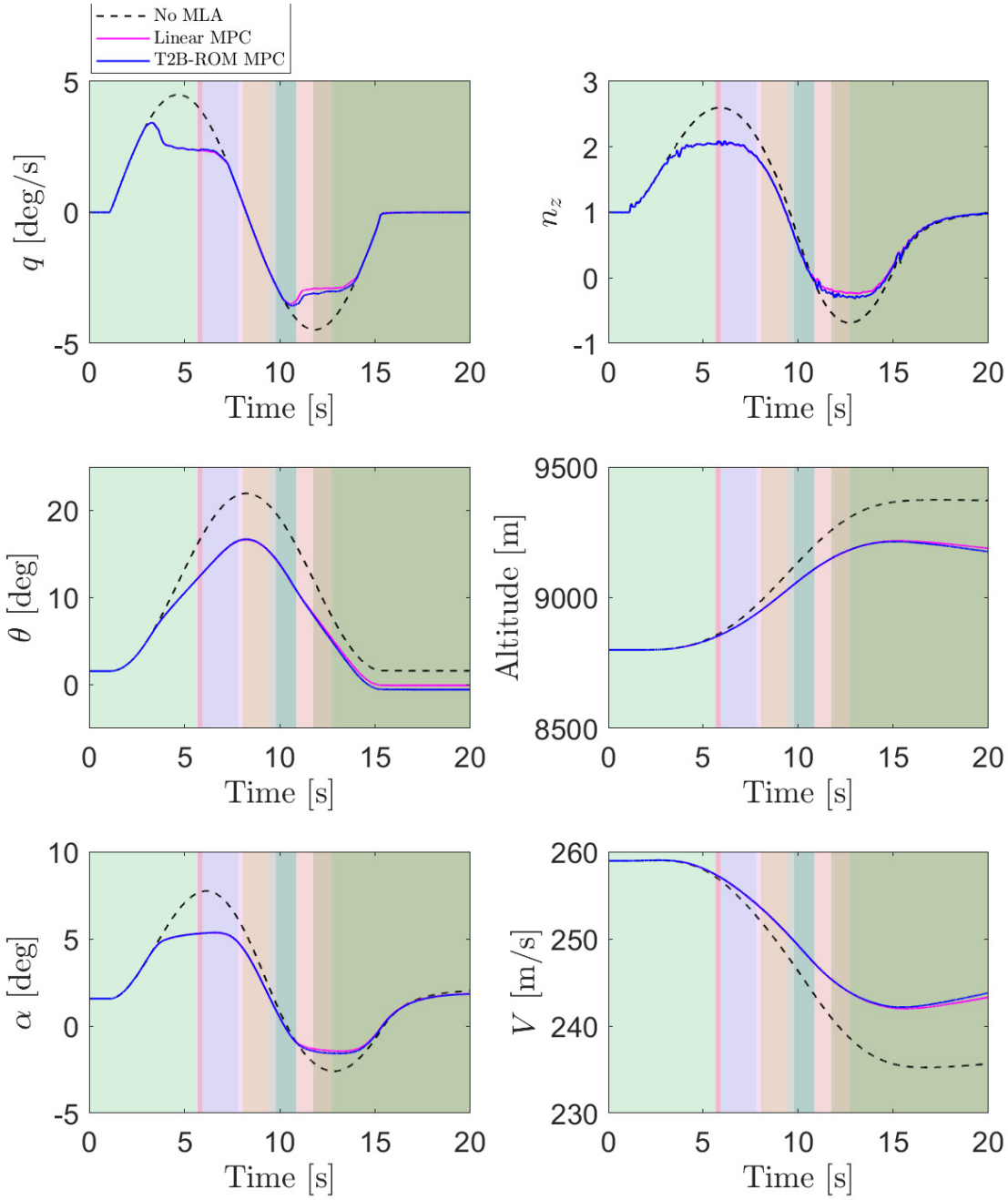

Figure 4.19: Rigid body outputs of XRF1-HARW using configuration 1 of control surfaces.

Even though the out-of-plane curvature constraints on the wing and HTP were satisfied, the flight control system was not capable of accurately tracking the pitch rate command when these constraints were enforced. A reduction in the pitch rate, with a consequent reduction in

the developed pitch angle and load factor, resulted in a deviation from the baseline trajectory, as can be observed in the altitude plot. Nevertheless, reductions of 31.52% in the bending moment on the wing root, and of 42.93% on the HTP root were obtained. The other critical stations on the wing had a similar load reduction, but the constraints did not become active.

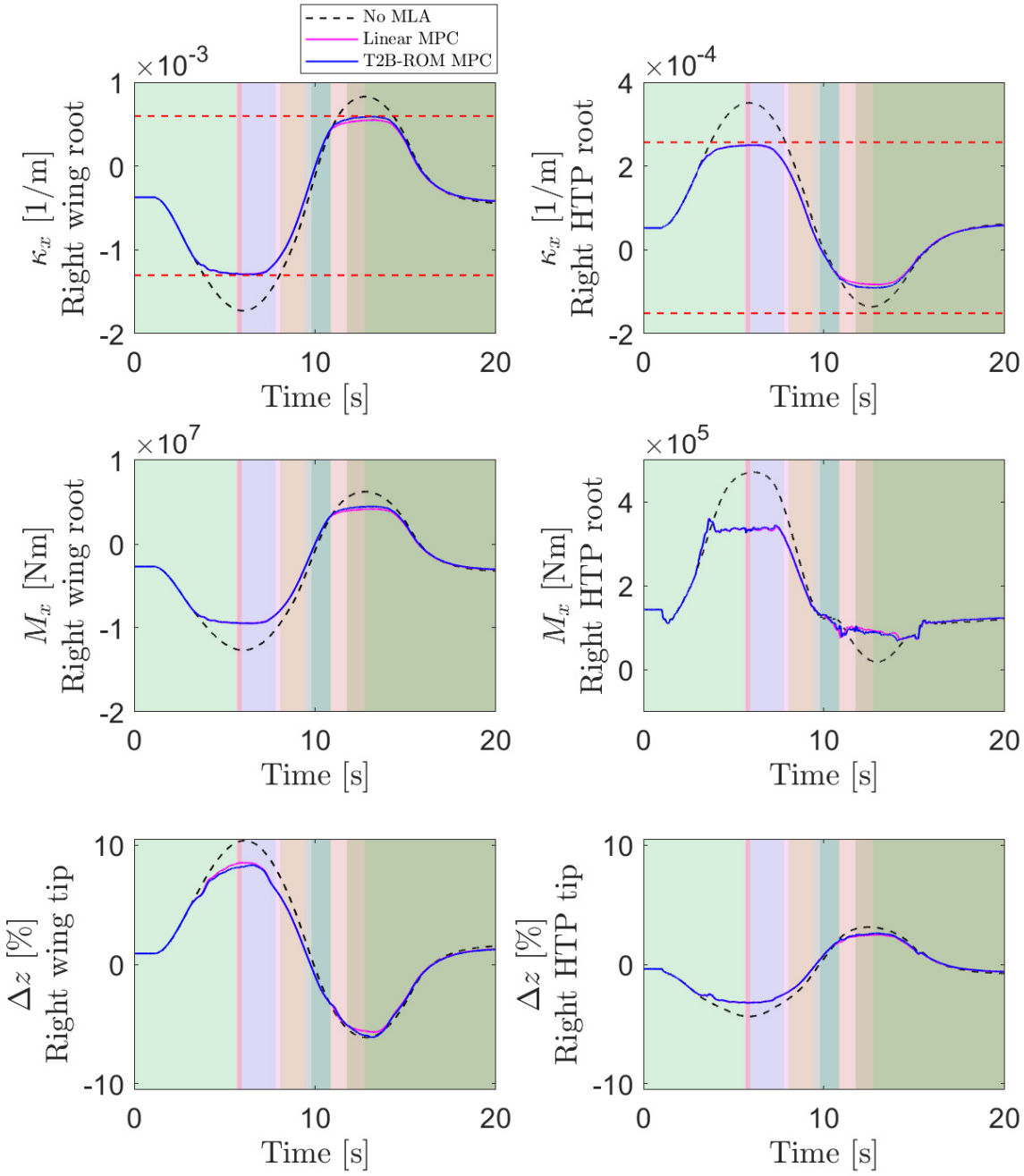

Figure 4.20: Structural outputs of XRF1-HARW using configuration 1 of control surfaces. κ_x: out-of-plane curvature, M_x: out-of-plane moment, Δz: vertical deflection.

The significant trajectory deviation can be explained by the reduction in the elevator input to enforce the MLA constraints, as shown in Fig. 4.21. For the XRF1-HARW model, the outer elevons alone have low efficacy in reducing the curvature at the wing root, even with large deflections such as the ones observed in this example. Furthermore, they cannot compensate for the loss of pitch rate due to the necessary reduction in elevator input to enforce the HTP constraints, since there are no dedicated MLA control effectors on the tail. Consequently, the elevators play the primary role in reducing maneuver loads, while compromising the tracking performance.

Configuration 2:

The flaperon is added to the set of control effectors dedicated to perform MLA in hopes of minimizing the trajectory deviation. Figure 4.22 and 4.23 show the rigid body and structural outputs of XRF1-HARW using configuration 2. In this example, the subspace was switched ten times in the following order: $\{54, 53, 59.58, 64,\ 63, 62, 68, 67, 73, 79, 85\}$. Now, the pitch rate is close to the reference command, and therefore the pitch angle and altitude have smaller deviations from the baseline values. The vertical load factor follows a similar trend as of the MVS profile, but a peak value of 2.9g is developed instead of the desired 2.5g.

The MLA constraints on both wing and HTP critical stations were satisfied. The resulting maximum bending moment alleviation was approximately 36.5% at the wing root, and 21.9% and the HTP root. Similar results were obtained for adjacent critical stations. To achieve such results, the control inputs in Fig. 4.24 were applied to the vehicle. Note that, despite the fact that the elevator input was reduced, the aircraft was still able to track the pitch rate command by deflecting the flaperons. The coordination between flaperons, elevons, and elevators made possible the achievement of both tracking and load alleviation objectives, in contrast to the results of configuration 1. However, the demanded flaperon deflection is somewhat large, even though the elevon deflections are now smaller, which can cause an increase in drag.

In both configurations, the MPC controller designed with the T2B ROM had a similar performance as the standard linear MPC design with a fixed prediction model. Some marginal benefits of the T2B ROM prediction model can be observed in a slightly better signal tracking performance (Fig. 4.19), a lesser conservative constraint satisfaction (Figs. 4.20 and 4.23), and smaller control inputs (Figs. 4.21 and 4.24). It is worth noting that in both cases the wing and HTP tip displacements, as shown in Figs. 4.20 and 4.23, were smaller than 10%, indicating that the MVS maneuver may not sufficiently excite geometric nonlinear effects that would justify the use of the T2B ROM.

On the downside, the MPC design with the T2B ROM has a considerably higher computational cost. Table 4.10 shows a comparison between the maximum and average computation

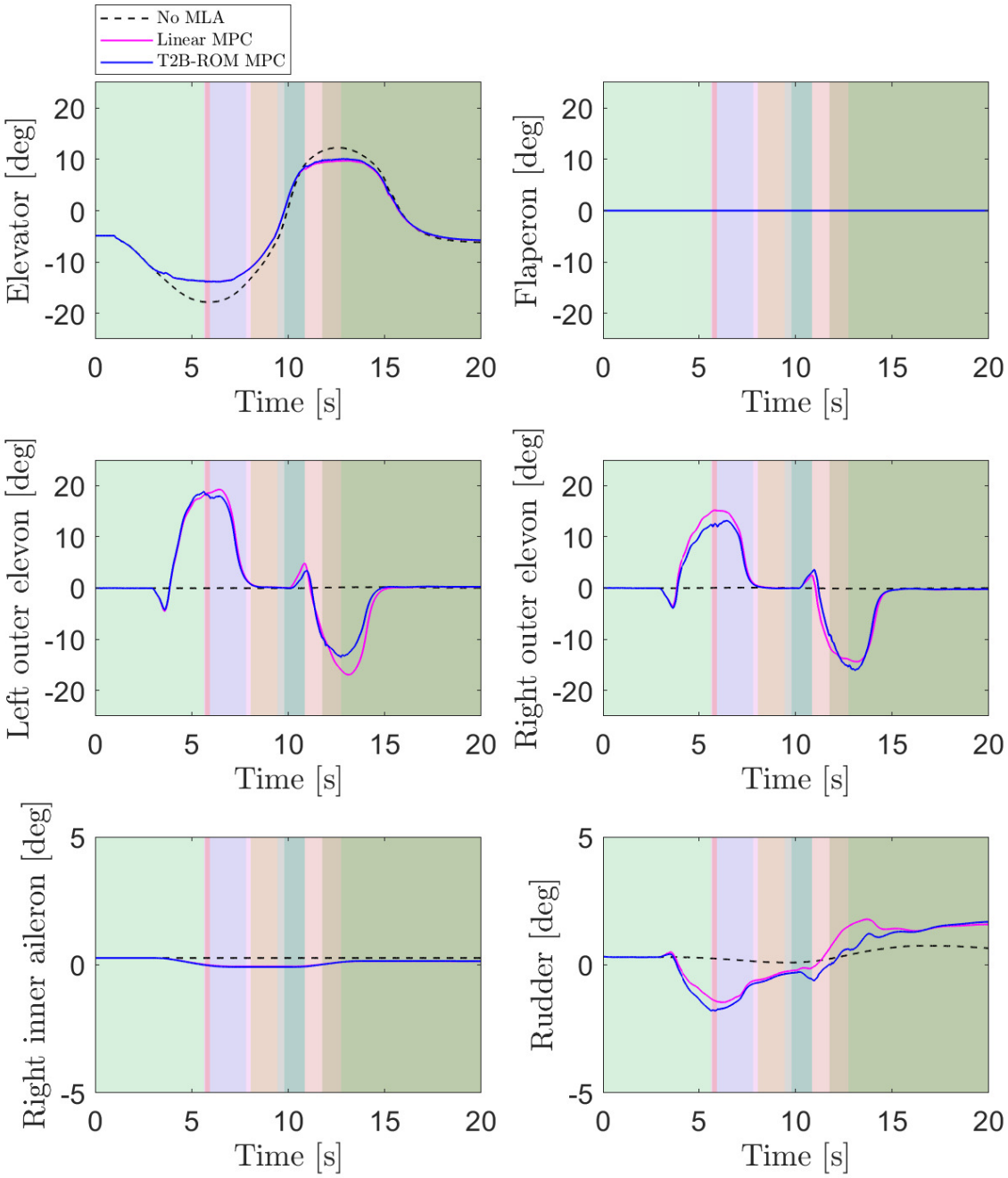

Figure 4.21: Control inputs applied to XRF1-HARW using configuration 1 of control surfaces.

time of an MPC step for the design with a fixed linear model and the T2B ROM. This substantial increase is due to the necessity of updating the T2B ROM model at each MPC iteration, in addition to the condensation process, as discussed in Section 4.2. For the standard linear MPC design, these computations are done offline, thus making it more attractive to real-time implementations.

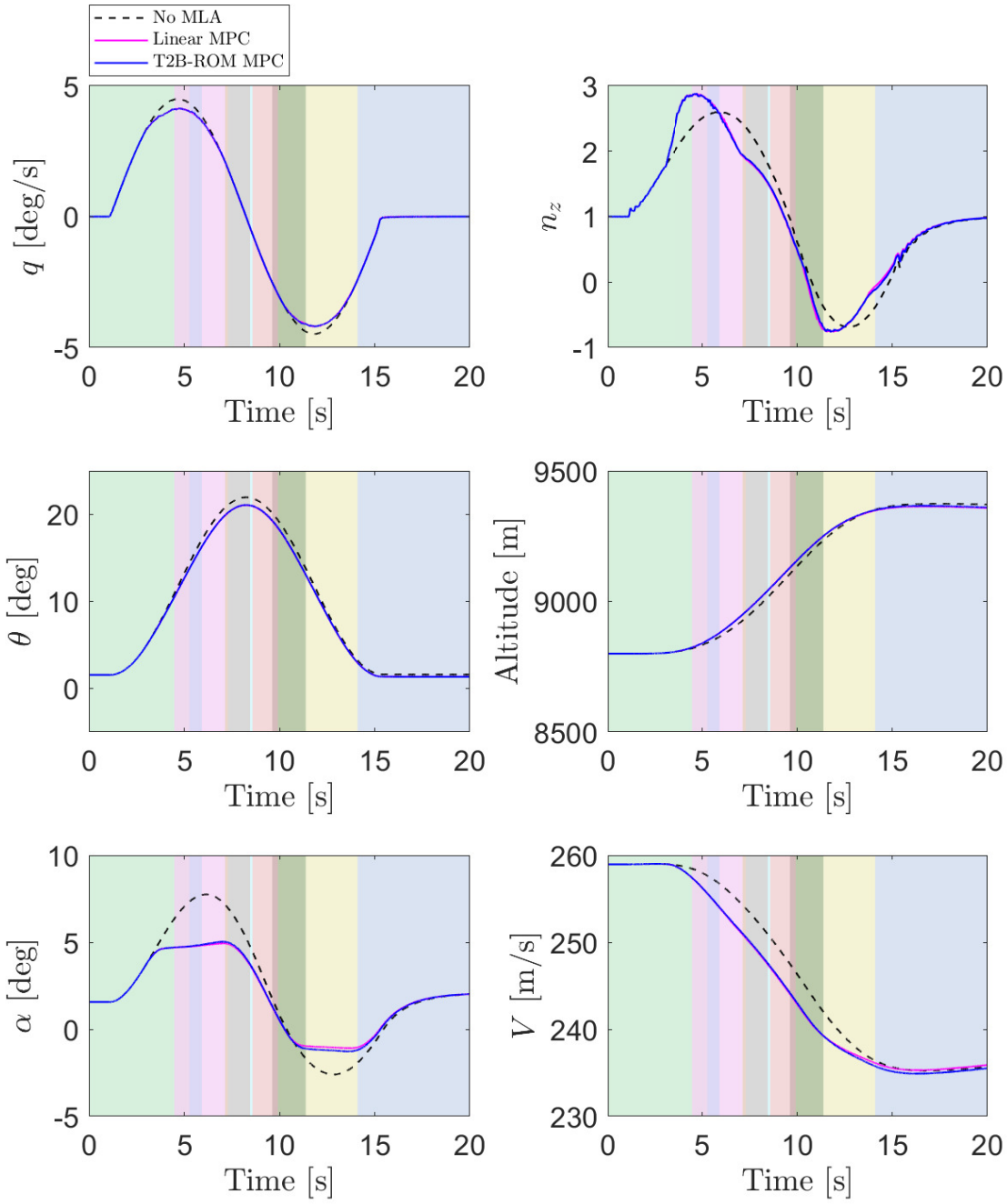

Figure 4.22: Rigid body outputs of XRF1-HARW using configuration 1 of control surfaces.

Table 4.10: MPC step computation time when using the T2B model.

	Max. [s]	**Avg.** [s]
Linear MPC	0.3082	0.0319
T2B-ROM MPC	21.99	7.762
Augmentation factor	74.4	243

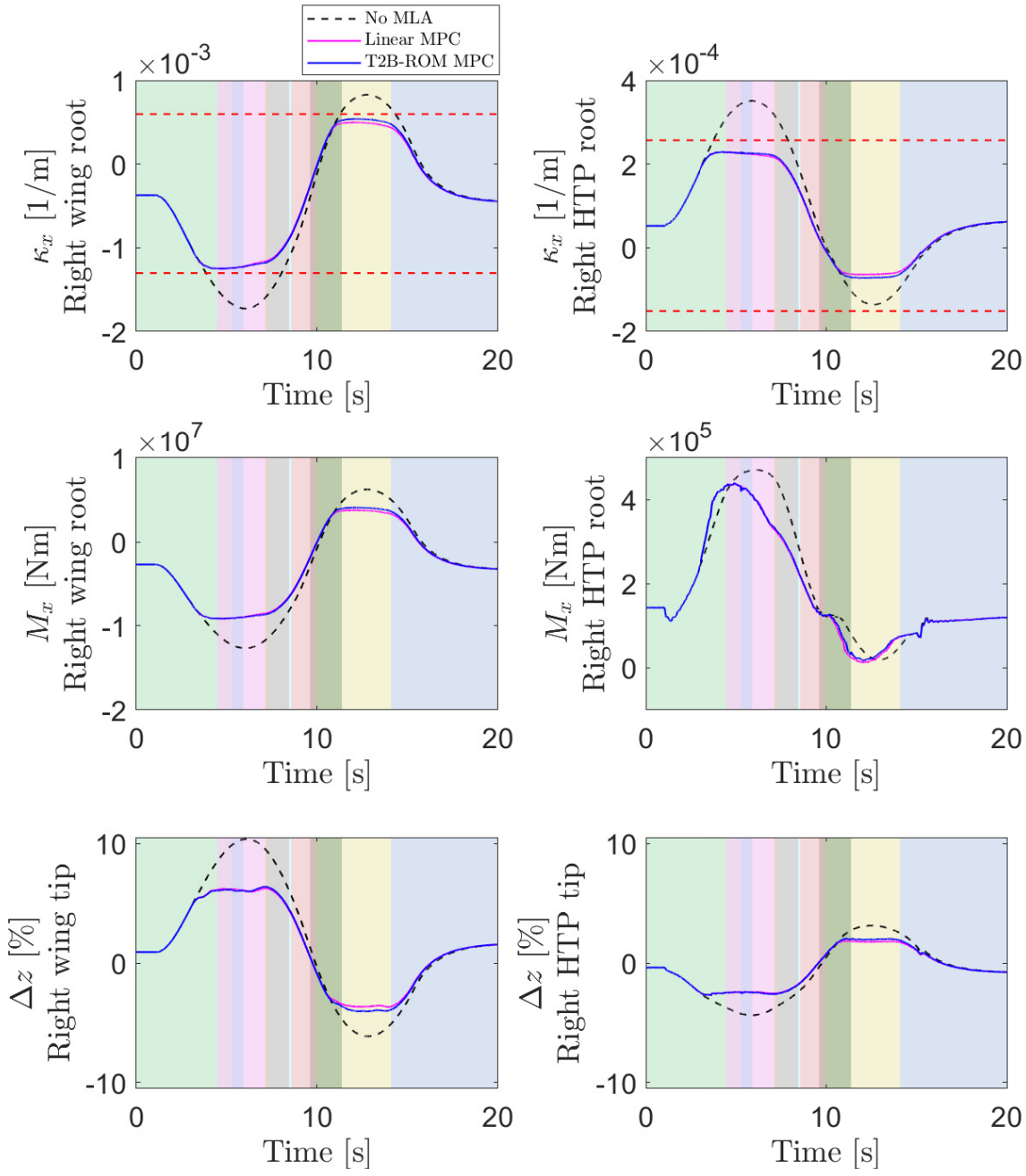

Figure 4.23: Structural outputs of XRF1-HARW using configuration 1 of control surfaces. κ_x: out-of-plane curvature, M_x: out-of-plane moment, Δz: vertical deflection.

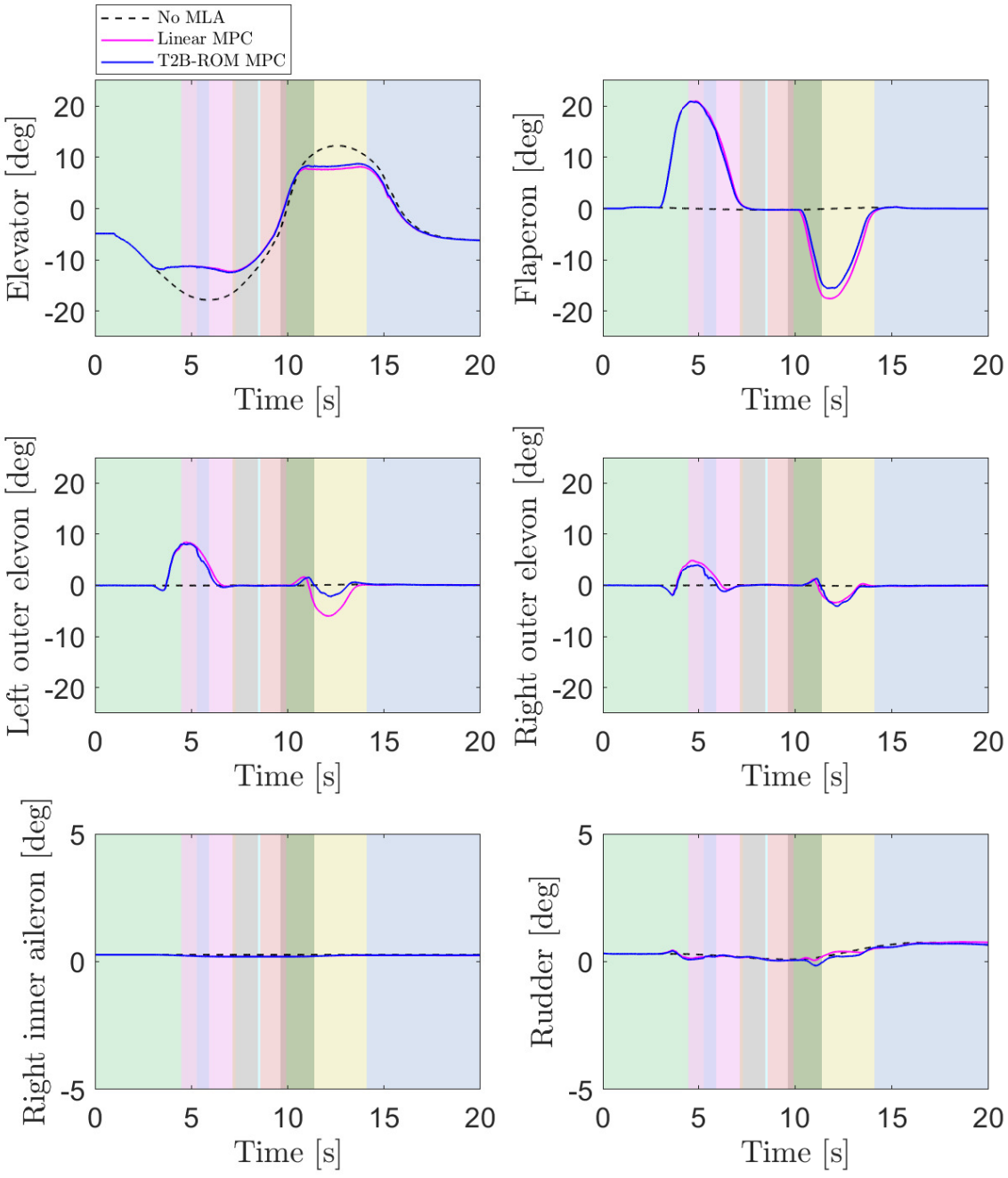

Figure 4.24: Control inputs applied to XRF1-HARW using configuration 1 of control surfaces.

CHAPTER 5

Gust Load Alleviation

Atmospheric disturbances are a problem in aircraft operation due to, among other things, the undesirable dynamic loads generated that may result in reduction of the airframe structural life or even catastrophic failure. To overcome these undesirable effects without the need of structural reinforcements, gust load alleviation (GLA) systems can be incorporated into the automatic flight control system (FCS). The main objective of GLA systems is to attenuate loads caused by encounters with gusts or turbulence by using active controls. GLA systems can reduce loads due to airframe flexibility, decrease levels of acceleration at particular aircraft stations, and improve flying qualities. Consequently, fatigue life is increased, lightweight high-aspect-ratio designs are allowed, fuel expenditure is reduced, and flight comfort is enhanced. Furthermore, GLA systems can improve the airworthiness of the aircraft design in order comply with the standards specified by regulatory agencies.

5.1 GLA System Requirements

The main requirements of GLA systems for large transport flexible aircraft are:

1. Response time after gust detection at the aircraft nose should be at most 50 ms.
   This corresponds to the average time between the initial alpha probe measurements at the aircraft nose until the gust reaches the wing.

2. Actuator rates should be limited to 45 deg/s.

3. Maximum aileron deflection to perform GLA should not exceed 15 deg.
   Aileron deflection combining FCS and GLA system inputs should be at most 45 deg.

4. GLA system should not engage at intended changes in the incidence angle.
   GLA system should not interfere with the aircraft maneuverability.

5. Load attenuation between 20% and 33%.
   Even though a reduction above 33% is possible, any attenuation above 33% cannot be accounted for in structural design, since the structure itself should be able to sustain a certain load profile without GLA systems.

6. Altitude deviation should be less than 250 ft (76.8 m).
   FCS should generate a compensatory control input to counteract the pitching moment due to the GLA actuation.

7. Dynamic actuation of ailerons should be minimized.
   Moving the ailerons up and down excessively can potentially cause fatigue issues and excite structural modes.

8. GLA system should not be activated at medium or low turbulence.

9. GLA system should not engage if alpha correction is less than 1 deg.

10. Design should take into consideration different mass cases, center of gravity positions, fuel and payload re-partitions, and flight conditions.

11. Passenger comfort should not be compromised.
    Even though the structural integrity is the priority in the design of GLA systems, small load factor should be enforced in to order to preserve passenger comfort throughout the flight.

12. Failure mode handling.
    GLA system should be robust against actuator and sensor failures.

These requirements apply to the aircraft category CS25 as defined in the European Union Aviation Safety Agency [7].

Similar to the MLA system design presented in Chapter 4, the objective of the GLA system is to reduce the magnitude of peak loads on critical station of the aircraft.

5.2 Gust Models

During flight missions, aircraft constantly encounter atmospheric disturbances that affect their motion, such as gusts or turbulence. In general, when the wind profile is continuous, the atmospheric disturbance is referred to as turbulence, whereas when it consists of more or less isolated pulses, the single pulse is referred to as a gust. Gust loads are ordinarily considered to be the result of a change in angle of attack due to a component of gust velocity

at right angles to the flight path. The net change in angle of attack of the vehicle depends on both the wind velocity and the airplane motion induced by the gust as the aircraft proceeds through the gust profile [129].

Design loads for encounters with gusts are a combination of the steady level 1-g flight loads, and the gust incremental loads including the dynamic response of the aircraft. The steady 1-g flight loads can be realistically defined by external parameters such as speed, altitude, weight and fuel load, using static aeroelastic methods [7]. Figure 5.1 shows the basic elements taken into consideration when performing a gust response analysis.

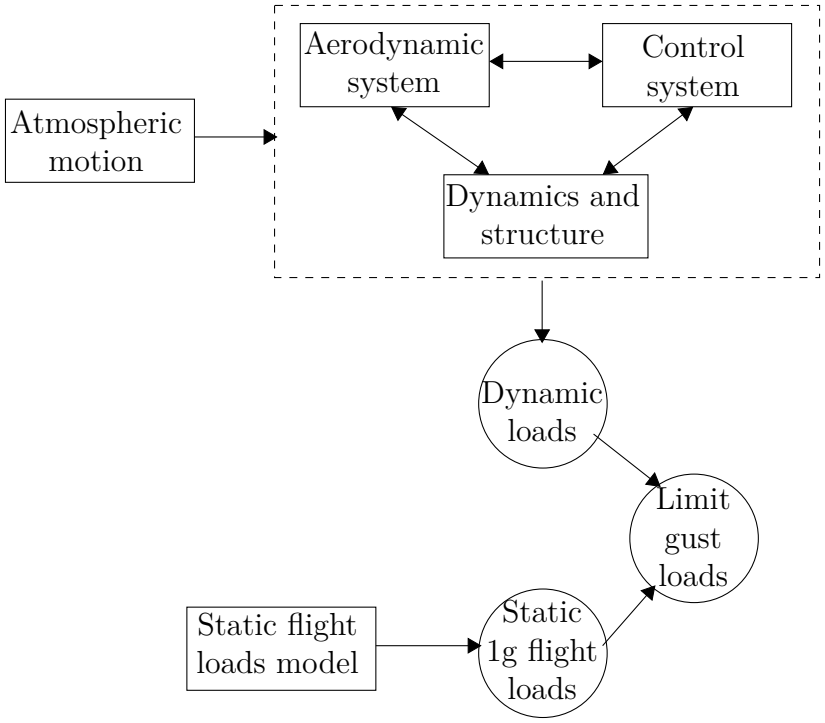

Figure 5.1: Basic elements of the gust response analysis [7].

The atmospheric disturbance encountered by an aircraft can have different sources. The first type is convective turbulence, the most common source of severe turbulence, which occurs in and around clouds, especially thunderstorms and cumulus clouds [37, 129]. The other main type of turbulence, usually less severe, occurs in clear air and can have several causes. These include wind shear at altitude due to flight through or near the jet stream, wind shear close to the ground caused by the Earth's boundary layer, wind flowing over mountains, and updrafts caused by heating of the air [129].

Some assumptions considered for gust models for loads include:

- The gust field velocity is only space dependent;

- Isotropic atmosphere;
- The gust velocity is one-dimensional (cylindrical).

There are two common methods for modeling atmospheric disturbances for aircraft design and simulation, including the design of GLA systems. These are the discrete method, where the gust is modeled using a one-minus-cosine profile, and the continuous method, where the gust is modeled as a stochastic process with a known power spectral density [37].

The gust load requirements are presented in the Certification Specifications for Large Aeroplanes (CS25) [7] in the following sections:

- CS25.341 (completed by AMC 25.341)
  - 25.341 (a): Discrete Gust Design Criteria
  - 25.341 (b): Continuous Turbulence Design Criteria
  - 25.341 (c): Supplementary Gust Conditions for Wing Mounted Engines
    - 25.345 c1: Round-the-clock Gust
    - 25.345 c1: Multi-axis Gust
- CS 25.335 (d): Design speed for maximum gust intensity
- CS 25.343 (b) (1) (iii): Design fuel and oil loads
- CS 25.349 (b) Unsymmetrical gust.

The next Sections describe the discrete and continuous gust models. These models have been implemented in the UM/NAST Gust module.

5.2.1 Discrete Model

The discrete gust idealization provides a representation of individual turbulence as a single or repeating disturbance with a one-minus-cosine model. Discrete gusts are generally considered deterministic, have simple forms, and are typically treated in the time domain [39]. For the purpose of obtaining static gust loads, CS 25.341 specifies the one-minus-cosine shape, which is given by the following expression :

$$U_{gust} = \frac{U_{\text{ds}}}{2}\left[1 - \cos\left(\frac{\pi S}{H}\right)\right], \tag{5.1}$$

where U_{ds} is the design gust airspeed amplitude, H is the gust length, and S, $0 \leq S \leq 2H$ is the gust penetration distance, as shown in Fig 5.2. The maximum velocity for a discrete

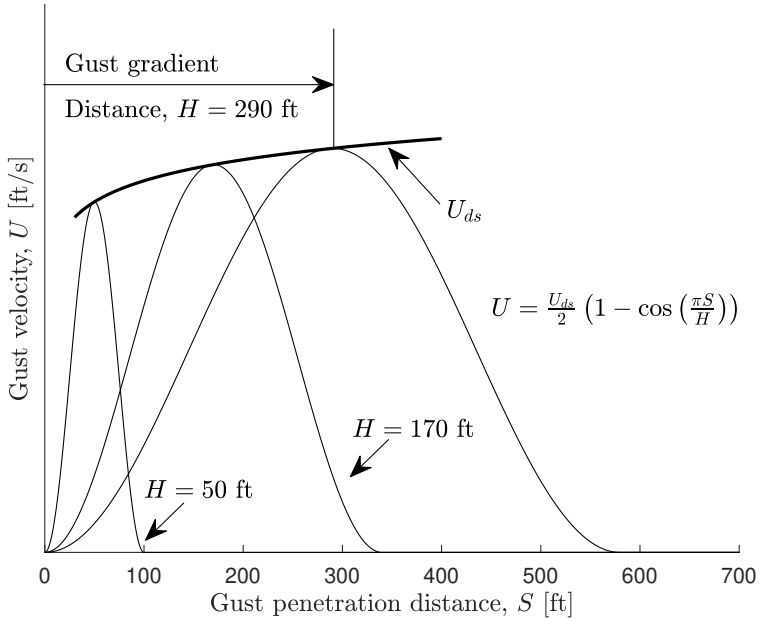

Figure 5.2: One-minus-cosine gust model [7].

gust is calculated using a reference gust velocity, U_{ref}, a flight profile alleviation factor, F_g, and an expression which modifies the maximum velocity as a function of the gust gradient distance, H. The description in CS 25.341 [7] for each of these parameters are shown below.

- Reference gust velocity, U_{ref}: Derived effective gust velocities representing gusts occurring once in 70,000 flight hours are the basis for design gust velocities. These reference velocities are specified as a function of altitude in CS 25.341(a)(5) and are given in terms of feet per second equivalent airspeed for a gust gradient distance, H, of 107 m (350 ft).

- Flight profile alleviation factor, F_g: The reference gust velocity, U_{ref}, is a measure of turbulence intensity as a function of altitude. In defining the value of U_{ref} at each altitude, it is assumed that the aircraft is flown 100% of the time at that altitude. The factor F_g is then applied to account for the expected service experience in terms of the probability of the aeroplane flying at any given altitude within its certification altitude range. F_g is a minimum value at sea level, linearly increasing to 1.0 at the certified maximum altitude. The expression for F_g is given in CS 25.341(a)(6) by:

$$F_g = 0.5(F_{gz} + F_{gm}), \tag{5.2}$$

where

$$F_{gz} = 1 - \frac{Z_{mo}}{76200}, \tag{5.3}$$

$$F_{gm} = \sqrt{R_2 \tan\left(\frac{\pi R_1}{4}\right)}, \tag{5.4}$$

$$R_1 = \frac{\text{Maximum landing weight}}{\text{Maximum take-off weight}}, \tag{5.5}$$

$$R_2 = \frac{\text{Maximum zero-fuel weight}}{\text{Maximum take-off weight}}, \tag{5.6}$$

$$Z_{mo} = \text{maximum operating altitude in meters.} \tag{5.7}$$

- Gust gradient distance, H: The gust gradient distance is that distance over which the gust velocity increases to a maximum value. Its value is specified as ranging from 9.1 to 107 m (30 to 350 ft).

- Design gust airspeed, U_{ds}: Maximum velocities for design gusts are proportional to the sixth root of the gust gradient distance, H. The maximum gust velocity for a given gust is then defined as:

$$U_{\text{ds}} = U_{\text{ref}} F_g \left(\frac{H}{350}\right)^{1/6}. \tag{5.8}$$

5.2.2 Continuous Model

The turbulence model idealization is a stationary Gaussian random process, i.e., it is considered to be of infinite duration and its statistical properties have the same Gaussian distribution wherever it may be sampled. Such idealization is more realistic than discrete-gust models, especially because of the proper superposition of very short gradient gusts that excite the various elastic modes with the longer gradient gusts that give the largest rigid-body airplane loads. The stochastic idealization allows the determination of the statistical characteristics of the airplane response, such as accelerations and loads, directly from the statistical description of the gust velocity profile using power-spectral analysis [129].

This method of turbulence modeling is based on the notion of power spectral density, which gives one knowledge of how the mean squared value of a signal is distributed as a function of frequency [37]. The von Kármán model is prescribed by the CS25.341 [7], with power spectral density of:

$$\Phi(\Omega) = \frac{L}{\pi} \frac{1 + \frac{8}{3}(1.339 L\Omega)^2}{[1 + (1.339 L\Omega)^2]^{11/6}} \tag{5.9}$$

where Ω is the reduced frequency ($\Omega = \omega/V,\ V$ =airspeed) and L is the scale of turbulence. Figure 5.3 shows a plot of the power spectral density for $L = 2500$ ft. For the von Kármán spectrum, the desired filter can be approximated by [129]:

$$G_{vk}(s) = \sqrt{\frac{\tau}{\pi}} \frac{(1 + 2.187\tau s)(1 + 0.1833\tau s)(1 + 0.021\tau s)}{(1 + 1.339\tau s)(1 + 1.118\tau s)(1 + 0.1277\tau s)(1 + 0.0146\tau s)}, \tag{5.10}$$

where $\tau = L/U_x$ is a time constant, and U_x is the forward velocity component of the aircraft.

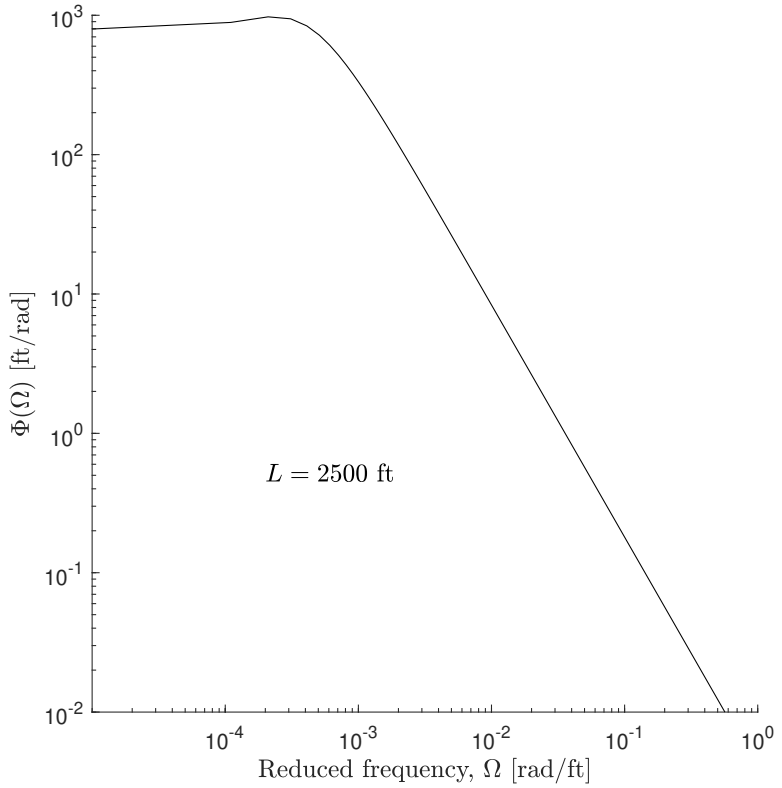

Figure 5.3: Von Kármán power spectral density for vertical-lateral gust; L = 2500 ft [7].

The design gust velocity, U_σ, applied in the analysis is given by the product of the reference gust velocity, $U_{\sigma\text{ref}}$, and the profile alleviation factor, F_g, as follows:

$$U_\sigma = U_{\sigma\text{ref}} F_g, \tag{5.11}$$

where $U_{\sigma\text{ref}}$ is specified in CS 25.341(b)(3) as varying linearly with altitude from 27.43 m/s at sea level to 24.08 m/s at 7315 m (24000 ft) and is then constant at 24.08 m/s up to the altitude of 18288 m (60000 ft) [7]. U_σ can be interpreted as the root mean square (RMS) value

of the turbulence at each altitude, factorized by a number fixing the accepted probability of exceeding the design turbulence in the aircraft lifetime.

Alternatively, the von Kármán spectrum can be defined in two dimensions as follows [130]:

$$\Phi_2(\Omega_x, \Omega_y) = \frac{4U_\sigma^2(1.339L)^4}{9\pi} \frac{\Omega_x^2 + \Omega_y^2}{\left[1 + (1.339L)^2(\Omega_x^2 + \Omega_y^2)\right]^{7/3}}, \tag{5.12}$$

where Ω_x and Ω_y are, respectively, the reduced frequencies in the longitudinal and lateral directions. References [131] and [132] present a numerical method to create a realization of this turbulence based on its power spectral density, which was used in the UM/NAST implementation.

5.3 GLA System Design

From a control design point of view, MLA is more aligned with signal tracking problems, whereas GLA is more aligned with disturbance rejection problems. The fundamental difference is that, in the former, the signal is generated internally, either from pilot or guidance system input, and can be manipulated before being fed into the closed loop system. On the other hand, in the latter, the disturbance is originated from external sources and its magnitude is usually unknown and cannot be changed before hitting the plant.

Nonetheless, MLA and GLA systems share similar objectives, namely, to maintain loads on the aircraft within the prescribed safety limits. Hence, the same structure of the MLA system architectures presented in Chapter 4 can be preserved, and some adjustments can be made to enable them to handle gust disturbances. In doing so, the resulting control system will combine the MLA and GLA functionalities with the same objective, therefore potentially simplifying the design and integration processes.

The load constraints can be transformed into curvature constraints for shape control, similar to what was presented in Section 4.2.1. The procedure described in that Section to choose the critical stations where the curvature constrains will be enforced is still applicable to GLA design. Similarly, the selection of control surfaces for load alleviation presented in Section 4.2.2 can also be used in here.

One of the critical aspects in the GLA design is the response time of the GLA system after the gust disturbance detection. Conventional GLA systems utilize α-probes mounted on the aircraft nose to provide measurements of angle of attack during flight. Changes in such parameter can be used to detect gust disturbances after they have reached the aircraft, but before reaching the wings. More recent designs have explored the use of LIDAR sensors, also

mounted on the aircraft nose, to anticipate the gust disturbance before it hits the aircraft, thus allowing longer time margins to compute and apply the load alleviation control.

The two load alleviation system architectures presented in section 3.2 are modified by the addition of a LIDAR sensor, as shown in Fig. 5.4 and Fig. 5.5 (LA governor architecture). In both architectures, the LIDAR sensors, as described in Section 5.3.2, can enable feed-forward control actions by integrating the gust preview into the prediction model. A gust reconstruction algorithm can also be integrated into the system to estimate the components of the wind velocity at different points on the aircraft (see discussion in Section 5.3.3).

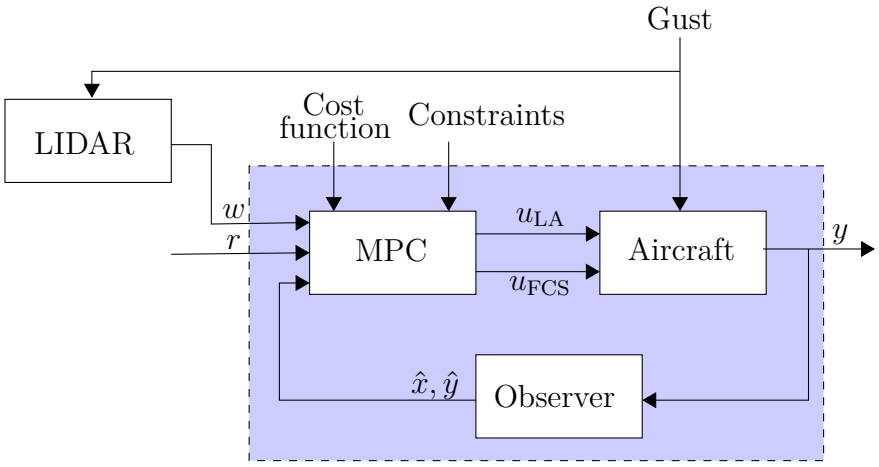

Figure 5.4: MPC architecture with LIDAR.

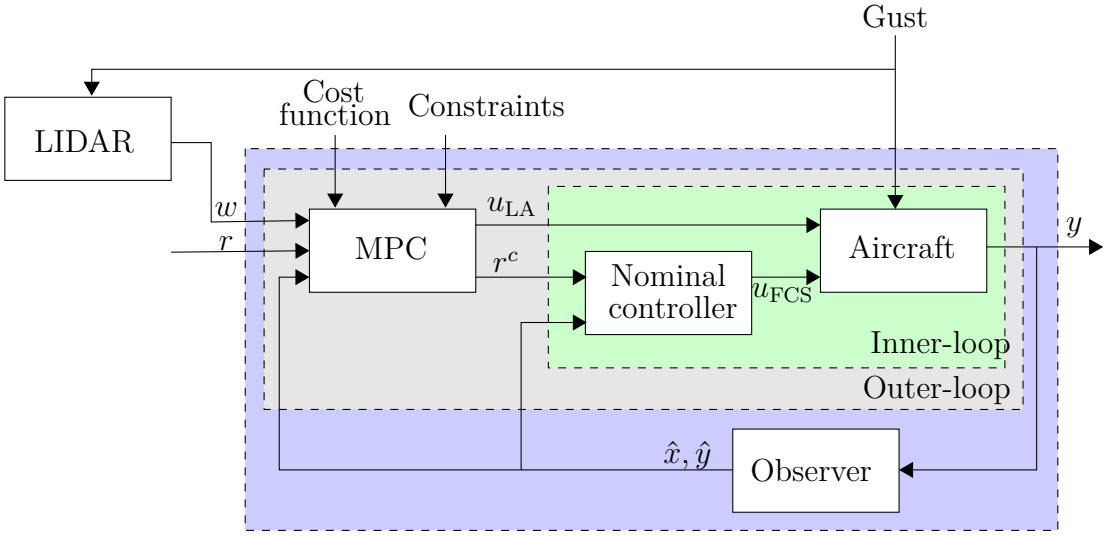

Figure 5.5: LA governor architecture with LIDAR.

In terms of wind velocity, the most important component for loads is the vertical compo-

nent, since this component has the greatest influence on angle of attack, consequently on the local lift. The lateral component is only secondary for load alleviation purposes and finally the longitudinal component has an effect on the lift through a change of the airspeed, but this effect is usually negligible [133].

The following shows how the control architectures considered in here could satisfy the requirements presented in Section 5.1.

1. Response time after gust detection at the aircraft nose should be at most 50 ms.
   The addition of LIDAR sensors to the load alleviation system will potentially provide sufficient time margins to compute the control action to reduce loads before the gust disturbance hits the vehicle. In fact, typical lengths of LIDAR measurements reach up to to 300 m ahead of the aircraft nose, i.e., approximately 1.2s before the gust encounter at cruise speed. The proposed sampling rate of the MPC controller is 50 Hz, while the maximum actuator deflection can be achieved in 0.33 s.

2. Actuator rates should be limited to 45 deg/s.
   A constraint can be added to the MPC problem on the upper and lower bounds on the control deflection rate.

3. Maximum aileron deflection to perform GLA should not exceed 15 deg
   A constraint can be added to MPC problem on the upper and lower bounds on the control deflection. Since the u_{LA} control effectors are primarily assigned to perform load alleviation, such restriction should not impact the FCS performance at attitude control.

4. GLA system should not engage at intended changes in the incidence angle
   The LIDAR sensor along with a high-pass filter should avoid the activation of the GLA system during maneuvers.

5. Load attenuation between 20% and 33%.
   Load constraints can be directly incorporated into the MPC design and be enforced pointwise-in-time in order to keep them within the desired bounds.

6. Altitude deviation should be less than 250 ft (76.8 m).
   As discussed in Section 4.2, this can be achieved by the proper selection of gains in the controllers.

7. Dynamic actuation of ailerons should be minimized.
   The rate o deflection of the ailerons, as well as their magnitude, are directly accounted for in the cost function of the MPC problem on both architectures.

8. GLA system should not be activated at medium or low turbulence.
   The LIDAR along with the high pass filter will wash out small disturbances in order to avoid excessive and superfluous GLA actuation.

9. GLA system should not engage if alpha correction is less than 1 deg.
   A logic could be added into the MPC problem to activate the load constraints only when the said threshold is surpassed. However, since the MPC controller only performs GLA if there is a danger of violating constraints, this requirement is directly satisfied by the control architectures considered in here.

10. Design should take into consideration different mass cases, center of gravity positions, fuel and payload re-partitions, and flight conditions.
    The scenario-based MPC presented in Section 3.4 and illustrated in Section 4.3.3 can be used to design a single controller that can handle multiple aircraft configurations.

11. Passenger comfort should not be compromised.
    Constraints on load factor at different locations on the fuselage can be added to he MPC problem.

12. Failure mode handling.
    As discussed in Section 4.2, redundancy of actuators and sensors is the standard approach to handle failures, and it is indirectly taken into consideration here by the selection of these components. A systematic way to incorporate this objective into MLA design is not addressed in this work.

5.3.1 Feedforward Control

LIDAR sensors can measure turbulence ahead of the aircraft. Hence, these sensors can provide preview information on future gust disturbances that would allow the GLA system to compute feedforward control actions to engage the control effectors before the first gust hit.

To introduce gust preview into MPC design, firstly the prediction model should be changed to make use of information regarding future gust disturbances $\tilde{w}_g \in \mathbb{R}^{(N_w+1)n_w}$ provided by LIDAR sensors over a horizon N_w. Hence, the nonlinear prediction model in Eq. 3.1 becomes

$$x^+ = f_s(x, u, \tilde{w}_g), \tag{5.13}$$

and the linear prediction model in Eq. 3.17 becomes

$$f_s(x, u, \tilde{w}) = A^d \Delta x + B^d \Delta u + \tilde{B}_w^d \tilde{w}_g. \tag{5.14}$$

where $\tilde{B}_w^d \in \mathbb{R}^{n_x \times (N_w+1) n_w}$ is defined as

$$\tilde{B}_w^d = \begin{bmatrix} B_w^d & 0 & \cdots & 0 \end{bmatrix} \tag{5.15}$$

and B_w^d is the discrete-time version of gust influence matrix B_w defined in Eq. 2.39.

The OCP formulation for the MPC architecture presented in Section 3.2.1 (Eq. 3.54) now becomes:

$$V_N^*(\hat{x}) = \min_{\delta\mathbf{x}, \delta\mathbf{u}, \boldsymbol{\varepsilon}_s} ||e_N||_{P_f}^2 + \sum_{k=0}^{N-1} ||e_k||_{Q_e}^2 + ||\delta u_k||_R^2 + ||u_{\mathrm{LA},k}||_{R_{\mathrm{LA}}}^2 + \mu \varepsilon_{s,k}^2, \tag{5.16}$$

$$\text{s.t.} \quad \delta x_{k+1} = f_s(x_{k+1}, u_{k+1}, \tilde{w}_{g,k+1}) - f_s(x_k, u_k, \tilde{w}_{g,k}) \quad \text{for} \quad k \in \mathbb{Z}_{[0,N-1]} \tag{5.17}$$

$$e_k = r - S^{\mathrm{track}} g(x_k, u_k) \quad \text{for} \quad k \in \mathbb{Z}_{[0,N]} \tag{5.18}$$

$$\tilde{w}_{g,k+1} = A_w \tilde{w}_{g,k} \quad \text{for} \quad k \in \mathbb{Z}_{[0,N_w]} \tag{5.19}$$

$$u_{k+1} = u_k + \delta u_k \quad \text{for} \quad k \in \mathbb{Z}_{[0,N-1]} \tag{5.20}$$

$$x_{k+1} = x_k + \delta x_k \quad \text{for} \quad k \in \mathbb{Z}_{[0,N-1]} \tag{5.21}$$

$$x_0 = \hat{x}, \tag{5.22}$$

$$(\mathbf{x}, \mathbf{u}) \in \mathcal{F}_N^{\varepsilon} \tag{5.23}$$

$$\boldsymbol{\varepsilon}_s \succeq 0. \tag{5.24}$$

The OCP for the LA governor architecture presented in Section 3.2.2 (Eq. 3.76) is also modified in a similar fashion:

$$V_N^*(\hat{x}, \hat{y}) = \min_{\mathbf{x}, \delta\mathbf{u}^r, \boldsymbol{\varepsilon}_s} \sum_{k=0}^{N-1} ||r_k^c - r||_{Q_c}^2 + ||\delta u_k^r||_R^2 + ||u_{\mathrm{LA},k}||_{R_{\mathrm{LA}}}^2 + \mu \varepsilon_{s,k}^2, \tag{5.25}$$

$$\text{s.t.} \quad x_{k+1} = f_s(x, u_{\mathrm{LQI}}(\hat{x}, \hat{y}, r, u_{\mathrm{LA},k}), \tilde{w}_{g,k}) \quad \text{for} \quad k \in \mathbb{Z}_{[0,N-1]} \tag{5.26}$$

$$\tilde{w}_{g,k+1} = A_w \tilde{w}_{g,k} \quad \text{for} \quad k \in \mathbb{Z}_{[0,N_w]} \tag{5.27}$$

$$u_{k+1}^r = u_k^r + \delta u_k^r \quad \text{for} \quad k \in \mathbb{Z}_{[0,N-1]} \tag{5.28}$$

$$x_0 = \hat{x}, \tag{5.29}$$

$$(\mathbf{x}, \mathbf{u}) \in \mathcal{F}_N^{\varepsilon} \tag{5.30}$$

$$\boldsymbol{\varepsilon}_s \succeq 0, \tag{5.31}$$

Note the inclusion of Eqs. 5.19 and 5.27 in these modified formulations. In here, $\tilde{w}_k$

represents the future disturbance w_k values over a time window of N_w steps. For $k > N_w$, we consider that $w_k = w_{N_w}$. To incorporate such a disturbance preview into the MPC design, the auxiliary model in Eq. 5.19 and 5.27 are added to the optimization problem to work as a shift register, in which

$$A_w = \begin{bmatrix} 0 & I & 0 & \cdots & 0 \\ 0 & 0 & I & \cdots & 0 \\ \vdots & \vdots & \vdots & \ddots & \vdots \\ 0 & 0 & 0 & \cdots & I \\ 0 & 0 & 0 & \cdots & I \end{bmatrix} \in \mathbb{R}^{(N_w+1)n_w \times (N_w+1)n_w}, \tag{5.32}$$

generating the preview sequence

$$\bar{w_0} = \begin{bmatrix} w_0 \\ w_1 \\ \vdots \\ w_{N_w-1} \\ w_{N_w} \end{bmatrix}, \quad \bar{w_1} = \begin{bmatrix} w_1 \\ w_2 \\ \vdots \\ w_{N_w} \\ w_{N_w} \end{bmatrix}, \quad \bar{w_2} = \begin{bmatrix} w_2 \\ w_3 \\ \vdots \\ w_{N_w} \\ w_{N_w} \end{bmatrix}, \quad \text{etc.} \tag{5.33}$$

The LIDAR measurements can also be used to enhance the state estimation in the Kalman filter when gust disturbances are present.

5.3.2 Sensors for GLA

The section presents the typical sensors used to detect gust disturbances. In addition to the sensors presented here, the ones described in Section 4.2.3 may also be considered in the load alleviation system design.

5.3.2.1 Alpha Probes

Alpha probes are usually mounted on the aircraft nose to provide measurements of angle of attack during flight. Changes in such parameter can be used to detect gust disturbances after they have reached the aircraft. Classical approaches for GLA systems (e.g., Ref. [41]) utilize alpha probe measurements to activate the control effectors responsible for load alleviation. To avoid unnecessary actuation of these effectors, changes in the angle of attack due to maneuvers or for constant non-turbulent wind should not activate the GLA system.

5.3.2.2 Inertial Sensors

Inertial sensors can be used to detect local changes in either the attitude or acceleration at different stations on the flexible aircraft due to external disturbances. These sensors are reactive, that is, they detect disturbances after they have reached the aircraft and perturbed its states.

5.3.2.3 LIDAR Sensors

LIDAR sensors use the Doppler effect (wave frequency shift due to the relative motion between the emitter and receiver) to measure turbulence ahead of the aircraft. Hence, these sensor can provide preview information on future gust disturbances that would allow the GLA system to compute feedforward control actions to engage the control effectors before the first gust hit.

As explained in Ref. [133], the LIDAR sensor emits a short pulse of laser light, which illuminates a specific area ahead of the aircraft. The pulse of light travels in the laser direction and at each location a tiny fraction of this pulse is scattered by air or aerosol molecules. The scattering occurs in a wide range of directions and part of the scattered light goes back to the LIDAR sensor. The frequency of the light that is scattered back to the LIDAR sensor is then compared against the one of the light that was emitted. A shift toward higher frequencies indicates that the sensor and the molecules that scattered the light back were moving toward each other. Otherwise, if they are moving away from each other, then the wave will be shifted towards lower frequencies. Figure 5.6 shows a schematic of a LIDAR sensor.

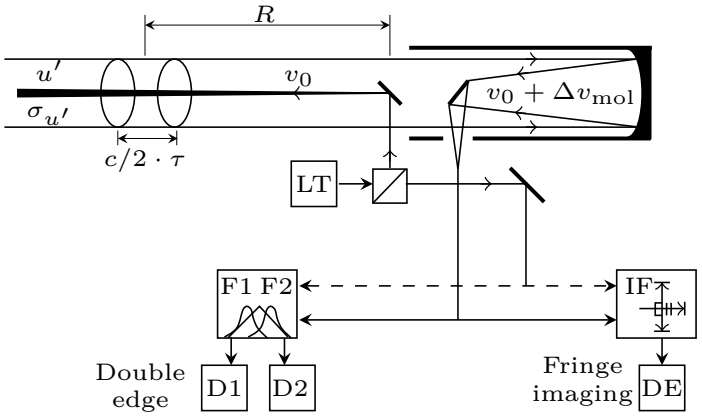

Figure 5.6: LIDAR sensor. LT: laser transmitter; F1 and F2: spectral filters; IF: interferometer; DE: line detector; D1 and D2: detectors [8].

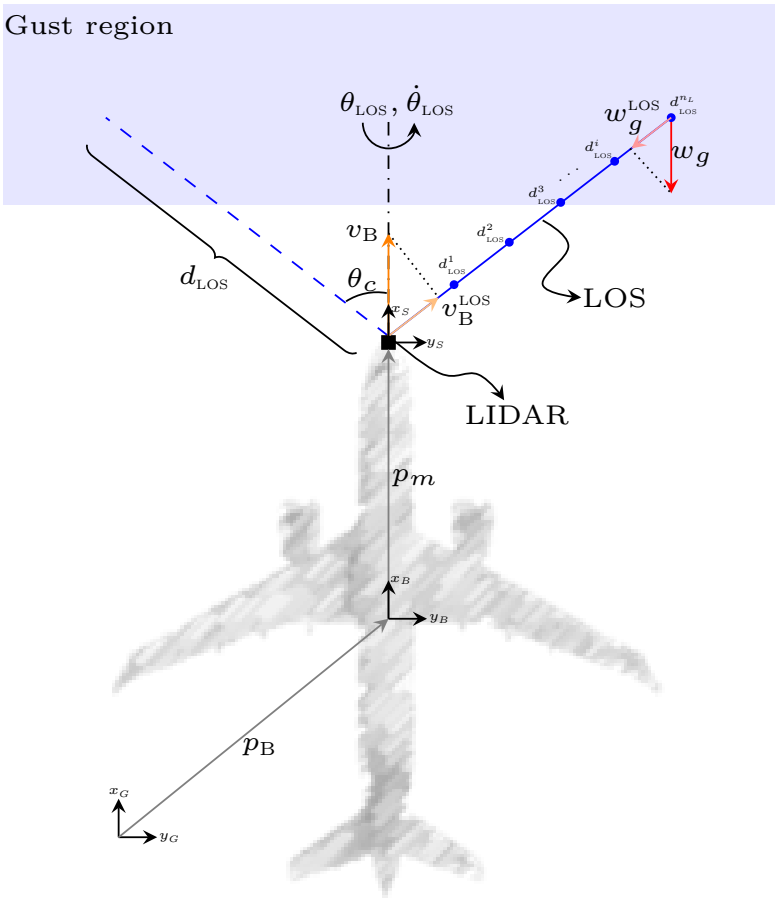

Figure 5.7: LIDAR measurement.

When using Doppler LIDAR sensors, only the relative wind component in the direction of the laser beam is measured, usually in directions that are collinear with the flight path. Therefore, the sensor readings are measuring the basically the true airspeed and not the vertical and lateral components. A way to estimate or reconstruct the missing information is to measure the wind at locations with various vertical and lateral offsets with respect to the airplane flight path. The resulting line-of-sight (LOS) directions are not collinear anymore and the analysis of the differences between the different sensor readings allows to estimate the lateral and vertical components of the wind [133].

Based on this idea, a LIDAR sensor was implemented in UM/NAST Sensors module. The sensor consists of a rotating laser beam that scans the area ahead of the aircraft. The LOS rotation forms a cone with angle θ_c, as shown in Fig. 5.7. The typical LOS length (d_{LOS}) of current LIDAR sensors is between 60 and 300 m [133]. Along the LOS, n_L measurements are taken at distances $d^i_{\text{LOS}}, i \in \mathbb{Z}_{[1,n_L]}$. For a constant rotation frequency $\dot{\theta}_{\text{LOS}}$, the position of ith measuremnt in the sensor frame is given by:

$$p_s^i(t) = C^{\text{LOS}}(t) \begin{bmatrix} d^i_{\text{LOS}} \\ 0 \\ 0 \end{bmatrix}, \tag{5.34}$$

where,

$$C^{\text{LOS}}(t) = \begin{bmatrix} \cos(\theta_c) & 0 & \sin(\theta_c) \\ \sin(\theta_c)\sin(\theta_{\text{LOS}}(t)) & \cos(\theta_{\text{LOS}}(t)) & -\cos(\theta_c)\sin(\theta_{\text{LOS}}(t)) \\ -\sin(\theta_c)\cos(\theta_{\text{LOS}}(t)) & \sin(\theta_{\text{LOS}}(t)) & \cos(\theta_c)\cos(\theta_{\text{LOS}}(t)) \end{bmatrix}, \tag{5.35}$$

$$\theta_{\text{LOS}}(t) = \theta^0_{\text{LOS}} + \dot{\theta}_{\text{LOS}} t, \tag{5.36}$$

t is the current time and θ^0_{LOS} is the initial LOS angular position. The LIDAR sensor is attached to a flexible structure, therefore he sensor frame can rotate with respect to the body frame when the structural member deforms. Therefore, the position of the ith measurement in the ground frame is given by:

$$p^i_G(t) = p_B(t) + (C^{BG}(t))^T p_m(t) + C^{GS}(t) p^i_s(t) \tag{5.37}$$

where p_B is the inertial position of the aircraft in the ground frame, p_m is the position of the sensor in the body frame, C^{BG} is the rotation matrix from the ground to the body frame, and C^{GS} is the rotation matrix from the sensor to the ground frame. The position p_m can be obtained from the h_w vector in Eq, 2.3, while p_B is a state of the aircraft. If p^i_G is inside the gust region of influence, then the LIDAR will measure the gust disturbance. Otherwise, it returns zero.

The LIDAR measurement returns a scalar with the magnitude of the relative gust velocity along the LOS. If w^i_g is the gust velocity vector at a given position inside the gust field, then its projection onto the LOS is given by:

$$w^{i,\text{LOS}}_g(t) = \left((C^{GS}(t))^T w^i_g(t) \cdot \hat{p}_s(t)\right) \hat{p}_s(t). \tag{5.38}$$

Similarly, the projection of the aircraft velocity v_B onto the LOS is given by:

$$v^{\text{LOS}}_B(t) = \left((C^{BS}(t))^T v_B(t) \cdot \hat{p}_s(t)\right) \hat{p}_s(t), \tag{5.39}$$

where $\hat{p}_s$ is a unit vector in the sensor frame along the LOS:

$$\hat{p}_s(t) = \frac{p^i_s(t)}{||p^i_s(t)||}. \tag{5.40}$$

The measurement at a given time t is then given by:

$$m_i^{\mathrm{L}}(t) = (w_g^{i,\mathrm{LOS}}(t) - v_B^{\mathrm{LOS}}(t)) \cdot \hat{p}_s(t), \quad \text{for } i \in \mathbb{Z}_{[1,n_L]}. \tag{5.41}$$

5.3.3 Gust Field Reconstruction

As suggested by Fezans et al. [133], it is advantageous to reconstruct the complete wind field from a set of LOS wind measurements. Otherwise, a set of different measurements without wind field reconstruction may not account for the fact that these measurements were not made simultaneously and, therefore, they are not located at the same distance from the aircraft. In [133], algorithm is proposed to determine the wind field that the best fits the considered measurements. A free-form model structure is used, in which the gust/turbulence wind field is represented by a mesh where a velocity vector is set for each node of the mesh. Any wind field can in principle be represented by such a mesh, as long as enough nodes are taken.

An implementation of the gust field reconstruction using a free-form model was created for UM/NAST. In this implementation, the LIDAR measurements $m_i^{\mathrm{L}}(t)$ are saved in a buffer of size n_b In addition to these measurements, the following metadata is also saved for each measurement:

- The aircraft orientation and position in the ground frame;
- The aircraft velocity;
- The position and orientation of the LIDAR with respect to body frame;
- The cone angle, θ_c;
- The LOS angle, θ_{LOS};
- The position d_{LOS}^i along the LOS where the LIDAR measurement was taken.

A regression model is then created to estimate the local velocity vector $\hat{w}_g^i(t) \in \mathbb{R}^3$ that would likely result in measurement $m_i^{\mathrm{L}}(t)$. To this end, a maximum likelihood estimator (MLE) is used. It is assumed that the inputs (measurement metadata, denoted by x^L) and outputs (LIDAR measurements $m_i^{\mathrm{L}}(t)$) have the following relationship:

$$m_i^{\mathrm{L}}(t) = M_{\mathrm{MLE}}(x_i^L(t), w_g^i(t)) + \xi, \tag{5.42}$$

where $\xi \sim \mathcal{N}(0, \sigma^2)$ and

$$M_{\text{MLE}}(x_i^L(t), w_g^i(t)) = \Big((C^{GS}(k))^T w_g^i(k) - (C^{BS}(k))^T v_B(k)\Big) \cdot \hat{p}_s(k). \tag{5.43}$$

Let $\boldsymbol{w}_g \in \mathbb{R}^{3n_L n_b}$ be the vector that concatenates the gust velocities $w_g^i(k), i \in \mathbb{Z}_{[1,n_L]}, k \in \mathbb{Z}_{[1,n_b]}$. The likelihood function is then given by:

$$\mathscr{L}(\boldsymbol{w}_g) = \prod_{k=1}^{n_b} \prod_{i=1}^{n_L} \left(-\frac{\Big[m_i^{\text{L}}(k) - M_{\text{MLE}}(x_i^L(k), w_g^i(k))\Big]^2}{2\sigma^2} \right). \tag{5.44}$$

The MLE solution is then obtained by solving the following optimization problem:

$$\hat{\boldsymbol{w}}_g = \underset{\boldsymbol{w}_g}{\text{argmax}}\ \mathscr{L}(\boldsymbol{w}_g), \tag{5.45}$$

In the log-likelihood form, the optimization problem can be reformulated as follows:

$$\hat{\boldsymbol{w}}_g = \underset{\boldsymbol{w}_g}{\text{argmin}}\ \frac{1}{\sigma^2} \sum_{k=1}^{n_b} \sum_{i=1}^{n_L} \Big[\Big((C^{GS}(k))^T \hat{w}_g^i(k) - (C^{BS}(k))^T v_B(k) \Big) \cdot \hat{p}_s(k) - m_i^{\text{L}}(k) \Big]^2, \tag{5.46}$$

which is a nonlinear unconstrained optimization problem, which can be solved by suing, for instance, the BFGS algorithm. Once a solution is available, the gust disturbance at the aircraft nodes can be calculated by interpolating their positions with respect to the estimated disturbance at the known p_G^i positions.

The next examples illustrate the performance of the LIDAR and gust field reconstruction algorithm implemented in UM/NAST Sensors module. In the simulation, the LOS length was 60 m and the LIDAR had a cone angle of $\theta_c = 40$ deg, rotated at $\dot{\theta}_{\text{LOS}} = 8$ Hz, and took $n_L = 4$ measurements along the LOS. The buffer has size $n_B = 15$. The MLE problem was solved using the BFGS algorithm with $\sigma = 0.01$.

Discrete gust: In this example, the vertical gust disturbance was defined by a one-minus cosine model. Figure 5.8 shows the result of reconstructed vertical gust with $\theta_c = 40°$, $\dot{\theta}_{\text{LOS}} = 30$ Hz, $n_b = 250$, $n_L = 4$, and $d_{\text{LOS}} = 133$ m. The algorithm was able to accurately reconstruct the shape of the disturbance 0.26 s ahead of the first hit on the aircraft.

Continuous gust: In this example, the vertical gust disturbance was generated by the 1D von Kármaán spectrum. Figure 5.9 shows the result of reconstructed vertical gust. The same parameters used in the discrete gust reconstruction were used in here. The algorithm was able to anticipate the disturbance in 0.26 s and approximately capture its magnitude. However, it failed to estimate short and sharp peaks in the gust velocity. This is due to the finite number of measurements used to estimate a stochastic signal. A better matching

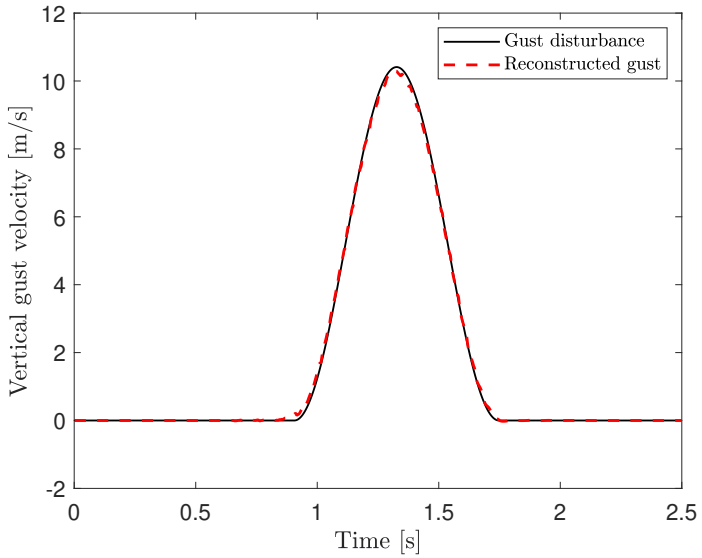

Figure 5.8: Reconstructed one-minus-cosine gust disturbance with 0.26 s anticipation.

could be possibly obtained by increasing the number of measurement at the expense of computational cost.

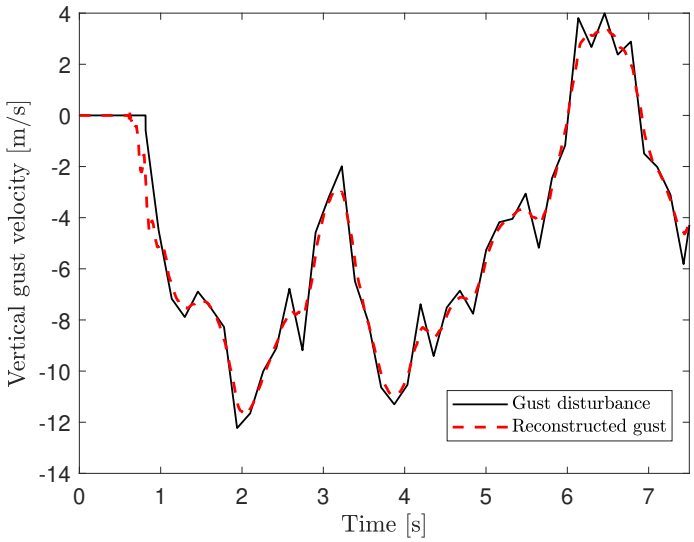

Figure 5.9: Reconstructed von Kármán gust disturbance with 0.26 s anticipation.

5.4 Numerical results

This section presents nonlinear simulation results to evaluate the performance of the GLA system in reducing loads due to gust disturbances. Results are shown for both the XRF1 and XRF1-HARW aircraft flying through a one-minus-cosine (Fig. 5.8) and von Kármán 5.9 gust fields. The LA governor architecture with linear MPC and a LIDAR sensor placed on the aircraft nose is considered here. The MPC controller was designed with a sampling time of 0.02 s, a prediction horizon of 100 steps, and gust preview of 13 steps. Results are shown for the case when the GLA system is deactivated (baseline response), when it active but with no gust preview, and when it it active with gust preview.

Table 5.1 shows the input and output constraints enforced in XRF1 and XRF1-HARW models. The curvature constrains were selected such that the load alleviation at the encounter with a one-minus-cosine disturbance was reduced by approximately 33% from the baseline response.

Table 5.1: Output and input constraints for XRF1 and XRF1-HARW GLA simulation.

Description	**Min**	**Max**	**Unit**
Out-of-plane curvature (κ_x) at XRF1 wing root	-8.0×10^{-4}	8.0×10^{-4}	[1/m]
Out-of-plane curvature (κ_x) at XRF1-HARW wing root	-3.1×10^{-3}	3.31×10^{-4}	[1/m]
Out-of-plane curvature (κ_x) at critical stations on the HTP	-1.51×10^{-4}	1.51×10^{-4}	[1/m]
Elevons deflection	-15	15	[deg]
Other control surfaces deflection	-30	30	[deg]
Rate of deflection of control surfaces	-45	45	[deg/s]
Rate of deflection of flaperon	-30	30	[deg/s]

In all simulations, the following parameters were used for the LIDAR and gust reconstruction: $\theta_c = 40°$, $\dot{\theta}_{\text{LOS}} = 30$ Hz, $n_b = 250$, $n_L = 4$, $d_{\text{LOS}} = 133$ m, and $\sigma = 0.01$ m/s. The gust reconstruction returns the preview of gust velocities at all aircraft. To reduce the computational cost of propagating this information in the MPC prediction model, just a small set of this information is used: the predicted velocities in seven nodes on each semi-wing equally distributed along the span, and in three nodes on each tail plane. The gust velocities were considered to be constant in neighboring nodes of the selected ones.

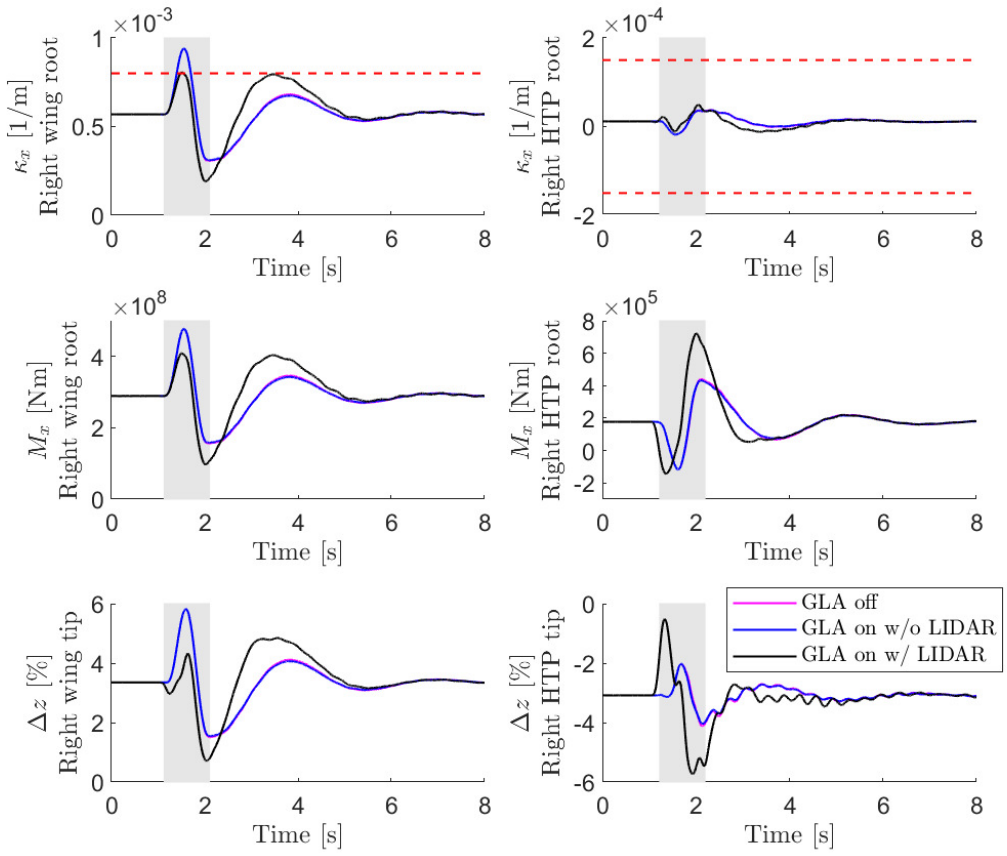

Figure 5.10: XRF1 out-of-plane curvature, bending moment, and tip deflection when flying through one-minus-cosine gust field.

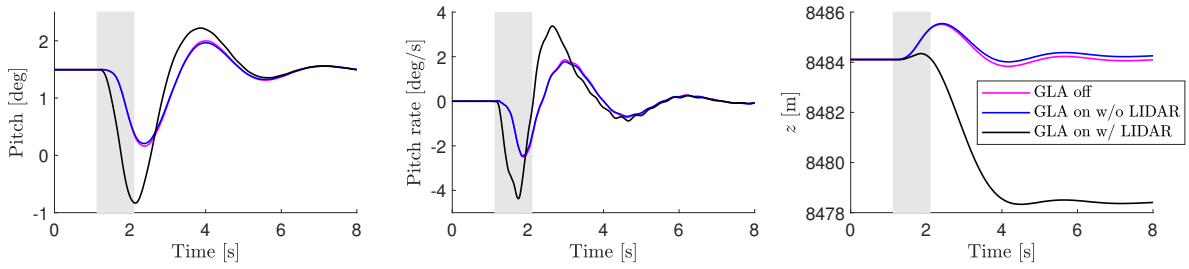

Figure 5.11: XRF1 pitch and pitch rate when flying through one-minus-cosine gust field.

5.4.1 GLA for XRF1

Figure 5.10 shows the out-of-plane curvature and bending moment at the wing and HTP root while, as well as the tip deflection of XRF1 while flying through a one-minus-cosine gust field. The gray area in the figure shows the time interval in which the gust disturbance

was nonzero. The GLA system with the LIDAR measurements kept the curvature withing the specified limits, resulting a reduction of 33% in the bending moment on the wing root at the first gust hit in comparison with the baseline response. Note that the GLA system without the gust preview cannot reduce the loads generated by the encounter with the gust, which indicates the gain in performance by the addition of the LIDAR sensor. The curvature constraints on the tail did not become active, therefore load alleviation was not performed in that member.

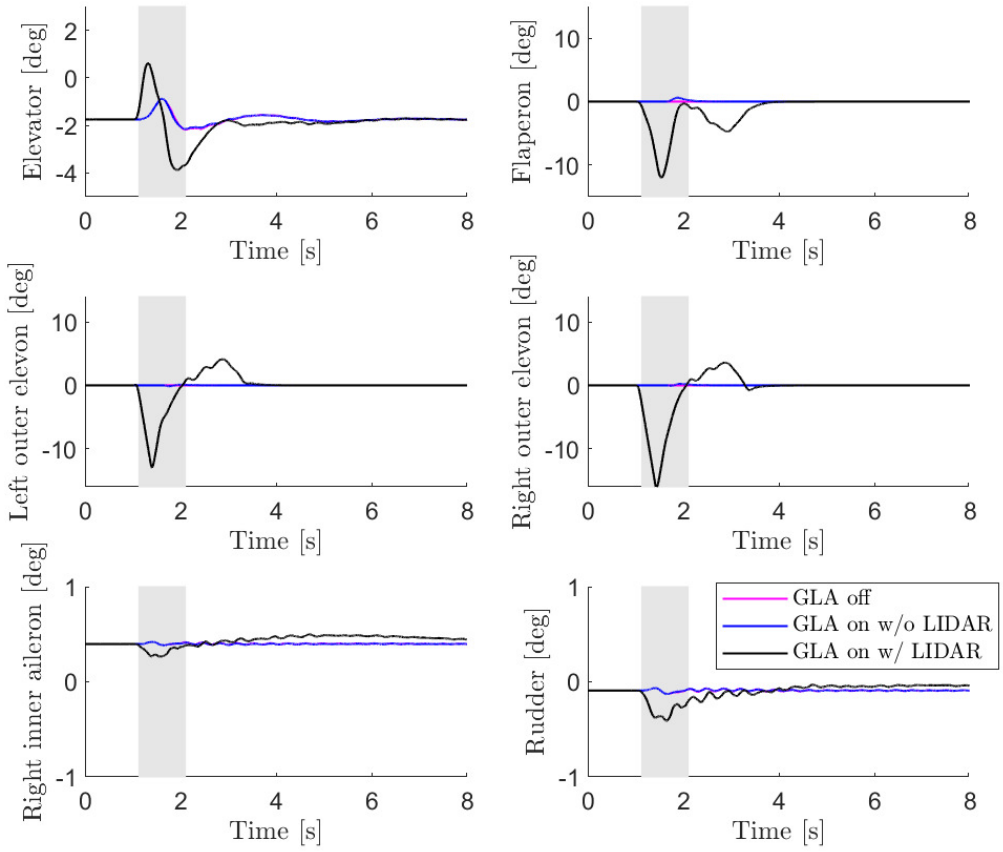

Figure 5.12: XRF1 control surfaces histories when flying through one-minus-cosine gust field.

Figure 5.11 shows the longitudinal response of the aircraft, while Fig. 5.12 shows the control surfaces histories. When the gust preview was used by the GLA system, the control surfaces were deployed as soon as constraint violation due to the gust was detected (approximately 0.26 s anticipation), which helped in reducing the loads at the first gust hit. Note that not only the outer elevons and flaperons responded to the gust preview information, but also the elevator, which caused an early pitch response. The control surfaces used for

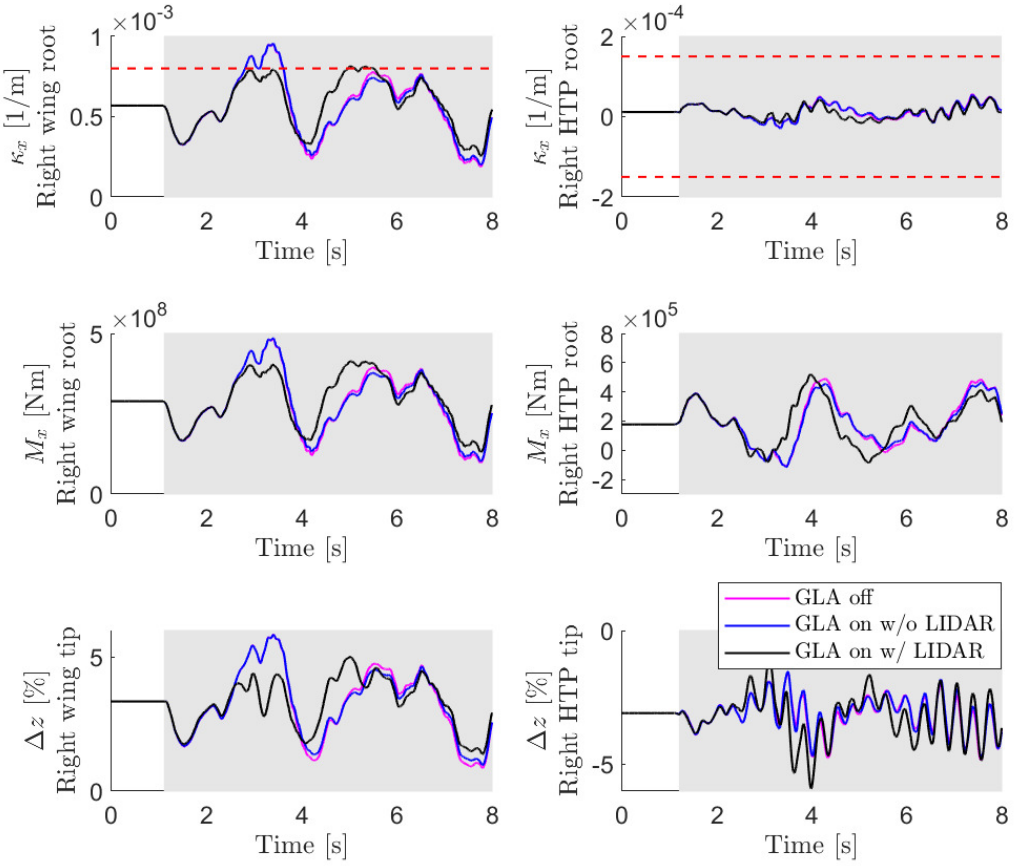

Figure 5.13: XRF1 out-of-plane curvature, bending moment, and tip deflection when flying through von Kármán gust field.

GLA had magnitude equal or less than 15 deg and rate equal or less than 45 deg/s, therefore meeting the requirement. There was a small altitude deviation of 6 m due to the load alleviation system, which still satisfies the requirements in Section 5.1.

The performance of the GLA system when the XRF1 aircraft flies through a von Kármán gust field is shown in Fig. 5.13. The LA governor with LIDAR measurements kept the wing curvature within the limits throughout the simulation, therefore reducing the peak out-of-plane bending moment at that station. Note that the baseline response and the response of the GLA system with no gust preview violate the constraints, resulting in higher peak loads. A 40% load reduction was achieved. Similarly to the encounter with the discrete gust, the HTP constraints did not become active.

The longitudinal attitude of the aircraft is shown in Figure 5.14, and the control surfaces histories are shown in Fig. 5.15. The flaperons and elevons were deflected to their maximum

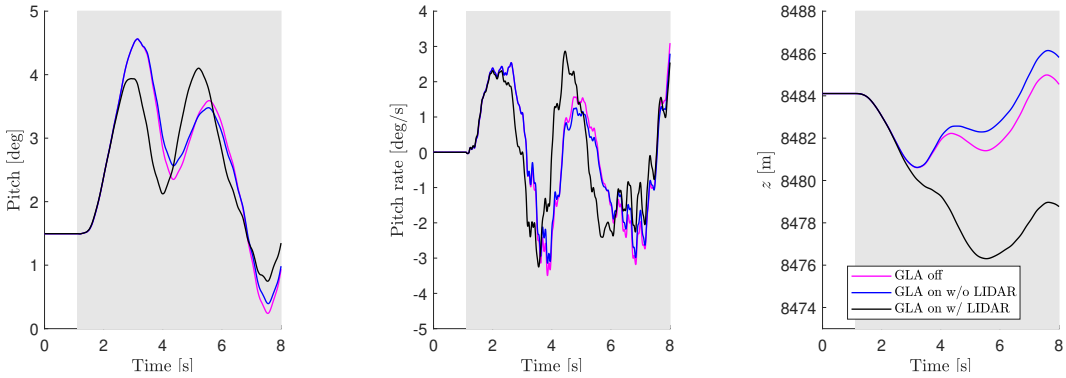

Figure 5.14: XRF1 pitch and pitch rate when flying through von Kármán gust field.

magnitude to prevent load violations, at the same time that the elevator deflection was increased to counteract the adverse pitch moment. The altitude deviation was approximately 8 m, which is still much smaller that the maximum allowed in the requirements.

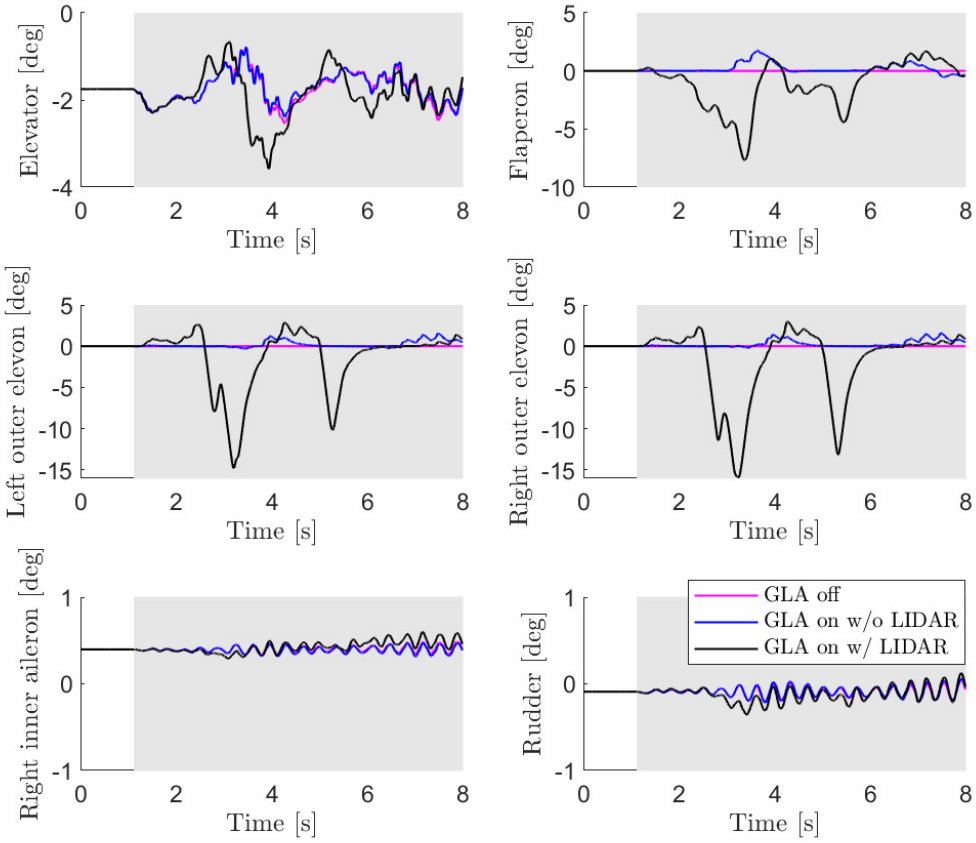

Figure 5.15: XRF1 control surfaces histories when flying through von Kármán gust field.

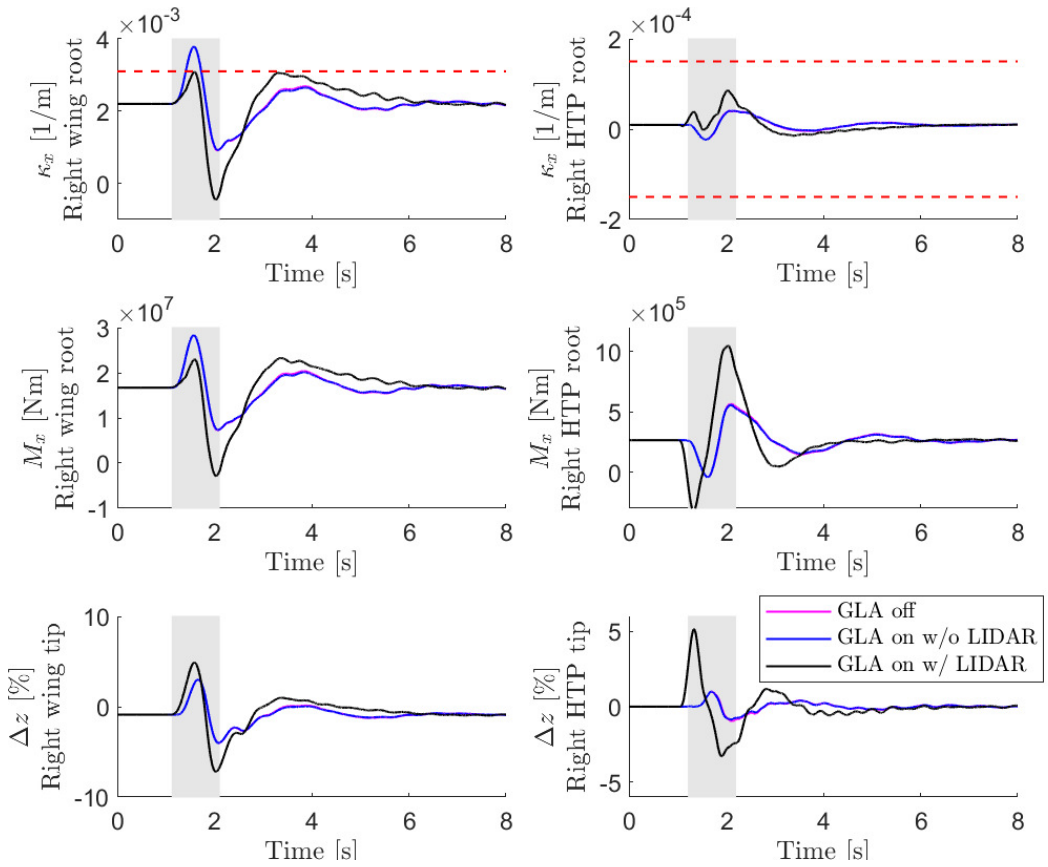

Figure 5.16: XRF1-HARW out-of-plane curvature, bending moment, and tip deflection when flying through one-minus-cosine gust field.

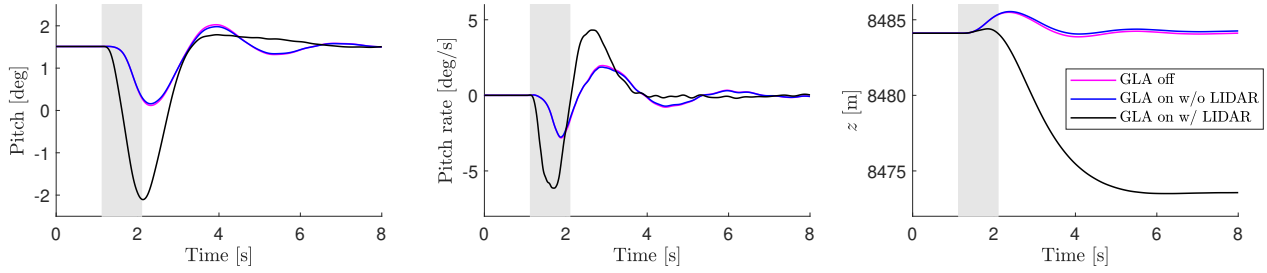

Figure 5.17: XRF1-HARW pitch and pitch rate when flying through one-minus-cosine gust field.

5.4.2 GLA for XRF1-HARW

The LA governor was also used to reduce loads in XRF1-HARW. In comparison with the design used for XRF1, the MPC controller gains were reduced. Figure 5.17 shows the resulting out-of-plane curvature and bending moment at the wing and HTP root. Similar to the results seen for XRF1, the performance of the GLA system without gust preview was

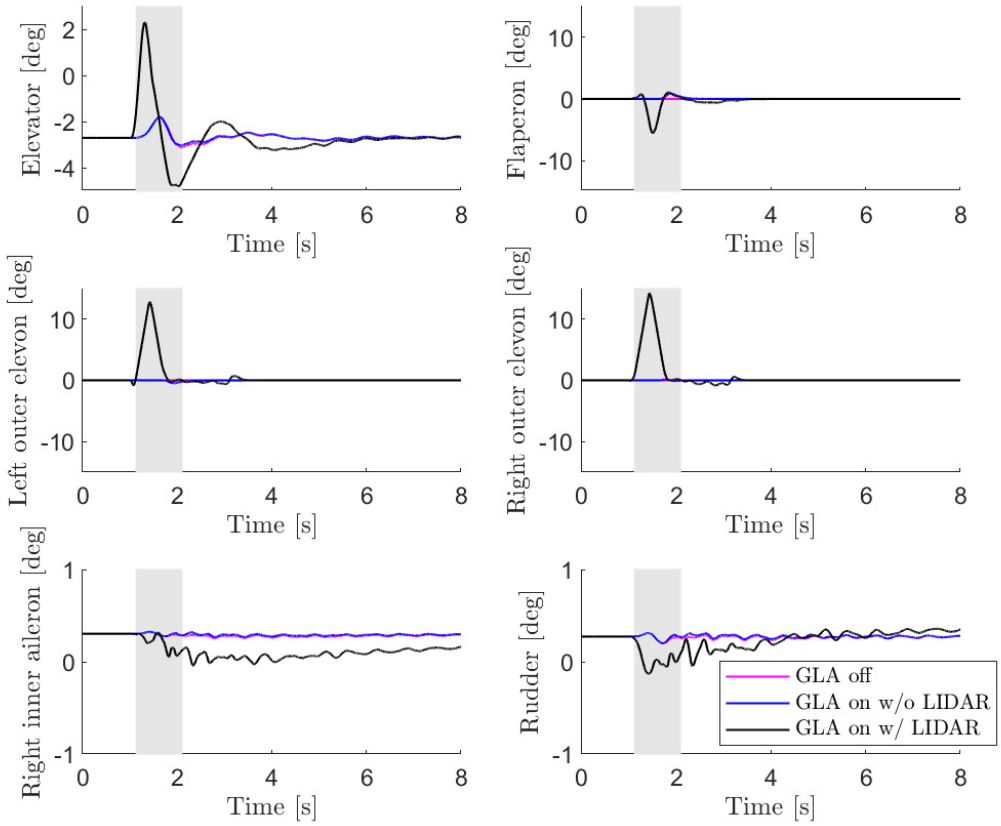

Figure 5.18: XRF1-HARW control surfaces histories when flying through one-minus-cosine gust field.

comparable to the case when no load constraints are enforced, which led to a large peak in curvature and bending moment on the wing. When the LIDAR measurement were used for feedforward control, the GLA system could keep the curvature within the specified bounds, reducing the peak moment in 35%.

The altitude deviation due to the GLA actuation, even though still within the maximum allowed, is larger than what was observed for XRF1. As shown in Fig. 5.17, at the end of the simulation the altitude was approximately 12 m smaller than the baseline response. The control surfaces histories are shown in Fig. 5.18. While the flaperons were deflected to negative values (corresponding to an upward deflection) similarly to what was seen in XRF1, the elevons were deflected to positive values, an opposite behavior as seen in XRF1. This may indicate a control reversal in XRF1-HARW caused by the longer and more flexible wing.

The performance of the GLA system in reducing loads in XRF1-HARW while flying

through a von Kármán gust field is shown in Fig. 5.19. The reduction on the wing root out-of-plane bending moment was of 33% when the gust preview was used for feedforward control. The constraints on the HTP did not become active during the simulation.

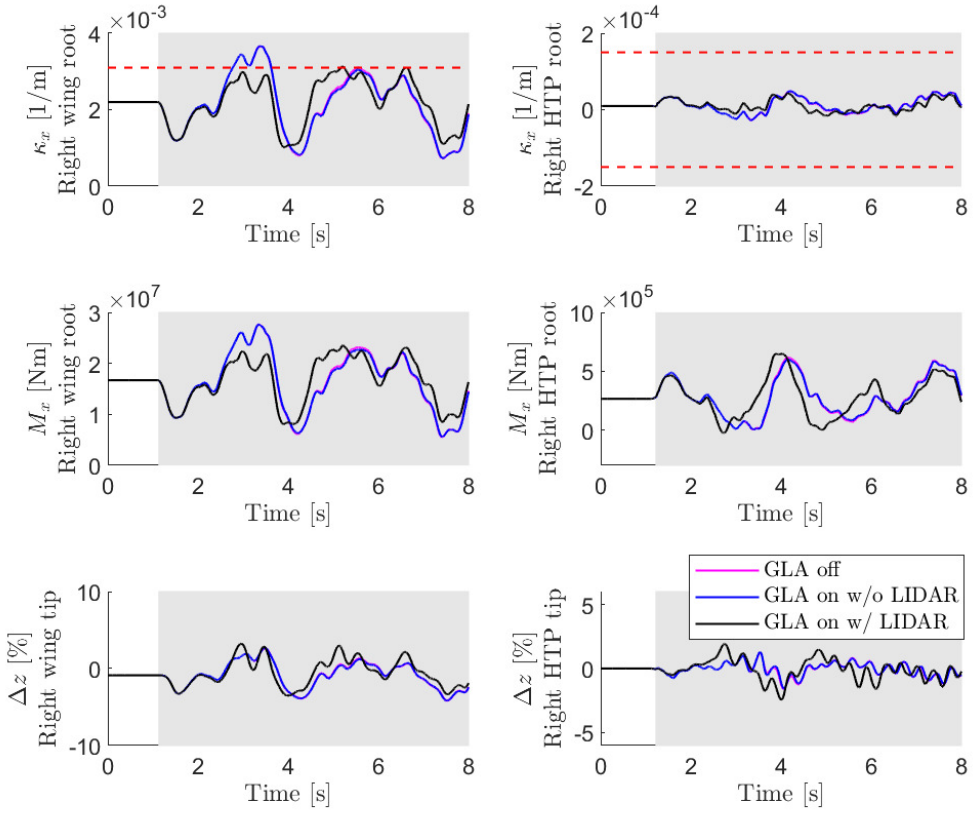

Figure 5.19: XRF1-HARW out-of-plane curvature, bending moment, and tip deflection when flying through von Kármán gust field.

As shown in Fig. 5.20, the altitude deviation was approximately 11 m, which is comparable to the one seen in Fig. 5.17 and larger than the one observed for XRF1. The reverse response of the elevons is again observed in this case (Fig. 5.21). Note that the control effectors become active several times during the maneuver, but they eventually return to the trim condition whenever there is no danger of violating the curvature constraints.

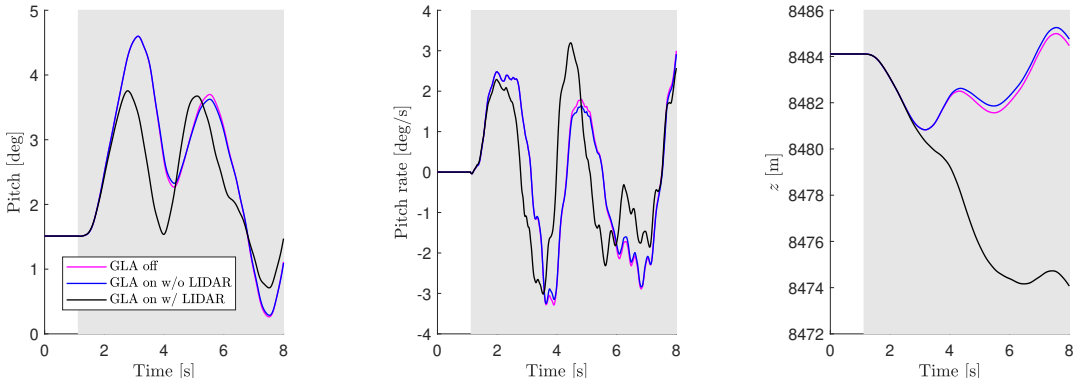

Figure 5.20: XRF1-HARW pitch and pitch rate when flying through von Kármán gust field.

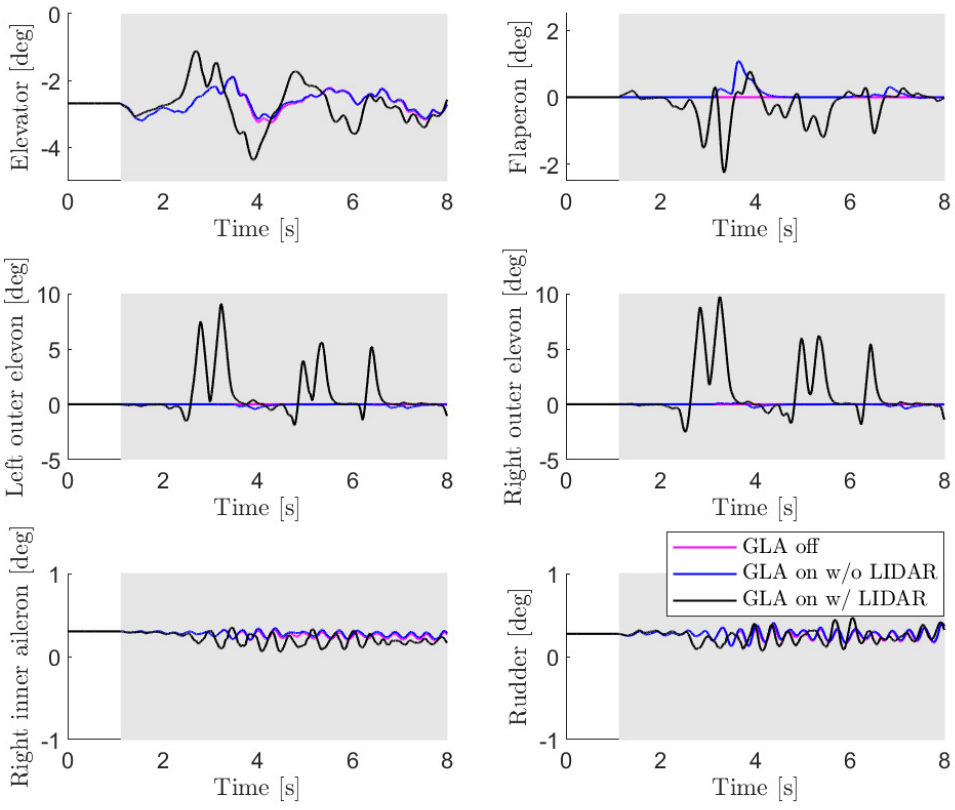

Figure 5.21: XRF1-HARW control surfaces histories when flying through von Kármán gust field.

CHAPTER 6

Experimental Validation

This Chapter presents the experimental work toward the validation of MPC-based MLA systems for a VFA. To this end, wind tunnel tests were conducted using an enhanced aeroservoelastic (EASE) model, a new demonstrator of MLA solutions in controlled environments.

6.1 Experimental Setup

The EASE model is a half airplane configuration that is allowed free pitching motion about its center of mass. The wing was designed to be the only flexible member of the model, showing geometrically nonlinear behavior within the operating conditions of the test. The EASE model was designed and manufactured by the University of Michigan's Active Aeroelasticity and Structural Dynamics Laboratory (A^2SRL). This Section describes the aircraft model and the facilities used in the experiment.

6.1.1 Facilities

The University of Michigan's subsonic wind tunnel was the testing facility used for this work. This wind tunnel features a 335-ft center-line closed return loop design, a 15:1 contraction ratio, and a 25-ft long, 5-ft by 7-ft test section (see Fig. 6.1). The airspeed in the test section can reach speeds up to 76 m/s.

The PaPA, a side-wall mounting device, was used in this work to constrain the model to the wall of the wind tunnel in the aft portion of the test section (Fig. 6.2). Although the mounting device allows the pitch and plunge motions, in the designed experiment, the model was constrained in plunge and only pitch will be allowed. The PaPA setup also features its own sensors to support the experimental activities, which will be presented in Section 6.1.3.

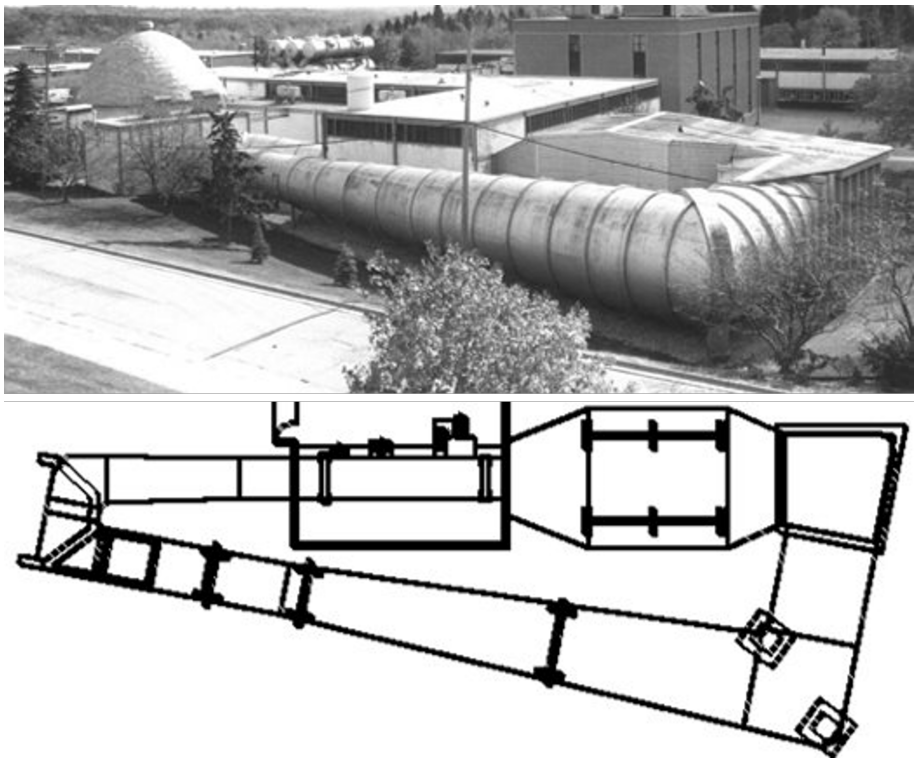

Figure 6.1: University of Michigan's subsonic wind tunnel.

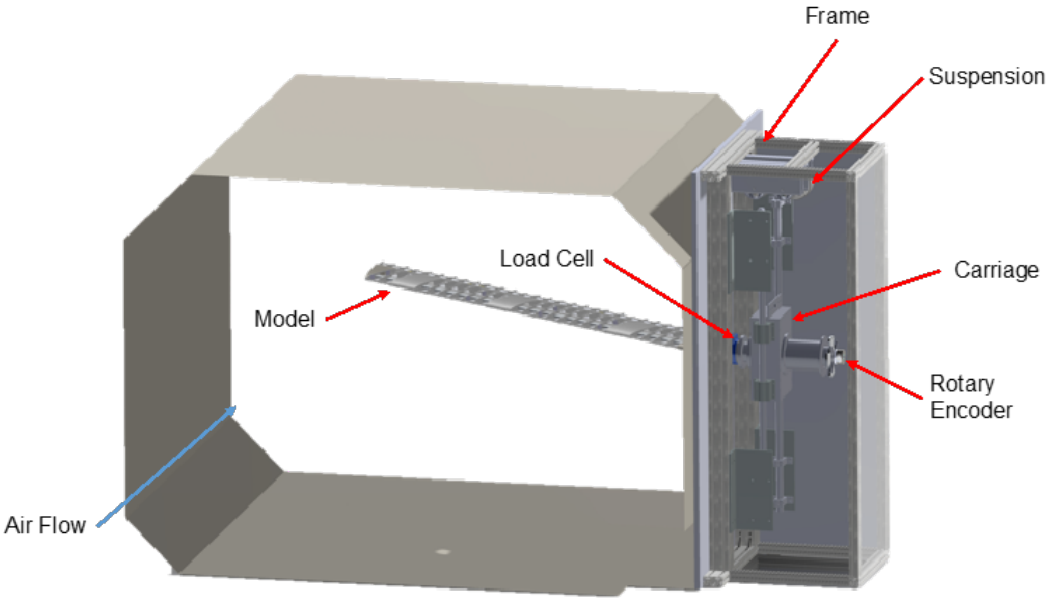

Figure 6.2: Schematic of PaPA mechanism.

6.1.2 EASE Model

The EASE model was designed as a half aircraft, and consists of a flexible main swept wing, a HTP with elevator, and a fuselage that connects the two lifting elements with the PaPA mechanism located on the wind-tunnel wall, allowing for the free pitch degree of freedom. The overall dimensions of the EASE model are shown in 6.3.

The wing was designed to be flexible while the tail and fuselage were designed to be rigid. In order to ensure easy and accurate modeling of the elastic properties of the wing, those were based on a main spar. To remove the stiffness effect of the rest of the wing construction, it was designed as a series of airfoil-shaped sections (pods), each fixed to a single spar spanwise location.

Figure 6.4 shows the finished model manufactured by A^{2}SRL in the wind tunnel. Appendix G present a summary of the design process and properties of the model. The detailed description can be found in Ref. [134].

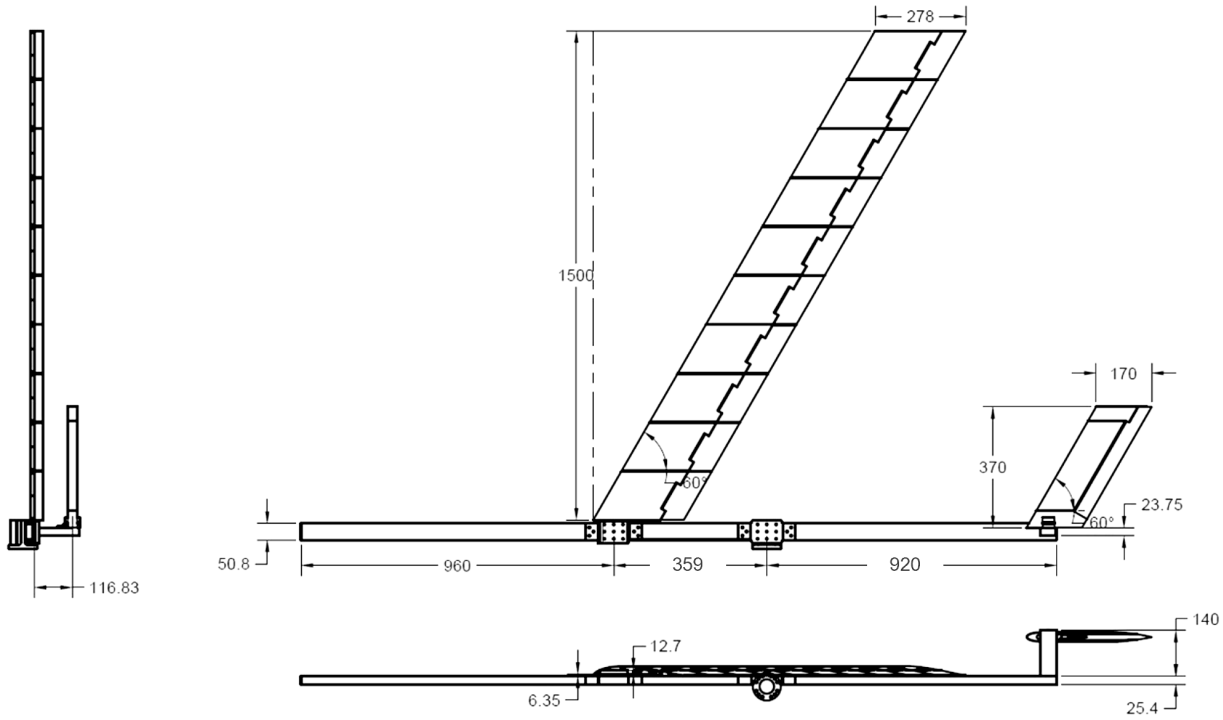

Figure 6.3: EASE model drawing (all dimensions in mm)

Figure 6.4: EASE model in University of Michigan's wind tunnel.

6.1.3 Instrumentation

This section describes instrumentation used in the EASE model experiment. It includes both the instrumentation in the model itself and what is offered by the PaPA and wind tunnel.

Figure 6.5 shows the relative location of various sensors associated with the EASE model. These sensors can be classified into three groups, i.e.:

1. Critical for feedback control
    - IMUs (accelerometers + gyroscopes)
2. Refined response characterization
    - Load cells and strain gauges
    - Rotary encoders for control surfaces position
    - PaPA's rotary encoder for pitch attitude
    - Fiber optics for wing root bending strain
    - Fiber optics wing shape sensing
3. Flow condition
    - Pitot tube for airflow speed
    - Thermometer

Group 1 contains the sensors that were used for state estimation in the EASE model. Because the MPC controller requires information about all internal states in the model, a

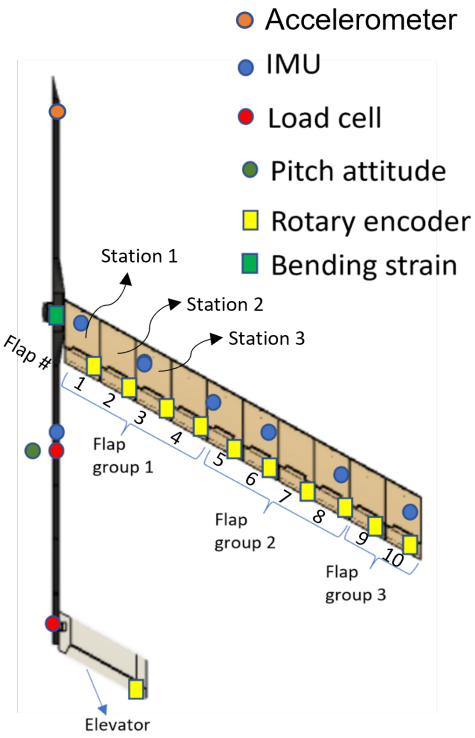

Figure 6.5: Test instrumentation and control effectors overview.

Kalman filter was be designed to estimate these sates based on the sensors measurements. These states are the structural strain states, pitch attitude and rate. Figure 6.6 shows a more detailed schematic of the sensor placement in the wing and HTP. The IMU units on the wing were the primary sensors used to estimate the strain states in this member. Because the HTP is treated as a rigid member, there was no need to estimate the strain states on this structure and, therefore, no IMU units were placed there. Figure 6.6 also shows the servos placement for each control surface on the model.

Group 2 of sensors included the rotary encoders used to record the rotation of the control surfaces, that is, the wing flaps and HTP elevator. It also included the load cell and strain gauges that provided information about the loads. Additionally, the fiber optics system that provided strain measurements along the spanwise direction on the wing. Such measurement allowed the recovery of the wing shape and an additional source for loads estimation. Group 3 of sensors included the wind tunnel sensors, such as the pitot tube and thermometer, used to monitor the airflow condition during the experiment.

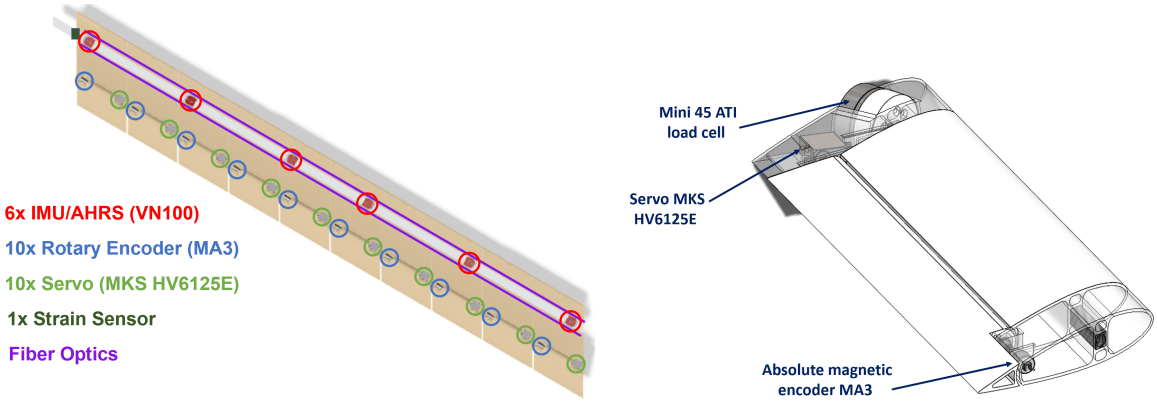

(a) Wing instrumentation. (b) Tail instrumentation.

Figure 6.6: Wing and HTP sensor distribution.

6.2 Numerical Model

A UM/NAST model for the EASE aircraft was created for design and analysis using the geometry and material properties reported in [134]. The model represents the full symmetric EASE aircraft with very flexible wing, and rigid fuselage and HTP. The symmetric representation was chosen to facilitate the implementation and trim of the model. For control design purposes, the states representing the left wing aeroelastic dynamics were eliminated in a post-process, as it will be described later in this Section. Appendix G presents some EASE model properties.

The spanwise distributions of aerodynamic loads on the wing and tail were adjusted based on data obtained from AVL [135]. These data were used to define weights on the aerodynamic kriging model to determine the aerodynamic forces and moments not only based on the angle of attack and Reynolds number, but also the spanwise position in order to take into consideration finite wing and 3D effects. In addition to that, AVL was also used to create a model for the downwash effect created by the wing on the HTP.

To represent the attachment between the EASE model and the PaPA device in the wind tunnel, a large concentrated mass and inertia are added to the model at the rotation point, in addition to a vertical force to balance the extra weight. Such mass restraints the translation of the model and its lateral motion. Only the longitudinal motion around the rotation axis is preserved.

A model order reduction (MOR) was performed to reduce the number of states in the linearized model to facilitate the control design and implementation. The MOR is performed in following three steps:

1. The rigid body states describing the inertial position and lateral motion were removed

from the model, given the fact that they are constant and equal to zero due to the rigid attachment between the EASE model and the PaPA device. Furthermore, the aeroelastic states describing the dynamics of the left wing were eliminated by making them equal to the right wing states, i.e., imposing symmetric deflections. Similarly, the control inputs on the left side of the model were eliminated by imposing symmetric actuation with respect to the right-hand side. Finally, the flaps on the wing were grouped as follows to reduce the control degrees of freedom (see Fig. 6.5):

- Group 1: the four most inboard flaps (flaps 1-4);
- Group 2: the four midboard flaps (flaps 5-8);
- Group 3: the two most outboard flaps (flaps 9-10).

Therefore, the resulting model had 164 states and 4 control inputs.

2. An eigenvalue decomposition of the state matrix was performed, and then the system was put in the modal form. This way, the mode shape amplitudes and frequencies are explicitly represented in the linearized model, and the ones of interest can be selected. For the planned experiment, those would be frequencies below 20 Hz, which capture the longitudinal rigid-body modes, in addition to the first three out-of-plane aeroelastic modes, first in-plane mode, and first torsion mode.

3. A residualization was performed to eliminate modes above 20 Hz.

The final reduced-order model (ROM) has the following form:

$$\Delta\dot{x}_r = A_r\Delta x_r + B_r\Delta u_r \tag{6.1}$$

$$\Delta y = C_r\Delta x_r + D_r\Delta u_r, \tag{6.2}$$

where Δx_r contains 14 states, Δu_r contains 4 inputs, and Δy contains 38 outputs (described in Section 6.3).

The flaps and elevator motion on the EASE model are controlled by the servo MKS HV6125E. The unloaded servo dynamics was experimentally identified in the frequency domain. The following second-order transfer function describes the servo response within the device's operating range:

$$\frac{U_r(s)}{U_s(s)} = \frac{169.6s + 2875}{s^2 + 187.2s + 2887}. \tag{6.3}$$

The servo transfer functions for each one of the flap groups and elevator in the model in

Eq. 6.1 were transformed into state-space form and concatenated in the following model

$$\dot{x}_s = A_s x_s + B_s u_s \tag{6.4}$$
$$u_r = C_s x_s + D_s u_s. \tag{6.5}$$

where x_s represent the servos internal states and u_s represents the inputs fed into the servos.

Models in Eqs. 6.1 and 6.4 can be combined into a single linear model that describes the local dynamics of the EASE aircraft:

$$\dot{x} = Ax + Bu \tag{6.6}$$
$$y = Cx + Du \tag{6.7}$$

where

$$x \triangleq \begin{bmatrix} \Delta x_r \\ x_s \end{bmatrix}, \quad u \triangleq u_s, \tag{6.8}$$

and

$$A = \begin{bmatrix} A_r & B_r C_s \\ 0 & A_s \end{bmatrix}, \quad B = \begin{bmatrix} B_r D_s \\ B_s \end{bmatrix}, \quad C = \begin{bmatrix} C_r & D_r C_s \end{bmatrix}, \quad D = D_r D_s. \tag{6.9}$$

This augmented linearized model has 22 states, 4 inputs, and 38 outputs.

6.3 Control System Design

The main control objective was to run the MPC controller in real-time to keep the loads on the airframe within prescribed safety limits while performing a longitudinal maneuver. The Maneuver Vertical Stretched (MVS) was considered in the experiment. To keep the loads on the model within safety bounds during the MVS maneuver, the controller should enforce constraints on the shape of the wing by limiting the curvature at selected stations. The shape control should be performed by deflecting the available control surfaces on the model. The experiment focused on limiting the out-of-plane moment at critical wing and HTP stations.

The LA governor architecture presented in Section 3.2.2 was designed to accomplish these objectives. The three flap groups are used as control effectors u_{LA} to perform load alleviation on the wing, while the elevator is used as the control effector u_{FCS} manipulated by the inner-loop controller to control the aircraft attitude. In here, the discrete-time LQ-I controller is designed to track a pitch angle reference while regulating the pitch rate. The update rate of

the inner-loop is 20 ms.

A linear MPC design based on the linear ROM is considered for the outer-loop, with an update rate of 60 ms. Slack variables are used to avoid feasibility problems, and input blocking is used to reduce the OCP size. The prediction horizon was chosen to be 30 steps (corresponding to a 1.8 s look ahead in time), and the control horizon was chosen to be 20 steps.

The reduction in the out-of-plane bending moment on the wing is achieved by imposing constraints on the minimum and maximum out-of-plane curvatures at the ith wing station:

$$\kappa_{x,i}^{\min} \leq \kappa_{x,i} \leq \kappa_{x,i}^{\max}. \tag{6.10}$$

Since the EASE wing has uniform properties along its span, the maximum curvatures, and thus the maximum bending moments, are expected to be developed at inboard stations. Therefore, three stations on the three most inboard wing pods are chosen.

The EASE model has an HTP whose bending moment must also be reduced. As discussed in Section 4, the deflection of the flaps to reduce the loads on the wing generates an adverse pitch moment that is then corrected by the elevator, thus resulting in an increase in bending moment on the HTP. Controlling the shape for load alleviation is not possible in this case, since the EASE model's HTP is modeled as a rigid element. Alternatively, the constraints are imposed directly on the HTP root moment ($M_{\text{tail}}^{\text{root}}$), which is calculated as:

$$M_{\text{tail}}^{\text{root}} = \frac{3}{8} L_{\text{tail}} b_{\text{tail}} + x_{tail}^{\text{cg}} m_{tail} (q_B r_{tail} - g), \tag{6.11}$$

where L_{tail} is the total lift on the HTP, m_{tail} is the HTP mass, b_{tail} its span, x_{tail}^{cg} is the spanwise position of its center of gravity (c.g.), r_{tail} is the distance between the tail root and the rotation point, q_B is the aircraft pitch rate, and g the acceleration of gravity. The HTP root moment should then be kept within some prescribed bounds:

$$M_{\text{tail,min}}^{\text{root}} \leq M_{\text{tail}}^{\text{root}} \leq M_{\text{tail,max}}^{\text{root}}. \tag{6.12}$$

Upper and lower limits on the wing curvature and HTP root moment can be added to the MPC formulations as linear constraints. Similarly, bounds can be enforced on the control effectors magnitudes and rate of change.

The input and output constraints considered are shown in Tab. 6.1. The out-of-plane curvature constraints are enforced in three inboard stations on the wing. The bending moment constraint is enforced on the HTP root. The constraints on the control surfaces deflection and rate are in accordance with typical values found in actual large commercial

aircraft. The final QP problem has 130 decision variables and 750 constraints.

Table 6.1: Output and input constraints.

Variable	**Description**	**Min**	**Max**	**Unit**
κ_x, wing station 1	Out-of-plane curvature at critical station on the wing	-0.35	0.35	[1/m]
κ_x, wing station 2	Out-of-plane curvature at critical station on the wing	-0.30	0.30	[1/m]
κ_x, wing station 3	Out-of-plane curvature at critical station on the wing	-0.22	0.22	[1/m]
$M_{\text{tail}}^{\text{root}}$, HTP	Out-of-plane bending moment at HTP root	-1.6	1.6	[Nm]
u_{FCS}	Elevator deflection	-30	30	[deg]
u_{LA}	Flap deflection	-30	30	[deg]
δu_{FCS}	Rate of deflection of elevator	-45	45	[deg/s]
δu_{LA}	Rate of deflection of flaps	-45	45	[deg/s]

State estimation is performed using the Kalman filter in recursive form as presented in Section 3.5, with the tuning procedure described in Appendix E. A total of 38 sensor outputs were used for feedback, namely:

- Triaxial linear accelerations and angular velocities provided by the six IMU units placed on the wing;
- Pitch angle and pitch rate measured by the IMU unit placed on the fuselage near the rotation point.

Due to the sensor noise and disturbances, such as turbulence in the wind tunnel, the following low-pass second-order Butterworth filter

$$B(z) = \frac{0.1453z^2 + 0.2906z + 0.1453}{z^2 - 0.6710z + 0.2523}, \tag{6.13}$$

with sampling time of 20 ms and cut-off frequency of 8 Hz was used to filter the sensor outputs before feedback.

The control design was performed for the model at 25 m/s and initial angle of attack of 2.5 deg.

6.4 Numerical Verification

Nonlinear closed-loop simulations were run in UM/NAST to verify the control design. Figure 6.7 shows the different pitch angle profiles tracked by the controller and the resulting pitch rate in two scenarios: i) the curvature and bending moment constraints were deactivated (MPC off), serving as a baseline; ii) the MLA system was on, therefore the MLA constraints were added to the MPC controller objective to alleviate loads. In this example, the aircraft performs three consecutive cycles of the MVS maneuver.

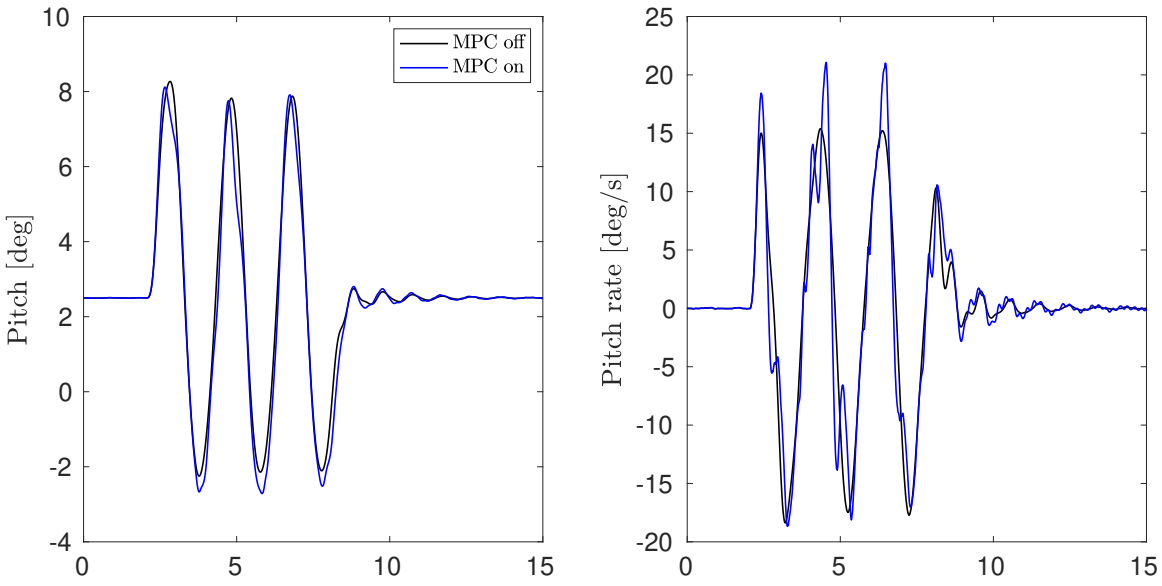

Figure 6.7: EASE aircraft longitudinal response in simulations.

Figure 6.8 shows the out-of-plane (OOP) curvature at the three inboard wing stations on which constraints were enforced. Note that the baseline response surpasses the curvature upper limits. However, When the MLA system is on, the MPC controller is able to keep the curvature within the prescribed limits. As a result, the OOP bending moment on each of these stations, also shown in Fig. 6.8, is reduced. The average load reduction on station 1 was 33%.

Similarly, the load on the HTP was reduced. As shown in Figure 6.9, the OOP bending moment at the HTP root was kept within the desired bounds during the simulations. Apparently this constraint was enforced slightly conservatively, what could possibly be explained by estimation errors given the fact that the Kalman filter uses a linearized model to estimate the nonlinear plant. The constraint considered in the simulations was ± 1.25 Nm, which differs from the one in Tab 6.1 used in the actual experiment due to the identified model

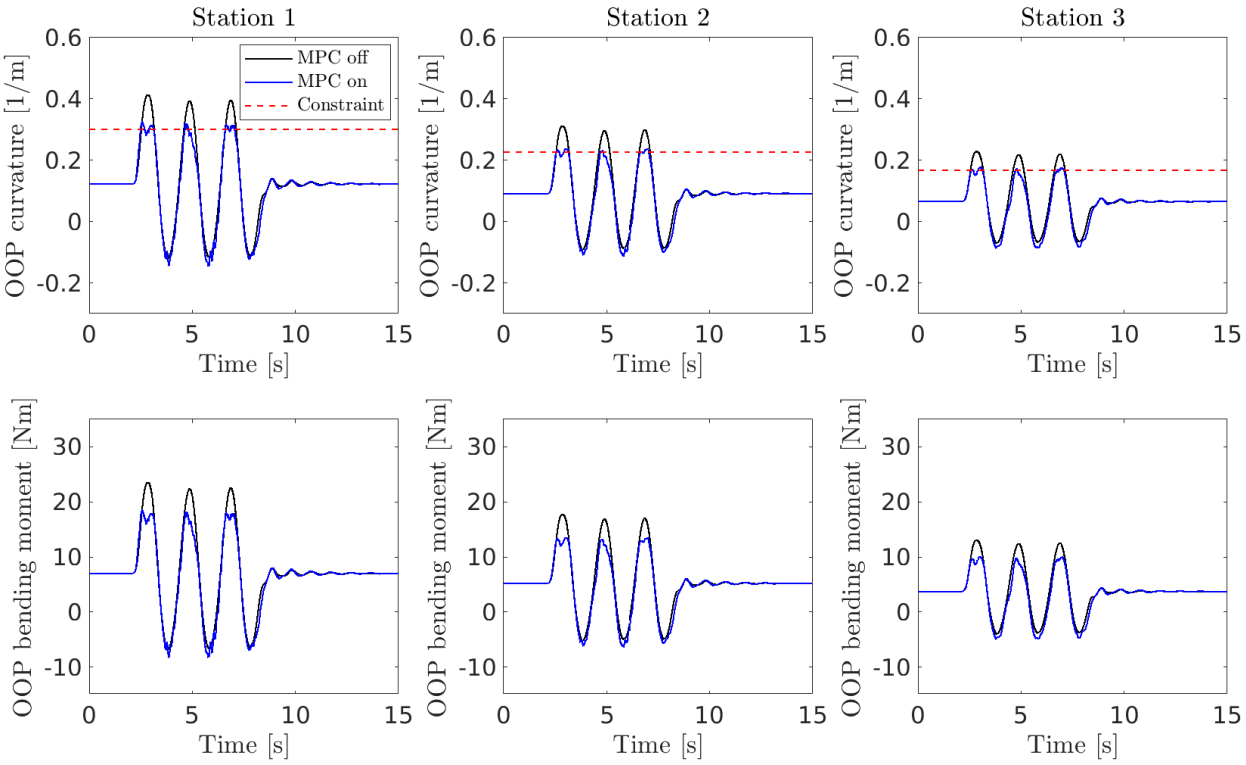

Figure 6.8: Loads on EASE wing in simulations.

mismatch, which will be discussed in Section 6.6.

Figure 6.10 shows the control surfaces deflection during the maneuver. When the MLA constraints were deactivated, only the elevator was engaged to track the desired pitch angle. When the MLA constraints were added to the control problem, then the flaps were deflected to keep the curvature of the wing within the defined limits. Flap group 2 had the largest deflections. Note that the elevator deflection also changed when the MLA constraints were active. This is due to the load constraint on the HTP root, and the corrections on the pitch attitude to counteract the adverse pitch moment created by the flaps on the wing when performing MLA.

Finally, Fig. 6.11 shows the vertical force at the rotation point when the EASE model performs the MVS maneuver in the nonlinear simulation. In Fig. 6.7, note that the amplitude of the maneuver in the negative angles of attack when the MLA system is active is slightly bigger in order to maintain the same total vertical force in the aircraft. This correction is necessary due to the change in lift caused by the deployment of the flaps when performing MLA. This vertical force makes up the most significant part of the total load factor in the maneuver.

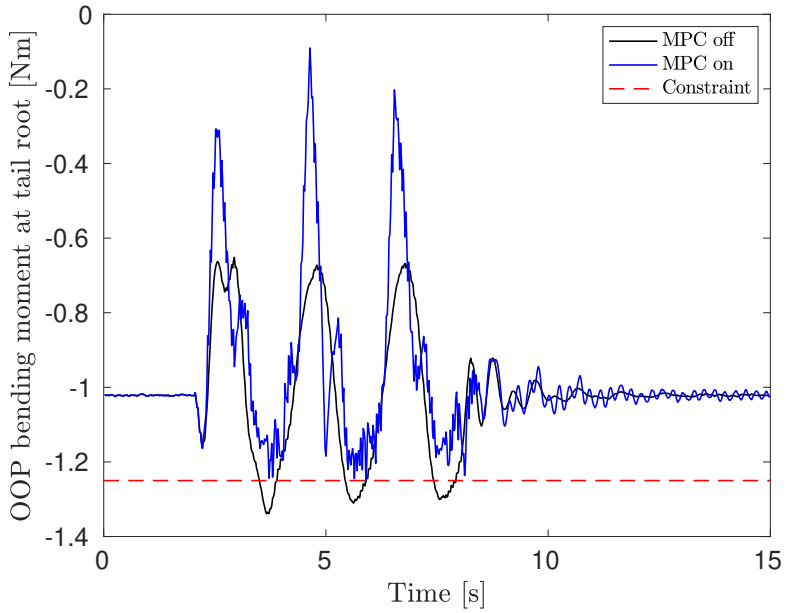

Figure 6.9: Load on EASE HTP in simulations.

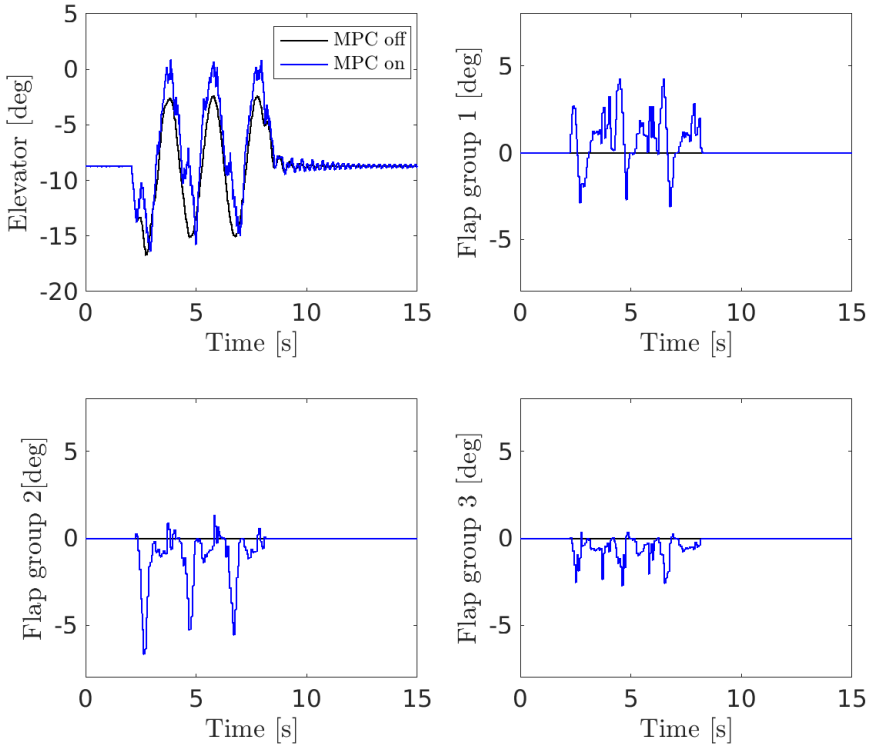

Figure 6.10: EASE aircraft control surfaces in simulations.

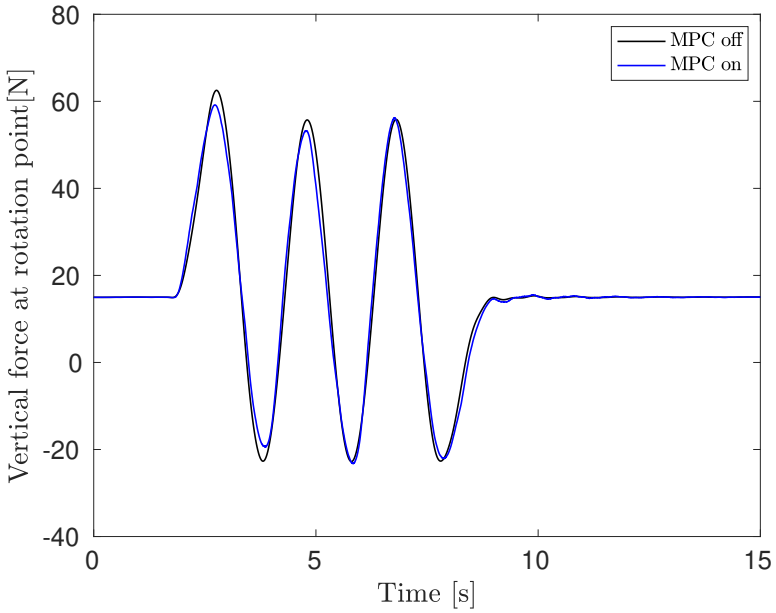

Figure 6.11: Vertical force at rotation point simulations.

6.5 Control System Implementation

The experimental closed-loop setup used in the wind tunnel experiment consisted of a National Instruments data acquisition system (DAQ), which samples the sensors mounted on the EASE model and sends the measurements to a real time server (RT server) running Linux through a UDP/IP link, at 500Hz. The RT server run the controller, and it is outfitted with a PCI board capable of generating pulse-width modulated (PWM) signals (PWM generator), which sends a new position command to the servos at a frequency of 100Hz. Figure 6.12 shows a schematic of the experimental setup.

The DAQ records the readings of a 6-d.o.f. load cell attached to the rotation point, seven IMU units and one accelerometers on the wing and fuslage, rotary encoders on all control surfaces and strain gauges at the wing root.

The RT server is a Dell PowerEdge R540 outfitted with a 4-core/8-thread 3.8 GHz Intel Xeon Gold 5222 CPU, 6×8 GB RAM (3200 MT/s) and a 480 GB SSD. It runs the Debian operating system with a real time Linux kernel. It is connected to an Applied Dynamics International (ADI) Systems' PCI-565-DPGA board, which generates the PWM commands for the servos.

The RT server also runs ADEPT, a software provided by ADI systems for real-time applications. ADEPT Was used to implement the controller in C++, create an interface between the DAQ system and the controller, and an interface between the controller and

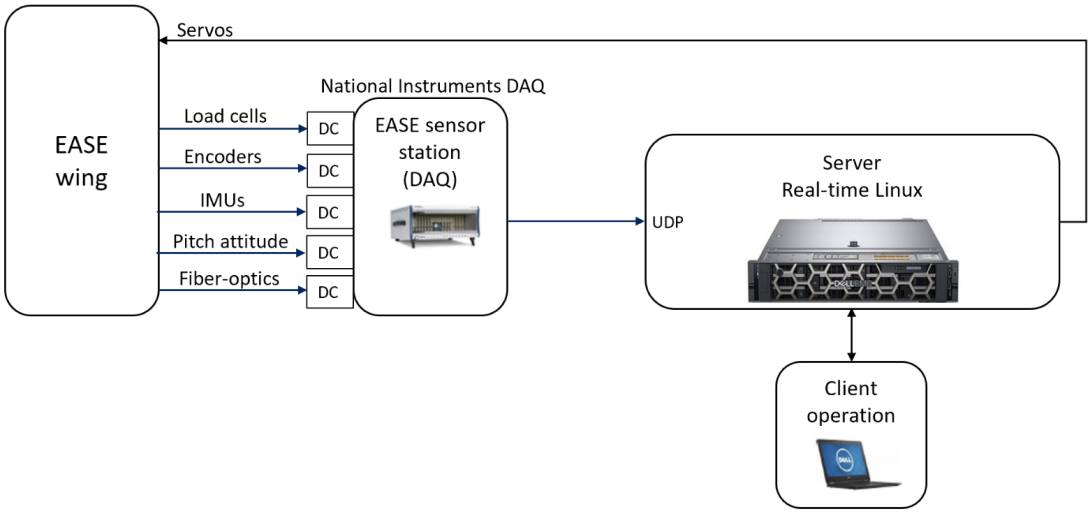

Figure 6.12: Experimental setup.

the PWM generator. The measurements of the load cell on the tail are received directly by ADEPT. ADEPT was also used to set the controller parameters and record internal variables, such as the ones related to the frame time, the commanded control action, and the optimization solver performance.

In the MPC controller implementation, qpOASES [87], an active set method based QP solver, was used to solve the optimal control problem. Previous solutions of the QP problem were used to warmstart the next iterations, the maximum number of iterations were set to 80, and the tolerance for convergence was set to $5 \times 10^{-}4$. The inner and outer-loops were implemented in a serial fashion. Therefore, the effective controller frame time (e.g., the time for receiving data from the DAQ, calculating the control action, and generating the PWM signal) had to be within 20 ms.

6.6 Experimental Results

The EASE model and the controller described in Section 6.3 were tested in a wind tunnel campaign that spanned six days in a total of 8.5 hours of air time. Table 6.2 presents a summary of the tests that were conducted. For all of them, the wind tunnel speed was 25 ± 0.4 m/s, and the temperature varied from -1.1^{o}C to 14.4^{o}C depending on the day and time of the tests.

The tests were divided into two categories: open-loop and closed-loop tests. The open-loop tests were performed to verify the UM/NAST model, in particular the aerodynamic loads generated by the wing and tail. To this end, a sequence of step, impulse, and frequency

sweeps for each control surface, or groups of control surfaces, was commanded for different magnitudes between their minimum and maximum excursion. The open-loop tests also tested the authority of the elevator in changing the pitch attitude of the EASE aircraft.

The closed-loop tests consisted of incrementally testing the inner and outer-loop controller in the LA governor architecture. A sequence of step commands were given to test the tracking performance, and a sequence of MVS maneuvers, in groups of 1, 3 or 6 cycles, were performed to evaluate the load alleviation system. In the latter, it was tested the case when no MLA constraints were enforced, when only the wing shape constraints were present, and when both the wing and HTP constraints were enforced.

6.6.1 Open-loop Tests

Figures 6.13, 6.15, and 6.14 show the static loads obtained from open-loop tests at 2.5 deg angle of attack for the deflection of flap 5, elevator, and flap group 2, respectively. In each one of these figures, the vertical force and out-of-plane (OOP) moment at the rotation point and HTP root are shown as a function of the normalized control deflection (CS). The deflection spans the excursion limits for these surfaces, where +1 represents the upper limit (30 deg), and -1 represents the lower limit (-30 deg). The loads at the rotation point are a function of both the loads generated by the wing and the HTP, being the former the most significant one. Both the experimental results and the nonlinear simulation results predicted by UM/NAST are shown in these figures. Additional open-loop tests results are presented in Appendix H.

These results show that the UM/NAST model for the EASE aircraft overestimates the loads generated by the lifting surfaces and their control surfaces. Figures 6.13 and 6.14, in particular, show that the loads generated by the wing when no flaps are deflected (CS=0) have a significant error in comparison with the experimental results. This indicates that the aerodynamic modeling of this member in UM/NAST was not accurate. Similarly, when the flap deflection is nonzero, either for a single or a group of flaps, the UM/NAST model predicts a higher authority for these surfaces than what was observed in the experimental results. This is evident from the different slopes in these figures.

Figure 6.15 shows that the UM/NAST model provided a better matching for the loads on the HTP when the elevator deflection was zero. However, Similarly to what was seen for the wing, the control authority predicted by UM/NAST is higher than what was observed in the wind tunnel. It is interesting to highlight that the UM/NAST model considered a rigid HTP member, therefore the static loads are constant when the elevator deflection is also constant. In the experiment, however, the load cell on the HTP root captured variations on

Table 6.2: Open-loop (OL) and closed-loop (CL) experimental tests.

TestID	**Type**	**Signal**	**Inner loop**	**Outer loop**	**MLA wing**	**MLA HTP**	**Notes**
100-115	OL	Step	off	off	off	off	Locked pitch. Control surface variation between min and max excursion.
120-135	OL	Sweep	off	off	off	off	Locked pitch. Control surface variation between min and max excursion. Frequency: 0.5–10Hz.
140-154	OL	Impulse	off	off	off	off	Locked pitch. Control surface variation between min and max excursion.
321	CL	Step	off	off	off	off	Free pitch. Aero id at angles of attack from -7.8 to 9 deg.
331, 540, 560, 580	CL	Step	on	off	off	off	Sequence of pitch step commands from -2.5 to 7.5 deg.
520-523, 541-543, 561-563	CL	MVS	on	off	off	off	1, 3 and 6 consecutive cycles of MVS maneuver. Low, medium, and high gains for inner loop.
524-526, 544-546, 564-566, 581-583	CL	MVS	on	on	off	off	1, 3 and 6 consecutive cycles of MVS maneuver. Combination of low, medium, and high gains for controller loops.
527-529, 547-550, 567-569, 584-587, 601-604	CL	MVS	on	on	on	off	1, 3 and 6 consecutive cycles of MVS maneuver. Combination of low, medium, and high gains for controller loops.
530-534, 551-555, 570-572, 588-592, 605-607	CL	MVS	on	on	on	on	1, 3 and 6 consecutive cycles of MVS maneuver. Combination of low, medium, and high gains for controller loops.

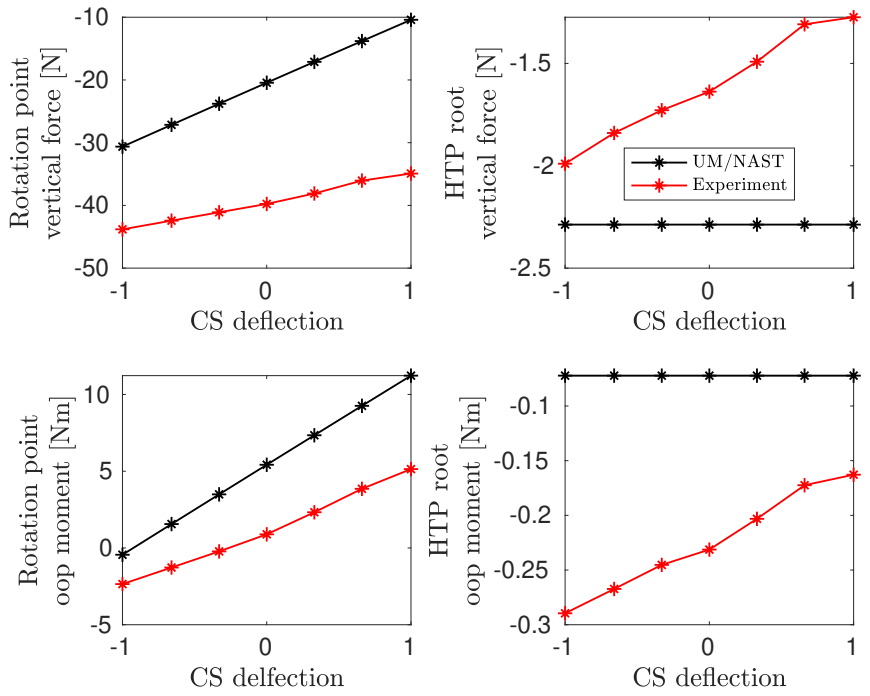

Figure 6.13: Static load cell measurements (TestID 104). CS = flap 5.

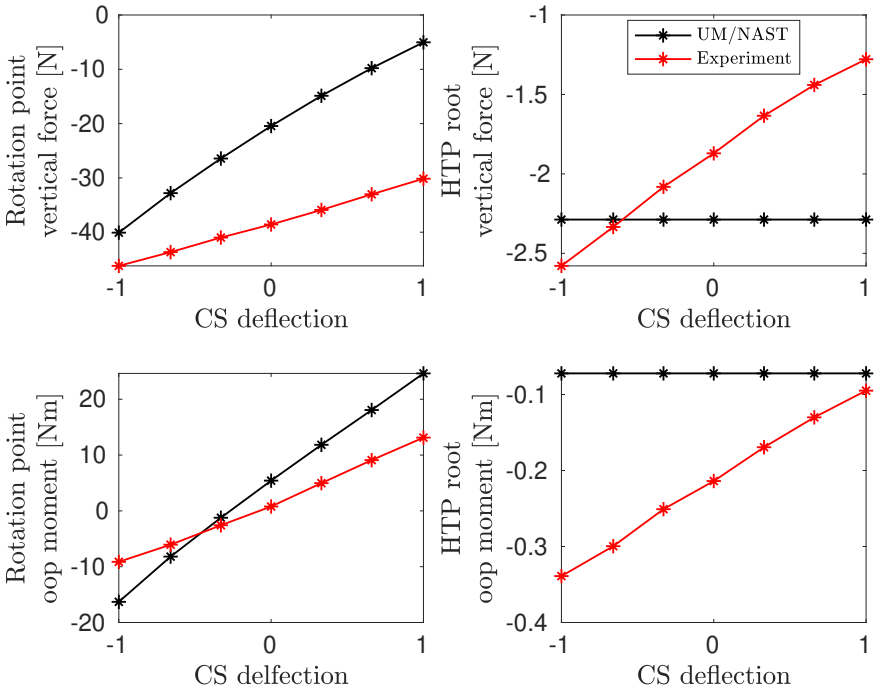

Figure 6.14: Static load cell measurements (TestID 112). CS = flap group 2.

both the force and moment on this member. Potential causes are: i) the variation in the interference of the wing on the tail due to the deflection of the wing flaps; ii) fluctuations in

speed and/or temperature at different test points; iii) the inherent flexibility of the HTP is non-negligible.

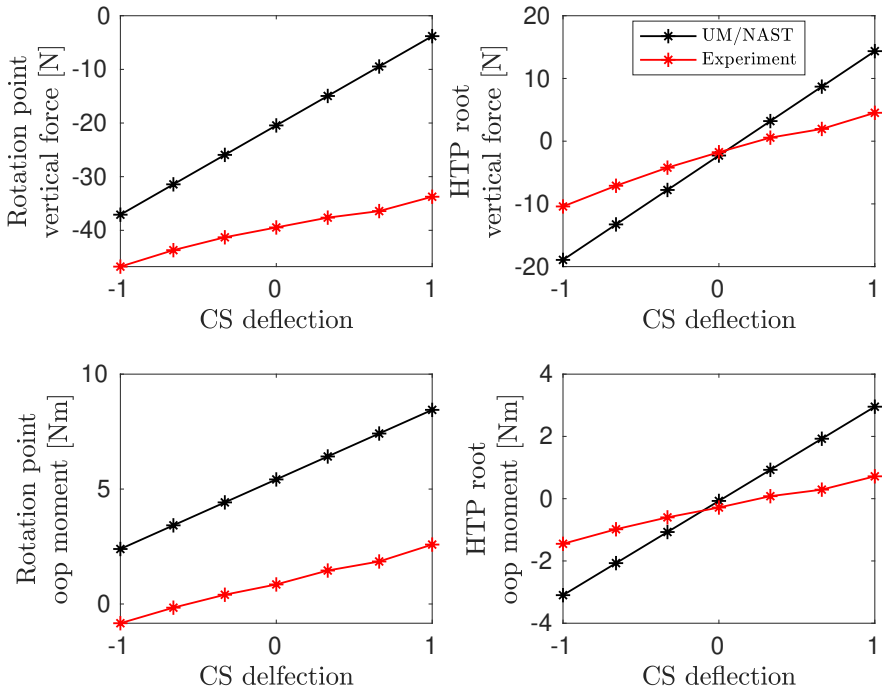

Figure 6.15: Static load cell measurements (TestID 111). CS = elevator.

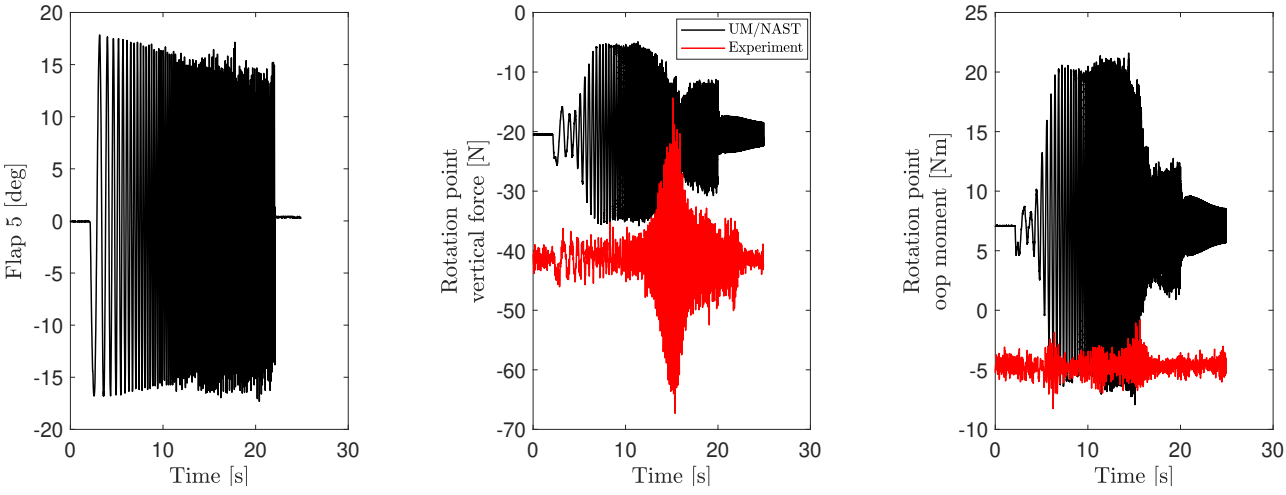

Figure 6.16: Dynamic load cell measurements (TestID 125). CS = flap 5.

The different loads on the wing generated a different geometry on the flexible structure than what was predicted by UM/NAST. As a consequence, the dynamical behavior of the wing was changed. This is demonstrated in Fig. 6.16. In this test, a frequency sweep from

0.5 to 10 Hz and 20 deg of amplitude was input to flap 5. Fig. 6.16 shows the resulting control deflection as recorded by the encoder, and the loads at the rotation point. Note that the amplitude of the flap deflection decreases with the frequency due to the servo dynamics. The same flap deflection was then used to run an equivalent dynamic simulation in UM/NAST. From the force and moment amplitudes, it is clear that the sweep excites different frequencies in the numerical and real models. This, alongside the static results, show that the UM/NAST model did not capture the dynamics of the system accurately.

A byproduct of the open-loop tests was the realization that the HTP with zero incidence angle was not providing enough pitch control authority for positive pitch angles. Therefore, the tail incidence angle was reduced to -5 deg to correct this problem and allow symmetric maneuvers such as the MVS. The closed-loop results shown in the next section were obtained with the corrected HTP incidence angle.

6.6.2 Closed-loop Tests

6.6.2.1 Inner-loop Controller

Figure 6.18 shows the inner-loop controller (ILC) performance in tracking a sequence of pitch angles starting at 2.5 deg and varying between -2.5 deg and 7.5 deg. The elevator was the only control surfaces used for controlling the pitch attitude, while the flaps on the wing remained at zero deflection. These results show that the ILC is able to drive the pitch angle to the desired reference value without saturating the controller. However, oscillations are seen whenever the controller tracks a constant command. This can be explained by external factors, such as turbulence in the wind tunnel, or any delay in the control system.

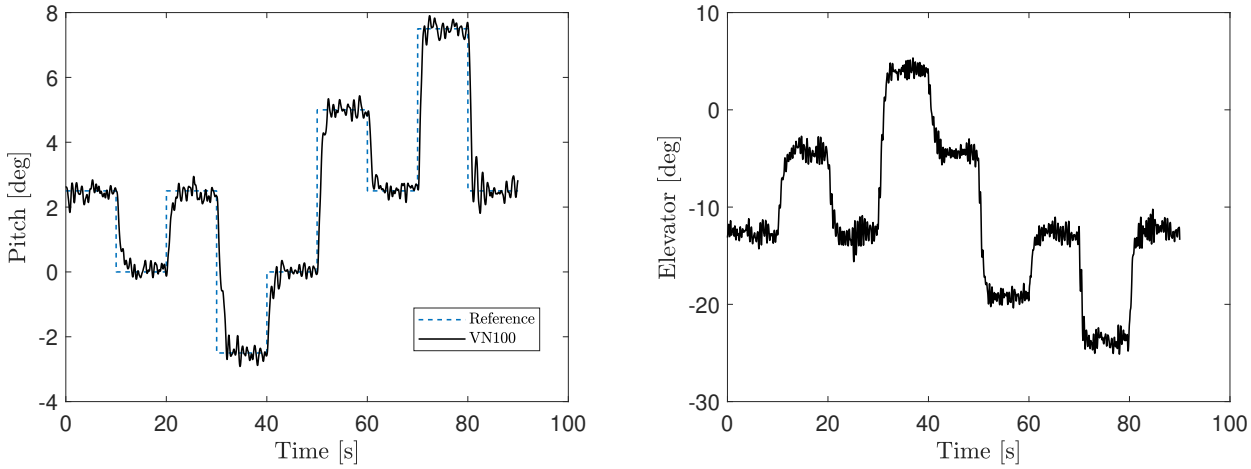

Figure 6.17: ILC tracking step commands (TestID 331).

Figure 6.18 shows a comparison between the three different gain levels for the ILC. The high gain controller had the shortest rise time, followed the medium gain controller and the low gain controller. Note that each one of the tests had a different initial condition, which affected the step response of these controllers. The high and medium gain controllers resulted in slightly larger oscillations on the pitch response, and significantly larger control effort.

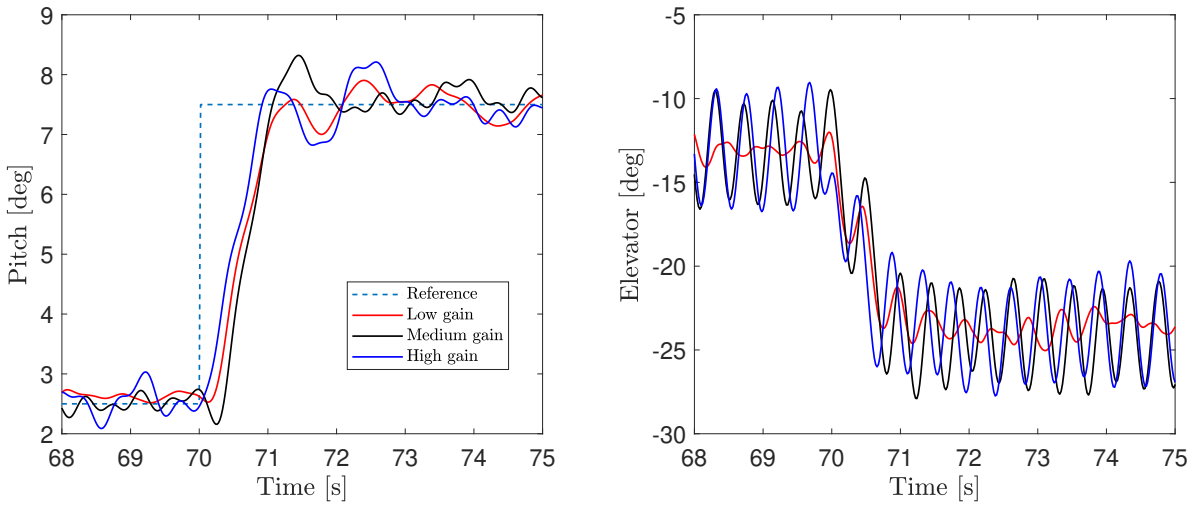

Figure 6.18: Comparison between different gain levels of ILC (TestID 331, 540, 580).

Table 6.3 shows a comparison between the rise time seen in nonlinear UM/NAST simulations, and the one observed in the wind tunnel experiment for each ILC gain level. It is apparent that the ILC in the actual vehicle was slower than predicted.

Table 6.3: Inner-loop controller rise time.

Gain level	**UM/NAST**	**Experiment**
Low	1.0 s	2.1 s
Medium	0.5 s	1.6 s
High	0.3 s	1.2 s

6.6.2.2 Baseline MVS Maneuver

Figure 6.19 shows the pitch response of the closed-loop system using medium level gains when tracking one cycle of the MVS maneuver. In the figure, it is shown the results for the configuration in which only the ILC is present (MPC off), and the configuration in which the MPC in the outer-loop (MPC on) is active, but no MLA constraints are imposed. The MPC

off case serves as a baseline to assess the performance of the outer-loop. For each one of these configurations, it is shown the reference commanded by the user, the reference received by the ILC, and the pitch response as measured by the VN100 IMU unit on the fuselage. As

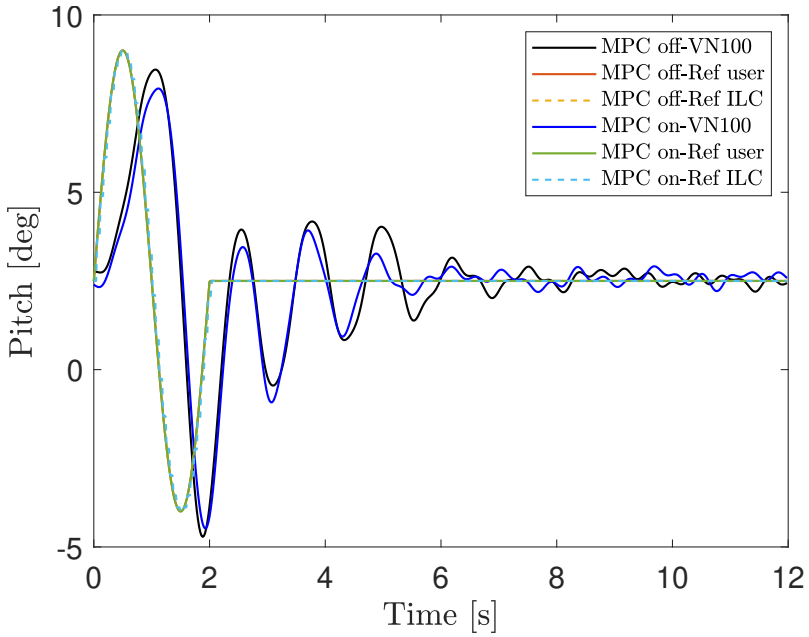

Figure 6.19: MVS, 1 cycle, No MLA constraints (TestID 544). Commanded pitch angle and aircraft response.

shown in Fig. 6.19, the outer-loop preserves the reference fed into the inner-loop, which is expected since no load constraints are present in the problem. Small differences between the pitch responses is due to the variations in the initial condition of the maneuver or in airflow condition. In both cases shown in the figure, it is clear that the tracking error is nonzero due to differences in amplitude and phase, and that the transient after the maneuver is over is large. Figure 6.20 shows the out-of-plane bending moment at the HTP root, and the strain along the wing spar at the root station. The strain measurement was obtained from the strain gauge and it is proportional to the out-of-plane bending moment at that station. No significant change in these loads were observed between the two responses.

The control surfaces histories to perform the baseline MVS maneuver are shown in Fig. 6.21. In the cases shown, only the elevator was engaged while the flaps remained at the trim condition, since no load alleviation was performed.

Figure 6.22 shows the tracking of three consecutive cycles of the MVS maneuver. Similarly to the case shown in 6.20, no MLA constraints were enforced. This longer maneuver, however, shows a worse performance of the ILC after the first cycle of the maneuver, with a larger tracking error. This can be possibly explained by the more pronounced motion of the wing

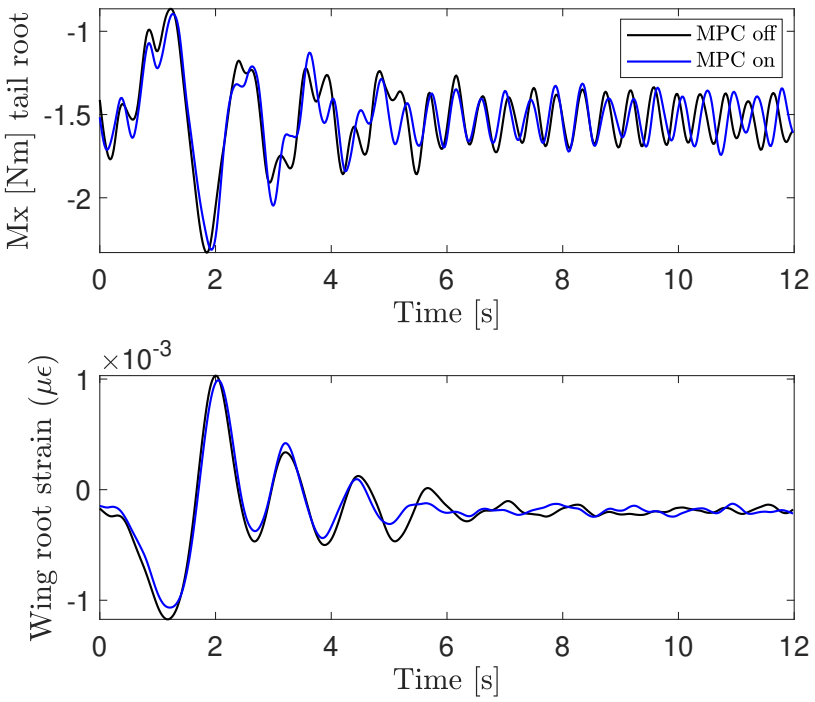

Figure 6.20: MVS, 1 cycle, No MLA constraints (TestID 544). Out-of-plane bending moment on HTP tail root, and strain on wing root.

after the dip, which impacted the performance of the ILC in tracking subsequent cycles.

Figure 6.23 shows the loads on the HTP and wing root, while Fig. 6.23 shows the control histories to perform the three cycle maneuver. The smaller pitch magnitudes after the first cycle is connected with smaller elevator deflection and, consequently, to a reduction in the loads in comparison to the ones observed in the first cycle.

Additional results for the one (TestID 544) and three cycle (TestID 545) MVS maneuver are shown in Figs. H.3-H.6 and H.21-H.24, respectively, in Appendix H.

6.6.2.3 MVS Maneuver with MLA Constraints on Wing

Figure 6.25 shows the pitch response of the EASE aircraft to one MVS cycle while the MLA constraints on the three wing stations were enforced. The constraints on the HTP were not present in this case. This response is compared against the baseline MVS response when the outer-loop is deactivated as shown in Fig. 6.19. Note that the pitch reference received by the ILC when the wing MLA constraints were included is the same as the user reference, except for a short period of time when it deviates to negative values. This behavior usually happens when the MPC controller cannot find a feasible solution with only the flap deflection to avoid the load violation. Nevertheless, the pitch response was close to the baseline response.

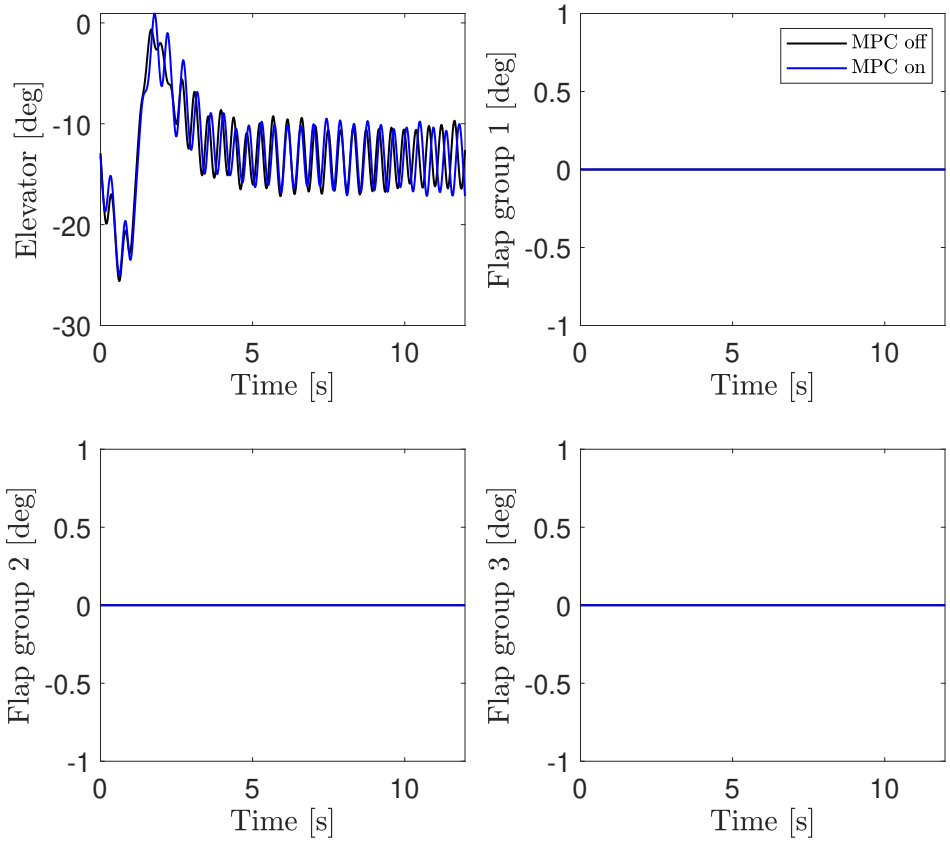

Figure 6.21: MVS, 1 cycle, No MLA constraints (TestID 544). Control surfaces histories.

The MPC controller was able to reduce the loads on the wing, as can be seen in Fig. 6.26. Compared to the baseline response, the strain on the wing root at the first dip was reduced by 25%, while at the first peak it was reduced by 11%. This shows that the LA governor architecture could preserve the pitch response while reducing the loads on the wing. The reduction, however, did not reach the 33% target. The peak loads on the HTP remained the same.

The control surfaces histories are shown in Fig. 6.27. Differently from the cases seen in Section 6.6.2.2, now the flaps were deflected to perform load alleviation on the wing. After the maneuver was finished, the flaps returned to their trim value in order to reduce drag. The flaps deflection was below its maximum allowed magnitude, however, its rate of change did hit the limits. The MPC controller was able to find a feasible solution in all updates throughout the entire test. Figure 6.28 shows the number iteration taken by the QP solver to find the solution, the feasibility status (status 1 means that a feasible solution was found), and the computation time. The latter is divided into the time taken by the QP solver to find

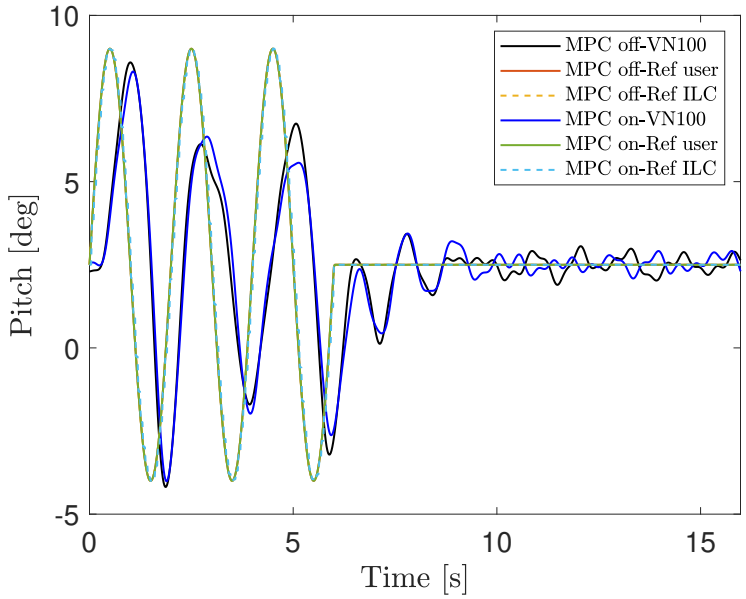

Figure 6.22: MVS, 3 cycles, No MLA constraints (TestID 545). Commanded pitch angle and aircraft response.

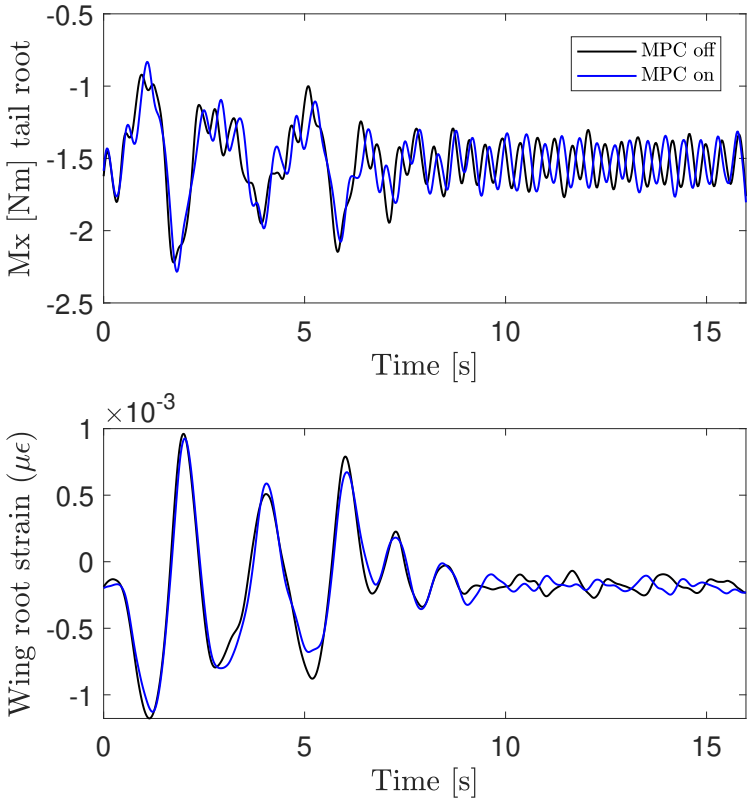

Figure 6.23: MVS, 3 cycles, No MLA constraints (TestID 545). Out-of-plane bending moment on HTP tail root, and strain on wing root.

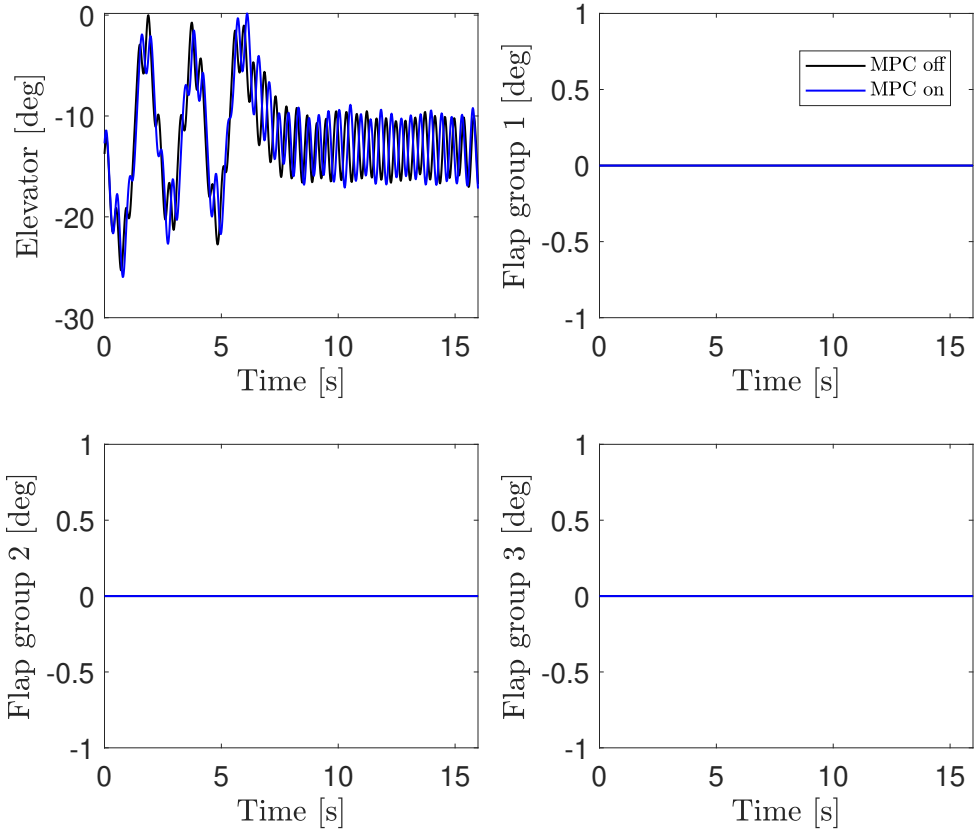

Figure 6.24: MVS, 3 cycles, No MLA constraints (TestID 545). Control surfaces histories.

the solution, and the frame time which included the entire control system update. Similar results were seen for all wind tunnel tests. This indicates the potential of implementing MPC-based MLA systems for large scale aircraft models in real-time.

The pitch response of the EASE model when tracking the three-cycle MVS maneuver is shown in Fig. 6.29. Similarly to the baseline response presented in Fig. 6.25, the tracking error increases after the first cycle. However, when performing the MLA on the wing, the pitch response had a magnitude closer to the desired reference, probably due to the interference of the flap deflection in the pitch motion. The loads developed during the three cycle maneuver are shown in Fig. 6.30. The load reduction was comparable to the one seen in Fig. 6.26: 25% reduction at the first dip, and 12% reduction at the first peak. The loads on the tail after the first cycle increased, probably due to the adverse pitch moment created by the flap deflections, which had to be corrected by the elevator. This behavior can be confirmed by analyzing the control surfaces histories in Fig. 6.30. There is a visible difference between the elevator responses during the maneuvers. The flaps, similarly to

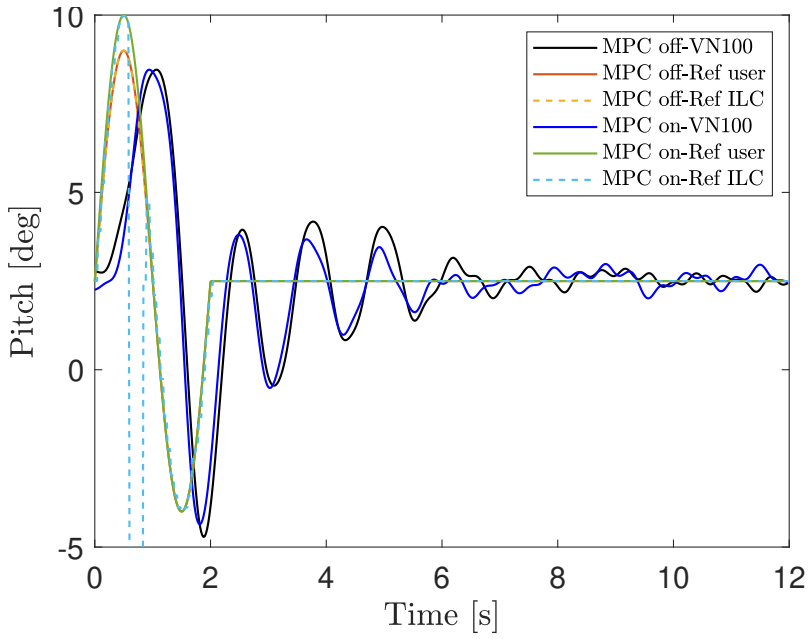

Figure 6.25: MVS, 1 cycle, MLA constraints on wing only (TestID 547). Commanded pitch angle and aircraft response.

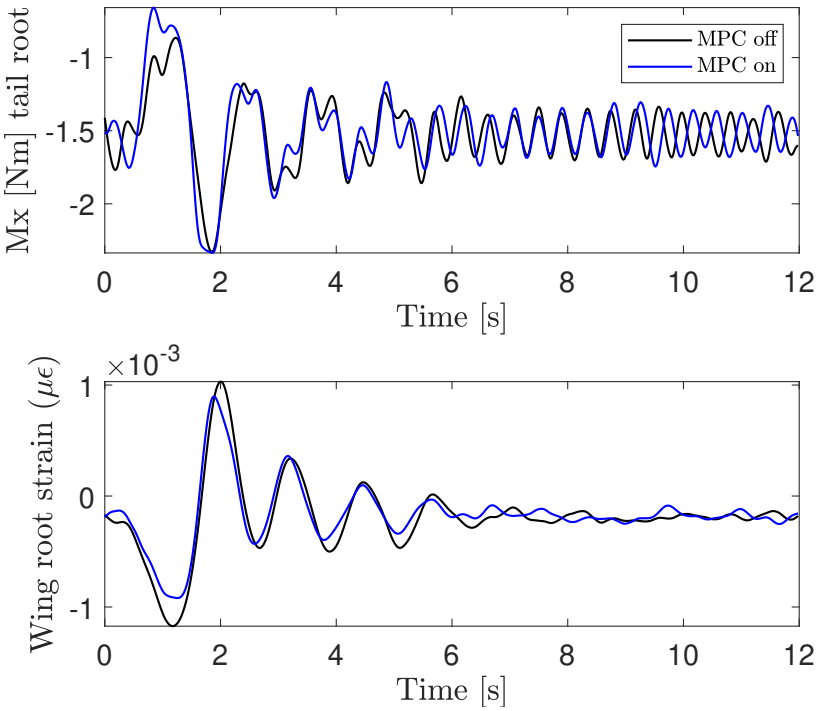

Figure 6.26: MVS, 1 cycle, MLA constraints on wing only (TestID 547). Out-of-plane bending moment on HTP tail root, and strain on wing root.

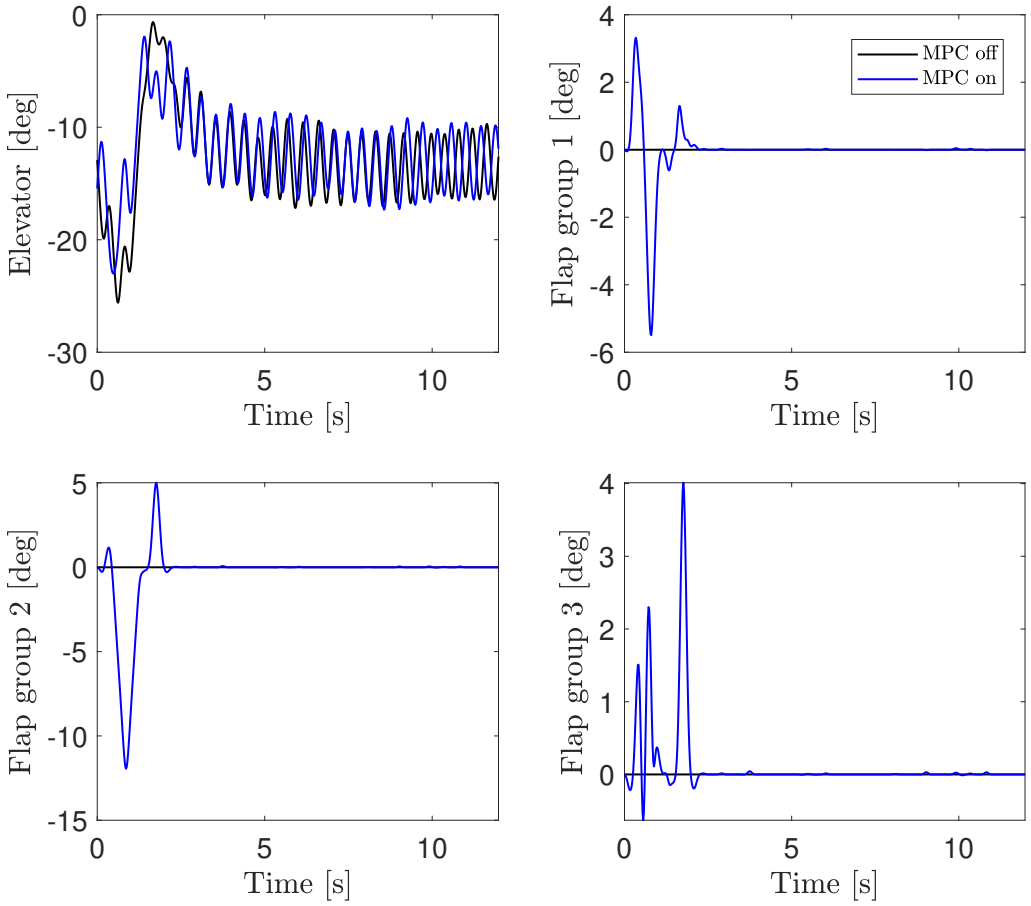

Figure 6.27: MVS, 1 cycle, MLA constraints on wing only (TestID 547). Control surfaces histories.

Fig. 6.27, were deflected only when the load constraints became active, and then returned to the trim condition. In both Figs. 6.27 and 6.31, the flap group 2 had the largest deflection to avoid constraint violations, indicating its largest efficiency in performing MLA. This can be explained by their more outboard position than that of flap group 1, and their larger contribution to the total lift than that of flap group 3.

Additional results for the one (TestID 547) and three cycle (TestID 548) MVS maneuver are shown in Figs. H.7-H.9 and H.25-H.28, respectively, in Appendix H. Even though load alleviation was observed in several attempts to perform the MVS maneuver as shown in the results presented here, there were some instances in which little or no load reduction was seen, probably due to variations in the initial conditions of the maneuver. Figures H.10-H.16 (TestID 547-b) in Appendix H illustrate one of these occurrences.

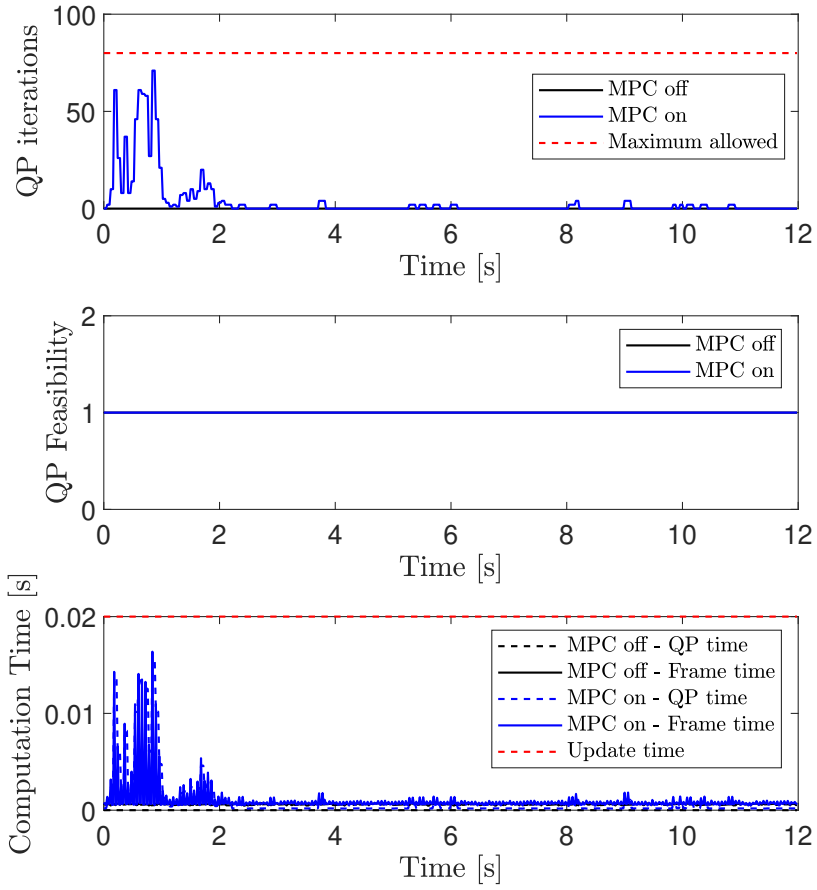

Figure 6.28: MVS, 1 cycle, MLA constraints on wing only (TestID 547). Computational time and optimization solver performance.

6.6.2.4 MVS Maneuver with MLA Constraints on Wing and Tail

The HTP root moment constraints were included in the wind tunnel tests shown next, in addition to the curvature constrains on the wing. Figure 6.32 shows the reference received by the ILC and the pitch response for a one cycle MVS maneuver. Different from the results seen in Sections 6.6.2.2 and 6.6.2.3, the reference generated by the outer-loop has substantial discrepancies from the user-defined signal. This is seen not only during the maneuver, but also after the maneuver ends. Consequently, a large tracking error is observed, especially after 1.8 s, which fails to satisfy the MLA system requirement of minimizing trajectory deviation (Chapter 4).

Figure 6.33 shows the resulting loads on the aircraft during the maneuver. There was a reduction in the peak loads on both wing and HTP. On the wing root, the strain was

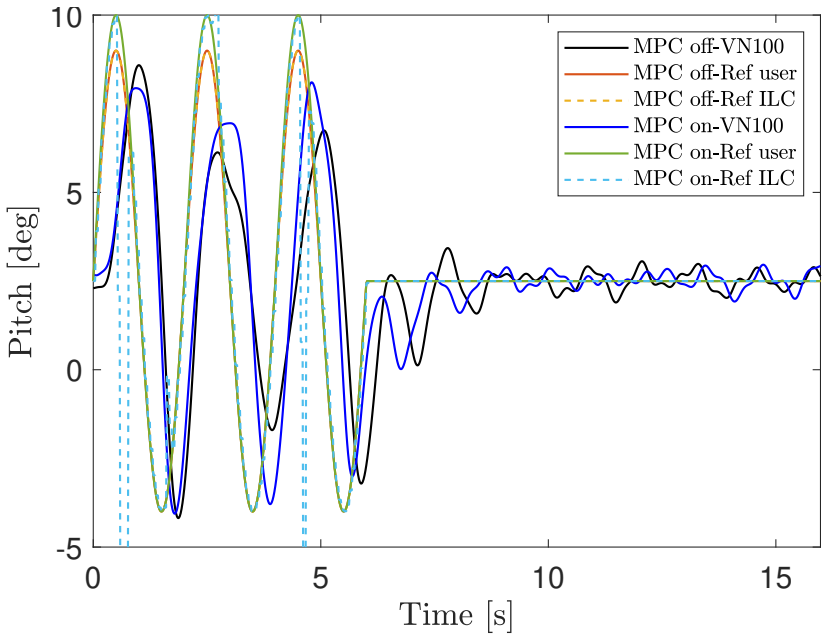

Figure 6.29: MVS, 3 cycles, MLA constraints on wing only (TestID 548). Commanded pitch angle and aircraft response.

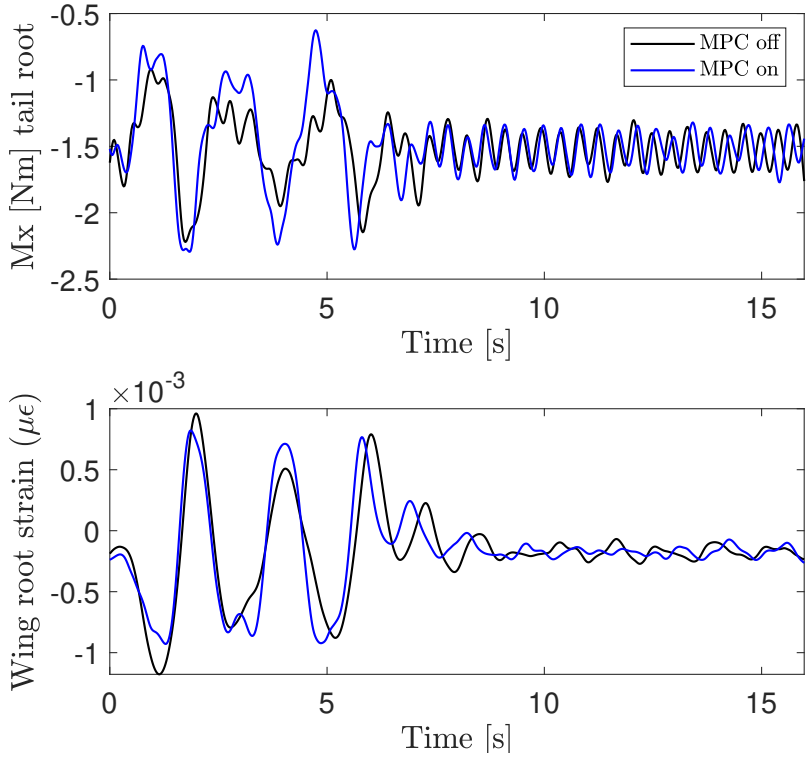

Figure 6.30: MVS, 3 cycles, MLA constraints on wing only (TestID 548). Out-of-plane bending moment on HTP tail root, and strain on wing root.

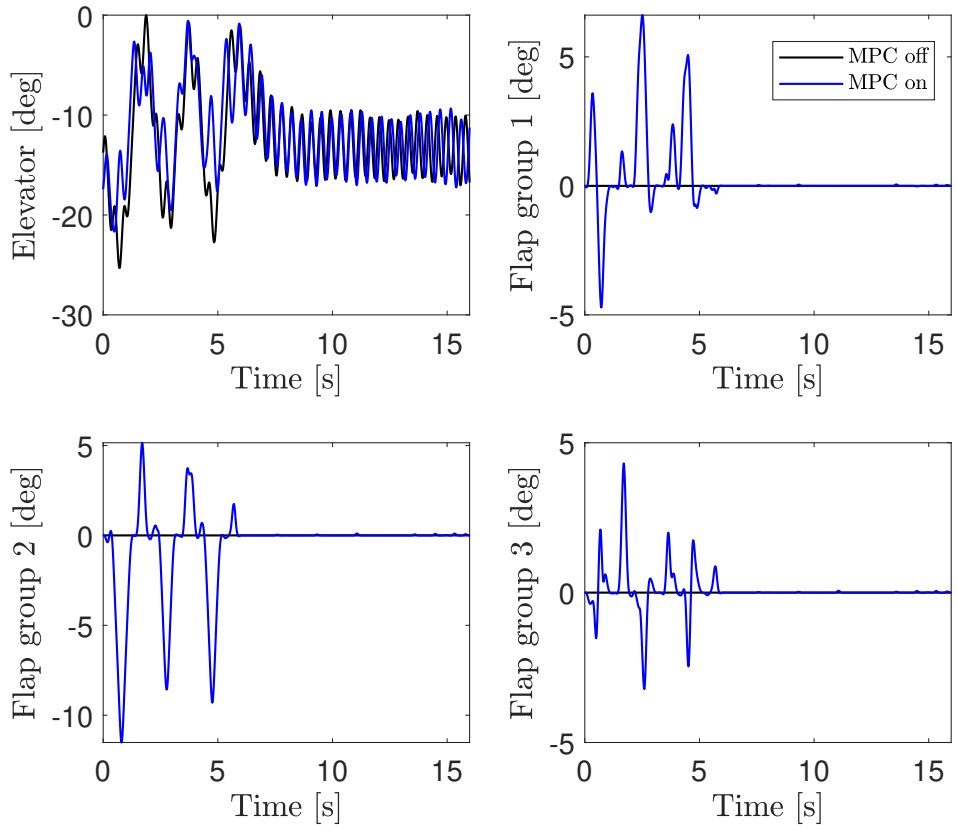

Figure 6.31: MVS, 3 cycles, MLA constraints on wing only (TestID 548). Control surfaces histories.

reduced by 32% at the first dip, and the 23% at the first peak. At the tail root, the moment was reduced by 43%. Note that the loads on the wing after the maneuver ended are higher than the baseline result due to the erratic behavior of the pitch response in that segment. However, these loads were still below the peak loads developed during the maneuver. The high percentage of reduction in the tail indicate that the MPC controller was over-actuating to keep the loads within the bounds.

Figure 6.34 shows the control surfaces histories. Similar to the reference generated by the outer-loop, the flaps presented an unintended behavior after the maneuver was ended. The deflection reached values close to 12 deg, when they should have been zero. The elevator deflection had a considerable deviation from the baseline result due to the wrong pitch reference generated by the LA governor. This erratic behavior is probably due to the wrong prediction of the MPC controller that would led to constraint violations, while in reality the aircraft was in a safe condition. As shown in Section 6.6.1, the UM/NAST model used for

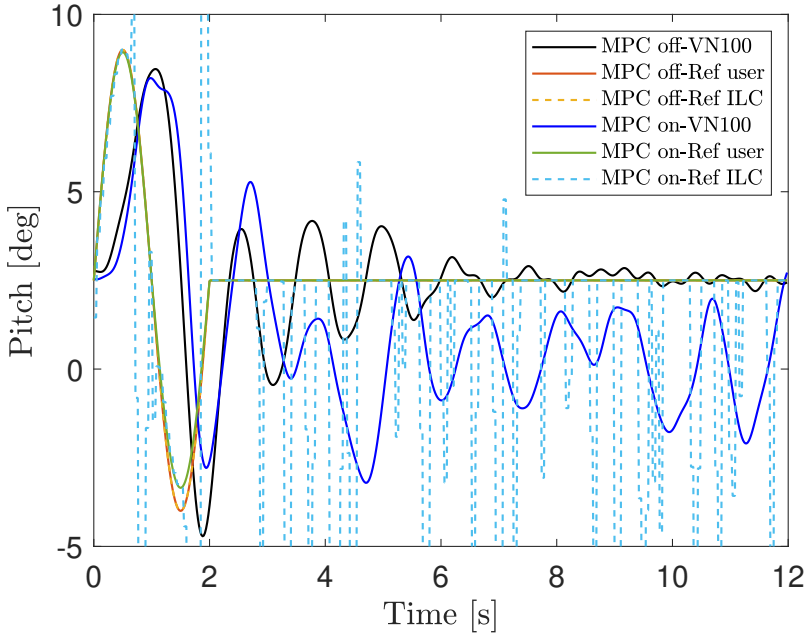

Figure 6.32: MVS, 1 cycle, MLA constraints on wing and HTP (TestID 570). Commanded pitch angle and aircraft response.

prediction had considerable differences in load output than what was observed in the wind tunnel, what could explain the wrong MPC prediction and actuation.

The pitch response for an equivalent test for the three-cycle MVS maneuver is shown in Fig. 6.35. Again, the inclusion of the tail constraint resulted in significant trajectory deviations. Furthermore, the reference generated by the outer-loop had an undesired behavior after the maneuver ended due to the possible wrong prediction in the MPC controller. Despite the erratic behavior, the LA governor was able to reduce loads on the wing and tail. Figure 6.36 shows a 43% reduction in the wing strain at the first dip, a 29% reduction at the first peak. At the HTP root, the reduction was 59% at the first dip, and 30% at the third dip. The control surfaces deflections to achieve these results are shown in Fig. 6.21.

Additional results for the one (TestID 570) and three cycle (TestID 554) MVS maneuver are shown in Figs. H.17-H.20 and H.29-H.32, respectively, in Appendix H.

6.7 Conclusions of Experimental Work

The results presented in Section 6.6 elucidate some important achievements towards the validation of MPC-based MLA systems:

1. The LQ-I controller in the inner-loop was able to change the pitch attitude of the

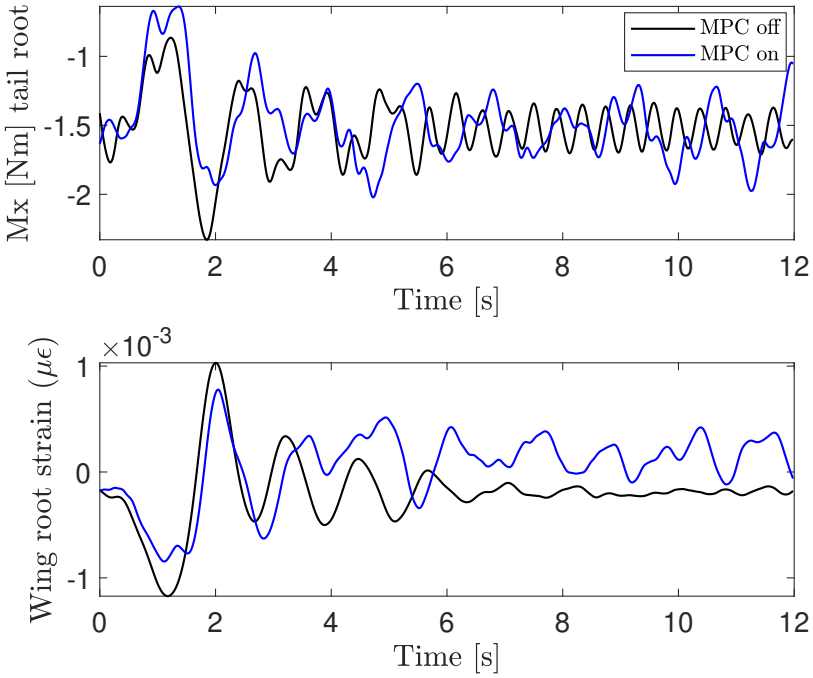

Figure 6.33: MVS, 1 cycle, MLA constraints on wing and HTP (TestID 570). Out-of-plane bending moment on HTP tail root, and strain on wing root.

aircraft to track the desired reference. Moreover, the outer-loop wrapped around the inner-loop preserved the nominal response of the LQ-I controller when the MLA constraints were inactive. It is important to note that this LQ-I controller is a proxy for a FCS system in an actual aircraft. As discussed in Section 3.2.2, the LA governor architecture can preserve the existing control systems in an aircraft and augment it to enable load alleviation through constrained control.

2. The MPC-based load alleviation system was able to reduce loads on the wing and tail, either singly or simultaneously. This showcases the ability of this controller technique to satisfy multiple objectives. As discussed in Section 1, most traditional load alleviation systems cannot achieve load reduction in multiple stations on the wing and tail.

   Furthermore, the LA governor based on a linear MPC design was able to reduce the peak loads despite the considerable model mismatch and the nonlinear behavior of the VFA. This showcases the robustness of the controller in enforcing constraints, and indicates that a linear MPC design may be sufficient for handling the load alleviation problem in VFA.

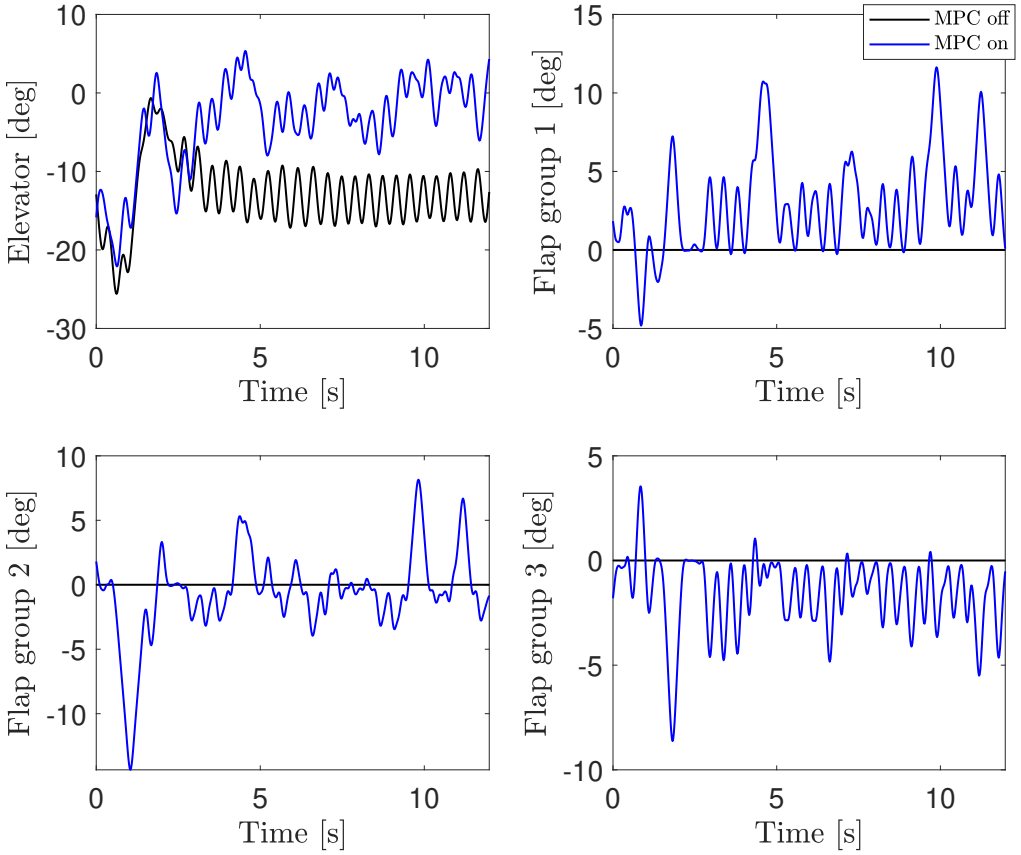

Figure 6.34: MVS, 1 cycle, MLA constraints on wing and HTP (TestID 570). Control surfaces histories.

3. The MPC controller for a large-scale system was implemented successfully in real-time. The LA governor operated continuously for several hours in the wind tunnel experiment and provided feasible solutions at every update. This indicates the potential feasibility of implementing MPC-based load alleviation systems for FA and VFA.

The experiment also uncovered some shortcomings in both the aircraft model used for design and the control system design:

4. The open-loop test results showed a considerable discrepancy between the loads predicted by the UM/NAST model and the actual loads measured by the experiment. The UM/NAST model overestimates the loads on both wing and tail. This error is likely to be associated with a poor representation of the aerodynamic model for the EASE aircraft, and the possible causes include: i) the wing pod gaps were not considered when modeling the wing member; ii) the interference of the wind tunnel wall on the

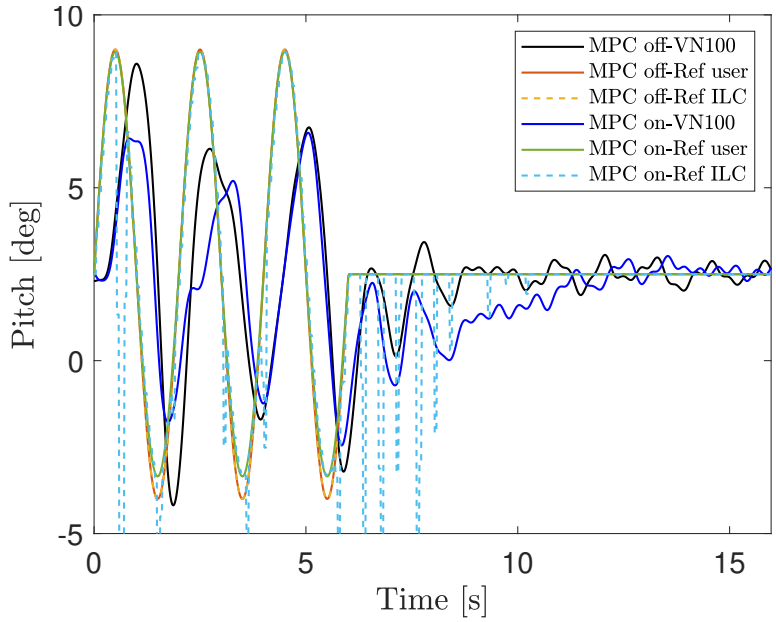

Figure 6.35: MVS, 3 cycles, MLA constraints on wing and HTP (TestID 548). Commanded pitch angle and aircraft response.

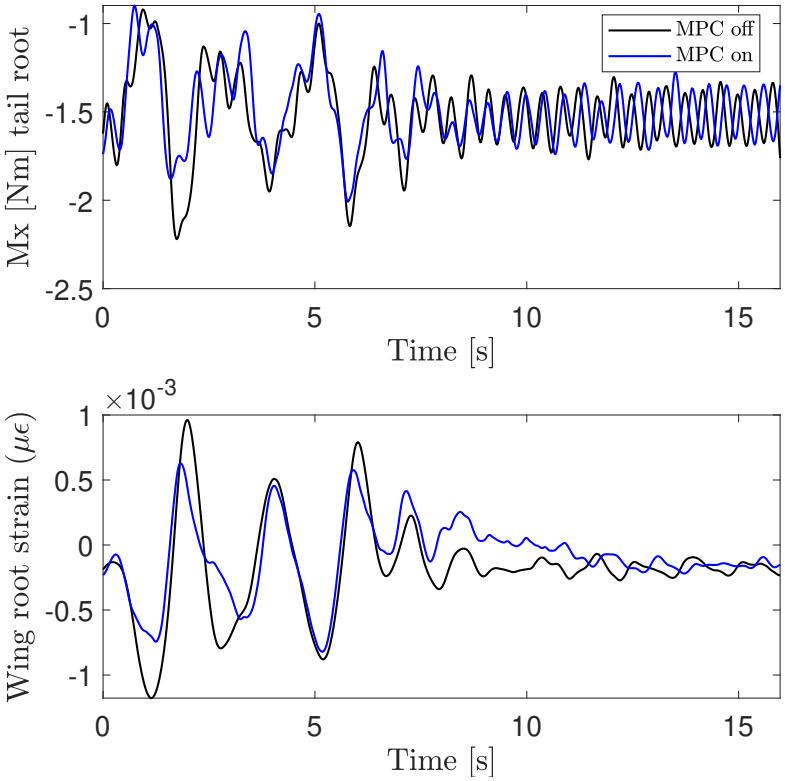

Figure 6.36: MVS, 3 cycles, MLA constraints on wing and HTP (TestID 554). Out-of-plane bending moment on HTP tail root, and strain on wing root.

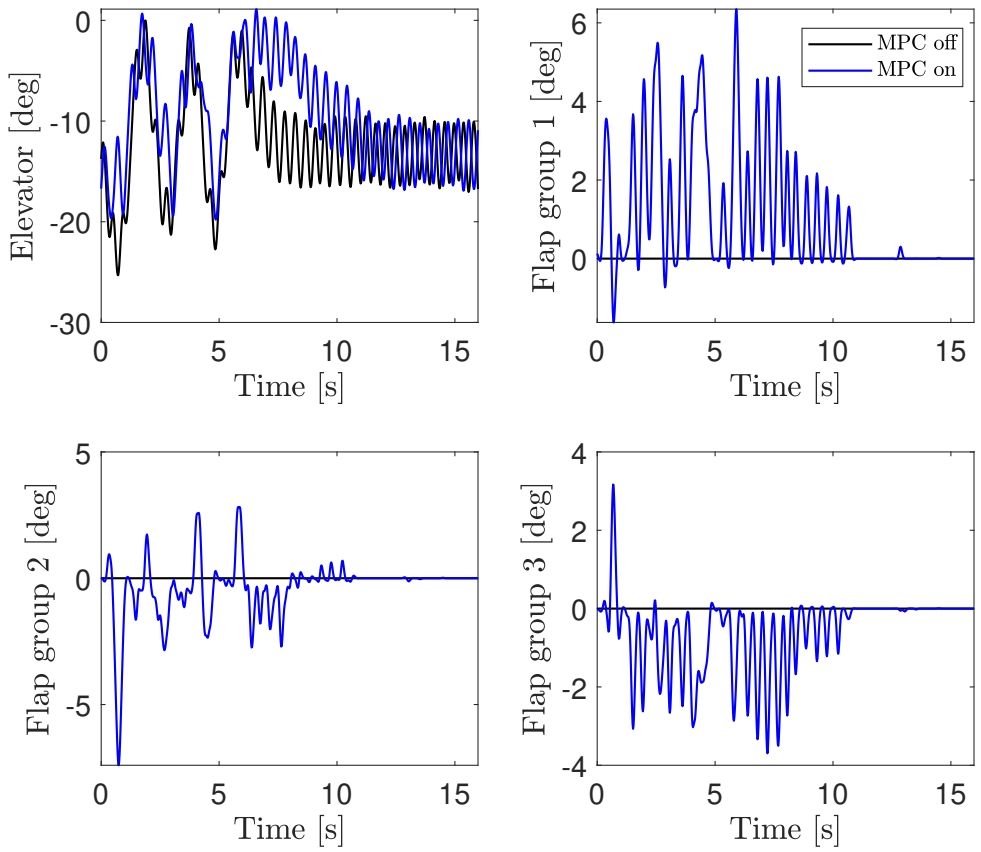

Figure 6.37: MVS, 3 cycles, MLA constraints on wing and HTP (TestID 554). Control surfaces histories.

tail and inboard section of the wing. Additionally, it is important to note that the fuselage flexibility and aerodynamics were neglected in the UM/NAST model. Even though these factors may not contribute directly to the vertical force and out-of-plane bending moment errors seen in Section 6.6.1, they can affect the pitch motion of the aircraft by creating drag and induce vibrations on the wing and tail members.

5. The inner-loop controller was slower than predicted in simulations, and had poor performance in tracking the sinusoidal (MVS) maneuver, especially after the first cycle. Potential causes for this behavior are: i) the LQ-I controller could not handle the coupled rigid body pitch motion and flexible wing motion, which may indicate that a nonlinear controller may be needed; ii) the rate limits on the elevator were too stringent, thus not allowing a faster response of the controller; iii) the latency in the system due to the DAQ and servos. After the experiment, it was determined that the combined delay could have been as high as 60 ms.

6. The load alleviation percentage was smaller than predicted in simulations, and incon-

sistent between different attempts to perform the maneuver. Furthermore the MPC controller mistakenly predicted constraint violations when the HTP constraints were included that led to the overuse of flaps and deviation from the nominal pitch trajectory. The model mismatch is probably the main cause for this behavior for two reasons: i) the authority of the flaps on the wing was overestimated; ii) the loads on the tail were overestimated, therefore leading the constraints to become active even when the aircraft was in a safe condition. Moreover, the constraints on the stringent flap rates could also explain the smaller reduction in loads.

It is apparent that model tuning and controller redesign are needed for improving the performance of the LA governor architecture. The open-loop test results can be used for adjusting the aerodynamic model of EASE aircraft in UM/NAST. For the inner-loop controller, the LQ-I controller could be modified to include an echo system representing the MVS maneuver, or it could be replaced by other linear (e.g., H_∞ synthesis with a peak filter at the MVS maneuver frequency) or nonlinear (e.g., dynamic inversion) control techniques.

CHAPTER 7

Conclusions and Recommendations

This Chapter provides a summary of this work, including the main conclusions and key contributions of the constrained control design for load alleviation in flexible and very flexible aircraft. Recommendations are given for future work.

7.1 Summary and Main Conclusions

This work has investigated constrained control for designing load alleviation systems for flexible and very flexible aircraft. These control methods, in particular MPC and reference governor, can provide several advantages to these systems due to their ability to enforce pointwise-in-time constraints. Two scenarios were investigated: the reduction of loads induced by maneuvers, which is connected to a reference tracking problem, and the reduction of loads at the encounter of gusts, which is connected to disturbance rejection problems. The objective was to reduce the peak out-of-plane bending moment while complying with requirements usually observed by the aeronautical industry.

Two MPC-based architectures for load alleviation were presented: the MPC architecture, which integrates the flight control system and load alleviation system; and the LA governor architecture, which is an MPC-based add-on to the conventional FCS to enable load alleviation. The control design formulation for both architectures was presented and their performance was evaluated through numerical simulations of a VFA. The results showed that the MPC architecture may have a smaller computational cost. On the other hand, the LA governor architecture has salient practical advantages for preserving the existing FCS, which could be a more cost-effective choice for airframe manufacturers.

Several strategies to reduce the computational cost of designing and implementing these MPC-based load alleviation systems for VFA were presented. First, the use ROMs, either linear (balanced residualization) or nonlinear (B2T and T2B), facilitate the design of controllers for these large-scale systems by reducing the number of states. Second, the ag-

gregation of constraints in a smaller set of composite functions can result in up to 90% in the maximum computational time of an MPC update step. Dividing the constraints in groups and distributing these groups in time when updating the MPC controller can also contribute with a reduction in 67% in the maximum computation time. Third, move blocking techniques, such as input blocking, can reduce the number of decision variables in the OCP and, consequently, the computational cost. Furthermore, several remarks were made about the proper selection of the optimization solver for this application. In particular, active set methods with warmstarting provided the best performance among the solvers tested.

Numerical simulations were run to assess the performance of the proposed control systems in performing MLA in FA and VFA. The strategy to reduce bending moment by constraining the shape of the flexible wing and tail at critical stations showed to be efficient. Reductions between 20% and 58% percent were achieved with minimum trajectory deviation. To handle the different mass configurations that affect the response of the aeroservoelastic system, a scenario-based MPC was designed based on relevant configuration models. Using such an approach, a single MPC controller was able to enforce constraints for seven different aircraft model, which was not possible with the conventional design based on a single model.

To perform GLA, the load alleviation architectures were augmented with LIDAR measurements. The disturbance preview was obtained through the reconstruction of the gust field from these LIDAR measurements. The preview was incorporated into the MPC design to enable feedforward control action and avoid load violations at the first gust hit. Numerical simulations showed that the modified architectures can reduce loads at encounters with discrete and continuous gust disturbances by 33% in both FA and VFA.

A wind tunnel experiment was conducted to validate the proposed load alleviation system. A half-aircraft model with a very flexible wing and free pitch was designed to be a demonstrator of MLA solutions in a controlled environment. The LA governor architecture based on linear MPC was successfully implemented in real-time for coordinating multiple control surfaces to reduce loads on critical stations on both the wing and tail. Closed-loop tests were run to assess the performance of the control system while commanding the MVS maneuver. The system was able to reduce the out-of-plane bending moment on the wing root by 25%-43%, while the moment on the tail root was reduced by 43%-59%. While these reductions satisfy the design requirements, they were different from what was predicted in simulations. Furthermore, the control system had a poor performance in controlling the vehicle pitch and avoiding trajectory deviations from the baseline response, especially when the constraints on the tail were enforced. Open-loop wind tunnel tests revealed a substantial difference between the numerical model used for design and the actual aircraft response, which could explain the defective performance of the control system. Despite of the model

mismatch, the experiment showcased the capability of constrained control in coordinating multiple load alleviation objectives.

7.2 Key Contributions

The key contributions of this dissertation can be summarized as follows:

- Two MPC-based FCS with load alleviation capabilities were proposed that can replace or augment existing flight FCS. The advantages and disadvantages of each architecture were presented and illustrated in numerical simulations. Furthermore, it was shown how these architectures can satisfy the requirements of MLA and GLA system design for very flexible aircraft. In GLA design, it was also demonstrated that the integration of gust preview into the MPC design can enhance the response of the system to external disturbances.

- It was shown how constrained control can be used to perform load alleviation through shape control of flexible and very flexible aircraft. It was demonstrated how shape control can reduce the out-of-plane bending moment on multiple stations, both on wing and horizontal tail plane, by imposing curvature constraints in a small set of critical stations. A procedure to select these stations was also proposed.

- The feasibility of the proposed MLA system was demonstrated experimentally. An enhanced aeroservoelastic (EASE) model representing a half aircraft model was designed for demonstrating load alleviation solutions in very flexible aircraft. A wind tunnel experiment was conducted in which an MPC controller coordinated several control surfaces on the aircraft to alleviate loads on the wing and tail while the vehicle performed a longitudinal maneuver. The MPC controller for the large-scale systems was successfully implemented in real-time. The experimental results corroborated the potential of the proposed MLA system in reducing peak loads in very flexible aircraft.

- MPC with aggregated constraints was introduced. A connection between optimization problems with aggregated constraints and parametric optimization problems was established. Sufficient conditions for the existence and uniqueness of a local minimizer in the optimization problem with aggregated constraints were provided. A framework for nonlinear model predictive control with aggregated constraints (NMPC-AC) was established, as well as a procedure to perform the aggregation. The reduction of the domain of attraction as a result of constraint aggregation was characterized. The performance

of the NMPC-AC and its potential in load alleviation applications were illustrated via a numerical examples flexible and very flexible aircraft.

- It was shown how scenario-based optimization can be used to design an MPC-based load alleviation system that can handle multiple aircraft mass configurations. A method to implement reduce the computational cost of such an approach was proposed in which the constraints are enforced in separate groups that are distributed in time. Numerical simulations showed that the methods is able to enforce load constraints for several aircraft configurations with a reduced computational footprint.

- Several numerical tools were developed or enhanced under the UM/NAST v4 framework for studying load alleviation systems for very flexible aircraft. These include: (i) the enhancement and additional developments in the UM/NAST-Controller module for closed-loop simulations, such as the implementation of the MATLAB interface; (ii) The enhancement of existing sensor models in UM/NAST-Sensors, and the addition of new sensors such as the LIDAR sensor and the gust reconstruction algorithm; (iii) The addition of discrete and continuous gust models fixed in space in UM/NAST-Gust; (iv) The creation of UM/NAST-Optimization Solvers which contains a collection of solvers for constrained and unconstrained optimization especially designed for control and estimation applications; (v) The implementation of load calculation in UM/NAST; among other improvements in the UM/NAST Dynamic and Linearization Solvers.

7.3 Recommendations for Future Work

Over the course of this study, some aspects of the performance of the proposed load alleviation systems revealed areas for needed improvement.

- Despite the experimental work showing the potential of the MPC-based architecture for MLA, a thorough characterization and assessment of the controller performance was not possible. Additional wind tunnel testing is needed to improve the simulation models and re-tune the controller. Additionally, several opportunities to improve on the controller design were identified as discussed in Section 6.7.

- In addition to experimentally verifying the MLA system, the GLA system could also be tested in the wind tunnel. To this end, gust vanes would have to installed in the test section to generate the gust disturbance. Furthermore, the experimental validation of nonlinear MPC solutions would also be interesting, especially for comparing its performance against the linear MPC formulation.

- The computational cost of the MPC solution based on the top-to-bottom or bottom-to-top reduced-order models is high, what could preclude the deployment of these models in a real aircraft. The bottleneck appears to reside in the cost to update the models in consecutive controller updates. Adjustments in either the reduced-order models implementation or in the MPC formulation are necessary to fully benefit from the nonlinear approximations provided by these models in real-time applications.

- The robustness of the MLA systems against external disturbances and the plant's varying parameters (e.g., the aircraft mass) was addressed by the introduction of disturbance preview and scenario-based optimization into the MPC design. Even though the MPC controller is inherently robust to other types of uncertainties (e.g., model mismatch due to model order reduction or unmodeled dynamics, and sensor noise) it could benefit from a more systematic design framework that incorporates information about these uncertainties. Robust methods, such as tube-based MPC could be applied. However, research would have to be conducted to develop an efficient way to design such controllers for a large-scale system.

- The time-distributed constraint approach for scenario-based MPC has shown to be a less computationally expensive implementation than conventional methods, but it still lacks a more theoretical study. It would be interesting to understand the optimal way to define the constraint groups, and whether constraint tightening would be necessary to avoid violations, especially when uncertainties are present.

- Failure mode handling, one of the requirements of MLA/GLA systems, was indirectly addressed by selecting redundant sets of control effectors and sensors in the proposed load alleviation systems. A more robust system would benefit from a dedicated system to detect failures and an internal logic in the MPC controller to adapt to these changes in the plant.

- Even though this work has shed some light on the advantages and disadvantages of using nonlinear aeroelastic models for control design for very flexible aircraft, the results presented here were not conclusive. A more though investigation is needed to understand the limits of applicability of linear models in control design and the benefits of nonlinear representations as a function of the aircraft flexibility.

APPENDIX A

Aircraft Models Properties

A.1 XRF1

Each control effector of XRF1 has an associated actuator with first-order dynamics given by:

$$\text{Elevator}: \quad \frac{1}{\frac{1}{20\pi}s+1}, \tag{A.1}$$

$$\text{Inner ailerons}: \quad \frac{1}{\frac{1}{10\pi}s+1}, \tag{A.2}$$

$$\text{Outer ailerons}: \quad \frac{1}{\frac{1}{12\pi}s+1}, \tag{A.3}$$

$$\text{Rudder}: \quad \frac{1}{\frac{1}{6\pi}s+1}, \tag{A.4}$$

$$\text{Flap}: \quad \frac{1}{\frac{1}{4\pi}s+1}, \tag{A.5}$$

$$\text{Thrust}: \quad \frac{1}{\frac{1}{10}s+1}. \tag{A.6}$$

Seven different XRF1 mas cases are considered in this work, which vary in terms of total mass, mass distribution and, consequently, inertia properties. From the smallest to highest weight, these mass cases are called OWE, F000, FA2M, FA2T, FA9M, FC8T, FT8T, FT8T.

Figure A.1 shows the labels used to identify different stations on XRF1's wing and tail.

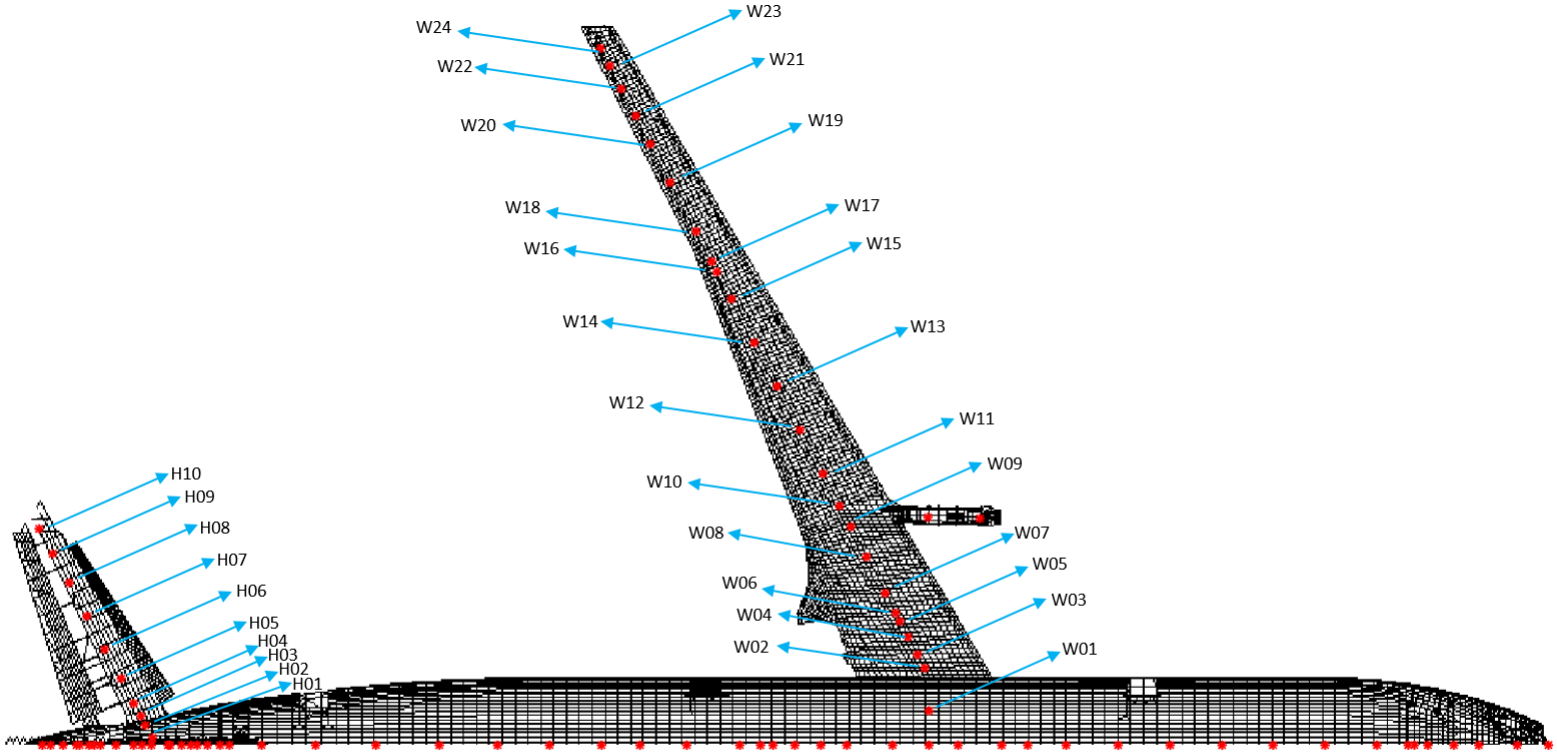

Figure A.1: XRF1: Stations on left wing and horizontal tail plane.

APPENDIX B

Condensed MPC Formulation

B.1 Condensed Linear MPC

Consider the linear time-invariant system

$$x_{k+1} = Ax_k + Bu_k, \tag{B.1}$$

$$y_k = Cx_k + Du_k, \tag{B.2}$$

with $x_k \in \mathbb{R}^{n_x}$, $u_k \in \mathbb{R}^{n_u}$, and $y_k \in \mathbb{R}^{n_y}$. Let x be the current state. The control objective is to design an MPC controller that minimizes the following cost function over a prediction horizon N:

$$V_N(x) = \min_{\mathbf{x},\mathbf{u}} x_N^T P_f x_N + \sum_{k=0}^{N-1} x_k^T Q x_k + u_k^T R u_k, \tag{B.3}$$

subject to:

$$x_0 = x, \tag{B.4}$$

$$x_{k+1} = Ax_k + Bu_k, \quad \text{for } k \in \mathbb{Z}_{[0,N-1]}, \tag{B.5}$$

$$E_0 + E_1 x_{k+1} + E_2 u_k \preceq 0, \quad \text{for } k \in \mathbb{Z}_{[0,N-1]}, \tag{B.6}$$

with $Q \in \mathbb{R}^{n_x \times n_x}, Q \succeq 0$, $R \in \mathbb{R}^{n_u \times n_u}, R \succ 0$, $P_f \in \mathbb{R}^{n_x \times n_x}, P_f \succ 0$, $E_0 \in \mathbb{R}^{n_c}$, $E_1 \in \mathbb{R}^{n_c \times n_x}$, and $E_2 \in \mathbb{R}^{n_c \times n_u}$. Equation B.6 contains n_c linear inequalities representing state, input and output constraints. Vectors $\mathbf{x} \in \mathbb{R}^{Nn_x}$ and $\mathbf{u} \in \mathbb{R}^{Nn_u}$ denote the concatenation of the state and input vectors, respectively, over the prediction horizon:

$$\mathbf{x} = \begin{bmatrix} x_1^T & x_2^T & \cdots & x_N^T \end{bmatrix}^T, \tag{B.7}$$

$$\mathbf{u} = \begin{bmatrix} u_0^T & u_1^T & \cdots & u_{N-1}^T \end{bmatrix}^T. \tag{B.8}$$

Equality constraints in Eq. B.5 can be written in matrix form as follows:

$$\mathbf{x} = S_c \mathbf{u} + M_c x_0 \tag{B.9}$$

$$S_c = \begin{bmatrix} B & 0 & \cdots & 0 \\ AB & B & \cdots & 0 \\ \vdots & \vdots & \ddots & \cdots \\ A^{N-1}B & A^{N-2}B & \cdots & B \end{bmatrix}, \quad M_c = \begin{bmatrix} A \\ A^2 \\ \vdots \\ A^N \end{bmatrix}. \tag{B.10}$$

Define matrices $Q_c \in \mathbb{R}^{Nn_x \times Nn_x}$ and $R_c \in \mathbb{R}^{Nn_u \times Nn_u}$ as follows:

$$Q_c \begin{bmatrix} I_{N-1} \otimes Q & 0 \\ 0 & P_f \end{bmatrix}, \quad R_c = I_N \otimes R. \tag{B.11}$$

Then, cost function in Eq. B.3 can be written in matrix form as follows:

$$V_N(x) = \mathbf{u}^T H_c \mathbf{u} + 2 q_c^T \mathbf{u} + c_c, \tag{B.12}$$

where

$$\begin{aligned} H_c &= S_c^T Q_c S_c + R_c, & \text{(B.13)} \\ q_c &= S_c^T Q_c M_c x_0, & \text{(B.14)} \\ c_c &= x_0^T (Q + M_c^T Q_c M_c) x_0. & \text{(B.15)} \end{aligned}$$

Similarly, by defining

$$\begin{aligned} G_c &= (I_N \otimes E_1) S_c + I_N \otimes E_2, & \text{(B.16)} \\ W_c &= (I_N \otimes E_1) M_c x_0 + 1_N \otimes E_0, & \text{(B.17)} \end{aligned}$$

inequalities in B.6 can be written in matrix form as follows

$$G_c \mathbf{u} + W_c \preceq 0. \tag{B.18}$$

Therefore, the OCP in Eqs. B.3-B.6 can be written in a more compact form as follows

$$\begin{aligned} V_N(x) = \quad & \min_{\mathbf{u}} \mathbf{u}^T H_c \mathbf{u} + 2 q_c^T \mathbf{u} & \text{(B.19)} \\ \text{s.t.} \quad & x_0 = x, & \text{(B.20)} \\ & G_c \mathbf{u} + W_c \preceq 0. & \text{(B.21)} \end{aligned}$$

Note that c_c was removed from the cost function in Eq. B.19 for being a constant with respect to the decision variables. By construction $H_c \succ 0$, thus the optimization problem in Eqs. B.19-B.21 is a convex QP. This QP is equivalent to the optimization problem in Eqs. B.3-B.6, however with a smaller number of decision variables and no equality constrains. This reduction was possible to the elimination of decision variables $\mathbf{u}$ by back substitution of the dynamic equation in B.9 into the original OCP. This procedure is referred to as condesing, and the OCP in Eqs. B.19-B.21 is called condensed MPC.

B.2 Condensed Nonlinear MPC

Consider the nonlinear time-invariant system

$$x_{k+1} = f_s(x_k, u_k), \tag{B.22}$$

$$y_k = g(x_k, u_k), \tag{B.23}$$

with $x_k \in \mathbb{R}^{n_x}$, $u_k \in \mathbb{R}^{n_u}$, and $y_k \in \mathbb{R}^{n_y}$. Functions $f_s : \mathbb{R}^{n_x} \times \mathbb{R}^{n_u} \to \mathbb{R}^{n_x}$ and $g : \mathbb{R}^{n_x} \times \mathbb{R}^{n_u} \to \mathbb{R}^{n_y}$ are assumed to be C^2 with respect to their arguments. Let x be the current state. The control objective is to design an MPC controller that minimizes the quadratic cost function in Eq. B.3 over a prediction horizon N subject to the following constraints:

$$x_0 = x, \tag{B.24}$$

$$x_{k+1} = f_s(x_k, u_k), \quad \text{for } k \in \mathbb{Z}_{[0,N-1]}, \tag{B.25}$$

$$h(x_k, u_k) \preceq 0, \quad \text{for } k \in \mathbb{Z}_{[1,N]}, \tag{B.26}$$

where $g : \mathbb{R}^{n_x} \times \mathbb{R}^{n_u} \to \mathbb{R}^{n_c}$ is assumed to be a C^2 function representing, state, input and output constraints.

Let $\mathbf{x}$ and $\mathbf{u}$ be defined as in B.7 and B.8, respectively. Functions $\bar{f}$ and $\bar{h}$ are defined as follows:

$$\bar{f}(\mathbf{x}, \mathbf{u}) \triangleq \begin{bmatrix} x_1 - f_s(x_0, u_0) \\ x_2 - f_s(x_1, u_1) \\ \vdots \\ x_N - f_s(x_{N-1}, u_{N-1}) \end{bmatrix}, \tag{B.27}$$

$$\bar{h}(\mathbf{x},\mathbf{u}) \triangleq \begin{bmatrix} h(x_0,u_0) \\ h(x_1,u_1) \\ \vdots \\ h(x_{N-1},u_{N-1}) \end{bmatrix}. \tag{B.28}$$

The Lagrangian function associated with this problem is

$$L(\mathbf{x},\mathbf{u},\lambda_{\text{eq}},\lambda_{\text{ineq}}) = V_N(x) + \lambda_{\text{eq}}^T \bar{f}(\mathbf{x},\mathbf{u}) + \lambda_{\text{ineq}}^T \bar{h}(\mathbf{x},\mathbf{u}), \tag{B.29}$$

where $\lambda_{\text{eq}} \in \mathbb{R}^{Nnx}$ and $\lambda_{\text{eq}} \in \mathbb{R}^{Nnc}_{++}$ are Lagrange multipliers.

If SQP is chosen as the numerical method to solve this OCP, the following QP problems are solved at each subiteration of the algorithm:

$$\min_{\Delta\mathbf{x},\Delta\mathbf{u}} \quad \frac{1}{2}\begin{bmatrix} \Delta\mathbf{x} \\ \Delta\mathbf{u} \end{bmatrix}^T \begin{bmatrix} H_{xx} & H_{xu} \\ H_{xu}^T & H_{uu} \end{bmatrix} \begin{bmatrix} \Delta\mathbf{x} \\ \Delta\mathbf{u} \end{bmatrix} + \begin{bmatrix} d_x \\ d_u \end{bmatrix}^T \begin{bmatrix} \Delta\mathbf{x} \\ \Delta\mathbf{u} \end{bmatrix} \tag{B.30}$$

$$\text{s.t.} \quad \bar{A}\Delta\mathbf{x} + \bar{B}\Delta\mathbf{u} + \bar{f}(\bar{\mathbf{x}},\bar{\mathbf{u}}) = 0, \tag{B.31}$$

$$\bar{E}_1\Delta\mathbf{x} + \bar{E}_2\Delta\mathbf{u} + \bar{h}(\bar{\mathbf{x}},\bar{\mathbf{u}}) \preceq 0, \tag{B.32}$$

where vectors $\bar{\mathbf{x}}$ and $\bar{\mathbf{u}}$ denote the evaluation of $\mathbf{x}$ and $\mathbf{u}$ at the current iteration point, and $\Delta\mathbf{x} \triangleq \mathbf{x} - \bar{\mathbf{x}}$ and $\Delta\mathbf{u} \triangleq \mathbf{u} - \bar{\mathbf{u}}$. Furthermore,

$$\bar{A} = \left.\frac{\partial \bar{f}(\mathbf{x},\mathbf{u})}{\partial \mathbf{x}}\right|_{(\bar{\mathbf{x}},\bar{\mathbf{u}})}, \quad \bar{B} = \left.\frac{\partial \bar{f}(\mathbf{x},\mathbf{u})}{\partial \mathbf{u}}\right|_{(\bar{\mathbf{x}},\bar{\mathbf{u}})}, \tag{B.33}$$

$$\bar{E}_1 = \left.\frac{\partial \bar{h}(\mathbf{x},\mathbf{u})}{\partial \mathbf{x}}\right|_{(\bar{\mathbf{x}},\bar{\mathbf{u}})}, \quad \bar{E}_2 = \left.\frac{\partial \bar{h}(\mathbf{x},\mathbf{u})}{\partial \mathbf{u}}\right|_{(\bar{\mathbf{x}},\bar{\mathbf{u}})}, \tag{B.34}$$

$$d_x = \left.\frac{\partial V_N(x)}{\partial \mathbf{x}}\right|_{(\bar{\mathbf{x}},\bar{\mathbf{u}})}, \quad d_u = \left.\frac{\partial V_N(x)}{\partial \mathbf{u}}\right|_{(\bar{\mathbf{x}},\bar{\mathbf{u}})}, \tag{B.35}$$

$$H_{xx} = \left.\frac{\partial^2 V_N(x)}{\partial \mathbf{x}^2}\right|_{(\bar{\mathbf{x}},\bar{\mathbf{u}})}, \quad H_{uu} = \left.\frac{\partial^2 V_N(x)}{\partial \mathbf{u}^2}\right|_{(\bar{\mathbf{x}},\bar{\mathbf{u}})}, H_{xu} = \left.\frac{\partial^2 V_N(x)}{\partial \mathbf{x}\partial \mathbf{u}}\right|_{(\bar{\mathbf{x}},\bar{\mathbf{u}})}. \tag{B.36}$$

Equation B.31 can be used to eliminate $\mathbf{x}$ from the decision variables by defining the following relation:

$$\Delta\mathbf{x} = -\bar{A}^{-1}\left(\bar{B}\Delta\mathbf{u} + \bar{f}(\bar{\mathbf{x}},\bar{\mathbf{u}})\right) = S_c\Delta\mathbf{u} + M_c. \tag{B.37}$$

Note that $\bar{A}$ is always non-singular because it is a lower diagonal matrix with ones in its main diagonal. Using back substitution of Eq. B.37 into Eqs, B.30-B.32, the following condensed

QP is obtained:

$$\min_{\Delta \mathbf{u}} \quad \frac{1}{2}\Delta \mathbf{u}^T H_c \Delta \mathbf{u} + q_c^T \Delta \mathbf{u} \tag{B.38}$$

$$\text{s.t.} \quad G_c \Delta \mathbf{u} + W_c \preceq 0, \tag{B.39}$$

where:

$$H_c = H_{uu} + S_c^T H_{xx} S_c H_{xu}^T S_c + S_c^T H_{xu} \tag{B.40}$$

$$q_c = d_u + H_{xu}^T \left(H_{xx} M_c + d_x\right) + H_{xu}^T M_c \tag{B.41}$$

$$G_c = \bar{E}_1 S_c + \bar{E}_2, \tag{B.42}$$

$$W_c = \bar{E}_1 M_c + \bar{h}(\bar{\mathbf{x}}, \bar{\mathbf{u}}). \tag{B.43}$$

The solution of this QP subproblem will return $\Delta \mathbf{u}^*$ and λ_{ineq}^*. Equation B.37 can be used to recover $\Delta \mathbf{x}^*$, while the Lagrangian function can be used to recover λ_{eq}^* given the fact that $\nabla_x L$ should be zero at the optimal solution:

$$\lambda_{\text{eq}}^* = -\bar{A}^{-T} \left(d_x + \bar{E}_1^T \lambda_{\text{ineq}}^*\right). \tag{B.44}$$

APPENDIX C

Review on Sensitivity Analysis

C.1 Notation

Given a nonlinear program (P_α), its feasible set is denoted by $\mathscr{F}_\alpha$. The set of Lagrange multipliers at a feasible point z is denoted by $\Lambda(z)$, while the set of local optimizers is denoted by $\mathcal{S}_{P_\alpha}$.

The symbols $\mathbb{Z}$ and $\mathbb{R}$ represent the set of integer and real numbers, respectively. $\mathbb{R}_+$ represents the set of nonnegative real numbers, while $\mathbb{R}_{++}$ represents the set of positive real numbers. $\mathbb{R}_{[a,b]}$ or $[a,b]$ denote a closed interval of real numbers, while $\mathbb{R}_{(a,b)}$ or (a,b) denote an open interval. Similar definitions $\mathbb{Z}_{[a,b]}$ and $\mathbb{Z}_{(a,b)}$ apply to subsets of $\mathbb{Z}$. The interior of a set S is denoted by int$S$.

Let $x \in \mathbb{R}^n$ be a vector. Then $||x||$ represents its Euclidean norm. An element of x is represented by x_i. The segment between elements a and b in vector x is represented by $[x_i]_{i=a}^b$. Let $A \in \mathbb{R}^{m\times n}$ be a matrix. Then $||A||_F$ is its Frobenius norm.

Let $f(x,y) : X \times Y \to \mathbb{R}$ be a function. The partial derivative of $f(x,y)$ with respect to x at (x,y) is represented by $\nabla_x f(x,y)$. The form $\nabla f(x,y)(h,d)$ represents $\nabla_x f(x,y)h + \nabla_y f(x,y)d$. The second partial derivative of $f(x,y)$ with respect to x at (x,y) is represented by $\nabla^2_{xx} f(x,y)$. The form $\nabla^2 f(x,y)(h,d)$ denotes $h^T\nabla^2_{xx} f(x,y)h + 2h^T\nabla^2_{xy} f(x,y)d + d^T\nabla^2_{yy} f(x,y)d$.

Let $x \in X$ and $g(x) : X \to \mathbb{R}$. Then $g(x) = o(x)$ means that $g(x)/||x|| \to 0$ as $x \to 0$. Furthermore, $g(x) = \mathcal{O}(x)$ means that $g(x)/||x||$ is bounded for all x in the neighborhood of $0 \in X$.

A continuous function $\alpha : [0,a) \to [0,\infty)$ is said to belong to class $\mathscr{K}$ if it is strictly increasing and $\alpha(0) = 0$.

C.2 Sensitivity analysis

Consider the perturbed nonlinear program of the form:

$$(\mathrm{P}_v): \quad p(v) = \min_{z \in \mathbb{R}^{n_z}} \{f(z,v) | z \in \mathscr{F}_v\} \tag{C.1}$$

with feasible set

$$\begin{aligned} \mathscr{F}_v \triangleq \Big\{ z \in \mathbb{R}^n | g_i(z,v) \leq 0, \text{ for } i \in \mathbb{Z}_{[1,n_c]}, \\ \text{and } g_i(z,v) = 0, \text{ for } i \in \mathbb{Z}_{[1+n_c,n_p]} \Big\}, \end{aligned} \tag{C.2}$$

where $v \in V \subseteq \mathbb{R}^{n_v}$ is the vector of perturbation parameters, and $z \in \mathbb{R}^{n_z}$ is the vector of decision variables. The functions $f(z,v) : \mathbb{R}^{n_z} \times V \to \mathbb{R}$, and $g_i(z,v) : \mathbb{R}^{n_z} \times V \to \mathbb{R}$ for all $i \in \mathbb{Z}_{[1,n_c]}$ are assumed to be twice continuously differentiable. An optimal solution of (P_v), assumed to exist, is denoted by $\bar{z}$. For $v = v_0$, the program (P_{v_0}) is referred to as the unperturbed problem. For such a problem, an optimal solution is z_0. Denote by $I(z,v)$ the set of inequality constraints active at z for a given v:

$$I(z,v) \triangleq \Big\{ i | g_i(z,v) = 0, \text{ for } i \in \mathbb{Z}_{[1,n_c]} \Big\}, \tag{C.3}$$

and $C(z,v)$ the critical cone associated with a feasible point z of (P_v) [136]:

$$\begin{aligned} C(z,v) \triangleq \{ h \in \mathbb{R}^{n_z} | \nabla_x f(z,v) h \leq 0, \\ \nabla_x g_i(z,v) h \leq 0, \text{ for } i \in I(z,v), \text{ and} \\ \nabla_x g_i(z,v) h = 0, \text{ for } i \in \mathbb{Z}_{[1+n_c,n_p]} \Big\}. \end{aligned} \tag{C.4}$$

The Lagrangian function associated with (P_v) is

$$L(z,v,\lambda) = f(z,v) + \sum_{i=1}^{n_p} \lambda_i g_i(z,v), \tag{C.5}$$

where $\lambda \in \mathbb{R}^{n_p}$ is the vector of Lagrange multipliers. The set of Lagrange multipliers at a feasible point z is denoted by $\Lambda(z,v)$.

For sensitivity analysis, a method based on estimates of the objective function value in the direction d along the path parameterized as

$$v(t) = v_0 + td + \frac{1}{2} t^2 r + o(t^2) \tag{C.6}$$

is employed. Consider the following linearization of (P_v) at a point (z_0, v_0) in a direction

$d \in V$:

$$(\mathrm{PL}_d): \quad p_{\mathrm{PL}_d} = \min_{h \in \mathbb{R}^{n_z}} \{\nabla f(z_0, v_0)(h, d) \mid h \in \mathscr{F}_d\}, \tag{C.7}$$

where

$$\begin{aligned} \mathscr{F}_d = \{h \in \mathbb{R}^{n_z} | \nabla g_i(z_0, v_0)(h, d) \leq 0, \text{ for} \\ i \in I(z_0, v_0), \text{and } \nabla g_i(z_0, v_0)(h, d) = 0, \\ \text{for } i \in \mathbb{Z}_{[1+n_c, n_p]}\Big\}. \end{aligned} \tag{C.8}$$

The problem (PL_d) is a linear program with its dual given by:

$$(\mathrm{DL}_d): \quad d_{\mathrm{PL}_d} = \max_{\lambda \in \Lambda(z_0, v_0)} \nabla_v L(z_0, v_0, \lambda) d. \tag{C.9}$$

Suppose that $\Lambda(z_0, v_0) \neq \emptyset$ and let $\bar{\lambda} \in \Lambda(z_0, v_0)$. Then, $\bar{\lambda} \in \mathcal{S}_{\mathrm{DL}_d}$ (i.e., the set of local optimizers of (DL_d)) if and only if [136]

$$\bar{\lambda}_i \nabla g_i(z_0, v_0)(h, d) = 0 \tag{C.10}$$

for $i \in \mathbb{Z}_{[1+n_c, n_p]} \cup I(z_0, v_0)$, and for any $\bar{\lambda} \in \mathcal{S}_{\mathrm{DL}_d}$,

$$\begin{aligned} \mathcal{S}_{\mathrm{PL}_d} = \{h \in \mathbb{R}^{n_z} | \nabla g_i(z_0, v_0)(h, d) = 0 \text{ for} \\ i \in \mathbb{Z}_{[1+n_c, n_p]} \cup I_+(z_0, v_0, \bar{\lambda}) \text{ and} \\ \nabla g_i(z_0, v_0)(h, d) \leq 0 \text{ for } i \in I_0(z_0, v_0, \bar{\lambda})\Big\}, \end{aligned} \tag{C.11}$$

where

$$I_+(z_0, v_0, \bar{\lambda}) = \{i \in I(z_0, v_0) | \bar{\lambda}_i > 0\}, \tag{C.12}$$

$$I_0(z_0, v_0, \bar{\lambda}) = \{i \in I(z_0, v_0) | \bar{\lambda}_i = 0\}. \tag{C.13}$$

Consider also the following problem associated with the dual problem of the second-order expansion of (P_v):

$$\begin{aligned} (\mathrm{PQ}) \qquad & p_{\mathrm{PQ}} = \\ & \min_{h \in \mathcal{S}_{\mathrm{PL}_d}} \left\{ \max_{\lambda \in \mathcal{S}_{\mathrm{DL}_d}} \nabla^2 L(z_0, x_0, \lambda)((h, d), (h, d)) \right\}. \end{aligned} \tag{C.14}$$

Definition 3 *(Gollan's condition):The directional regularity condition is said to hold at z_0 in a direction $d \in V$ if*

$$\begin{cases} \nabla_x g_i(z_0, v_0), \quad i \in \mathbb{Z}_{[1+n_c, n_p]} \text{ are linearly independent} \\ \exists h \in \mathbb{R}^{n_z}, \quad \begin{cases} \nabla g_i(z_0, v_0)(h, d) = 0, \text{ for } i \in \mathbb{Z}_{[1+n_c, n_p]} \\ \nabla g_i(z_0, v_0)(h, d) < 0, \text{ for } i \in I(z_0, v_0) \end{cases} \end{cases} \tag{C.15}$$

Proposition 2 ([136], Theorem 5.50) *Suppose that Gollan's condition holds in a direction d. Then $d_{PL_d} = p_{PL_d} < \infty$, and d_{PL_d} is finite if and only if the set $\Lambda(z, v)$ is nonempty.*

Definition 4 *The second-order sufficient optimality condition (SOSC) in a direction $d \in V$ is said to hold at a point z_0 if*

$$\sup_{\lambda \in \mathcal{S}_{DL_d}} \nabla^2_{zz} L(z_0, v_0, \lambda)(h, h) > 0, \tag{C.16}$$

$\forall h \in C(z_0, v_0) \setminus \{0\}$.

The next theorem presents one of the main results on the directional stability of the perturbed local minimum and correspondent optimal value function.

Theorem 3 ([136], Theorem 5.53) *Suppose that:*
(i) the unperturped problem has a unique optimal solution z_0,
(ii) Gollan's condition holds in the direction d,
(iii) the set $\Lambda(z_0, v_0)$ is nonempty,
(iv) the second-order sufficient condition holds
(v) $\bar{z}(t) \to z_0$ as $t \downarrow 0$.
Then for any $o(t^2)$-optimal solution $\bar{z}(t)$ of (P_v), where $v = v_0 + td$ and $t \geq 0$, the following holds:
a) $\bar{z}(t)$ is Lipschitz stable at z_0, i.e., $||\bar{z}(t) - z_0|| = \mathcal{O}(t)$,
b) the problem (PQ) has a finite optimal value, and the following expansion for the optimal value function holds:

$$p(v_0 + td) = p(v_0) + t p_{PL_d} + \frac{1}{2} t^2 p_{PQ} + o(t^2) \tag{C.17}$$

Remark 4 *In the case of isolated local minimizers, a dummy constraint $||z - z_0||^2 \leq r^2$ for a sufficiently small r can be added to reduce the analysis of these local solutions to the case of a unique minimizer. Since this constraint is not active at z_0, the results in Theorem 3 apply.*

C.3 Strong regularity

Consider a generalized equation (GE) of the form:

$$F(z, v) + N_K(z) \ni 0, \tag{C.18}$$

where $F(z, v) : Z \times V \to Z'$ is a function, K is a nonempty closed convex set, and $N_K : Z \rightrightarrows Z'$ is the normal cone operator:

$$N_K(z) \triangleq \begin{cases} \{y \in Z' | y^T(k - z) \leq 0, \ \forall k \in K\} & \text{if } z \in K, \\ \emptyset & \text{if } z \notin K. \end{cases} \tag{C.19}$$

Definition 5 *(Strong regularity, [137]): It is said that z_0 is a strongly regular solution of the GE in (C.18), for some v_0, if there exist neighborhoods $\mathcal{V}_Z$ and $\mathcal{V}_{Z'}$ of $z_0 \in Z$ and $0 \in Z'$, respectively, such that for every $\delta \in \mathcal{V}_{Z'}$, the linearized generalized equation (LGE)*

$$F(z_0) + \nabla F(z_0)(z - z_0) + N_K(z) \ni \delta \tag{C.20}$$

has a unique solution in $\mathcal{V}_Z$, denoted by $\zeta(\delta)$, and the mapping $\zeta : \mathcal{V}'_Z \to \mathcal{V}_Z$ is Lipschitz continuous with constant c.

The necessary optimality conditions given by the KKT system of (P_v), equipped with some type of constraint qualification, can be written as a GE as follows:

$$\begin{bmatrix} \nabla_x L(z, v, \lambda) \\ -[g_i(z)]_{i=1}^{n_c} \\ -[g_i(z)]_{i=1+n_c}^{n_p} \end{bmatrix} + N_{\mathbb{R}^{n_z} \times \mathbb{R}^{n_c}_+ \times \mathbb{R}^{n_p - n_c}} \begin{bmatrix} z \\ [\lambda_i]_{i=1}^{n_c} \\ [\lambda_i]_{i=1+n_c}^{n_p} \end{bmatrix} \ni 0. \tag{C.21}$$

Proposition 3 ([137]) *A pair (z, λ) for some $v \in V$ is a KKT point of (P_v) if and only if it is a solution of the GE in (C.21) .*

Definition 6 *The strong second-order sufficient optimality condition (SSOSC) is said to hold at a point z_0 if*

$$\nabla^2_{zz} L(z_0, v_0, \lambda)(h, h) > 0 \tag{C.22}$$

for any $\lambda \in \Lambda(z_0, v_0)$ and $h \neq 0$ such that $\nabla_z g_i(z_0, v_0)h = 0, \ i \in \mathbb{Z}_{[1+n_c, n_p]} \cup I_+(z_0, v_0, \lambda)$.

Proposition 4 ([137], Theorem 4.1; [136], Proposition 5.38) *Let z_0 be a locally optimal solution and λ_0 a corresponding Lagrange multiplier vector of (P_{v_0}). The critical point*

(z_0, λ_0) is strongly regular if and only if the linear independence constraint qualification (LICQ) and the SSOSC hold.

Remark 5 *Strong regularity implies regularity, i.e., the Mangasarian-Fromovitz condition holds. The latter, in turn, implies Gollan's condition [138, 139].*

Proposition 5 ***([138], Theorem 4.6; [139], Proposition 5.2)*** *Let z_0 be a local solution of (P_{v_0}) and λ_0 its unique Lagrange multiplier. If (z_0, λ_0) is a strongly regular solution of Eq. (C.18), then there exists a neighborhood $\mathcal{V}$ of z_0 such that, for all v sufficiently close to v_0, the perturbed problem (P_v) has a unique local minimizer $\bar{z} \in \mathcal{V}$ and an associated unique Lagrange multiplier $\bar{\lambda}$, such that $(\bar{z}, \bar{\lambda})$ is the unique solution of Eq. (C.18) in $\mathcal{V}$.*

APPENDIX D

Review on Scenario-based MPC

This section presents a brief review of MPCS based on references [122, 123, 140].

Consider the following uncertain discrete-time system:

$$x_{k+1} = A(\delta)x_k + B(\delta)u_k, \tag{D.1}$$

$$y_k = C(\delta)x_k + D(\delta)u_k, \tag{D.2}$$

where $x_k \in \mathbb{R}^{n_x}$ is the state vector, $u_k \in \mathbb{R}^{n_u}$ is the control input, $y_k \in \mathbb{R}^{n_y}$ is the output vector, and $\delta \in \Delta \subseteq \mathbb{R}^{n_\delta}$ is the vector of uncertain parameters.

Assumption 1: The set $\Sigma \triangleq \{A(\delta), B(\delta), C(\delta), D(\delta) : \delta \in \Delta\}$ is bounded. The parameters δ have a stochastic nature, and the probability measure on Δ is denoted by P_δ.

Assumption 2: The pair $(A(\delta), B(\delta))$ is stabilizable for any $\delta \in \Delta$.

The objective is to design an MPC controller that will steer the system states and/or outputs to desired values while enforcing state, output and input constraints, i.e., $x_k \in X(\delta), y_k \in Y(\delta), u_k \in U(\delta)\ \forall k$, respectively. Without loss of generality, we consider only the regulation problem.

Assumption 3: For any $\delta \in \Delta$, the sets $X(\delta) \subseteq \mathbb{R}^{n_x}$, $Y(\delta) \subseteq \mathbb{R}^{n_y}$, $U(\delta) \subseteq \mathbb{R}^{n_u}$ are convex and contain the origin in their interiors. These sets can be represented by:

$$X(\delta) = \{x \in \mathbb{R}^{n_x} : f_X(x, \delta) \preceq 0\}, \tag{D.3}$$

$$Y(\delta) = \{y \in \mathbb{R}^{n_y} : f_Y(y, \delta) \preceq 0\}, \tag{D.4}$$

$$U(\delta) = \{u \in \mathbb{R}^{n_u} : f_U(u, \delta) \preceq 0\}, \tag{D.5}$$

where $f_X : \mathbb{R}^{n_x} \times \Delta \to \mathbb{R}^{n_{g_x}}$, $f_Y : \mathbb{R}^{n_y} \times \Delta \to \mathbb{R}^{n_{g_y}}$, $f_U : \mathbb{R}^{n_u} \times \Delta \to \mathbb{R}^{n_{g_u}}$ are convex functions in x, y and u, respectively.

Assumption 4: A convex terminal set $X_f \triangleq \left\{x \in \mathbb{R}^{n_x} : f_{X_f}(x) \preceq 0\right\}$, $f_{X_f} : \mathbb{R}^{n_x} \to \mathbb{R}^{n_{g_{xf}}}$ convex, and a linear terminal control law $u = K_f x$, $K_f \in \mathbb{R}^{n_u \times n_x}$ exist such that X_f is a robustly invariant set, that is, $\forall x_k \in X_f, \forall \delta \in \Delta$, $(A(\delta) + B(\delta)K_f)\, x_k \in X_f$. Furthermore,

$\forall x_k \in X_f$ and $\forall \delta \in \Delta$, the terminal control law renders the origin of system D.1-D.2 robustly asymptotically stable.

Let $u_k = K_f x + v_k$ be the control law applied to the plant at time k, and define the closed-loop system

$$x_{k+1} = A_{cl}(\delta)x_k + B(\delta)v_k, \tag{D.6}$$

where $A_{cl}(\delta) \triangleq A(\delta) + B(\delta)K_f$, and v_k is the control correction computed as the solution to the min-max optimal control problem (OCP) defined as follows:

$$\begin{aligned} \underset{\{v_k \in \mathbb{R}^{n_u}\}_{k=0}^{N-1}}{\text{minimize}} \quad & \max_{\delta \in \Delta} \left\{ J(x_k, \delta, v_k) = \sum_{k=0}^{N-1} x_k^T Q x_k + u_k^T R u_k \right\} \\ \text{s.t.} \quad & x_{k+1} \in X(\delta), y_{k+1} \in Y(\delta), u_k \in U(\delta), x_N \in X_f, \forall \delta \in \Delta, \text{for } k \in \mathbb{N}_{[0;N-1]}, \end{aligned} \tag{D.7}$$

where $N \in \mathbb{N}^*$ is the prediction horizon, and $Q^T = Q \succ 0$, $R^T = R \succ 0$ are weighting matrices of appropriate size. The OCP in D.7 is usually too hard to solve, especially because Δ is often of high cardinality or even infinite.

Consider a finite number $M \in \mathbb{N}$ of randomly extracted scenarios of δ, which are collected in the multisample $\omega_M = \{\delta^{(1)}, \ldots, \delta^{(M)}\}$ whose probability measure is denoted by P_δ^M. The OCP is then reformulated in epigraph form as follows:

$$\begin{aligned} \underset{s}{\text{minimize}} \quad & \alpha + \mu\varepsilon \\ \text{s.t.} \quad & J(x_k, \delta^{(i)}, v_k) \leq \alpha, \quad \text{for } i \in \mathbb{N}_{[1;M]} \\ & f_X(x_k, \delta^{(i)}) - 1_{n_{g_x}}\varepsilon \preceq 0, \quad \text{for } i \in \mathbb{N}_{[1;M]}, k \in \mathbb{N}_{[1;N]} \\ & f_Y(y_k, \delta^{(i)}) - 1_{n_{g_y}}\varepsilon \preceq 0, \quad \text{for } i \in \mathbb{N}_{[1;M]}, k \in \mathbb{N}_{[1;N]} \\ & f_U(u_k, \delta^{(i)}) - 1_{n_{g_u}}\varepsilon \preceq 0, \quad \text{for } i \in \mathbb{N}_{[1;M]}, k \in \mathbb{N}_{[0;N-1]} \\ & f_{X_f}(x_N) - 1_{n_{g_{x_f}}}\varepsilon \preceq 0, \\ & \varepsilon \geq 0, \end{aligned} \tag{D.8}$$

where $s \triangleq \left[\; v_0^T, \ldots, v_{N-1}^T, \alpha, \varepsilon \; \right]^T$ is the vector of decision variables, and ε is a slack variable used to guarantee feasibility of the optimization problem by transforming the hard constraints into soft ones, and 1_n is a n-dimensional vector whose entries are ones. Note that the OCP in D.8 is a convex program.

Define the following function of the constraints in OCP D.8:

$$h(s,\delta^{(i)}) \triangleq \max\left\{\max_{k\in\mathbb{N}_{[0;N-1]}}\left\{f_X(x_{k+1},\delta^{(i)})-1_{n_{g_x}}\varepsilon, f_Y(y_{k+1},\delta^{(i)})-1_{n_{g_y}}\varepsilon, f_U(u_k,\delta^{(i)})-1_{n_{g_u}}\varepsilon\right\},\right.$$
$$\left. J(x_k,\delta^{(i)},v_k)-\alpha, f_{X_f}(x_N)-1_{n_{g_{xf}}}\varepsilon, -\varepsilon\right\}. \tag{D.9}$$

The reliability of the scenario optimization, which depends of the random multisample ω_M in D.8 is defined as:

$$\mathscr{R}(\omega_M) \triangleq P_\delta\left\{\delta : h(s^*,\delta^{(i)}) \leq 0\right\}, \tag{D.10}$$

where s^* denotes the optimal solution to D.8. Theorem 1 [123] defines the conditions in which a feasible solution of D.8 will also be feasible for D.7 for some user-defined reliability level.

Theorem 1 [123]: Let d be the number of decision variables in OCP D.8, let $p \in \mathbb{R}_{(0;1)}$ be a given desired reliability level, let $\beta \in \mathbb{R}_{(0;1)}$ be a given small probability level, and let M be an integer such that:

$$\Phi(p,d,M) = \sum_{j=0}^{d-1}\binom{M}{j}(1-p)^j p^{M-j} \leq \beta. \tag{D.11}$$

Then, it holds that:

$$P_\delta^M\left\{\omega_M : \mathscr{R}(\omega_M) \geq p\right\} \geq 1-\beta. \tag{D.12}$$

APPENDIX E

Noise Matrices Inflation in Kalman Filtering

The uncertainties w_k in the uncertain linear system in Eqs. 3.122-3.123 include nonlinearities, model reduction errors, and discretization errors, while v_k is commonly employed to account for sensor imperfections. However, v_k can also encompass model reduction errors and linearization errors.

The conventional approach for tuning w_k statistics is by trial-and-error. While this solution may be effective for small-scale projects, a large-order system precludes its use due to the large number of independent parameters to tune. Therefore, a systematic approach to tuning a large-scale Kalman filter is required. Furthermore, the analytic description of the differential equations in Eqs. 2.27-2.29 is often not available in high-order FSI simulations. Therefore, the tuning process must only use time series $x(t)$, $u(t)$, $y(t)$ from a finite number of M simulated trajectories. The next procedure was proposed by Dr. Leandro Lustosa.

To determine w_k statistics, its mean is set to zero (i.e., $E[w_k] = 0$) and its covariance is defined by FSI-based time series $x(t)$, $u(t)$, and $y(t)$ (e.g., solutions of the UM/NAST Dynamic Solver). For this purpose, w_k is written as

$$w_k = x_{r,k} - A_r^d x_{r,k-1} - B_r^d u_k \tag{E.1}$$

and thus

$$w_k = P_r x_k - A P_r x_{k-1} - B u_k, \tag{E.2}$$

where P_r is the linear transformation between the full order state to the reduced order state as defined in Eq. 2.43.

For each i^{th} trajectory, $i \in \mathbb{Z}_{[1,M]}$, Eq. E.2 results in a time series for $w^{(i)}$. These trajectories are chosen to represent likely flight conditions and disturbances. Additionally, $w^{(i)}$ can be thought as the error between the approximated and full models for the ith trajectory. If M trajectories are available, each with $N_s(i)$ data points in time, then the sample unbiased

estimate of

$$Q_w = E[ww^T] \tag{E.3}$$

is

$$\hat{Q}_w = \frac{\sum_{i=1}^{M} \sum_{k=1}^{N_s(i)} w_k^{(i)} \left(w_k^{(i)} \right)^T}{\sum_{i=1}^{M} N_s(i) - 1} \tag{E.4}$$

A similar approach to estimate

$$R_v = E[vv^T] \tag{E.5}$$

yields

$$\hat{R}_v = \frac{\sum_{i=1}^{M} \sum_{k=1}^{N_s(i)} v_k^{(i)} \left(v_k^{(i)} \right)^T}{\sum_{i=1}^{M} N_s(i) - 1} \tag{E.6}$$

Given the above offline estimates of $\hat{R}_v$ and $\hat{Q}_w$, the gains for the Kalman filter can be computed and applied online in practical applications.

APPENDIX F

Additional Simulation Results

The next figures show results of the closed-loop simulation of XRF1 with the LA governor for MLA presented in Section 4.3.2. Figure F.4 shows the loads on different stations on the wing and tail, which are identified by the names shown in Fig. A.1

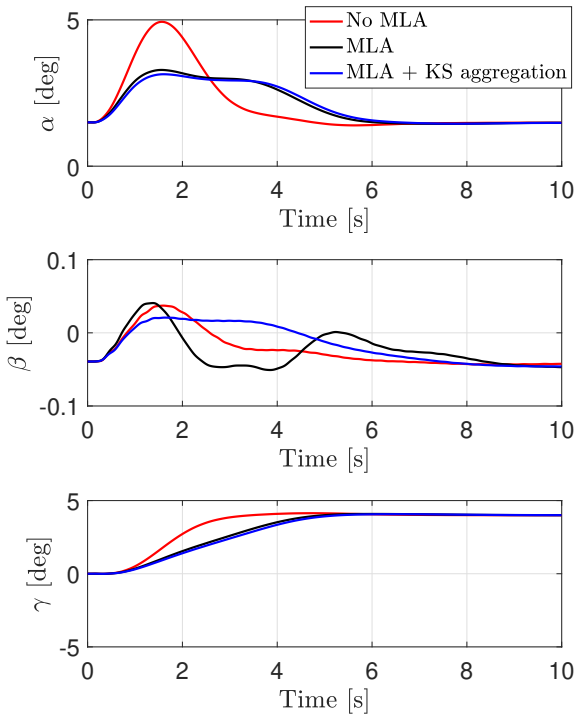

Figure F.1: Angle of attack, side-slip and flight path angles.

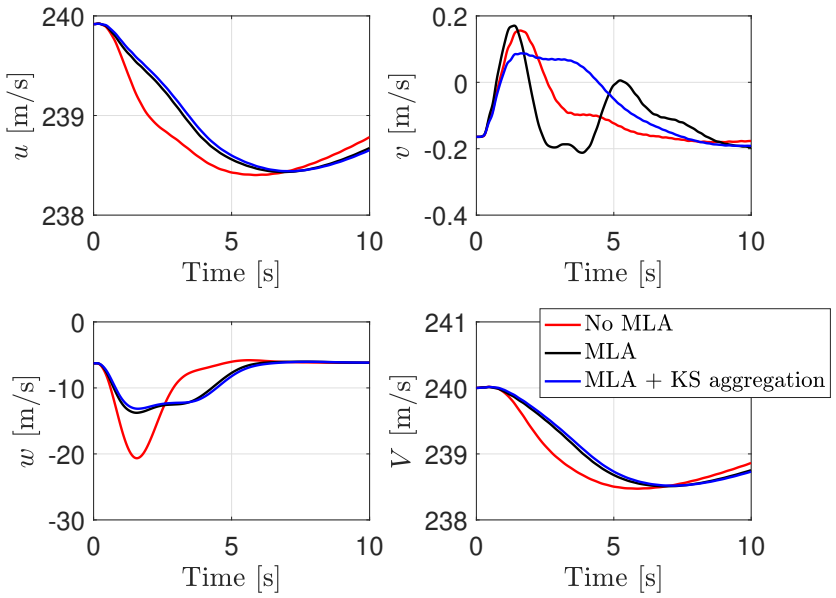

Figure F.2: Velocity.

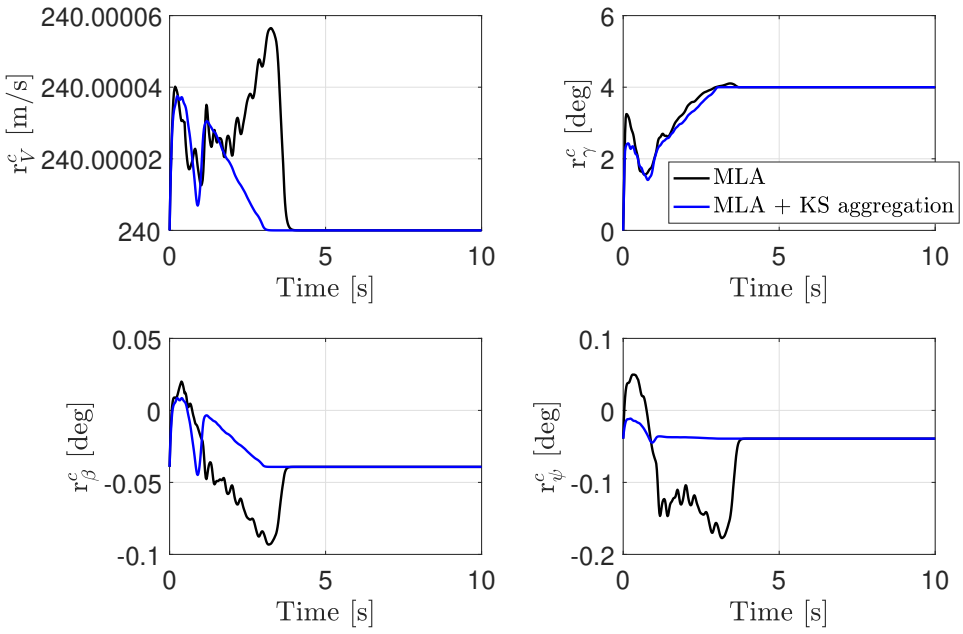

Figure F.3: Reference commands generated by the MLA governor.

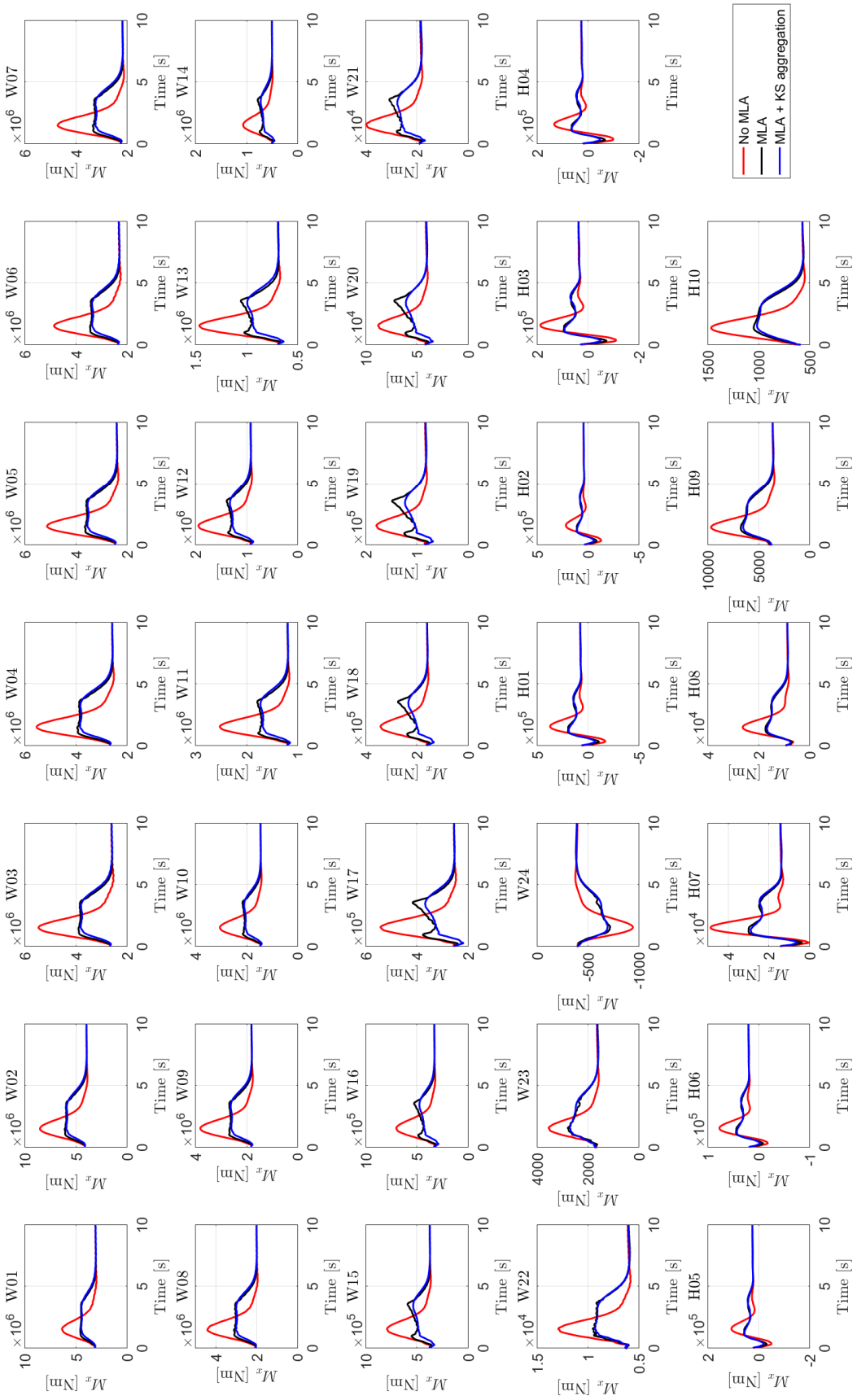

Figure F.4: XRF1: Moments on left wing and horizontal tail plane.

APPENDIX G

EASE Model Properties

The EASE model was designed and manufactured by the following A^{2}SRL team: Prof. Carlos Cesnik, Prof. Ilya Kolmanovsky, Bernardo Monteiro, Dr. Cristina Riso, Dr. Guilherme Barbosa, Mateus Pereira, Mauricio Pajon, Dr. Rafael Bertolin, and Dr. Thiago Versiani. The detailed design description is presented in Ref. [134]. This appendix presents a summary of the design process and decisions, as well as sample analysis results.

G.1 Model Requirements

The following key requirements guided the EASE model design:

- EASE model should be tested in the University of Michigan's 5-ft by 7-ft wind tunnel with the inclusion of the HTP for combined load alleviation.
- Wall-mounted, half-airplane model with free rigid pitch DOF in the University of Michigan's Pitch-and-Plunge Apparatus (PaPA).
- Flexibility restricted to wing only.
- Level of wing flexibility in the range of VFA wing deformation (10% to 25% tip wing deflection with respect to semi-span)

The derived model requirements were as follows

- Testing speed between 15 and 30 m/s.
- Wing tip displacement at trim should be higher than 10% of wing semi-span.
- The EASE wing should be free of flutter within the testing speed range.

G.2 EASE Model Description

The next sections present a description of the main components of the EASE aircraft model.

G.2.1 Wing

The wing has a uniform rectangular planform with a backsweep of 30°. It has a span of 1500 mm and chord of 278 mm. The constant airfoil section is based on the Selig S2027 airfoil. The choice was based on its good low-Reynolds performance and sufficient thickness to accommodate the control-surface's servo and rotary encoder mounted directly at the hinge line. In addition to this, a non-symmetric airfoil was preferred to facilitate reaching the desired 15% tip deflection at the operating condition. In order to capture the tip effects for the wing, the 2D airfoil coefficients were corrected by lift, drag and moment coefficient distributions obtained from AVL [135].

The wing structure consists of a main spar and 10 airfoil-shaped segments of equal length, so-called pods attached to it. The spar is a 7075-T6 Aluminum stock bar, with rectangular cross section of 1 1/2" by 1/4" (38.1 mm by 6.4 mm). Each one of the pods has an independently actuated trailing edge control surface spanning 30% of its chord. The pods are attached to the spar using three bolts aligned in the sparwise direction, centered at the 25% chord, mid-span point.

G.2.2 Horizontal Tail

The 37-cm span tail has constant chord of 17 cm and a 30-deg sweep angle. The tail contains an elevator whose chord corresponds to 30% of the HTP chord, similar to what is found in the XRF1's HTP. This control surface provides primary pitch control of the EASE model.

A constant symmetric airfoil section corresponding to the NACA 0018 airfoil is used along the HTP span. The NACA 0018 was selected due to its thickness (18% at 30% chord) which creates adequate volume to fit the servo actuator and rotary encoder inside it. Moreover, this airfoil presents a desirable moment coefficient as a function of angle of attack in the range between -5 and 5 deg. In order to capture the tip effects for the tail, the 2D airfoil coefficients were corrected by lift, drag, and pitch moment coefficient distributions obtained from AVL like it is done for the main wing.

3D printed parts in PLA material give the external shape of the member. The carbon fiber HTP spar has a square cross section and dimensions $10\times10\times8.5$ mm. The HTP load cell is attached to an aluminum plate adapter which then attaches to the root part and spar.

G.2.3 Fuselage

The EASE model fuselage is a collection of members that connect the main wing to the tail, and also attaches the model to the PaPA mechanism. It is divided into three main parts: front, middle, and tail sections. The load cell attachment point is also the attachment point between the model and the PaPA load cell, and the rotation point for the pitch attitude of the half-aircraft model. By design, such point is co-located with the center of mass of the model. The main fuselage metallic structure is wrapped around with foam, which serves as a fairing to reduce drag.

The Aluminum 6061 tubes have cross-sectional dimensions of 7.62×2.54×0.16 cm (3×1×0.065). The connectors for the wing and the PaPA are all machined 7075-T6 parts. The fairing is made of ROHACELL 31 IGF foam with density of 0.032 g/cm^3 or equivalent.

G.2.4 Sensors and Actuators

A description of the selected sensors for the EASE model is presented next.

- Main model load cell:
  The HBM MCS10 multicomponent sensor, size BG2, type 050 (see Fig. G.1(a)) was selected as the main load cell to provide force and moment measurements on the three axes. This load cell was placed at the rotation point, where the fuselage attaches to the PaPA mechanism (see Fig. 6.5).

- HTP load cell:
  The ATI Mini45 SI-290-10 (see Fig. G.1(b)) was selected as the HTP load cell to provide force and moment measurements on the three axes. This device has a diameter of 45 mm, height of 15.7 mm, and mass of 91.7 g, making it small enough to be placed at the root and inside the HTP pod (see Fig. 6.6(b)).

- Rotary encoder:
  The US Digital MA3 12-bit PWM (see Fig. G.1(c)) rotary encoder was selected to measure the control surfaces' deflection. This sensor was associated with each flap on the wing, and with the HTP elevator, for a total of 11 units (see Fig. 6.6).

- IMU:
  The Vectornav VN-100 (see Fig. G.1(d)) IMU sensor was selected for attitude and acceleration measurements. The VN-100 is a miniature, high-performance IMU and Attitude Heading Reference System (AHRS). Combining 3-axis accelerometers, gyros, and magnetometer, a barometric pressure sensor and a 32-bit processor, the VN-100

(a) HBM MCS10 load cell

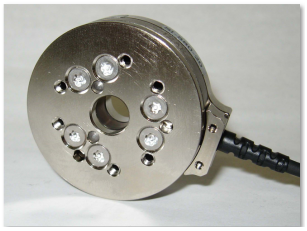

(b) ATI Mini45 load cell

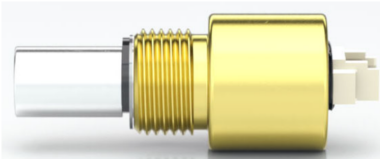

(c) MA3 rotary encoder

(d) VN-100 IMU

(e) Sensuron's RTS125 FOS interrogator

Figure G.1: Various sensors and sensor system used in support to the EASE model experimentation.

provides high-rate, calibrated IMU data and a real-time 3D attitude solution that is continuous over the complete 360 degrees of motion. Six VN-100 devices were placed along the wing spar and one device was placed on the fuselage close to the rotation point (see Fig. 6.6(a)).

- Fiber optic system (FOS):
  The Sensuron's RTS125 FOS interrogator (see Fig. G.1(e)) was selected for fiber-optics based shape measurement. This device monitors continuous strain distributions along up to eight optical fibers simultaneously. Each optical fiber can span up to 40 ft and contain over 2,000 sensors. The fibers were placed along the leading and trailing edges of the main spar (Fig. 6.6(a)).

- The EASE model was actuated with 10 servos in the wing and one servo in the tail. The MKS HV93i servos were selected for both wing and HTP for their size and performance.

G.3 EASE Model Properties

These are properties obtained for the UM/NAST model for the EASE aircraft.

G.4 Static Stability

The longitudinal static stability of an aircraft is related to the distance of its neutral point from its center of mass. The neutral point is the longitudinal position at which the variation of the aircraft coefficient of moment with angle of attack is zero. In a typical 6 d.o.f. aircraft, if the neutral point is located behind the center of mass, then the aircraft is statically stable, *i.e.*, the pitching moment that acts on the aircraft when its angle of attack is changed from the trim condition acts in such a way as to restore the aircraft to its original angle of attack. However, in a wind tunnel model with only the pitch d.o.f. such as the EASE model, the stability is actually related to the position of the neutral point with respect to the rotation point. In the EASE model, the rotation point is where the model attaches to the PaPA mechanism. To replicate the stability definition of a 6 d.o.f. aircraft, the EASE model was designed such that the center of mass is co-located with its rotation point. As for the aerodynamic center (a.c.) of the wing, as typically seen in commercial aircraft, such point is found between the aircraft center of mass and the neutral point. Table G.1 shows the position of these points of interest for the EASE model with respect to the rotation point. Negative number mean that the point is behind the rotation point.

Table G.1: EASE model's wing aerodynamic center, neutral point and static margin.

AoA [deg]	0	2.5	5	7.5	10
Wing a.c. [m]	-0.061	-0.037	-0.025	-0.019	-0.018
Neutral point [m]	-0.191	-0.195	-0.197	-0.202	-0.187
Static margin [%]	68.7	70.2	71.0	73.3	68.5

G.5 Wing Modal Characteristics

The structural modes of the clamped EASE wing are shown in G.2 and classified in G.2. The dominant mode is the out-of-plane bending.

G.6 Wing Deformation

Figure G.3 shows the static wing deformation for different angles of attack at 25 m/s.

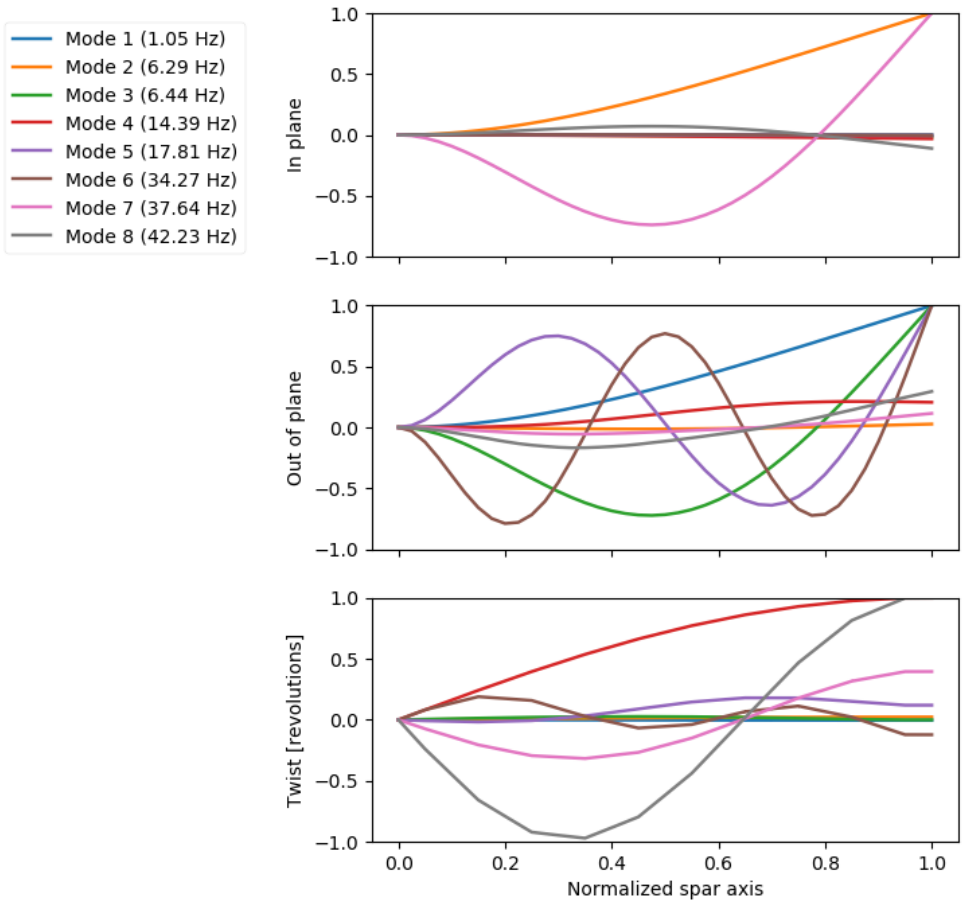

Figure G.2: Structural modes the unloaded clamped EASE wing.

Table G.2: Modal frequencies of the unloaded clamped EASE wing.

Type	**Frequency [Hz]**
First out-of-plane bending (OOP1)	1.05
First in-plane bending (IP1)	6.29
Second out-of-plane bending (OOP2)	6.44
First torsion (T1)	14.39
Third out-of-plane bending (OOP3)	17.81
Fourth out-of-plane bending (OOP4)	34.27
Second in-plane bending (IP2)	37.64
Second torsion (T2)	42.23

G.7 Model Mass

Table G.3 shows the mass properties of the actual EASE model's wing, fuselage and tail as measured experimentally.

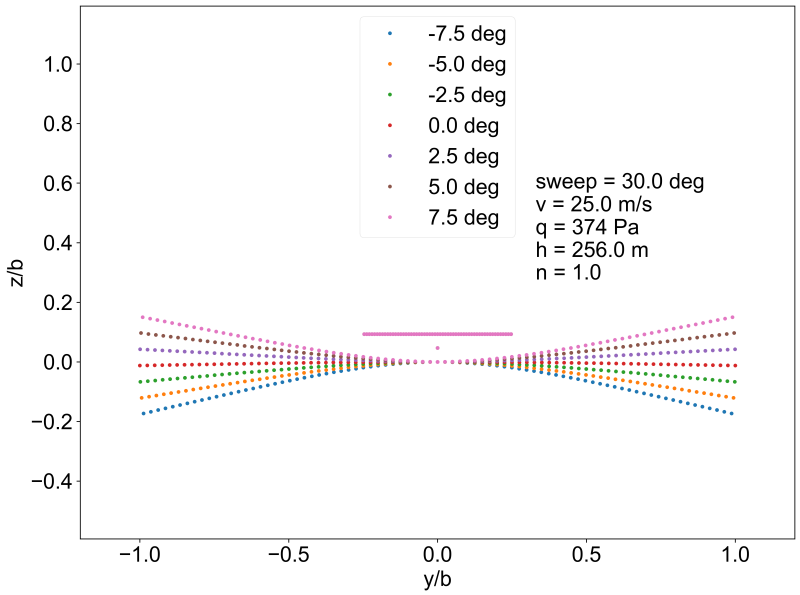

Figure G.3: EASE wing deformation at different angles of attack.

Table G.3: EASE model mass breakdown.

Component	**Mass [g]**
Wing	3392
Fuselage	2887
Tail	575
Total	6854

APPENDIX H

Additional Experimental Results

H.1 Open-loop Tests

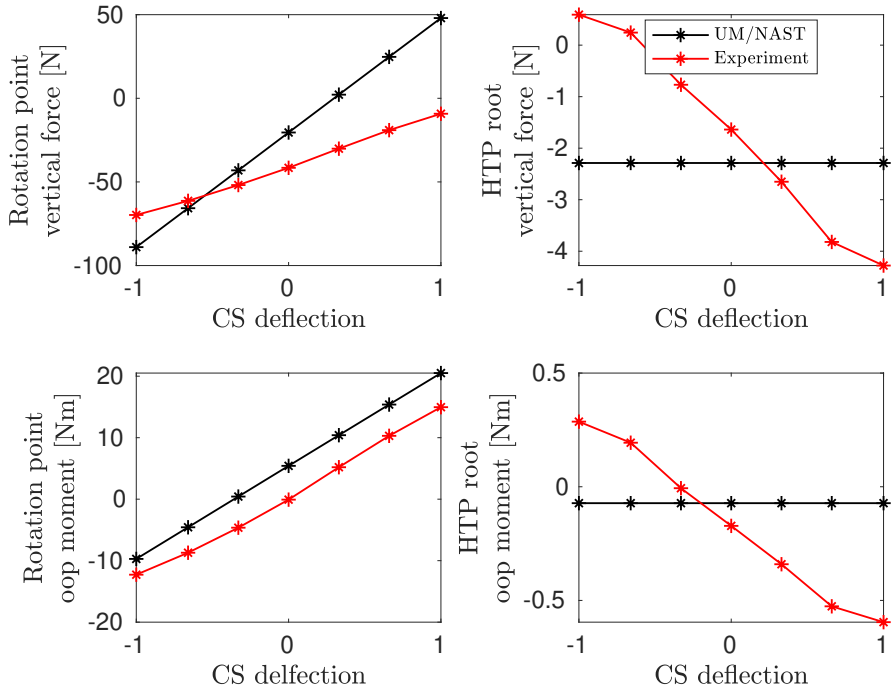

Figure H.1: Static load cell measurements (TestID 111). CS = flap group 1.

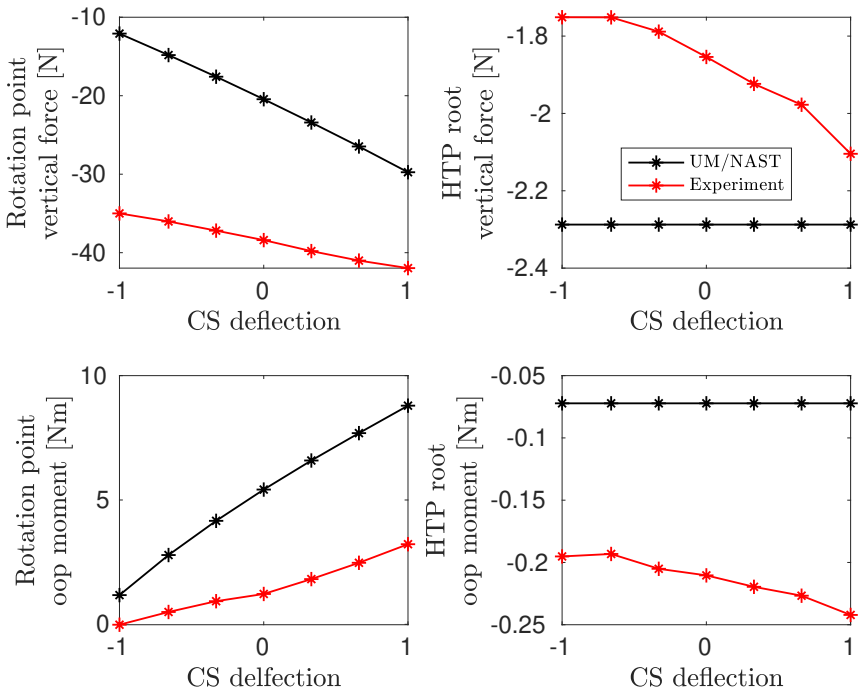

Figure H.2: Static load cell measurements (TestID 113). CS = flap group 3.

H.2 Closed-loop Tests

MVS, 1 cycle, No MLA constraints (TestID 544)

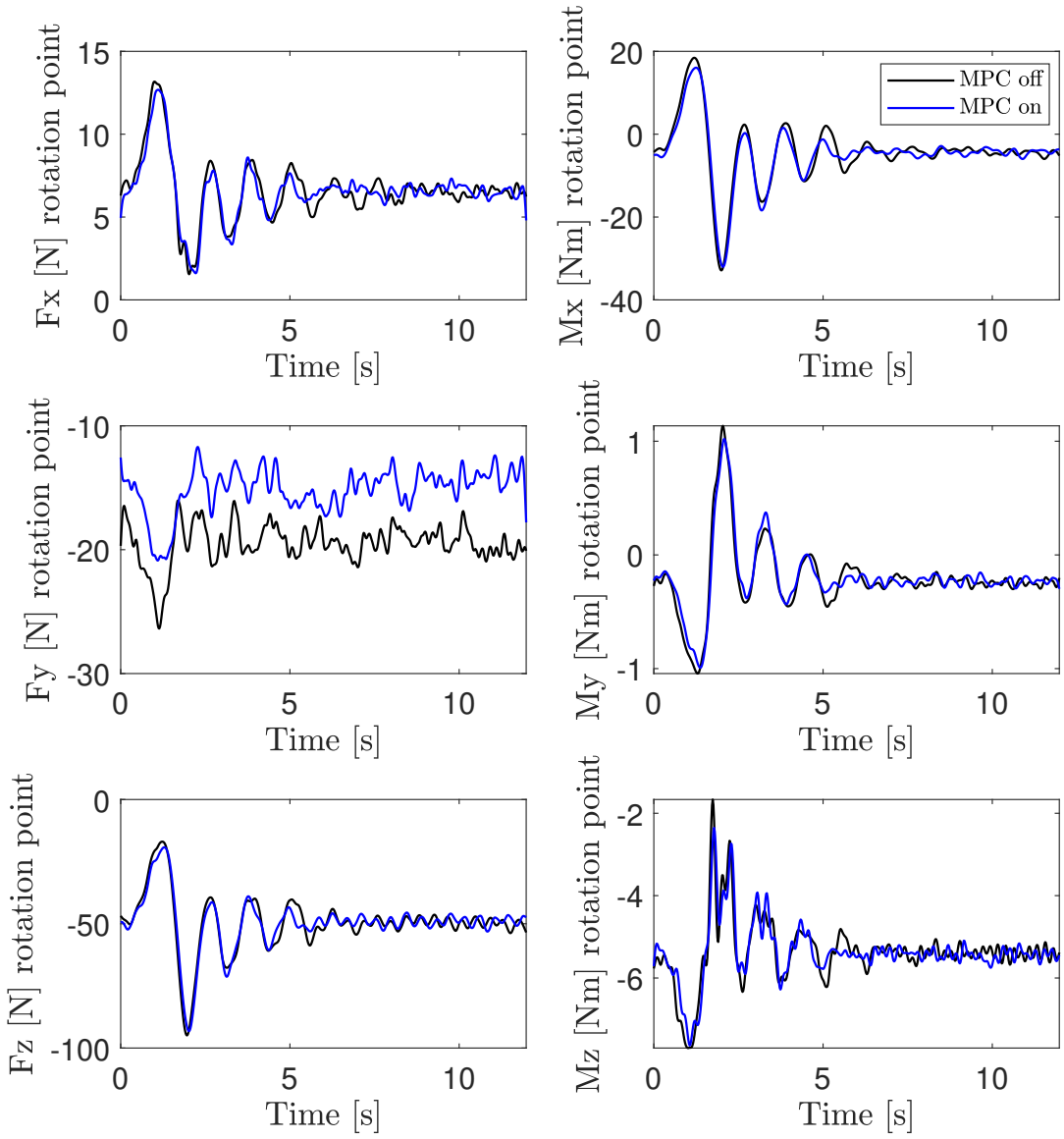

Figure H.3: MVS, 1 cycle, No MLA constraints (TestID 544). Forces and moments at rotation point.

MVS, 1 cycle, MLA constraints on wing only (TestID 544)

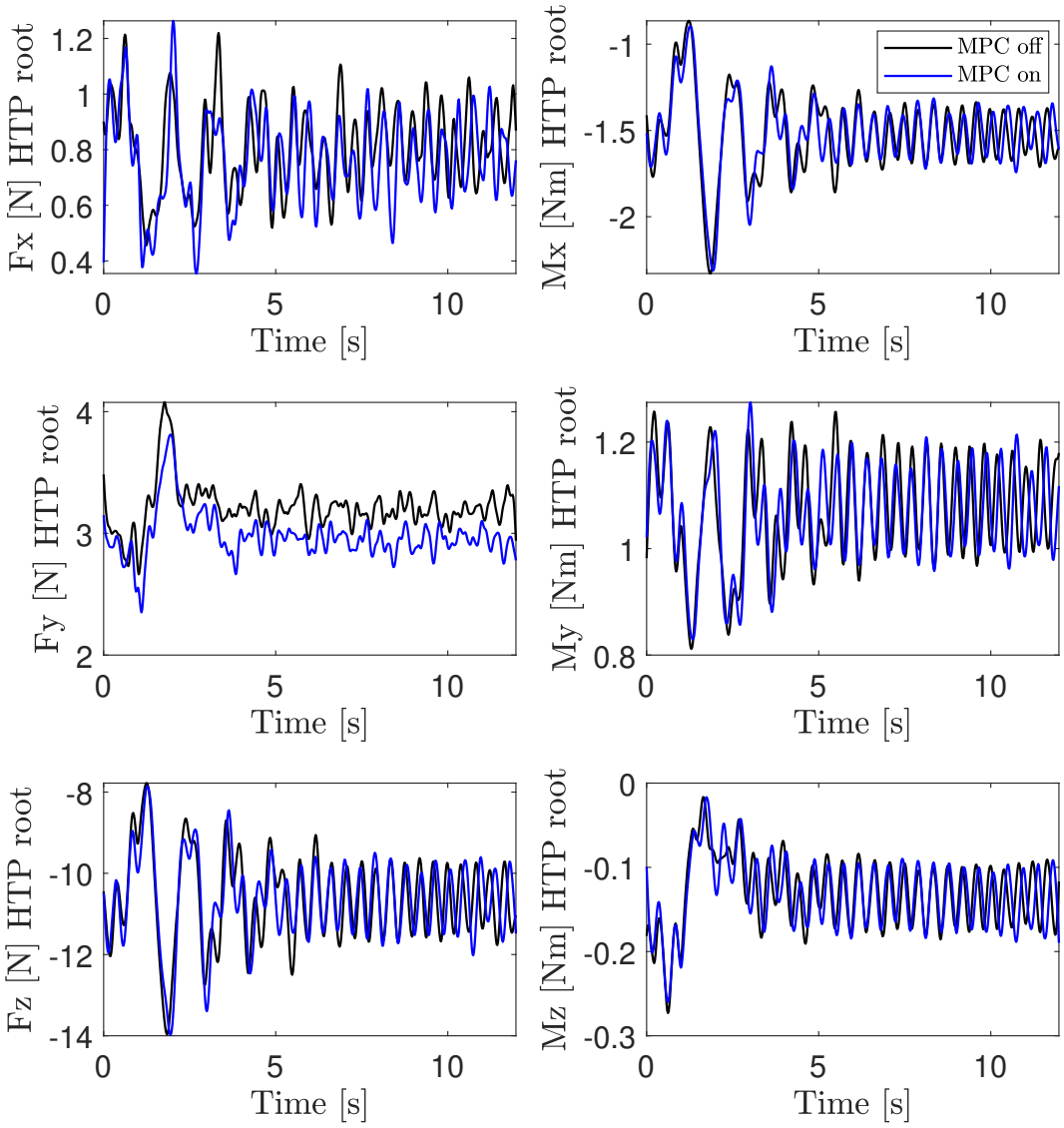

Figure H.4: MVS, 1 cycle, No MLA constraints (TestID 544). Forces and moments at HTP.

MVS, 1 cycle, MLA constraints on wing only (TestID 544-b)

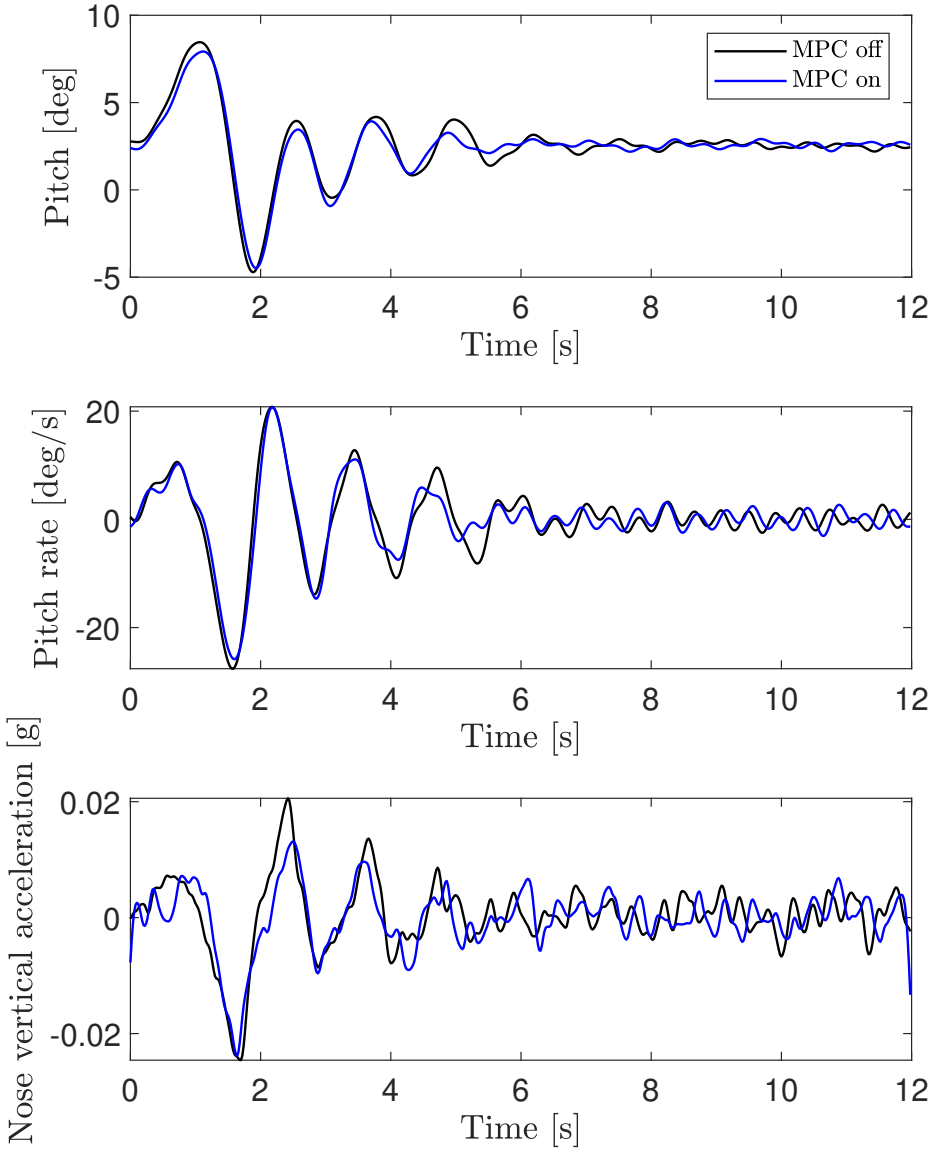

Figure H.5: MVS, 1 cycle, No MLA constraints (TestID 544). Pitch angle, pitch rate, and vertical acceleration at nose.

MVS, 1 cycle, MLA constraints on wing and HTP (TestID 570)

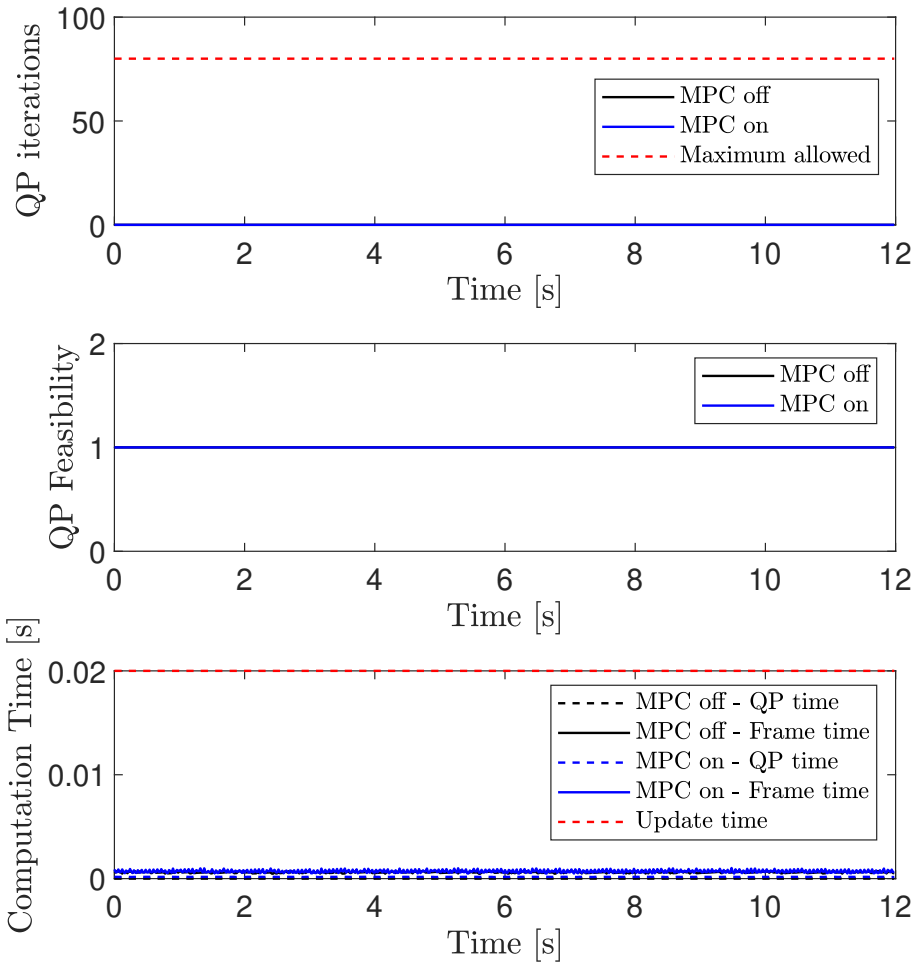

Figure H.6: MVS, 1 cycle, No MLA constraints (TestID 544). Computational time and optimization solver performance.

MVS, 3 cycles, No MLA constraints (TestID 545)

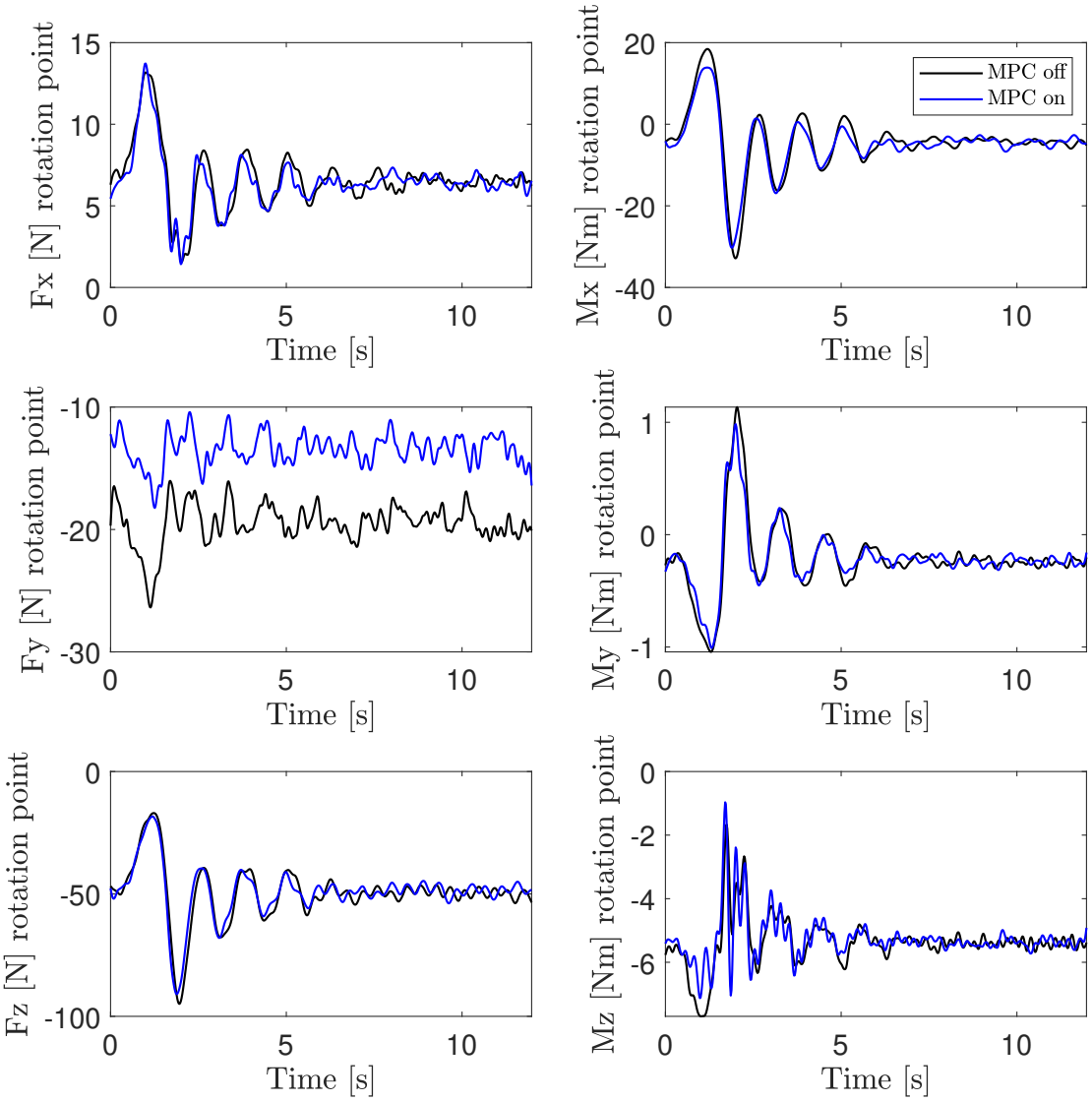

Figure H.7: MVS, 1 cycle, MLA constraints on wing only (TestID 547). Forces and moments at rotation point.

MVS, 3 cycles, MLA constraints on wing only (TestID 548)

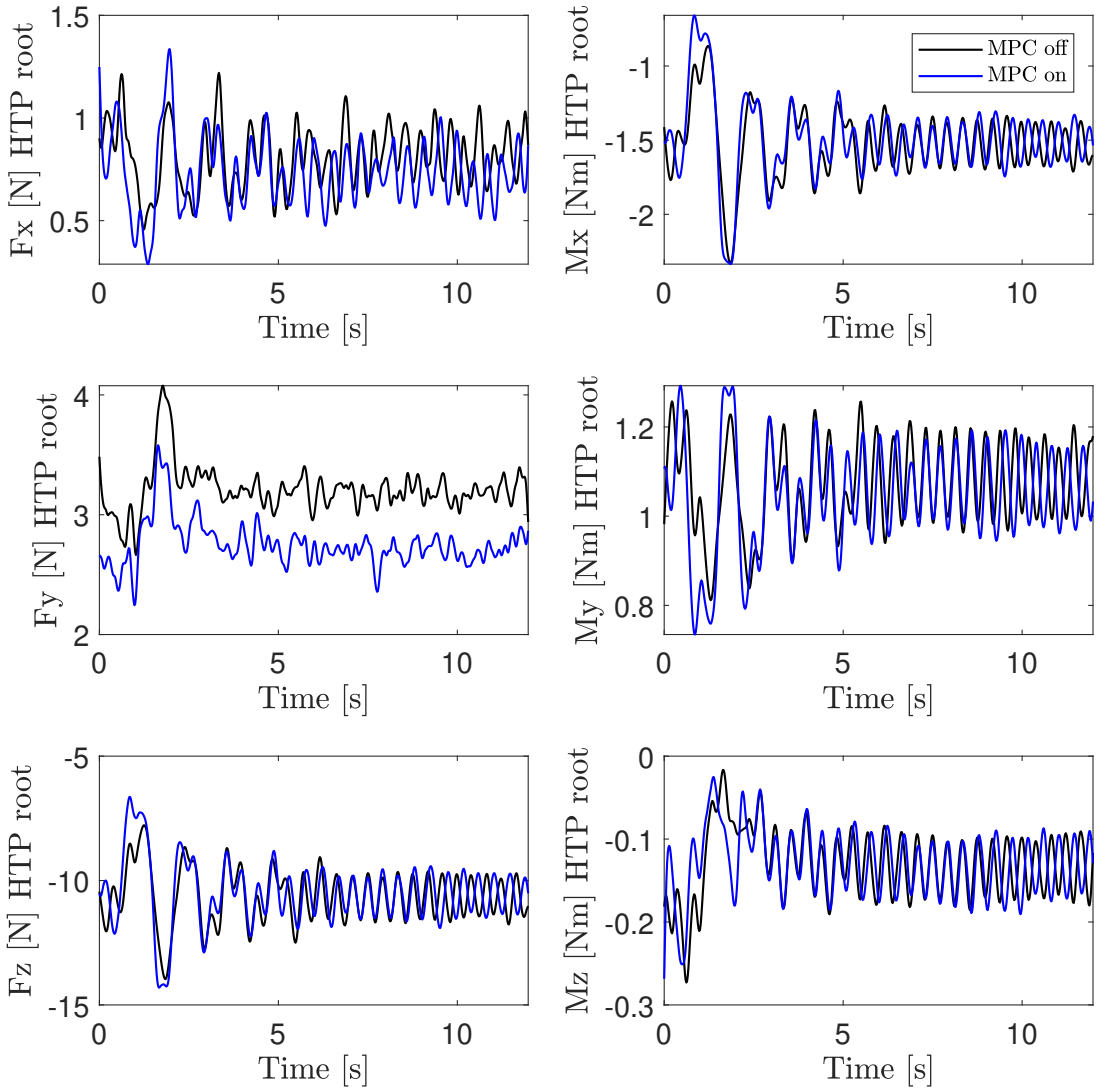

Figure H.8: MVS, 1 cycle, MLA constraints on wing only (TestID 547). Forces and moments at HTP.

MVS, 3 cycles, MLA constraints on wing and HTP (TestID 554)

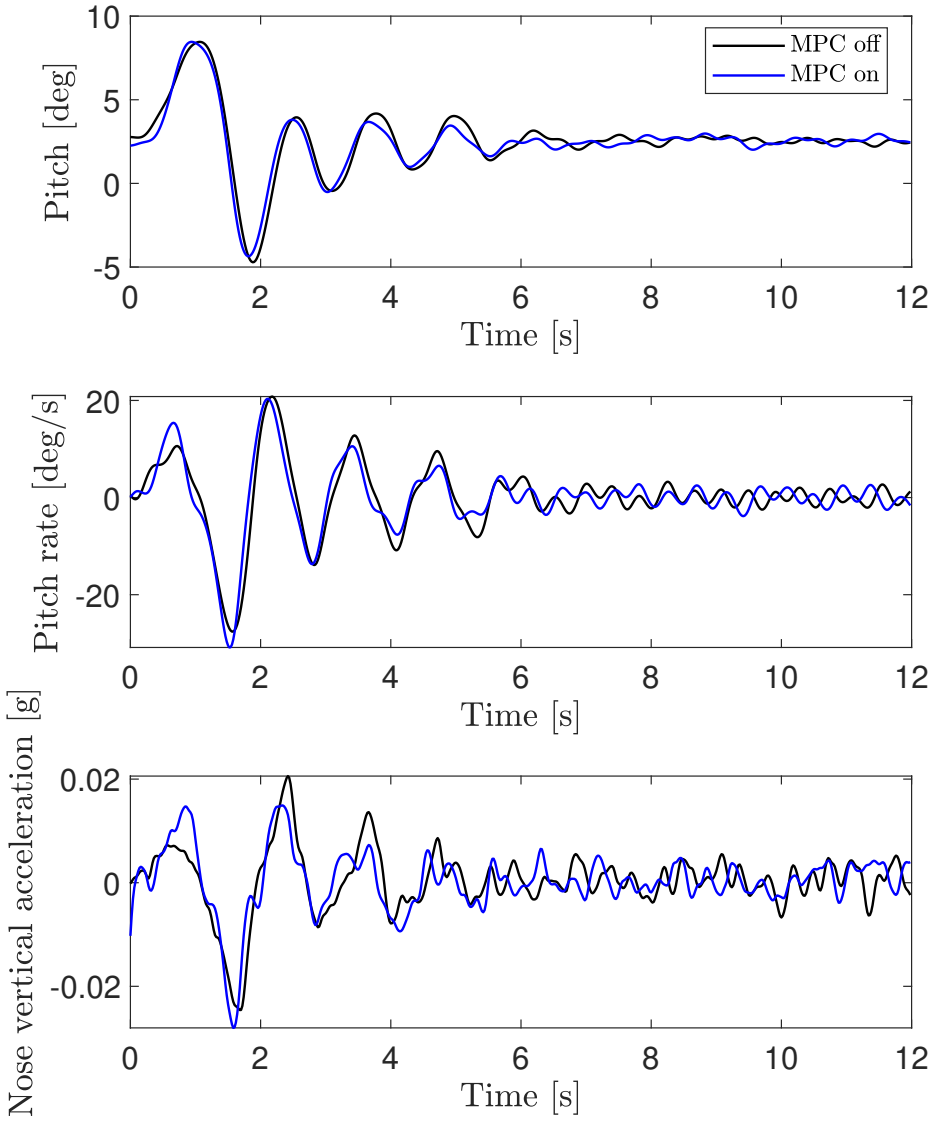

Figure H.9: MVS, 1 cycle, MLA constraints on wing only (TestID 547). Pitch angle, pitch rate, and vertical acceleration at nose.

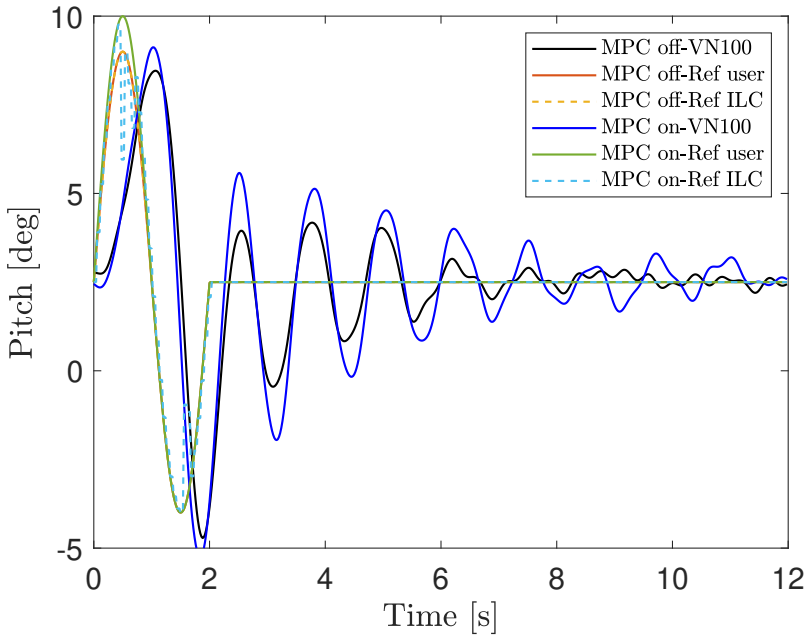

Figure H.10: MVS, 1 cycle, MLA constraints on wing only (TestID 547-b).Commanded pitch and aircraft response.

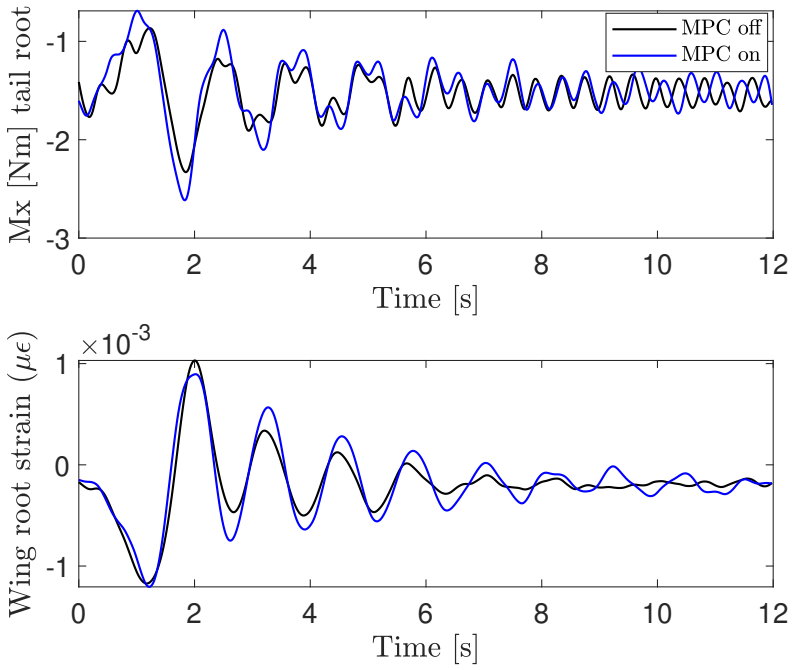

Figure H.11: MVS, 1 cycle, MLA constraints on wing only (TestID 547-b). Out-of-plane bending moment on HTP tail root, and strain on wing root.

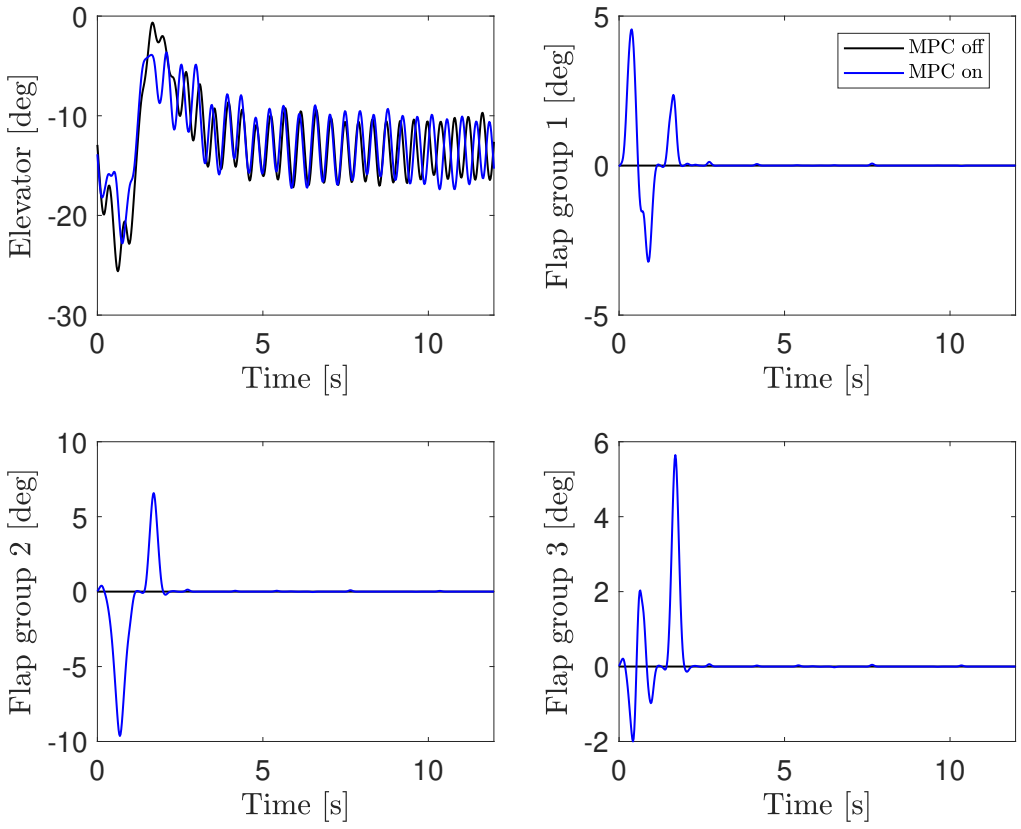

Figure H.12: MVS, 1 cycle, MLA constraints on wing only (TestID 547-b). Control surfaces histories.

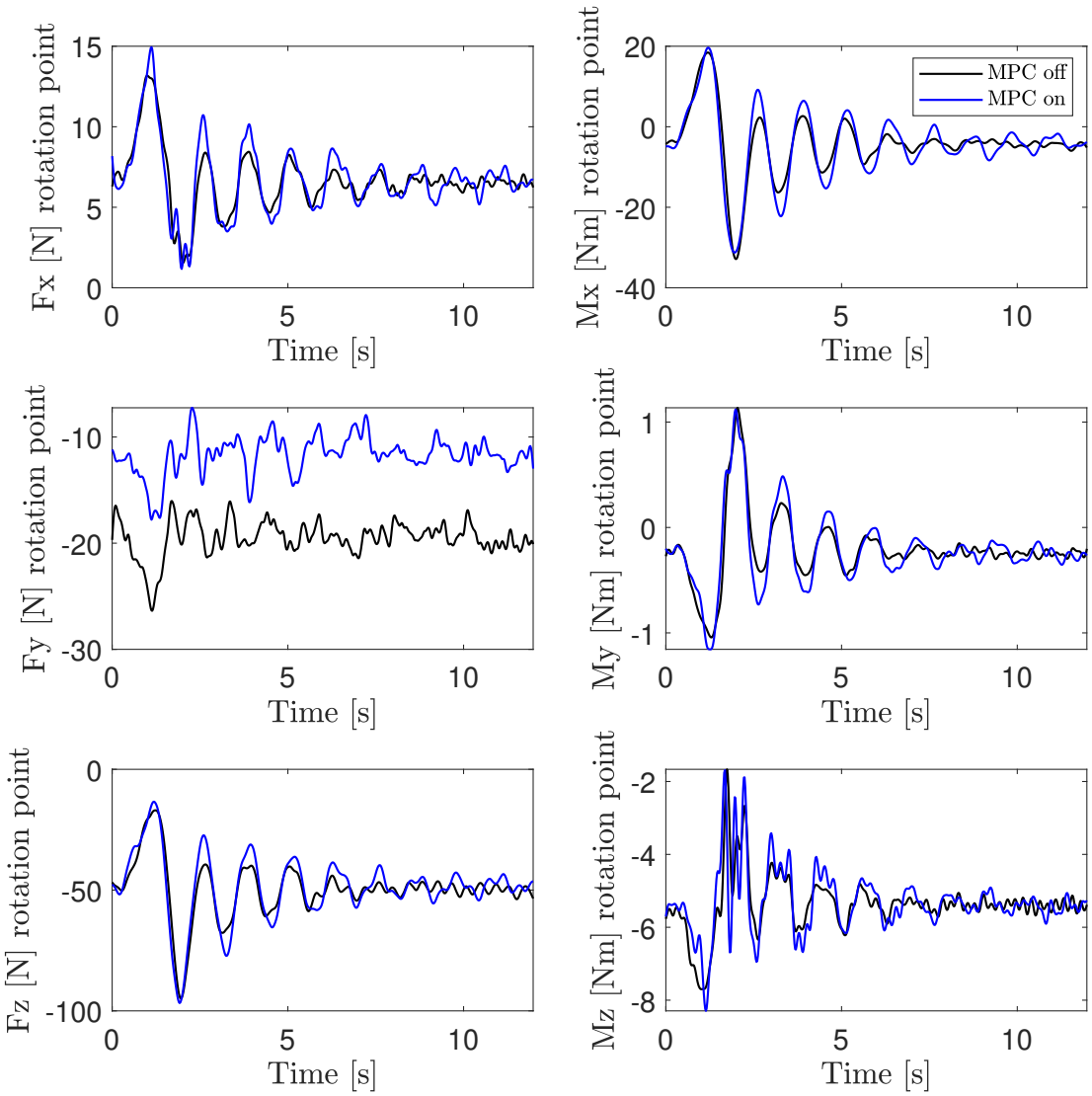

Figure H.13: MVS, 1 cycle, MLA constraints on wing only (TestID 547-b). Forces and moments at rotation point.

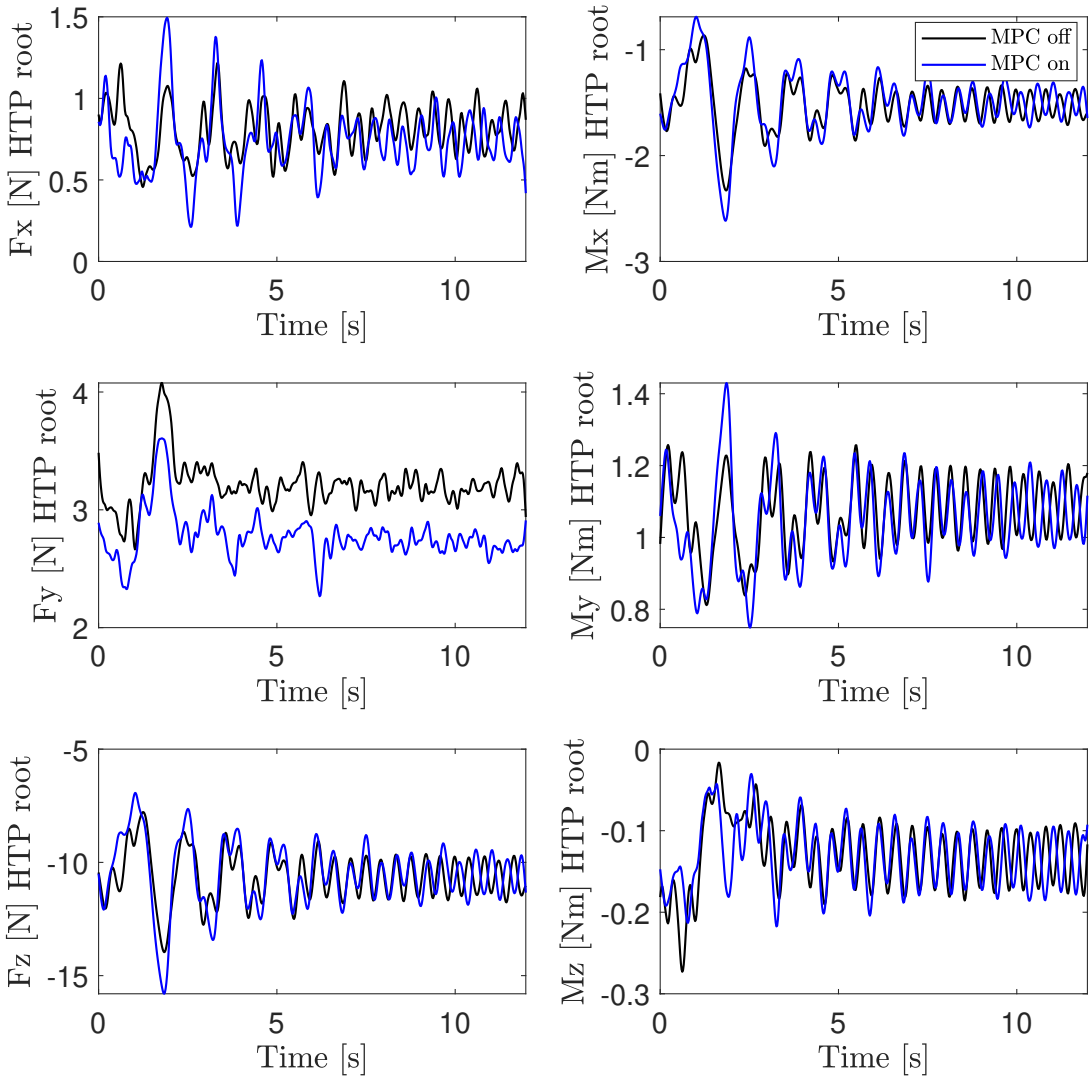

Figure H.14: MVS, 1 cycle, MLA constraints on wing only (TestID 547-b). Forces and moments at HTP.

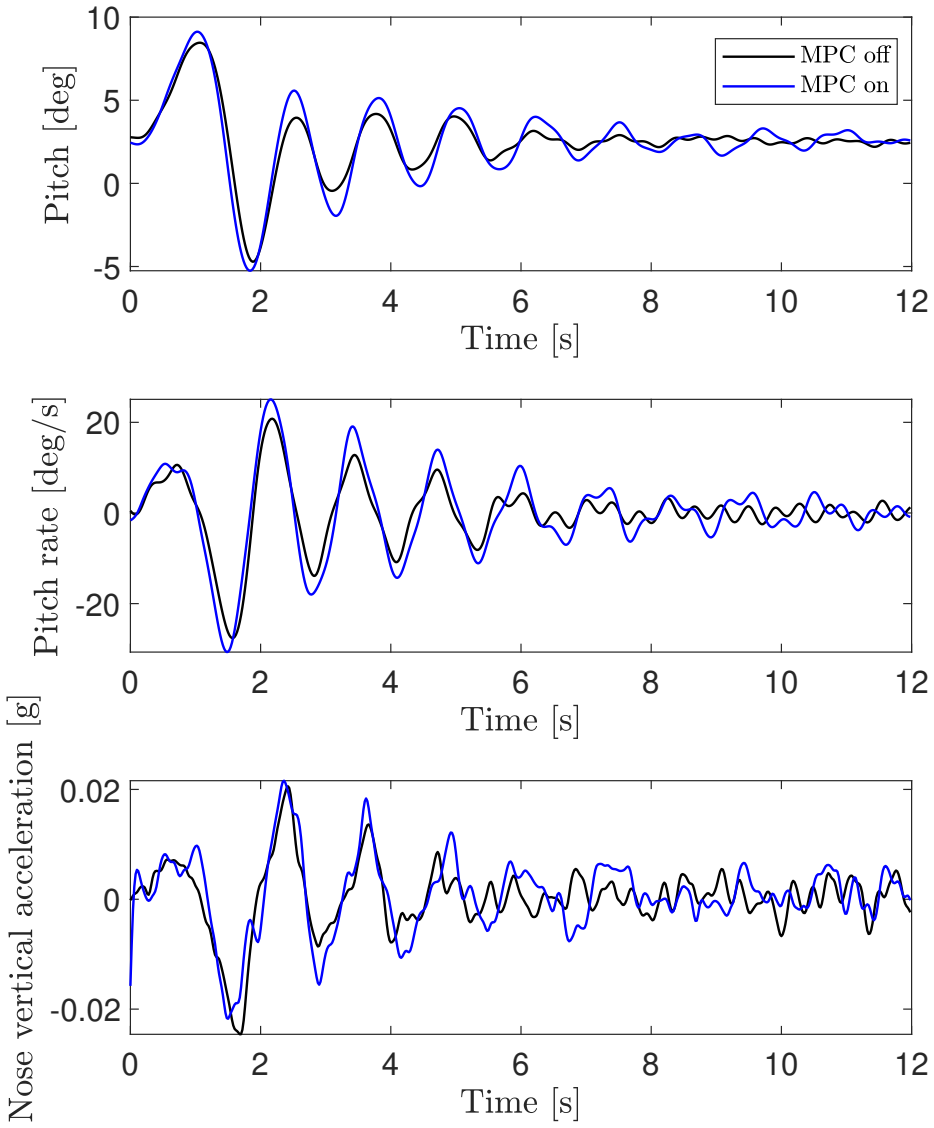

Figure H.15: MVS, 1 cycle, MLA constraints on wing only (TestID 547-b). Pitch angle, pitch rate, and vertical acceleration at nose.

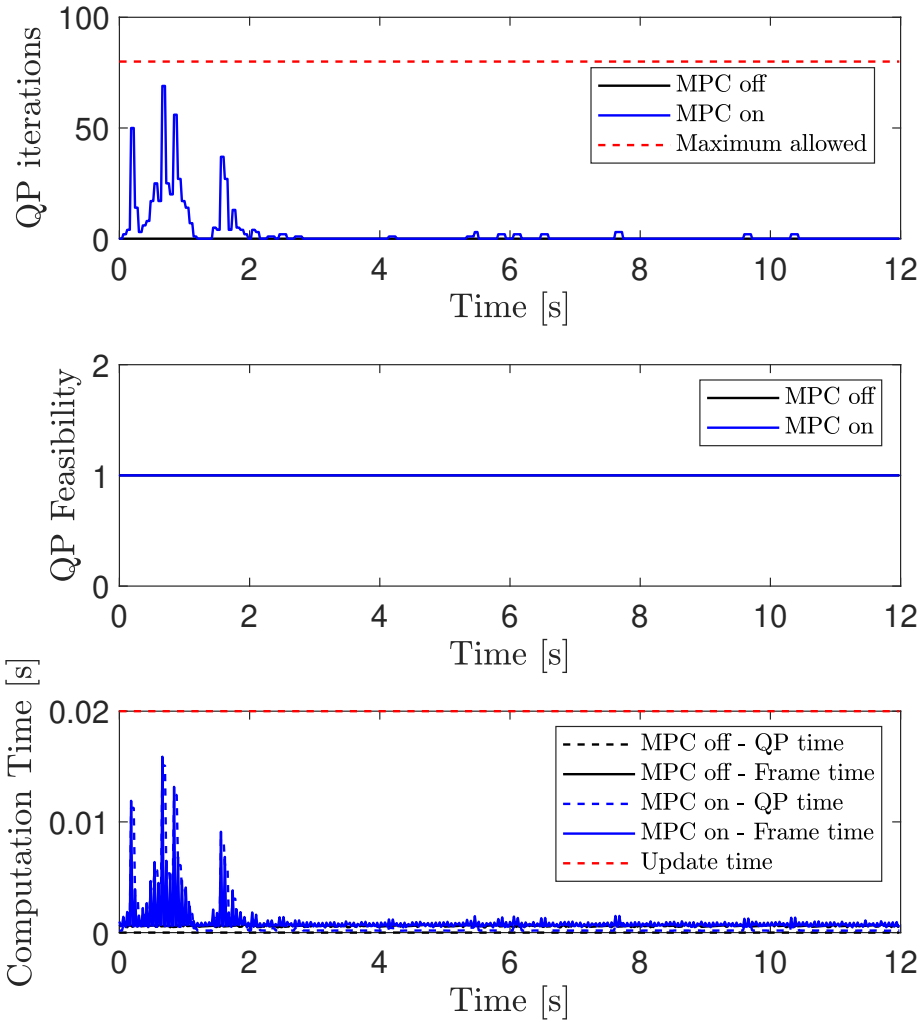

Figure H.16: MVS, 1 cycle, MLA constraints on wing only (TestID 547-b). Computational time and optimization solver performance.

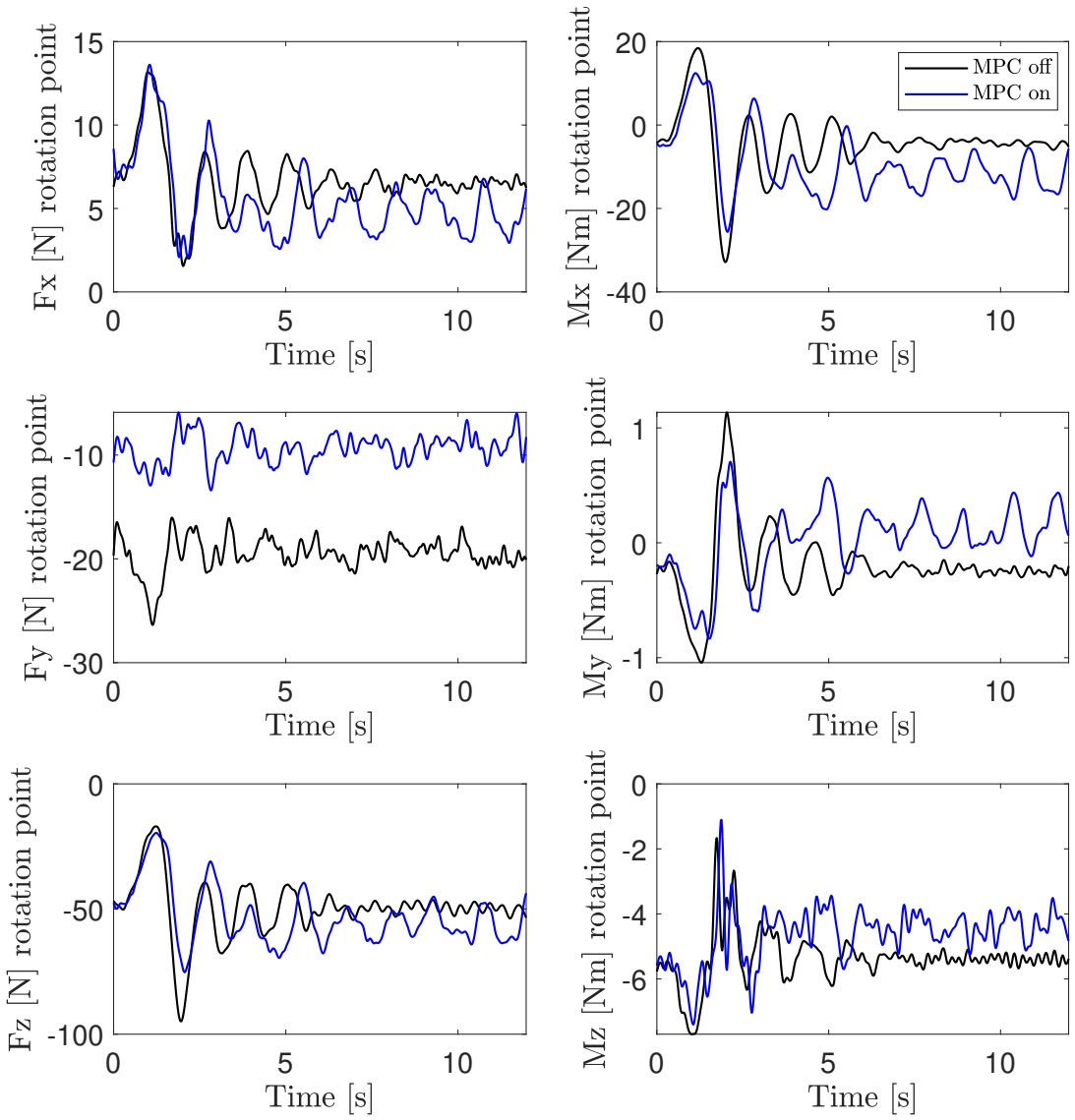

Figure H.17: MVS, 1 cycle, MLA constraints on wing and HTP (TestID 570). Forces and moments at rotation point.

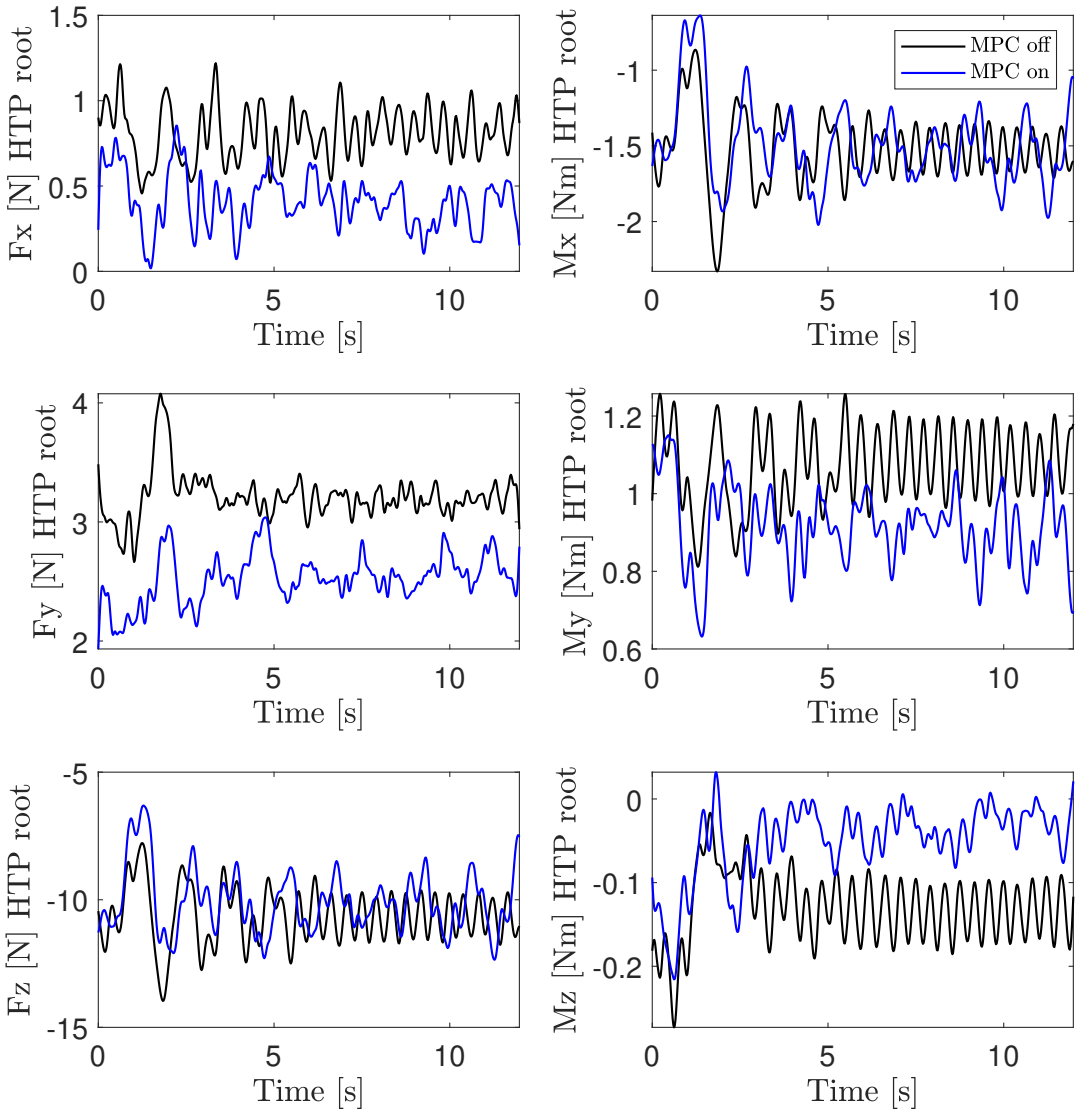

Figure H.18: MVS, 1 cycle, MLA constraints on wing and HTP (TestID 570). Forces and moments at HTP.

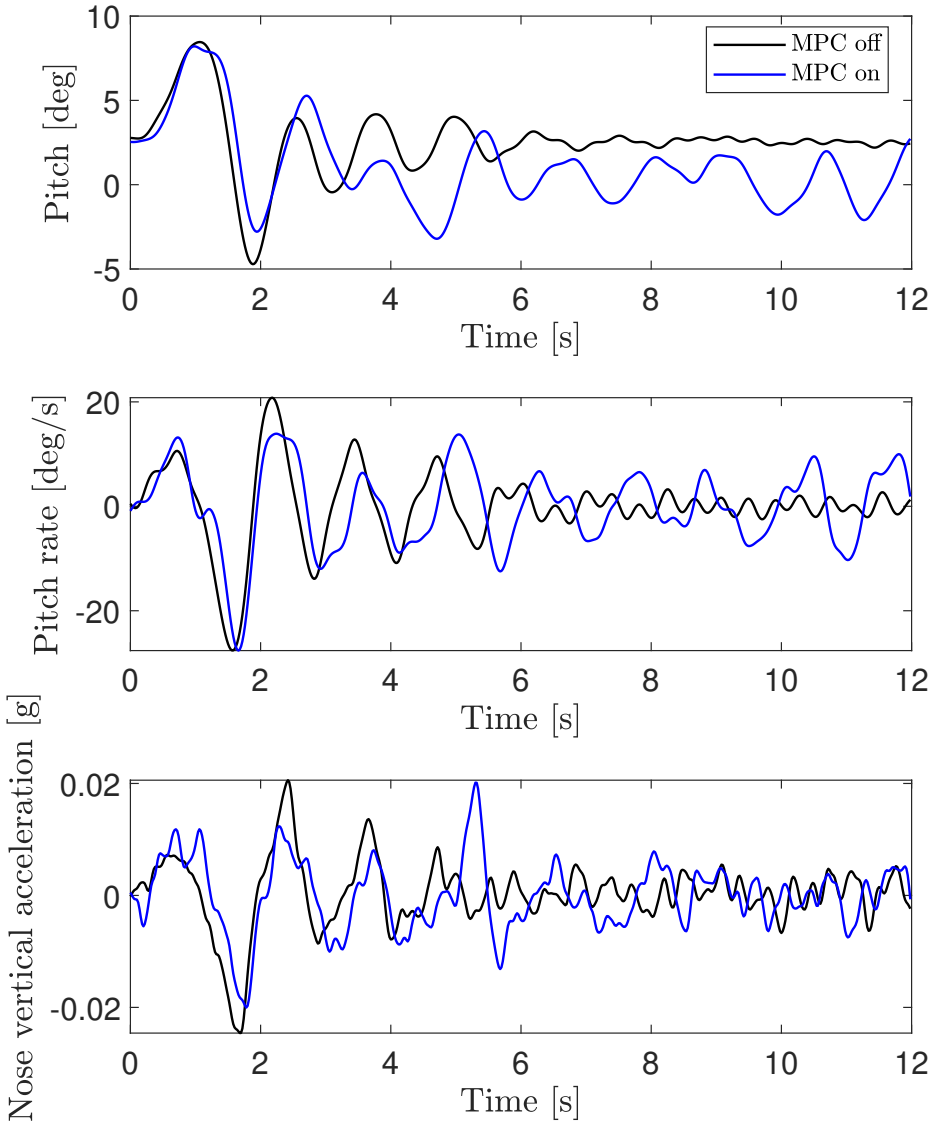

Figure H.19: MVS, 1 cycle, MLA constraints on wing and HTP (TestID 570). Pitch angle, pitch rate, and vertical acceleration at nose.

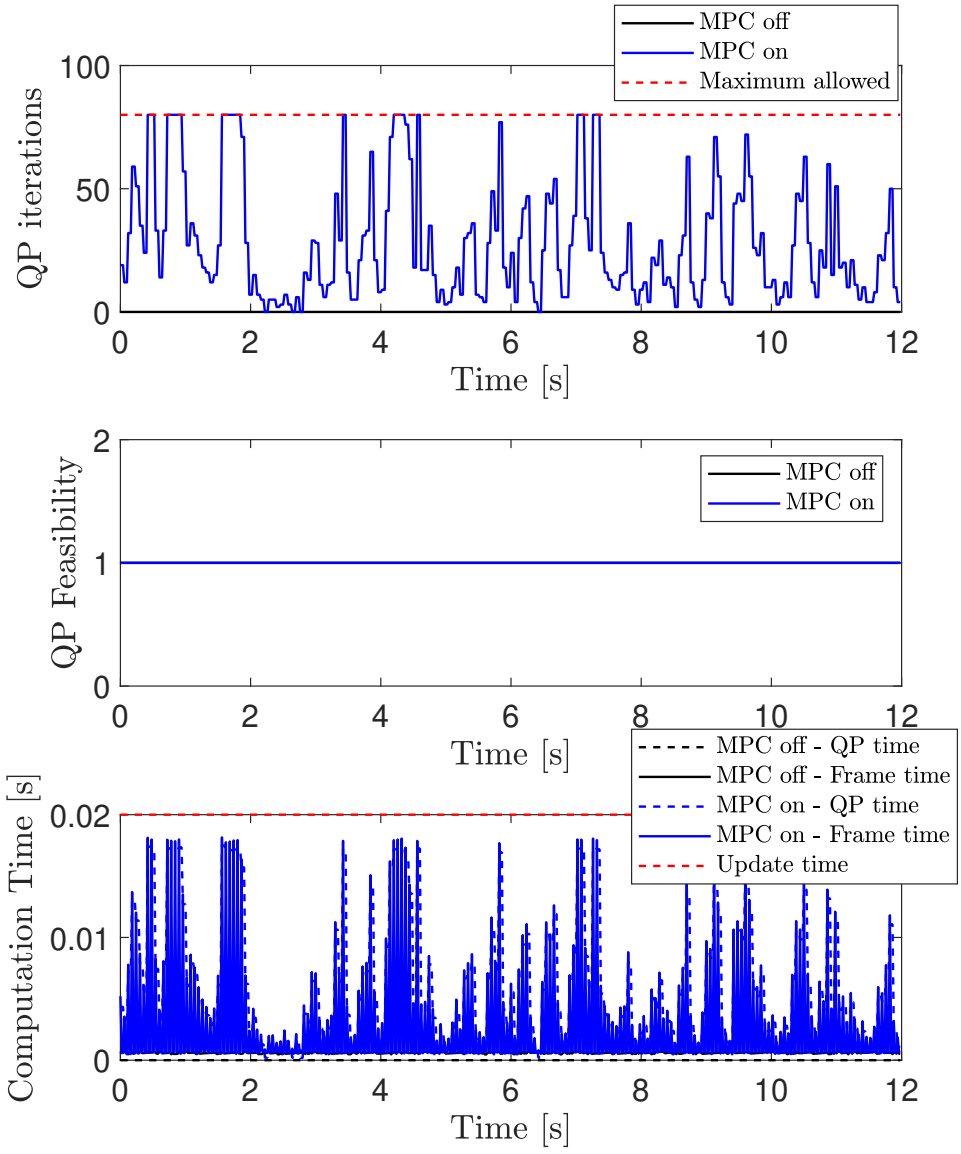

Figure H.20: MVS, 1 cycle, MLA constraints on wing and HTP (TestID 570). Computational time and optimization solver performance.

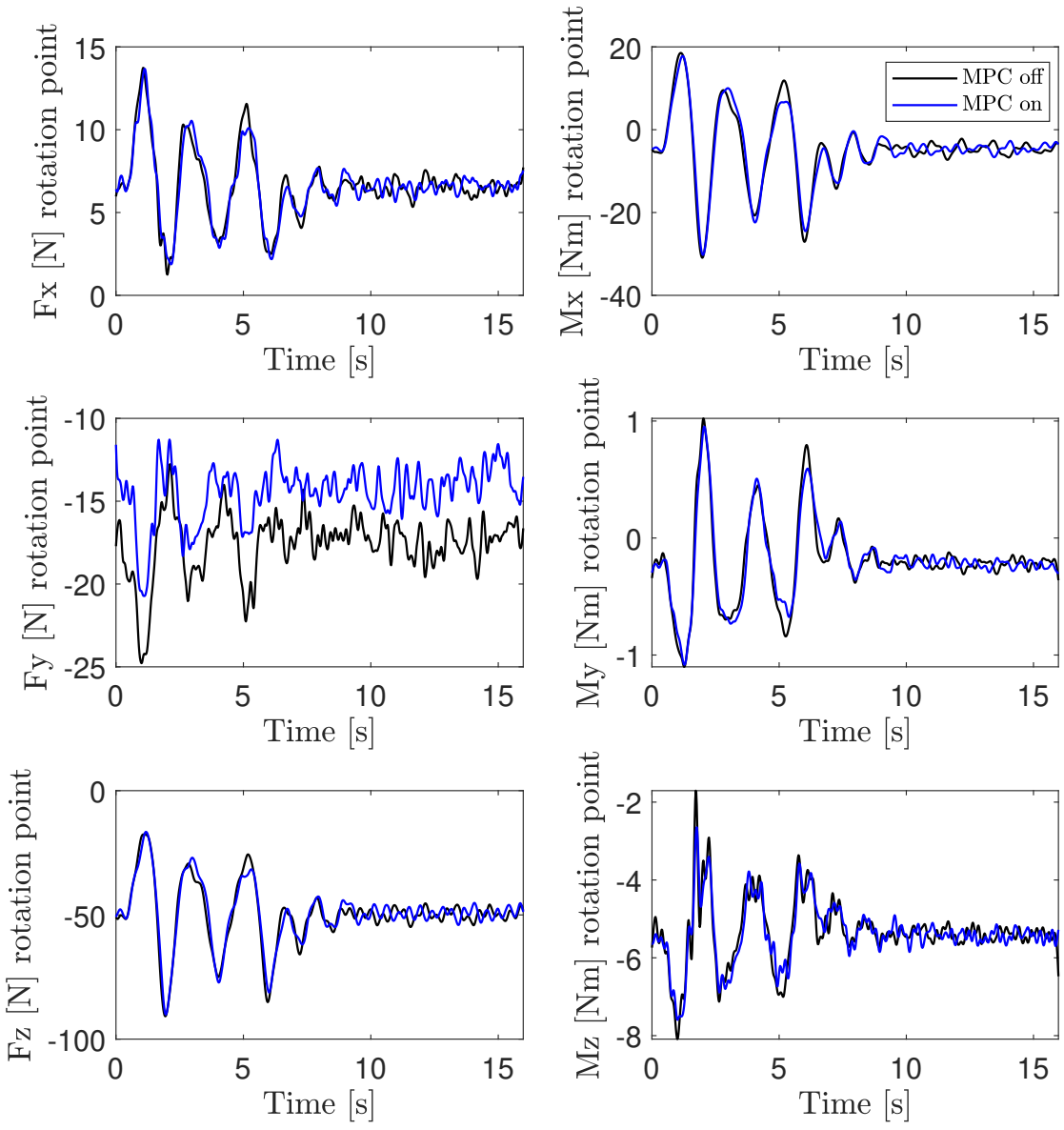

Figure H.21: MVS, 3 cycles, No MLA constraints (TestID 545). Forces and moments at rotation point.

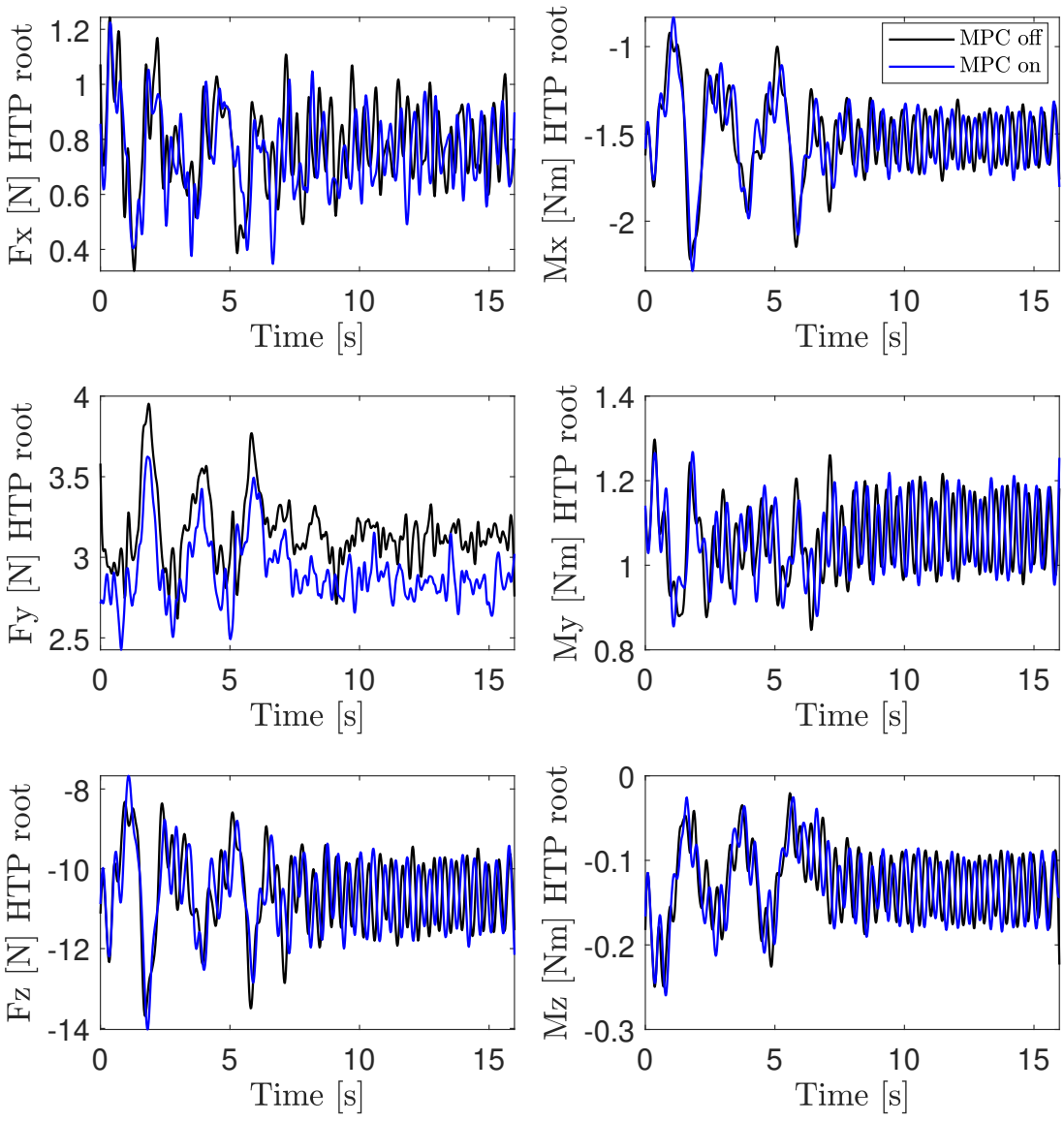

Figure H.22: MVS, 3 cycles, No MLA constraints (TestID 545). Forces and moments at HTP.

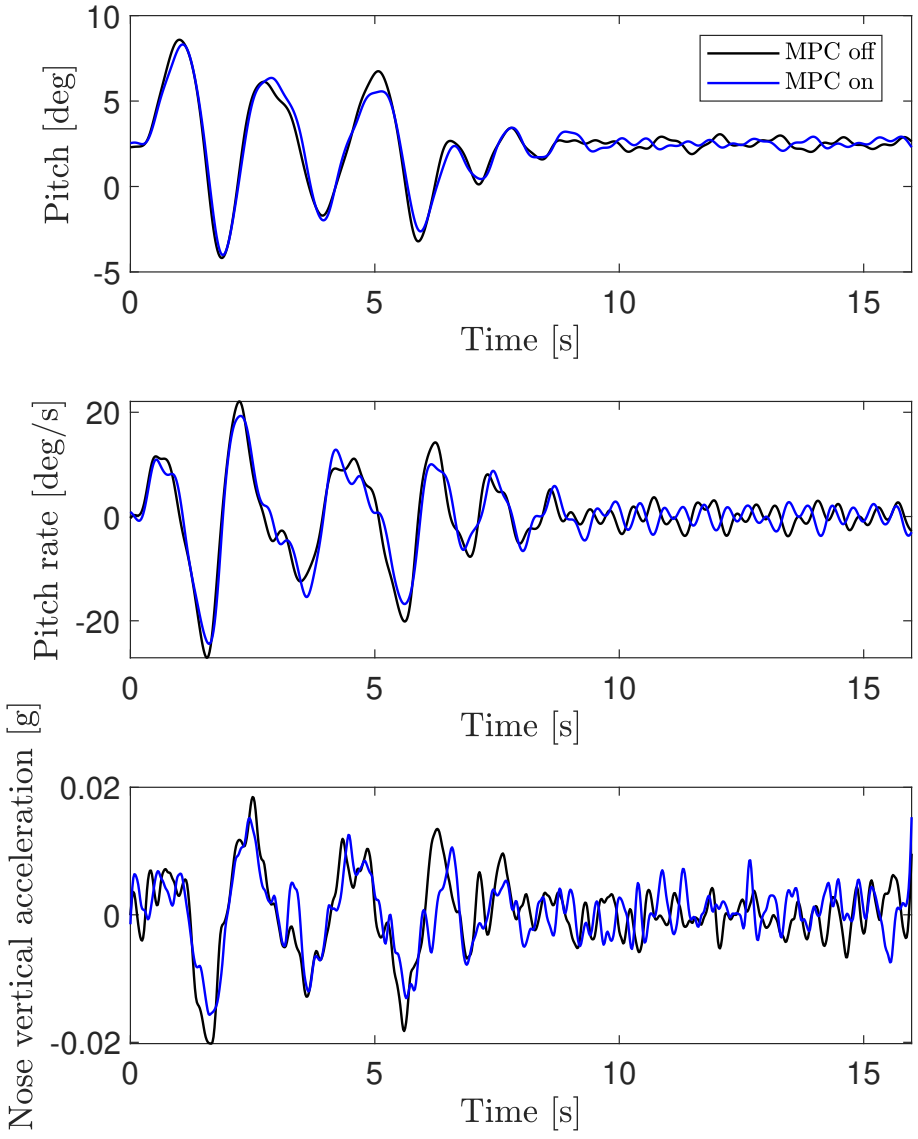

Figure H.23: MVS, 3 cycles, No MLA constraints (TestID 545). Pitch angle, pitch rate, and vertical acceleration at nose.

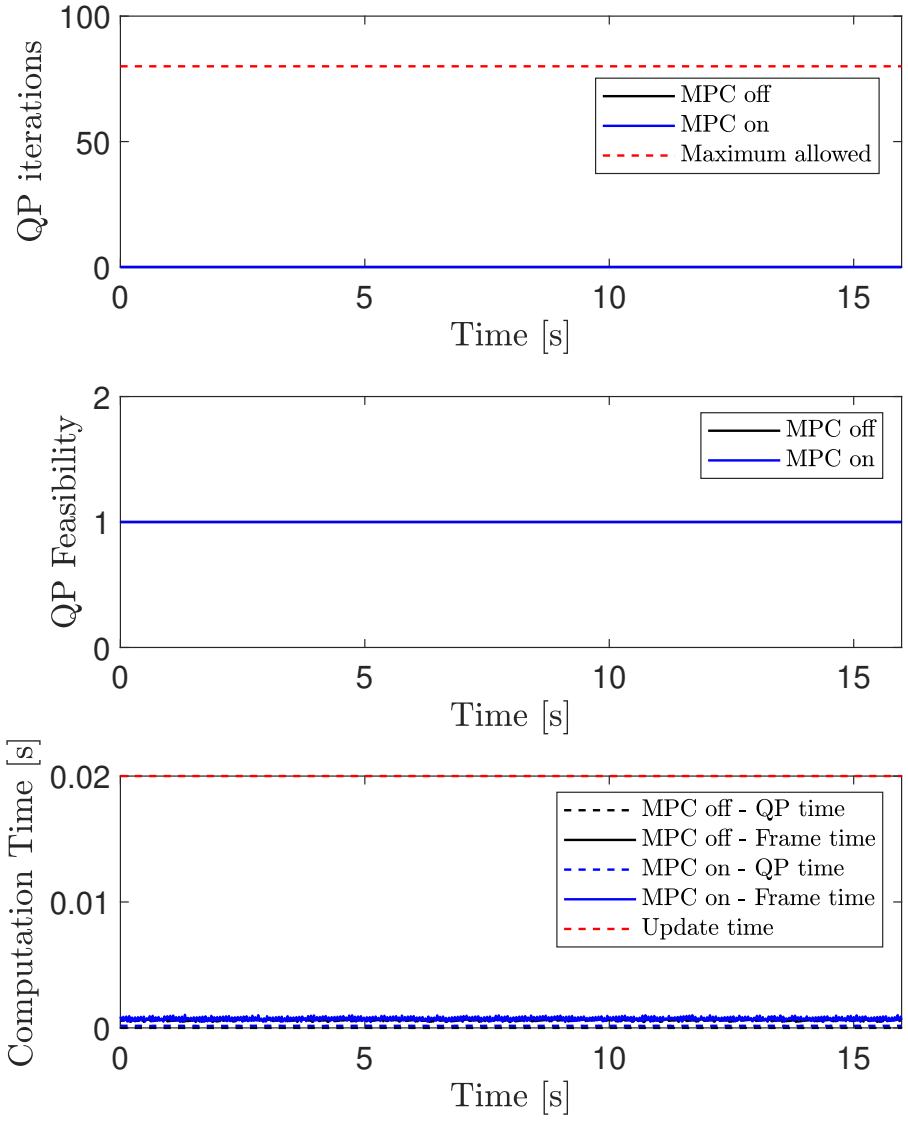

Figure H.24: MVS, 3 cycles, No MLA constraints (TestID 545). Computational time and optimization solver performance.

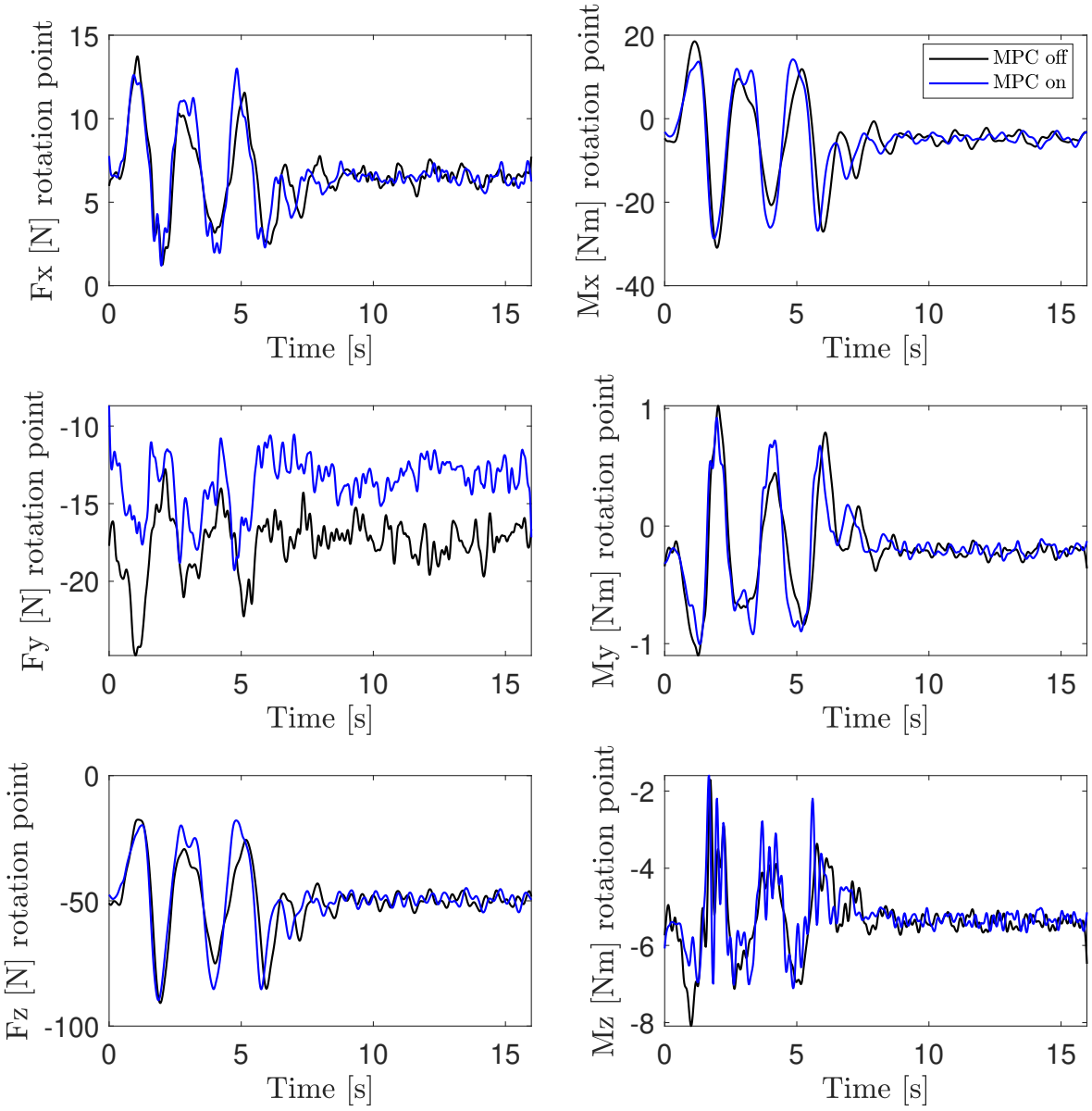

Figure H.25: MVS, 3 cycles, MLA constraints on wing only (TestID 548). Forces and moments at rotation point.

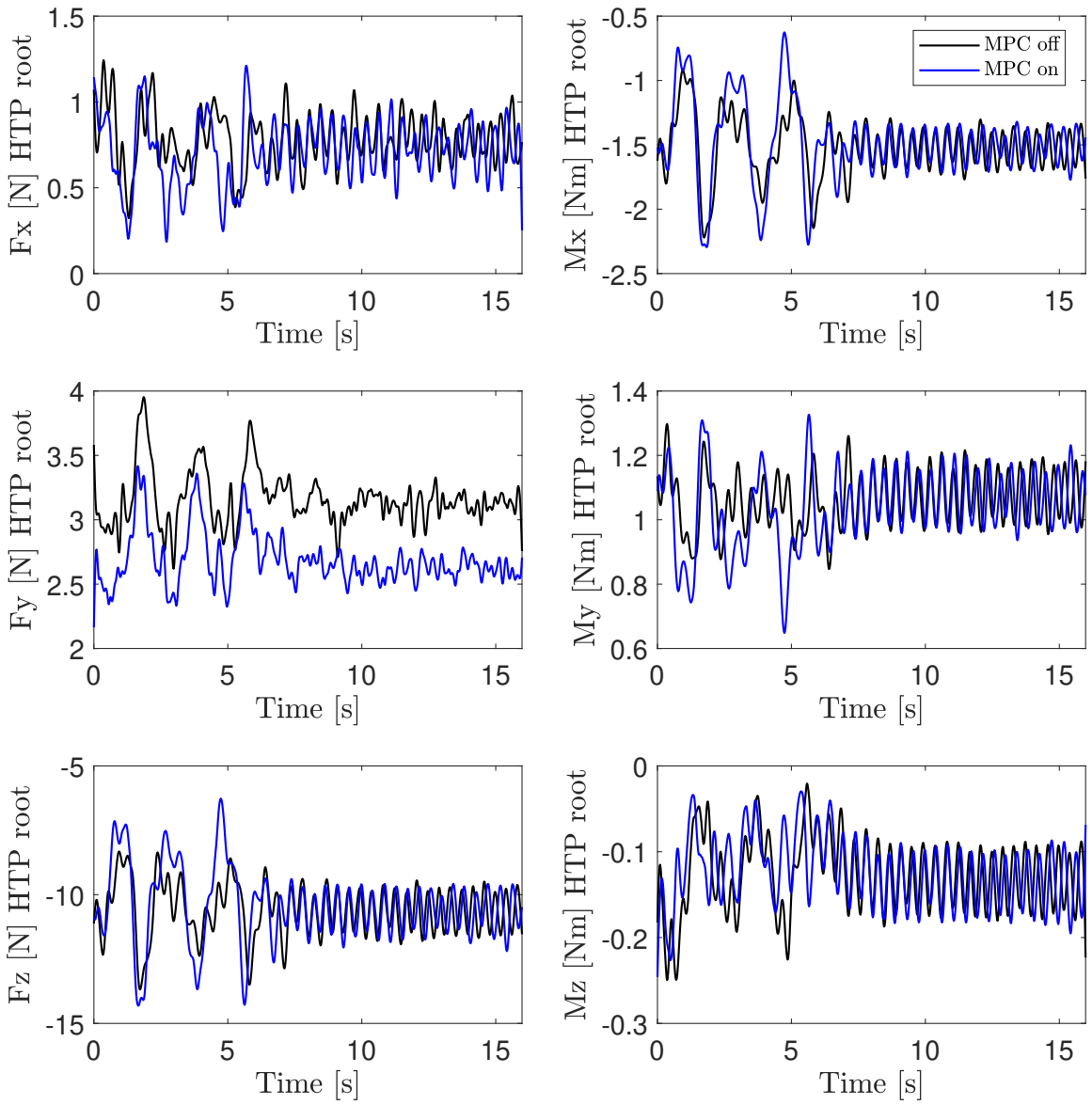

Figure H.26: MVS, 3 cycles, MLA constraints on wing only (TestID 548). Forces and moments at HTP.

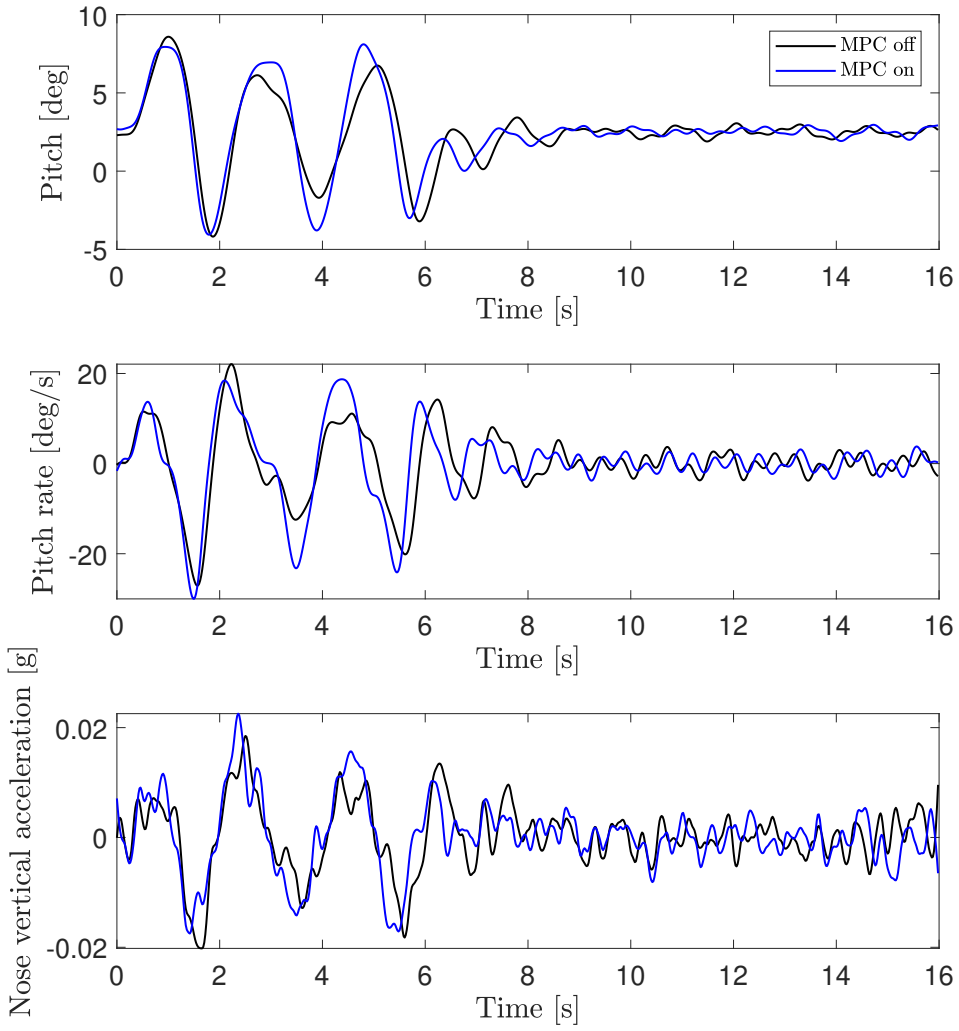

Figure H.27: MVS, 3 cycles, MLA constraints on wing only (TestID 548). Pitch angle, pitch rate, and vertical acceleration at nose.

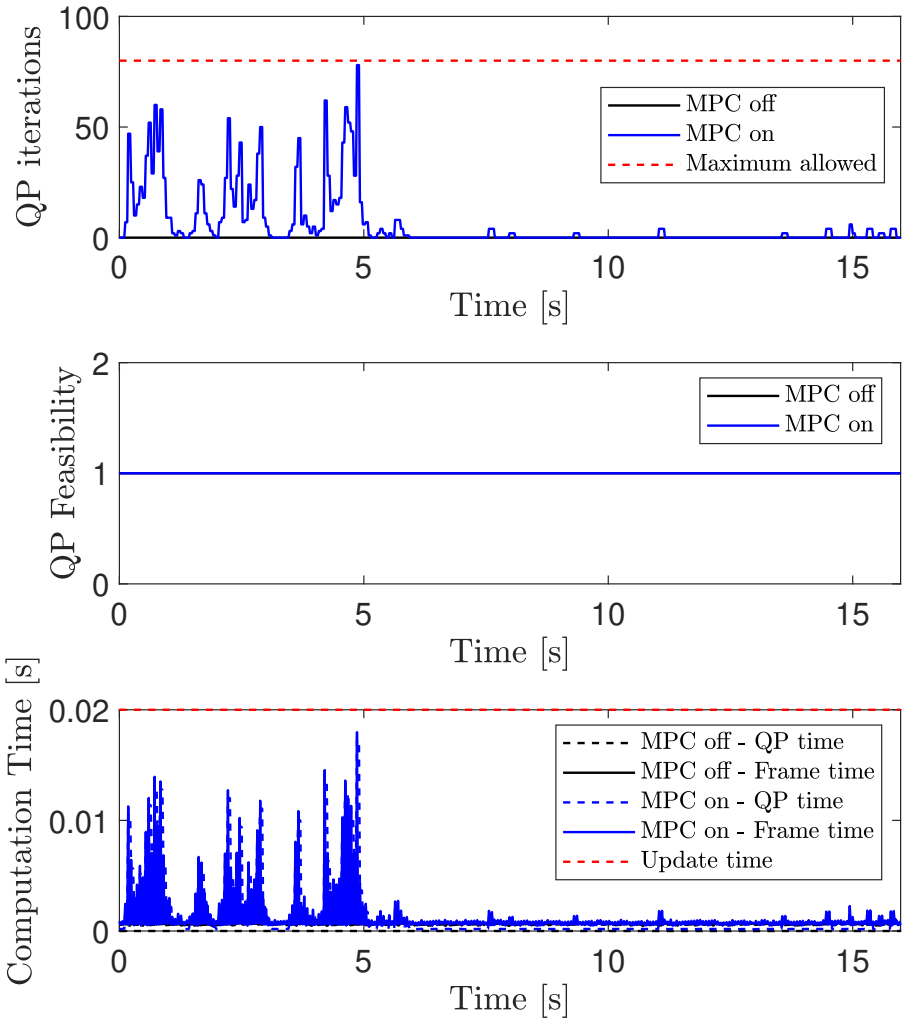

Figure H.28: MVS, 3 cycles, MLA constraints on wing only (TestID 548). Computational time and optimization solver performance.

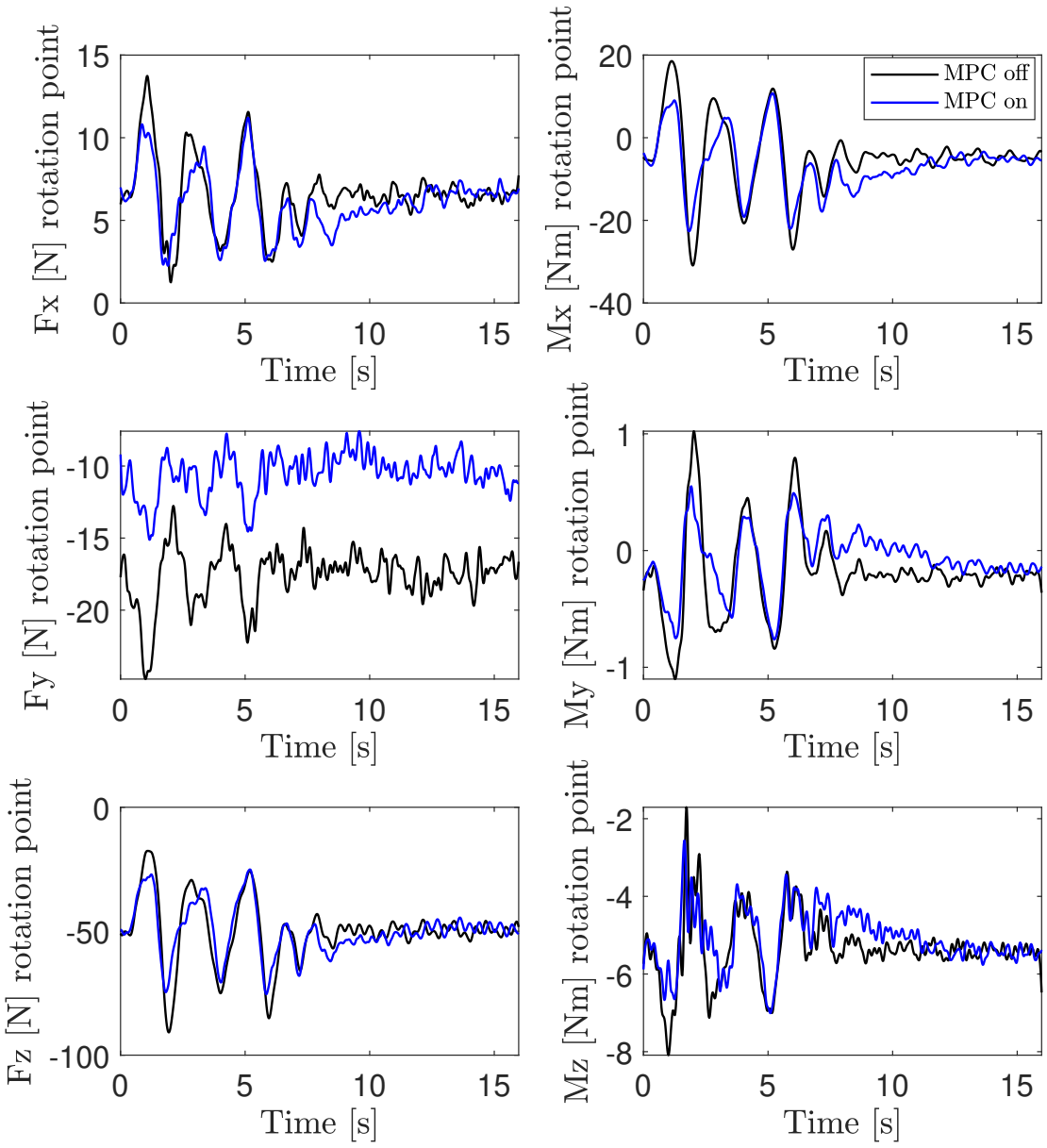

Figure H.29: MVS, 3 cycles, MLA constraints on wing and HTP (TestID 554). Forces and moments at rotation point.

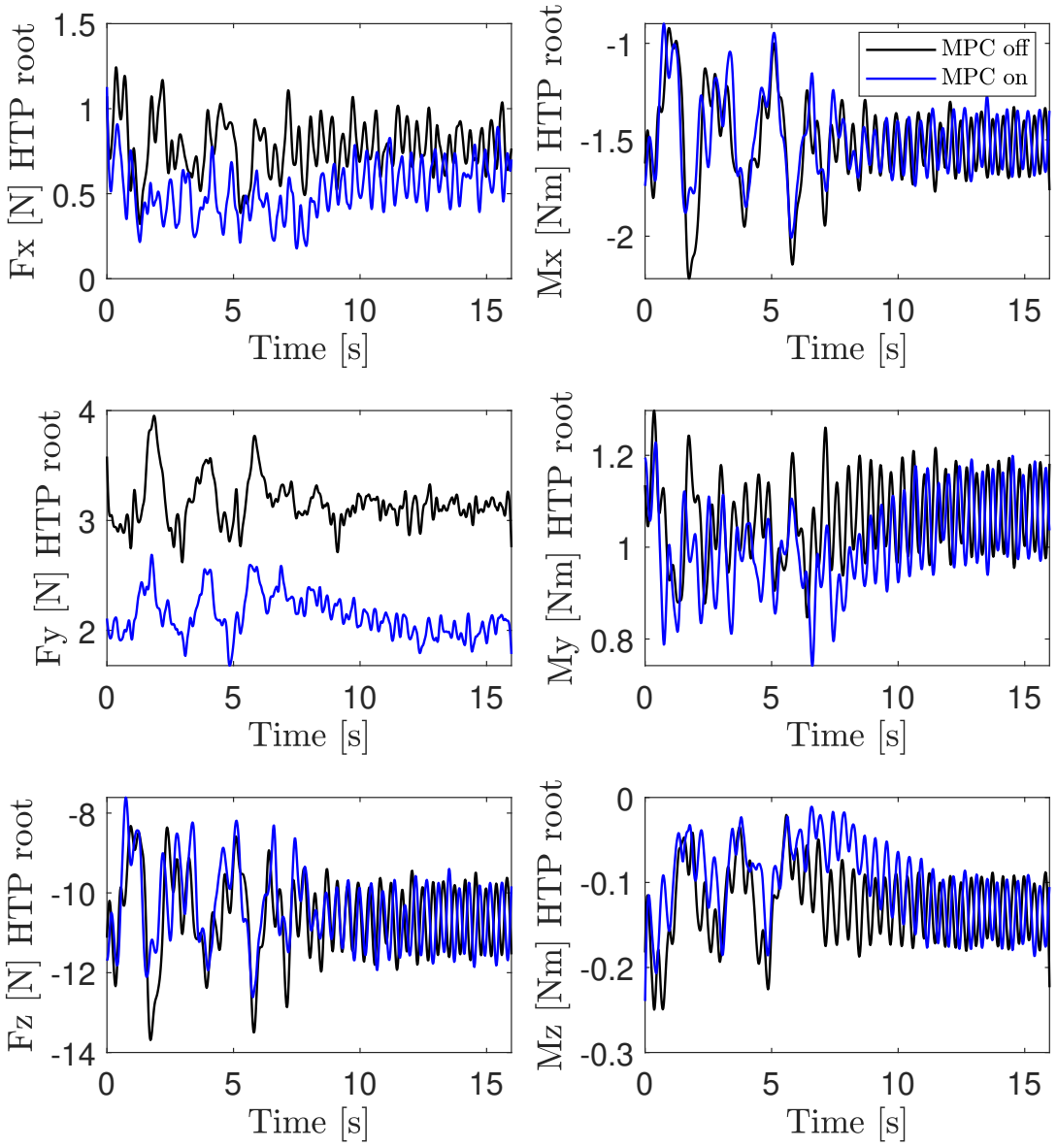

Figure H.30: MVS, 3 cycles, MLA constraints on wing and HTP (TestID 554). Forces and moments at HTP.

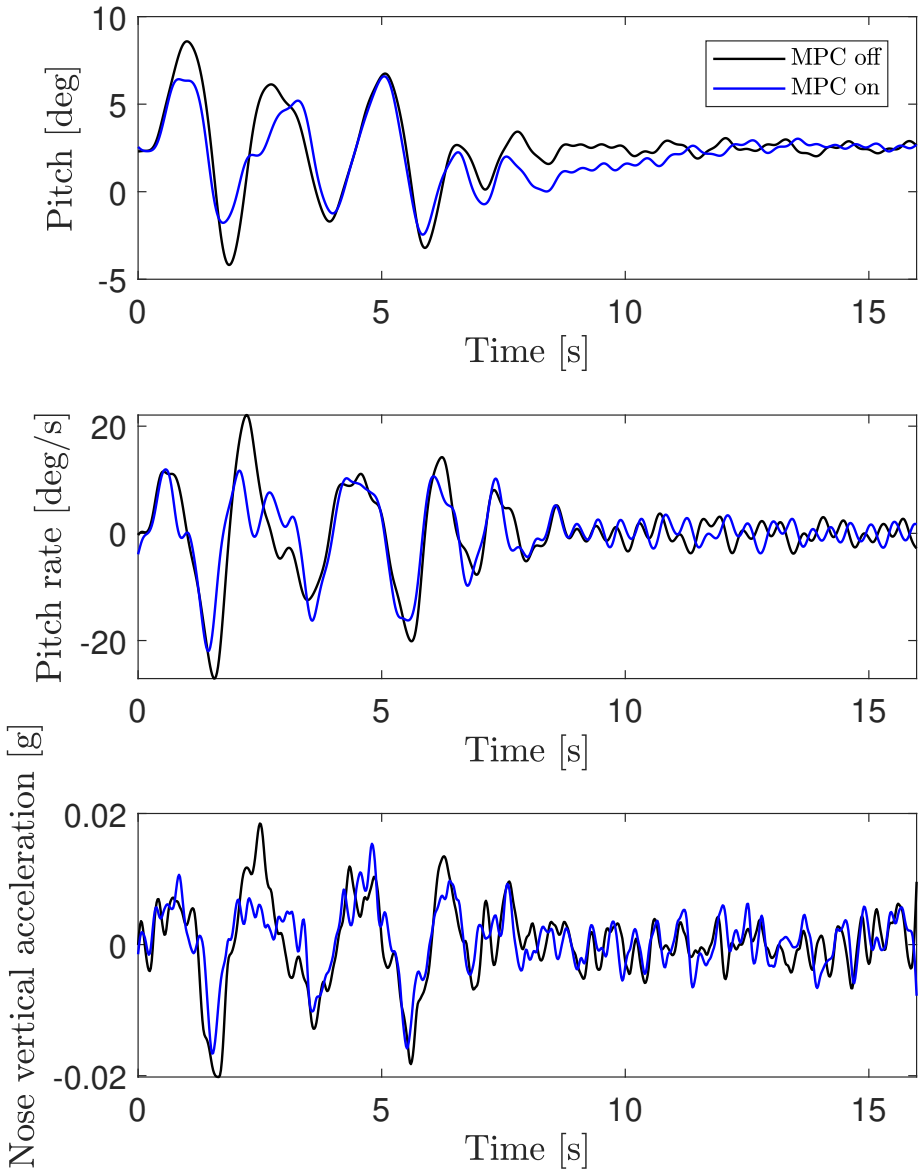

Figure H.31: MVS, 3 cycles, MLA constraints on wing and HTP (TestID 554). Pitch angle, pitch rate, and vertical acceleration at nose.

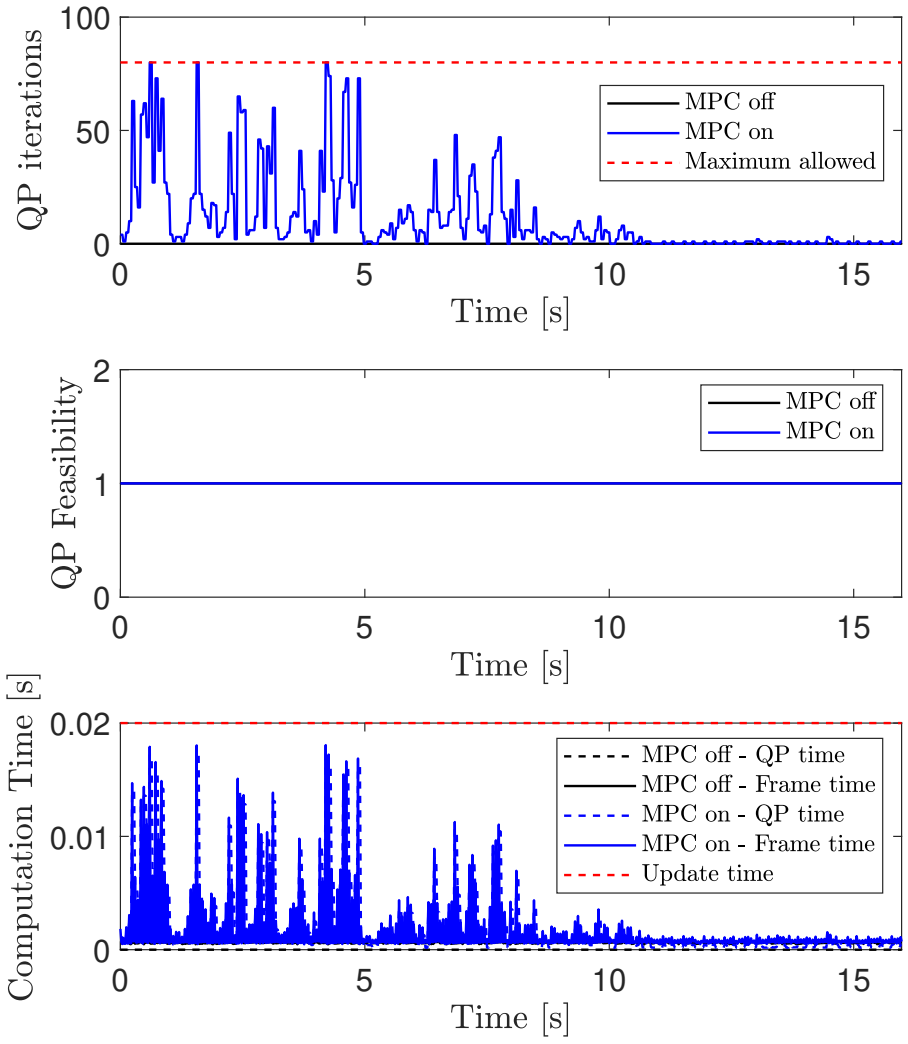

Figure H.32: MVS, 3 cycles, MLA constraints on wing and HTP (TestID 554). Computational time and optimization solver performance.

BIBLIOGRAPHY

[1] Xu, J. and Kroo, I., "Aircraft Design with Maneuver and Gust Load Alleviation," *29th AIAA Applied Aerodynamics Conference*, June 2011, pp. 1–15.

[2] Fabre, P., Tron, X. L., and Lacoste, P., "System for Reducing the Forces Applied to Wings and Particularly to the Root of the Wings of an Aircraft in Flight," *United States Patent US5186416*, No. 90, 1993.

[3] Blanc, S. and Humbert, M., "Method and Device for Reducing Actual Loads Generated on Airplane by an Aerodynamic Disturbance," *United States Patent US8374735*, No. 12, 2013.

[4] Shearer, C. M. and Cesnik, C. E. S., "Nonlinear Flight Dynamics of Very Flexible Aircraft," *Journal of Aircraft*, Vol. 44, No. 5, September 2007, pp. 1528–1545.

[5] Lanchares, M., Kolmanovsky, I., Cesnik, C. E., and Vetrano, F., "Model Order Reduction for Coupled Nonlinear Aeroelastic-Flight Mechanics of Very Flexible Aircraft," *International Forum on Aeroelasticity and Structural Dynamics - IFASD*, Savannah, Georgia, USA, June 2019.

[6] Duan, M., Cesnik, C. E., Kolmanovsky, I. V., and Vetrano, F., "Nonlinear Control-oriented Modeling for Very Flexible Aircraft," *AIAA Scitech 2021 Forum*, 2021, p. 1501.

[7] European Aviation Safety Agency , "Certification Specifications for Large Aeroplanes, CS25," 2009.

[8] Vrancken, P. S., "Airborne Remote Detection of Turbulence with Forward-pointing LIDAR," *Aviation Turbulence*, Springer, 2016, pp. 443–464.

[9] Cesnik, C. E. S. and Su, W., "Nonlinear Aeroelastic Simulation of X-HALE: a Very Flexible UAV," *49th AIAA Aerospace Sciences Meeting Including the New Horizons Forum and Aerospace Exposition*, Orlando, Florida, USA, January 2011, pp. 1–13.

[10] Airbus, "Zephyr: The first stratospheric UAS of its kind," *https://www.airbus.com/en/products-services/defence/uas/uas-solutions/zephyr*, Airbus, April 2022.

[11] Airbus, "ZEROe: Towards the World's First Zero-emission Commercial Aircraft," *https://www.airbus.com/en/innovation/zero-emission/hydrogen/zeroe*, Airbus, January 2022.

[12] Cesnik, C. E. S., Palacios, R., and Reichenbach, E. Y., "Reexamined Structural Design Procedures for Very Flexible Aircraft," *Journal of Aircraft*, Vol. 51, No. 5, September 2014, pp. 1580–1591.

[13] Simpson, R. J., Palacios, R., Hesse, H., and Goulart, P., "Predictive Control for Alleviation of Gust Loads on Very Flexible Aircraft," *55th AIAA/ASME/ASCE/AHS/SC Structures, Structural Dynamics, and Materials Conference*, National Harbor, Maryland, USA, January 2014, pp. 1–25.

[14] Giesseler, H. G., Kopf, M., Varutti, P., Faulwasser, T., and Findeisen, R., "Model Predictive Control for Gust Load Alleviation," *4th IFAC Conference on Nonlinear Model Predictive Control*, Vol. 4, IFAC, Noordwijkerhout, Netherlands, August 2012, pp. 27–32.

[15] Chiu, S., Chand, S., Moore, D., and Chaudhary, A., "Fuzzy Logic for Control of Roll and Moment for a Flexible Wing Aircraft," *IEEE Control Systems*, Vol. 11, No. 4, 1990, pp. 42 – 48.

[16] White, R., "Improving the Airplane Efficiency by Use of Wing Maneuver Load Alleviation," *Journal of Aircraft*, Vol. 8, No. 10, 1971, pp. 769–775.

[17] Yang, Y., Wu, Z., and Yang, C., "Control Surface Efficiency Analysis and Utilization of an Elastic Airplane for Maneuver Loads Alleviation," *54th AIAA/ASME/ASCE/AHS/ASC Structures, Structural Dynamics, and Materials Conference*, Boston, Massachusetts, USA, April 2013, pp. 1–7.

[18] Lei, X., Zheyu, Z., Shaojie, Z., Tao, L., and Modeling, A. A., "Gust Load Alleviation of Civil Aircraft Based on Model Prediction Control," *Guidance, Navigation and Control Conference (CGNCC)*, Nanjing, China, Aug. 2016, pp. 2198–2202.

[19] Gaulocher, S. L., Roos, C., and Cumer, C., "Aircraft Load Alleviation During Maneuvers Using Optimal Control Surface Combinations," *Journal of Guidance, Control, and Dynamics*, Vol. 30, No. 2, 2007, pp. 591–600.

[20] Duan, M., Kolmanovsky, I. V., and Cesnik, C. E., "Maneuver Load Alleviation of Very Flexible Aircraft via Nonlinear Decoupling Control," *AIAA Scitech 2021 Forum*, January 2021, p. 0501.

[21] Woods-Vedeler, J., Pototzky, A., and Hoadley, S., "Rolling Maneuver Load Alleviation using active controls," *Journal of Aircraft*, Vol. 32, No. 1, 1995, pp. 68–76.

[22] Andrews, S. P., *Modelling and Simulation of Flexible Aircraft: Handling Qualities with Active Load Control*, Ph.D. thesis, Cranfield University, Cranfield, UK, 2011.

[23] Maraniello, S., Simpson, R. J., and Palacios, R., "Optimal Manoeuvres with Very Flexible Wings," *Proceedings of 57th AIAA/ASCE/AHS/ASC Structures, Structural Dynamics, and Materials Conference*, Reston, Virginia, January 2016, pp. 1–17.

[24] Avanzini, G., Capello, E., Piacenza, I. a., Quagliotti, F., and Torino, P., "L1 Adaptive Control of Flexible Aircraft : Preliminary Results," *AIAA Atmospheric Flight Mechanics Conference*, August 2010, pp. 1–19.

[25] Che, J., Gregory, I., and Cao, C., "Integrated Flight/Structural Mode Control for Very Flexible Aircraft Using L1 Adaptive Output Feedback Controller," *AIAA Guidance, Navigation, and Control Conference*, AIAA, Minneapolis, Minnesota, 2012, pp. 1–19.

[26] Fan, W., Liu, H. H. T., and Kwong, R. H. S., "Gain-Scheduling Control of Flexible Aircraft with Actuator Saturation and Stuck Faults," *Journal of Guidance, Control, and Dynamics*, Vol. 40, No. 3, 2017, pp. 510–520.

[27] Gibson, T. E., Annaswamy, A. M., and Lavretsky, E., "Modeling for Control of Very Flexible Aircraft," *Proceedings of AIAA Guidance, Navigation, and Control Conference*, August 2011, pp. 1–19.

[28] Qu, Z., Annaswamy, A. M., and Lavretsky, E., "Adaptive Output-Feedback Control for a Class of Multi-Input-Multi-Ooutput Plants with Applications to Very Flexible Aircraft," *American Control Conference (ACC)*, July 2016, pp. 1613–1618.

[29] Qu, Z. and Annaswamy, A. M., "Adaptive Output-Feedback Control with Closed-Loop Reference Models for Very Flexible Aircraft," *Journal of Guidance, Control, and Dynamics*, Vol. 39, No. 4, 2015, pp. 873–888.

[30] Qu, Z., Lavretsky, E., and Annaswamy, A. M., "An Adaptive Controller for Very Flexible Aircraft," *AIAA Guidance, Navigation, and Control (GNC) Conference*, AIAA, Reston, Virginia, August 2013, pp. 1–11.

[31] Nguyen, N. and Hashemi, K., "Performance Optimizing Adaptive Control with Time-Varying Reference Model Modification," *18th Eighteenth Yale Workshop on Adaptive and Learning Systems*, New Haven, Connecticut, USA, June 2017, pp. 1–6.

[32] Li, H., Zhao, Y., and Hu, H., "Adaptive Maneuver Load Alleviation via Recurrent Neural Networks," *Journal of Guidance, Control, and Dynamics*, Vol. 40, No. 7, 2017, pp. 1821–1828.

[33] Lavretsky, E. Y. and Henderson, D. K., "A Neural Network-Based Approach to Active Structural Mode Suppression for Flexible Transport Aircraft," *Proceedings of American Control Conference*, San Diego, California, USA, June 1999, pp. 4168–4172.

[34] Mclean, D., "Neural Control of an Aircraft Load Alleviation cControl System," *Transactions of the Institute of Measurement and Control*, Vol. 18, No. 5, 1996, pp. 247–261.

[35] Noll, T. E., Brown, J. M., Perez-Davis, M. E., Ishmael, S. D., Tiffany, G. C., and Gaier, M., "Investigation of the Helios Prototype Aircraft Mishap. Volume 1: Mishap Report," Tech. Rep. January, NASA Langley Research Center, Virginia, 2004.

[36] McLean, D., "Gust-Alleviation Control Systems for Aircraft," *Proceedings of the Institution of Electrical Engineers*, Vol. 125, No. 7, 1978, pp. 675–685.

[37] Dillsaver, M. J., Cesnik, C. E. S., and Kolmanovsky, I. V., "Gust Load Alleviation Control for Very Flexible Aircraft," *AIAA Atmospheric Flight Mechanics Conference*, AIAA 2011-6368, Portland, Oregon, USA, August 2011.

[38] Sprater, A., "Stabilizing Device for Flying-machines." *United States Patent 1,119,324*, 1914.

[39] Regan, C. D. and Jutte, C. V., "Survey of Applications of Active Control Technology for Gust Alleviation and New Challenges for Lighter-weight Aircraft," Tech. Rep. April, NASA, 2012.

[40] Dillsaver, M., Cesnik, C., and Kolmanovsky, I., "Gust Response Sensitivity Characteristics of Very Flexible Aircraft," *AIAA Atmospheric Flight Mechanics Conference*, August 2012, pp. 1–20.

[41] Fabre-Raimbault, N., Adurno, M., Berthereau, M., and Cote, S., "Method and Device for Dynamically Alleviating Loads Generated on An Airplane," *United States Patent US8000845*, No. 12, 2011.

[42] Kopf, M., Giesseler, H. G., Varutti, P., Faulwasser, T., and Findeisen, R., "On the Effect of Enforcing Stability in Model Predictive Control for Gust Load Alleviation," *American Control Conference*, Chicago, Illinois, USA, 2015, pp. 2329–2334.

[43] Kopf, M., Bullinger, E., Giesseler, H. G., Adden, S., and Findeisen, R., "Model Predictive Control for Aircraft Load Alleviation: Opportunities and Challenges," *2018 Annual American Control Conference (ACC)*, IFAC, Milwaukee, Wisconsin, USA, June 2018, pp. 2417–2424.

[44] Artola, M., Goizueta, N., Wynn, A., and Palacios, R., "Modal-based Nonlinear Estimation and Control for Highly Flexible Aeroelastic Systems," *AIAA Scitech 2020 Forum*, 2020, p. 1192.

[45] Artola, M., Goizueta, N., Wynn, A., and Palacios, R., "Proof of Concept for a Hardware-in-the-Loop Nonlinear Control Framework for Very Flexible Aircraft," *AIAA Scitech 2021 Forum*, 2021, p. 1392.

[46] Haghighat, S., Liu, H. H. T., and Martins, J. R., "Model-Predictive Gust Load Alleviation Controller for a Highly Flexible Aircraft," *Journal of Guidance, Control, and Dynamics*, Vol. 35, No. 6, 2012, pp. 1751–1766.

[47] Wang, Y., Wynn, A., and Palacios, R., "Nonlinear Modal Aeroservoelastic Analysis Framework for Flexible Aircraft," *AIAA Journal*, Vol. 54, No. 10, October 2016, pp. 3075–3090.

[48] Hansen, J. H., Duan, M., Kolmanovsky, I., and Cesnik, C. E., "Control Allocation for Maneuver and Gust Load Alleviation of Flexible Aircraft," *AIAA Scitech 2020 Forum*, January 2020, p. 1186.

[49] Barzgaran, B., Quenzer, J. D., Mesbahi, M., Morgansen, K. A., and Livne, E., "Real-time Model Predictive Control for Gust Load Alleviation on an Aeroelastic Wind Tunnel Test Article," *AIAA SciTech 2021 Forum*, 2021, p. 0500.

[50] Dillsaver, M. J., Kalabic, U. V., Kolmanovsky, I. V., and Cesnik, C. E. S., "Constrained Control of Very Flexible Aircraft Using Reference and Extended Command Governors," *2013 American Control Conference*, IEEE, Washington, DC, USA, June 2013, pp. 1608–1613.

[51] Köthe, A., Luckner, R., González Ramirez, P. J., Silvestre, F. J., Pang, Z. Y., and Cesnik, C. E., "Development of Robust Flight Control Laws for a Highly Flexible Aircraft in the Frequency Domain," *AIAA Atmospheric Flight Mechanics Conference*, American Institute of Aeronautics and Astronautics, Reston, Virginia, June 2016, pp. 1–23.

[52] Gonzalez, P. J., Silvestre, F. J., Paglione, P., Köthe, A., Pang, Z. Y., and Cesnik, C. E. S., "Linear Control of Highly Flexible Aircraft based on Loop Separation," *AIAA Atmospheric Flight Mechanics Conference*, Washington, D.C., USA, June 2016, pp. 1–26.

[53] Theis, J., Pfifer, H., and Seiler, P. J., "Robust Control Design for Active Flutter Suppression," *AIAA Atmospheric Flight Mechanics Conference*, January 2016.

[54] González, P. J., Silvestre, F. J., Pereira, M. d. F. V., Pang, Z. Y., and Cesnik, C. E., "Loop-Separation Control for Very Flexible Aircraft," *AIAA Journal*, Vol. 58, No. 9, 2020, pp. 3819–3834.

[55] Aouf, N., Boulet, B., and Botez, R. M., "Robust Gust Load Alleviation for a Flexible Aircraft," *Canadian Aeronautics and Space Journal*, Vol. 46, No. 3, 2000, pp. 131–139.

[56] Cook, R. G., Palacios, R., and Goulart, P., "Robust Gust Alleviation and Stabilization of Very Flexible Aircraft," *AIAA Journal*, Vol. 51, No. 2, February 2013, pp. 330–340.

[57] Fezans, N. and Joos, H.-D., "Combined Feedback and LIDAR-based Feedforward Active Load Alleviation," *AIAA Atmospheric Flight Mechanics Conference*, 2017, p. 3548.

[58] Khalil, A. and Fezans, N., "Performance Enhancement of Gust Load Alleviation Systems for Flexible Aircraft Using H_∞ Optimal Control with Preview," *AIAA Scitech 2019 Forum*, 2019, p. 0822.

[59] Khalil, A. K. A. and Fezans, N., "A Multi-channel H_∞ Preview control approach to Load Alleviation Design for Flexible Aircraft," *CEAS Aeronautical Journal*, 2021, pp. 401–412.

[60] Cavaliere, D., Fezans, N., Kiehn, D., Quero, D., and Vrancken, P., "Gust Load Control Design Challenge Including LIDAR Wind Measurements and Based on the Common Research Model," *AIAA Scitech 2022 Forum*, 2022, p. 1934.

[61] Fournier, H., Massioni, P., Tu Pham, M., Bako, L., Vernay, R., and Colombo, M., "Robust Gust Load Alleviation of Flexible Aircraft Equipped with LIDAR," *Journal of Guidance, Control, and Dynamics*, Vol. 45, No. 1, 2022, pp. 58–72.

[62] Botez, R. M., Boustani, I., Vayani, N., Bigras, P., and Wong, T., "Optimal Control Laws for Gust Alleviation," *Canadian Aeronautics and Space Journal*, Vol. 47, No. 1, 2001, pp. 1–6.

[63] Dillsaver, M., Cesnik, C. E., and Kolmanovsky, I., "Trajectory Control of Very Flexible Aircraft with Gust Disturbance," *AIAA Atmospheric Flight Mechanics (AFM) Conference*, 2013.

[64] Liu, X. and Sun, Q., "Improved LQG Method for Active Gust Load Alleviation," *Journal of Aerospace Engineering*, Vol. 30, No. 4, 2017, pp. 1 –13.

[65] Zeng, J., Moulin, B., Callafon, R. D., and Brenner, M., "Adaptive Feedforward Control for Gust Load Alleviation," *Journal of Guidance, Control, and Dynamics*, Vol. 33, No. 3, 2010, pp. 862–872.

[66] Gregory, I. M., "Dynamic Inversion to Control Large Flexible Transport Aircraft," *AIAA Guidance, Navigation and Control Conference*, 1998, pp. 1224–1232.

[67] Gregory, I. M., "Modified Dynamic Inversion to Control Large Flexible Aircraft - What's Going On?" *AIAA Guidance, Navigation, and Control Conference*, American Institute of Aeronautics and Astronautics, Portland, Oregon, 1991, pp. 1–11.

[68] Gregory, I. M., "Stability Result for Dynamic Inversion Devised to Control Large Flexible Aircraft," *AIAA Guidance, Navigation, and Control Conference and Exhibit*, August 2001, pp. 1–13.

[69] Shearer, C. M. and Cesnik, C. E. S., "Trajectory Control for Very Flexible Aircraft," *Journal of Guidance, Control, and Dynamics*, Vol. 31, August 2008, pp. 340–357.

[70] Caverly, R. J., Girard, A. R., Kolmanovsky, I. V., and Forbes, J. R., "Nonlinear Dynamic Inversion of a Flexible Aircraft," *20th IFAC Symposium on Automatic Control in Aerospace*, Vol. 49, No. 17, 2016, pp. 338–342.

[71] Choroszucha, R. B. and Sun, J., "Empirical Riccati Covariance Matrices for Closed-Loop Model Order Reduction of Nonlinear Systems by Balanced Truncation," *American Control Conference (ACC)*, 2017, pp. 3476–3482.

[72] Hjartarson, A., Seiler, P. J., and Balas, G. J., "LPV Aeroservoelastic Control Using the LPVTools Toolbox," *AIAA Atmospheric Flight Mechanics (AFM) Conference*, 2013, pp. 1–25.

[73] Knoblach, A., Pfifer, H., and Seiler, P. J., "Worst Case Analysis of a Saturated Gust Loads Alleviation System," *AIAA Guidance, Navigation, and Control Conference*, January 2015, pp. 1–12.

[74] Seiler, P., Balas, G., and Moreno, C., "Linear Parameter Varying Control for the X-53 Active Aeroelastic Wing," *AIAA Atmospheric Flight Mechanics Conference*, August 2011.

[75] Shearer, C. M., *Coupled Nonlinear Flight Dynamics, Aeroelasticity, and Control of Very Flexible Aircraft*, Ph.D. thesis, University of Michigan, Ann Arbor, Michigan, USA, 2006.

[76] Su, W., *Coupled Nonlinear Aeroelasticity and Flight Dynamics of Fully Flexible Aircraft*, Ph.D. thesis, University of Michigan, Ann Arbor, Michigan, USA, 2008.

[77] Su, W. and Cesnik, C. E. S., "Nonlinear Aeroelasticity of a Very Flexible Blended-Wing-Body Aircraft," *Journal of Aircraft*, Vol. 47, No. 5, September 2010, pp. 1539–1553.

[78] Peters, D. A. and Johnson, M. J., "Finite-State Airloads for Deformable Airfoils on Fixed and Rotating Wings," *Symposium on Aeroelasticity and Fluid/Structure Interaction, ASME Winter Annual Meeting*, 1994, pp. 1–28.

[79] Pang, Z. Y., *Modeling, Simulation and Control of Very Flexible Unmanned Aerial Vehicle*, Ph.D. thesis, University of Michigan, Ann Arbor, Michigan, USA, 2018.

[80] Su, W. and Cesnik, C. E. S., "Strain-based Geometrically Nonlinear Beam Formulation for Modeling Very Flexible Aircraft," *International Journal of Solids and Structures*, Vol. 48, 2011, pp. 2349 – 2360.

[81] Lupp, C., *Inclusion of Geometrically Nonlinear Aeroelastic Effects into Gradient-Based Aircraft Optimization*, Ph.D. thesis, University of Michigan, Ann Arbor, Michigan, USA, 2020.

[82] Riso, C., Sanghi, D., Cesnik, C. E., Vetrano, F., and Teufel, P., "Parametric Roll Maneuverability Analysis of a High-aspect-ratio-wing Civil Transport Aircraft," *AIAA Scitech 2020 Forum*, 2020, p. 1191.

[83] Cesnik, C. E. S., Senatore, P. J., Su, W., Atkins, E. M., and Shearer, C. M., "X-HALE: A Very Flexible Unmanned Aerial Vehicle for Nonlinear Aeroelastic Tests," *AIAA Journal*, Vol. 50, No. 12, 2012, pp. 2820–2833.

[84] Mayne, D. Q., Rawlings, J. B., Rao, C. V., and Scokaert, P. O. M., "Constrained Model Predictive Control: Stability and Optimality," *Automatica*, Vol. 36, No. 6, 2000, pp. 789–814.

[85] Limón, D., Alamo, T., Salas, F., and Camacho, E. F., "On the Stability of Constrained MPC without Terminal Constraint," *IEEE Transactions on Automatic Control*, Vol. 51, No. 5, 2006, pp. 832–836.

[86] Liao-McPherson, D., Nicotra, M. M., and Kolmanovsky, I. V., "Time-distributed Optimization for Real-time Model Predictive Control: Stability, Robustness, and Constraint Satisfaction," *Automatica*, Vol. 117, 2020, pp. 108973.

[87] Ferreau, H., Kirches, C., Potschka, A., Bock, H., and Diehl, M., "qpOASES: A Parametric Active-set Algorithm for Quadratic Programming," *Mathematical Programming Computation*, Vol. 6, No. 4, 2014, pp. 327–363.

[88] Schmid, C. and Biegler, L., "Quadratic programming methods for reduced Hessian SQP," *Computers & Chemical Engineering*, Vol. 18, 1994, pp. 817–832.

[89] Liao-McPherson, D. and Kolmanovsky, I. V., "FBstab: A Proximally Stabilized Semismooth Algorithm for Convex Quadratic Programming," *Automatica*, Vol. 113, 2020, pp. 108801.

[90] Cagienard, R., Grieder, P., Kerrigan, E. C., and Morari, M., "Move Blocking Strategies in Receding Horizon Control," *Journal of Process Control*, Vol. 17, No. 6, 2007, pp. 563–570.

[91] Grüne, L. and Pannek, J., "Nonlinear Model Predictive Control," *Nonlinear Model Predictive Control*, Springer, 2017, pp. 45–69.

[92] Wang, Y. and Boyd, S., "Fast Model Predictive Control using Online Optimization," *IEEE Transactions on Control Systems Technology*, Vol. 18, No. 2, 2010, pp. 267–278.

[93] Bemporad, A., Morari, M., Dua, V., and Pistikopoulos, E. N., "The Explicit Linear Quadratic Regulator for Constrained Systems," *Automatica*, Vol. 38, No. 1, 2002, pp. 3–20.

[94] VanAntwerp, J. G. and Braatz, R. D., "Fast Model Predictive Control of Sheet and Film Processes," *IEEE Transactions on Control Systems Technology*, Vol. 8, No. 3, 2000, pp. 408–417.

[95] Lambe, A. B., Kennedy, G. J., and Martins, J. R. R. A., "An Evaluation of Constraint Aggregation Strategies for Wing Box Mass Minimization," *Structural and Multidisciplinary Optimization*, Vol. 55, No. 1, 2017, pp. 257–277.

[96] Kennedy, G. J. and Hicken, J. E., "Improved Constraint Aggregation Methods," *Computer Methods in Applied Mechanics and Engineering*, Vol. 289, 2015, pp. 332–354.

[97] Bloss, K. F., Biegler, L. T., and Schiesser, W. E., "Dynamic Process Optimization through Adjoint Formulations and Constraint Aggregation," *Industrial & Engineering Chemistry Research*, Vol. 38, No. 2, 1999, pp. 421–432.

[98] Jeon, M., "Parallel Optimal Control with Multiple Shooting, Constraints Aggregation and Adjoint Methods," *Journal of Applied Mathematics and Computing*, Vol. 19, No. 1-2, 2005, pp. 215.

[99] Li, S. and Ge, Y., "A Numerical Computation Approach for the Optimal Control of ASP Flooding Based on Adaptive Strategies," *Mathematical Problems in Engineering*, 2018.

[100] Richards, A., "Fast Model Predictive Control with Soft Constraints," *European Journal of Control*, Vol. 25, 2015, pp. 51–59.

[101] Kreisselmeier, G. and Steinhauser, R., "Systematic Control Design by Optimizing a Vector Performance Index," *Computer Aided Design of Control Systems*, 1980, pp. 113–117.

[102] Kreisselmeier, G. and Steinhauser, R., "Application of Vector Performance Optimization to a Robust Control Loop Design for a Fighter Aircraft," *International Journal of Control*, Vol. 37, No. 2, 1983, pp. 251–284.

[103] Raspanti, C. G., Bandoni, J. A., and Biegler, L. T., "New Strategies for Flexibility Analysis and Design under Uncertainty," *Computers & Chemical Engineering*, Vol. 24, No. 9-10, 2000, pp. 2193–2209.

[104] Poon, N. M. K. and Martins, J. R. R. A., "An Adaptive Approach to Constraint Aggregation using Adjoint Sensitivity Analysis," *Structural and Multidisciplinary Optimization*, Vol. 34, No. 1, 2007, pp. 61–73.

[105] Dontchev, A. L., Kolmanovsky, I. V., Krastanov, M. I., Nicotra, M., and Veliov, V. M., "Lipschitz Stability in Discretized Optimal Control with Application to SQP," *SIAM Journal on Control and Optimization*, Vol. 57, No. 1, 2019, pp. 468–489.

[106] Dinh, Q. T., Savorgnan, C., and Diehl, M., "Adjoint-based Predictor-corrector Sequential Convex Programming for Parametric Nonlinear Optimization," *SIAM Journal on Optimization*, Vol. 22, No. 4, 2012, pp. 1258–1284.

[107] Pereira, M. F. V., Kolmanovsky, I. V., Cesnik, C. E. S., and Vetrano, F., "Model Predictive Control for Maneuver Load Alleviation in Flexible Airliners," *International Forum on Aeroelasticity and Structural Dynamics - IFASD*, Savannah, Georgia, 2019.

[108] Pereira, M. F. V., Kolmanovsky, I. V., and Cesnik, C. E. S., "Model Predictive Control with Constraint Aggregation Applied to Conventional and Very Flexible Aircraft," *58th Conference on Decision and Control (CDC)*, IEEE, Nice, France, 2019, pp. 1–7.

[109] Boyd, S., Boyd, S. P., and Vandenberghe, L., *Convex Optimization*, Cambridge University Press, 2004.

[110] Cimini, G. and Bemporad, A., "Exact Complexity Certification of Active-set Methods for Quadratic Programming," *IEEE Transactions on Automatic Control*, Vol. 62, No. 12, 2017, pp. 6094–6109.

[111] Diehl, M., Bock, H. G., and Schlöder, J. P., "A Real-time Iteration Scheme for Nonlinear Optimization in Optimal Feedback Control," *SIAM Journal on Control and Optimization*, Vol. 43, No. 5, 2005, pp. 1714–1736.

[112] Argyros, I. K., *Convergence and Applications of Newton-type Iterations*, Springer Science & Business Media, 2008.

[113] Dontchev, A. L., Huang, M., Kolmanovsky, I. V., and Nicotra, M. M., "Inexact Newton-Kantorovich Methods for Constrained Nonlinear Model Predictive Control," *IEEE Transactions on Automatic Control*, 2018.

[114] Bock, H. G., "Recent Advances in Parameter Identification Techniques for ODE," *Numerical Treatment of Inverse Problems in Differential and Integral Equations*, 1983, pp. 95–121.

[115] Andersson, J. A. E., Gillis, J., Horn, G., Rawlings, J. B., and Diehl, M., "CasADi: A Software Framework for Nonlinear Optimization and Optimal Control," *Mathematical Programming Computation*, Vol. 11, No. 1, 2019, pp. 1–36.

[116] Goldfarb, D. and Idnani, A., "A Numerically Stable Dual Method for Solving Strictly Convex Quadratic Programs," *Mathematical Programming*, Vol. 27, No. 1, 1983, pp. 1–33.

[117] Nocedal, J. and Wright, S., *Numerical Optimization*, Springer Science & Business Media, 2006.

[118] Limon, D., Alamo, T., Raimondo, D., De La Peña, D. M., Bravo, J., Ferramosca, A., and Camacho, E., "Input-to-state Stability: a Unifying Framework for Robust Model Predictive Control," *Nonlinear Model Predictive Control*, Springer, 2009, pp. 1–26.

[119] Mayne, D. Q., Kerrigan, E. C., and Falugi, P., "Robust Model Predictive Control: Advantages and Disadvantages of Tube-based Methods," *IFAC Proceedings Volumes*, Vol. 44, No. 1, 2011, pp. 191–196.

[120] Mayne, D. Q., Kerrigan, E. C., Van Wyk, E., and Falugi, P., "Tube-based Robust Nonlinear Model Predictive Control," *International Journal of Robust and Nonlinear Control*, Vol. 21, No. 11, 2011, pp. 1341–1353.

[121] Mayne, D. Q., Raković, S., Findeisen, R., and Allgöwer, F., "Robust Output Feedback Model Predictive Control of Constrained Linear Systems," *Automatica*, Vol. 42, No. 7, 2006, pp. 1217–1222.

[122] Calafiore, G. C. and Fagiano, L., "Stochastic Model Predictive Control of LPV Systems via Scenario Optimization," *Automatica*, Vol. 49, No. 6, 2013, pp. 1861–1866.

[123] Calafiore, G. C. and Fagiano, L., "Robust Model Predictive Control via Scenario Optimization," *IEEE Transactions on Automatic Control*, Vol. 58, No. 1, 2012, pp. 219–224.

[124] Burlion, L., Poussot-Vassal, C., Vuillemin, P., Leitner, M., and Kier, T., "Longitudinal Manoeuvre Load Control of a Flexible Large-Scale Aircraft," *Proceedings of the 19th World Congress - The International Federation of Automatic Control (IFAC)*, Vol. 19, IFAC, Cape Town, South Africa, Aug. 2014, pp. 3413–3418.

[125] Molent, L., "A Unified Approach to Fatigue Usage Monitoring of Fighter Aircraft Based on F/A-18 Experience," *Proc. ICAS*, Vol. 98, 1998.

[126] Lustosa, L. R., Kolmanovsky, I., Cesnik, C. E., and Vetrano, F., "Aided Inertial Estimation of Wing Shape," *Journal of Guidance, Control, and Dynamics*, Vol. 44, No. 2, 2021, pp. 210–219.

[127] Pereira, M. F. V., Kolmanovsky, I. V., Cesnik, C. E. S., and Vetrano, F., "Model Predictive Control Architectures for Maneuver Load Alleviation in Very Flexible Aircraft," *AIAA SciTech 2019 Forum*, San Diego, USA, 2019, p. 1591.

[128] Pereira, M. F. V., Kolmanovsky, I. V., Cesnik, C. E., and Vetrano, F., "Time-distributed Scenario-based Model Predictive Control Approach for Flexible Aircraft," *AIAA Scitech 2021 Forum*, 2021, p. 0502.

[129] Hoblit, F. M., *Gust Loads on Aircraft: Concepts and Applications*, American Institute of Aeronautics and Astronautics, 1988.

[130] Etkin, B., *Dynamics of Atmospheric Flight*, John Wiley & Sons, 1972.

[131] Van Staveren, W. H. J. J., *Analyses of Aircraft Responses to Atmospheric Turbulence.*, Ph.D. thesis, Delft University of Technology, 2004.

[132] Wang, X., Van Kampen, E., Chu, Q., and De Breuker, R., "Flexible Aircraft Gust Load Alleviation with Incremental Nonlinear Dynamic Inversion," *Journal of Guidance, Control, and Dynamics*, Vol. 42, No. 7, 2019, pp. 1519–1536.

[133] Fezans, N., Joos, H.-D., and Deiler, C., "Gust Load Alleviation for a Long-range Aircraft with and without Anticipation," *CEAS Aeronautical Journal*, 2019, pp. 1–25.

[134] Cesnik, C. E. S., Pajon, M., Monteiro, B. B., Pereira, M. F. V., Chaves, G. B., Bertolin, R. M., Riso, C., Versiani, T. S. S., and Kolmanovsky, I. V., "Enhanced Aero-Servo-Elastic (EASE) Wind tunnel Model for Investigating Maneuver Load Alleviation Controllers," *International Forum on Aeroelasticity and Structural Dynamics - IFASD*, 2022.

[135] Drela, M. and Youngren, H., "AVL Overview," *https://web.mit.edu/drela/Public/web/avl/l*, MIT, 2004.

[136] Bonnans, J. F. and Shapiro, A., *Perturbation Analysis of Optimization Problems*, Springer Science & Business Media, 2000.

[137] Robinson, S. M., "Strongly Regular Generalized Equations," *Mathematics of Operations Research*, Vol. 5, No. 1, 1980, pp. 43–62.

[138] Bonnans, J. F. and Sulem, A., "Pseudopower Expansion of Solutions of Generalized Equations and Constrained Optimization Problems," *Mathematical Programming*, Vol. 70, No. 1-3, 1995, pp. 123–148.

[139] Bonnans, J. F. and Shapiro, A., "Optimization Problems with Perturbations: A Guided Tour," *SIAM Review*, Vol. 40, No. 2, 1998, pp. 228–264.

[140] Campi, M. C., Garatti, S., and Prandini, M., "Scenario Optimization for MPC," *Handbook of Model Predictive Control*, Springer, 2019, pp. 445–463.